DISSERTATION

SPACED-GNSS RECEIVER TECHNIQUES FOR IONOSPHERIC IRREGULARITY DRIFT VELOCITY AND HEIGHT ESTIMATION BASED ON HIGH-LATITUDE GNSS SCINTILLATION

Submitted by

Jun Wang

Department of Electrical and Computer Engineering

In partial fulfillment of the requirements

For the Degree of Doctor of Philosophy

Colorado State University

Fort Collins, Colorado

Summer 2018

Doctoral Committee:

Advisor: Y. Jade Morton

Charles Rino
J. Rockey Luo
Olivier Pinaud

ABSTRACT

SPACED-GNSS RECEIVER TECHNIQUES FOR IONOSPHERIC IRREGULARITY DRIFT VELOCITY AND HEIGHT ESTIMATION BASED ON HIGH-LATITUDE GNSS SCINTILLATION

Spaced-GNSS receiver measurements offer an inexpensive approach for remote-sensing the ionospheric irregularity drift velocity during ionospheric scintillations. Conventional approaches targeting equatorial amplitude scintillations are less applicable in high latitude regions where phase scintillations are more prominent. This dissertation demonstrates spaced-receiver techniques that use multi-GNSS carrier phase measurements to estimate irregularity drift velocity and effective irregularity height at high latitudes during scintillations. A time-domain method and a time-frequency domain method are implemented to extract time lag information between receiver pairs when observing the same irregularity structure. Based on the front velocity model and the anisotropy model, a hybrid correlation model is developed to account for the topology of the diffraction pattern induced by the irregularity. From the time lag information, the hybrid correlation model and known satellite-receiver geometry, the irregularity drift velocity can be obtained. In addition, an inversion technique for estimating the effective height of the irregularity is developed based on the anisotropy model. These techniques are applied to data collected by two GNSS receiver-arrays in Alaska, one at Gakona and the other at the Poker Flat Research Range. The GNSS-estimated drift velocities at Poker Flat are in general agreement with the measurements from the co-located incoherent scatter radar and the All-sky Imager. The effective height estimates also compared favorably against the incoherent scatter radar measurements.

ACKNOWLEDGEMENTS

The author sincerely thanks Dr. Y. Jade Morton for her support and guidance. The author would like to extend his thanks to Dr. Charles Rino, Dr. Margaret Cheney, Dr. Olivier Pinaud and Dr. J. Rockey Luo, as well as Harrison Bourne, Brian Breitsch, Steve Taylor, Yu Jiao, Dongyang Xu, Rong Yang, Ian Collett, Greg Myer, Robert Steenburgh and Kaixuan Kang for their time and effort. This project is supported by an AFOSR grant (FA9550-14-1-0265). The GNSS array was established with funding from AFOSR (FA9550-10-1-0346) and AFRL (FA8650-09-D-1451). The PFISR data is provided by the Madrigal database (http://isr.sri.com/madrigal). The PFISR is operated by SRI International on behalf of the US National Science Foundation under NSF Cooperative Agreement AGS-1133009. The Kp and Q/D days indices are obtained from the WDC for Geomagnetism operated by the Kyoto University (http://wdc.kugi.kyoto-u.ac.jp). The SSC information is available from the Ebre Observatory (http://www.obsebre.es/en/rapid), entrusted by the International Association of Geomagnetism and Aeronomy. NASA/GSFC's Space Physics Data Facility's OMNIWeb service (http://omniweb.gsfc.nasa.gov/index.html) provided measurements of interplanetary and geophysical parameters. The magnetometer data were obtained from the Geophysical Institute Magnetometer Array online service (http://magnet.gi.alaska.edu), INTERMAGNET (http://www.intermagnet.org), and SuperMAG (http://supermag.jhuapl.edu). Professors Bill Bristow and Donald Hampton, both from the University of Alaska Fairbanks provided the SuperDARN measurements, and the All-sky Imager measurements, respectively. The author also appreciates the support from staff members from HAARP and Poker Flat for helping with the setup and maintenance of the GNSS receiver array, as well as the experimental campaigns.

TABLE OF CONTENTS

LIST OF TABLES

LIST OF FIGURES

LIST OF ACRONYMS

ACF	Auto-Correlation Function
ADR	Accumulative Doppler Range
AE	Auroral Electrojet Index
APT	Adaptive Periodogram Technique
ATCF	As-the-crow-flies
ASI	All-Sky Imager
BP	Briggs-Parkin angle
CDCS	Continuously Displaced Coordinate System
CSR	Coherent Scatter Radar
C / N0	Carrier-to-Noise Ratio
DFT	Discrete Fourier Transform
DLL	Delay Lock Loop
Dst	Disturbance Storm Time Index
ECEF	Earth-Center, Earth-Fixed
GEO	Geostationary Earth Orbit
GLONASS	Global Orbiting Navigation Satellite System
GNSS	Global Navigation Satellite System
GPS	Global Positioning System
HAARP	High Frequency Active Auroral Research Program
IF	Intermediate Frequency
IGRF	International Geomagnetic Reference Field
IMF	Interplanetary Magnetic Field
IRPP	Irregularity Penetration Point
ISM	Ionospheric Scintillation Monitoring
ISR	Incoherent Scatter Radar
KOD	Kodiak SuperDARN
LOS	Line-of-sight
LS	Least-squares
OCXO	Oven-Controlled Crystal Oscillator
PLL	Phase Lock Loop
PNT	Position, Navigation and Timing
PRN	Pseudo-Random Noise
PSD	Power Spectral Density
PFISR	Poker Flat Incoherent Scatter Radar
PFRR	Poker Flat Research Range
RF	Radio Frequency
SCC	Sudden Storm Commencement
SDR	Software-Defined Receiver
SNR	Signal-to-Noise Ratio
SuperDARN	Super Dual Auroral Radar Network
SYM-H	Symmetric Geomagnetic Disturbance Index in the Horizontal Direction

TEC	Total Electron Content
TFA	Time-Frequency Analysis
USRP	Universal Software Radio Peripheral
UT	Universal Time
UTC	Coordinated Universal Time
WDC	World Data Center for Geomagnetism

1. CHAPTER 1 – INTRODUCTION

1.1. Ionospheric Scintillation

The ionosphere is a part of Earth's upper atmosphere produced by solar UV radiation, extending from about 85 km to 1000 km altitude. The F-region of the ionosphere extends from about 150 km to more than 500 km altitude, where free electrons are most concentrated [*Aarons*, 1982]. For decades, scientists have been studying the ionosphere using measurements obtained from radars, rockets, and satellites [*Singleton*, 1974; *Myers et al.*, 1979; *Rino*, 1979a, 1979b; *Fremouw et al.*, 1980; *Basu and Basu*, 1985]. With the advent of the Global Navigation Satellite System (GNSS), an alternative approach utilizing GNSS receiver measurements has gained popularity [*Van Dierendonck et al.*, 1993, 1996, 2004; *Aarons et al.*, 1996, 1997; *Morrissey et al.*, 2004; *Dyrud et al.*, 2005; *Crowley et al.*, 2011; *O'Hannon et al.*, 2011; *Taylor et al.*, 2013].

Activities from the Sun, Earth's magnetic field and interplanetary magnetic field sometimes disturb the ionosphere, leading to the formation of electron density irregularities in the ionospheric plasma. When sufficiently intense, these irregularities can scatter trans-ionospheric radio waves such as GNSS signals and cause random fluctuations in amplitude and phase of the received signals. This phenomenon is commonly called ionospheric scintillation [*Aarons*, 1982; *Yeh and Liu*, 1982]. It is well known that strong ionospheric scintillation can significantly degrade the performance of GNSS receivers in terms of both accuracy and reliability [*Skone et al.*, 2001; *Morrissey et al.*, 2004; *Kintner et al.*, 2007; *Seo et al.*, 2007; *Fortes et al.*, 2014; *Morton et al.*, 2014; *Jiao et al.*, 2014b, 2015; *Xu and Morton*, 2015]. With increasing reliance on GNSS for position, navigation, and timing (PNT) services, the impacts of scintillation on space-based systems have become a high priority [*Basu et al.*, 2002].

1.1.1. Low-latitude vs. High-latitude Scintillations

Ionospheric scintillations can be categorized by latitude as low-latitude, or equatorial scintillations (within 20° of Earths' magnetic equator) and high-latitude scintillations (within 30° of Earth's magnetic poles), as scintillations are generally confined to these regions [*Aarons,* 1982; *Aarons and Basu,* 1994; *Basu et al*., 2002].

In low-latitude regions, scintillation occurs primarily in the period after local sunset due to the Rayleigh-Taylor instability, often causing rapid and long lasting deep fading effects in the GNSS receiver measurements [*Kelley et al.,* 1981; *Hysell and Kudeki,* 2004; *Béniguel et al.,* 2009; *Jiao et al.,* 2015]. Solar activities play a secondary modulating role in the production of plasma structures, making low-latitude scintillations seasonally dependent and solar cycle dependent. In particular, they are more frequent and intense around equinoxes and subside in the summer [*Tsunoda,* 1985; *Kintner et al*., 2007; *Béniguel et al*., 2009]. The low-latitude scintillation fade patterns are expected to be highly elongated in the magnetic north-south direction, with widths on the order of a few hundred meters, and length typically over 10 km [*Basu and Basu,* 1981; *Kintner et al.,* 2004]. These irregularity patterns drift at a velocity primarily between 50-200 m/s in the eastward (zonal) direction perpendicular to the magnetic field lines [*Kintner et al.,* 2004]. This velocity is often referred to as the plasma drift velocity, or simply the drift velocity.

In high-latitude regions, the physical mechanism behind ionospheric scintillations is different from and more complex than that of low-latitude scintillations. The occurrence of high-latitude scintillations is largely dependent on space weather. The governing factors of these irregularities are presumed to the gradient drift instability and accelerated energetic electron precipitation along geomagnetic field lines [*Basu et al.,* 2002]. The scintillation process often involves interactions of many components, such as the Earth's magnetic field, solar activity,

interplanetary magnetic field, convective processes, local electric field and conductivity, wave interactions, etc. [*Tsunoda*, 1988; *Pi et al*., 1997; *Basu et al*., 2002; *Kintner et al.*, 2007; *Skone et al.*, 2008; *Smith et al.*, 2008]. As opposed to the low-latitude scintillation being a post-sunset phenomenon, several studies showed that auroral scintillation often occurs at nighttime, while the polar cap scintillation can take place at all local times [*Kintner et al*., 2007; *Li et al*., 2010; *Jiao et al*., 2013c]. On the other hand, high-latitude scintillations demonstrate seasonal patterns like low-latitude scintillations, with additional location-dependency [*Rino et al*., 1983; Kersley et al., 1988, 1995; *Aquino et al*., 2005; *Li et al*., 2010; *Alfonsi et al*., 2011; *Prikryl et al*., 2011; *Jiao et al*., 2013c]. These high-latitude scintillation irregularities have been observed to be rod-like and field-aligned similar to the low-latitude case [*Martin and Aarons*, 1977], while others have observed enhanced spatial coherence along the axis transverse to the field line, forming sheet-like or wing-like irregularity patterns [*Livingston et al.*, 1982]. These irregularity patterns drift at velocities much faster than the low-latitude case, typically around 300 to 500 m/s, and can exceed 1000 m/s during active conditions [*Aarons*, 1982].

1.1.2. Amplitude vs. Phase Scintillations

From the receiver measurement perspective, ionospheric scintillations are typically categorized into amplitude scintillations and phase scintillations [*Aarons and Basu*, 1994]. They refer to the fluctuations in the received signals' amplitude and carrier phase measurements.

For amplitude scintillations, the most adopted metric is the S_4 index. It is defined in Equation 1–1 as the standard deviation of the received signal power normalized to the average signal power [*Briggs and Parkin*, 1963]:

$$S_4 = \sqrt{\frac{\langle I^2 \rangle - \langle I \rangle^2}{\langle I \rangle^2}} \qquad (1\text{-}1)$$

where I is the detrended signal intensity measurement, and $\langle \cdot \rangle$ represents the expected value over the interval of interest [*Van Dierendonck et al*., 1993]. In this study, the interval of interest is set to 10 seconds to effectively capture scintillation features [*Pelgrum et al*., 2011]. After normalization, S_4 typically falls into the range of 0 to 1, except when saturation happens, in which case it can slightly exceed unity [*Singleton*, 1970]. Following the work of *Jiao* [2013], amplitude scintillations are empirically classified as $S_4 < 0.2$ for no obvious scintillations, $0.2 \leq S_4 < 0.5$ for weak/moderate scintillations and $S_4 \geq 0.5$ for strong scintillations.

For phase scintillations, the most adopted measuring metric is the σ_ϕ value. It is defined in Equation 1–2 as the standard deviation of the signal phase [*Yeh and Liu*, 1982]:

$$\sigma_\phi = \sqrt{\langle \phi^2 \rangle - \langle \phi \rangle^2} \qquad (1\text{-}2)$$

where ϕ is the detrended carrier phase measurement [*Van Dierendonck et al*., 1993]. The interval of interest is also set to 10 seconds [*Pelgrum et al*., 2011]. Unlike S_4, σ_ϕ is not a normalized metric. The measurable range of σ_ϕ is defined by the receiver's carrier tracking pull-in range. If the received carrier phase is beyond this range due to scintillation, then the receiver has a high probability of losing lock of the signal. At that point, σ_ϕ can still be used to identify phase scintillations, while its value carries no significance, unless specially developed receiver processing algorithms are used to maintain lock of the scintillation signals to generate meaningful measurements [*Xu and Morton*, 2017].

In order for σ_ϕ to correctly reflect the level of phase scintillation, the oscillator noise from both the satellite and the receiver needs to be considered, as the detrending process discussed later only removes low frequency components. For the receiver system used in this dissertation, the received phase noise is typically under 2.5° for the GPS L1 signal under nominal conditions [*Peng and Morton*, 2013; *Taylor et al.*, 2013]. Following *Jiao* [2013], phase scintillations are empirically

classified as $\sigma_\phi < 6°$ for no obvious scintillations, $6° \leq \sigma_\phi < 30°$ for weak/moderate scintillations and $\sigma_\phi \geq 30°$ for strong scintillations.

Note that in the calculations for both S_4 and σ_ϕ, the receiver measurements are required to be detrended to remove the low-frequency contributions from satellite-receiver range variations, antenna patterns, receiver and satellite oscillator drifts, ionosphere and troposphere delays etc. The conventional detrending method for both indices is based on a 6th order Butterworth filter with a cut-off frequency at 0.1 Hz [*Van Dierendonck et al*., 1993].

In general, amplitude scintillations are more prominent in the low-latitude regions while often accompanying simultaneous phase scintillations [*Aarons,* 1982]. On the contrary, high-latitude scintillation is usually observed to be dominated by phase scintillations often without obvious simultaneous amplitude scintillations [*Aarons,* 1997; *Valladares et al.,* 2002; *Doherty et al.,* 2003; *Aquino et al.,* 2005; *Skone et al.,* 2008; *Azeem et al*., 2013; *Jiao,* 2013; *Jiao et al*., 2013a].

The faster plasma drift velocity is considered a main reason for such a phenomenon [*Forte and Radicella*, 2002]. The major contribution to amplitude fluctuation spectra is at the Fresnel Frequency f_F according to *Rino* [1979a, 1979b], which is proportional to the apparent drift velocity (composed of the satellite scan velocity and the irregularity drift velocity). Since the irregularities drift with the background plasma, f_F varies with the plasma drift velocity, and faster plasma drift velocity implies higher f_F. However, during data detrending using the conventional 6th order Butterworth filter, a fixed cutoff frequency of 0.1 Hz is often adopted. Such a choice is not appropriate and can cause misleading data interpretations, for example, overestimations of phase scintillation at high latitudes [*Forte and Radicella*, 2002]. In fact, the effectiveness of this method has long been questioned by previous studies without a confirmed better replacement [*Forte and Radicella*, 2002; *Beach*, 2006; *Mushini et al.*, 2012; *Niu*, 2012].

1.2. Spaced-Receiver Techniques

Most of the GNSS scintillation studies focus on investigating the characteristics of ionospheric scintillation with the purpose of modeling and mitigating its effects on GNSS systems [*Secan et al.*, 1995; *Groves et al.*, 2000; *Hegarty et al.*, 2001; *Basu et al.*, 2002; *Béniguel et al.*, 2009; *Humphreys et al.*, 2010; *Jiao et al*., 2013b; *Zhang and Morton*, 2013]. Others take advantage of the occurrence of scintillation events and utilize scintillation signal characteristics to study space weather and atmospheric properties [*Groves et al*., 2000; *Ledvina et al.*, 2004; *Kintner and Ledvina*, 2005; *Jiao et al.*, 2013b; *Deshpande et al*., 2014]. In this dissertation, the spaced-receiver techniques developed for remote-sensing scintillation patterns are such applications.

1.2.1. Irregularity Drift Velocity Estimation

The scintillation-based spaced-receiver technique for irregularity drift velocity estimation was developed by *Mitra* [1949], *Briggs et al.* [1950], and *Briggs* [1968]. If two closely-spaced receivers can observe the same diffraction pattern, the time delay between the receivers' observations can be resolved by the cross-correlation of their signal intensity measurements and is used to infer the irregularity drift velocity.

One of the most common applications of this technique is to estimate the zonal irregularity drift velocity in the equatorial region, which is typically in the range of 50 to 200 m/s [*Basu and Basu*, 1981; *Kintner et al.*, 2004]. Early studies used UHF and L band devices to receive radio signals transmitted from various satellite systems [*Anderson and Mendillo*, 1983; *Vacchione et al.*, 1987; *Basu et al.*, 1991a]. Because of their compact, low cost, and globally distributed nature, GNSS receivers have gained popularity in recent years [*Basu et al.*, 1996; *Kil et al.*, 2000; *Kil et al.*, 2002; *Kintner et al.*, 2004]. The validity of this method has been supported by on-site incoherent scatter radar (ISR) measurements in a few studies [*Basu et al.*, 1991a; *Kil et al.*, 2002].

Previous work focused on the use of signal intensity measurements [*Basu et al.*, 1991a; *Kil et al.*, 2000; Otsuka et al., 2006] or total electron content (TEC) [*Ji et al.*, 2011] for drift velocity estimations during equatorial amplitude scintillations. At high latitudes, again, ionospheric scintillations are generally moderate while phase fluctuations are often more frequent and intense than amplitude scintillations. As a result, the conventional spaced-receiver estimation technique based on amplitude scintillations is less applicable at high latitude regions. Phase fluctuation measurements should be employed instead.

Little literature has been found, however, utilizing phase fluctuations in this area. This is possibly due to the many error sources contained in carrier phase measurements that may dominate the time domain correlation among closely-spaced antennas. For example, receiver oscillator-induced phase jitter and multipath often resemble that of scintillation effects. During strong scintillations, carrier phase measurements are often contaminated with cycle slips and missing data due to loss of lock of signals. Carrier phase detrending processes aimed to remove low frequency components, such as receiver-satellite dynamics, satellite orbit errors, receiver and satellite clock drifts, background ionosphere and troposphere-induced carrier phase trend, etc., are heuristic in nature and the appropriateness of their use is continuously under debate [*Beach*, 2006; *Mushini et al.*, 2012; *Niu et al.*, 2012]. These errors and uncertainties must be addressed for carrier phase measurements to be used effectively in irregularity drift velocity estimation.

The technique presented in this dissertation aims to minimize carrier phase errors while preserving features associated with ionospheric irregularities. First, the data collection system and signal processing algorithms are carefully designed to minimize contributions from the receiver oscillators and environmental multipath, two sources with similar spectral distributions to that of ionospheric irregularity-induced effects. Then, either custom-designed carrier tracking algorithms

or specialized ionospheric scintillation monitoring receivers are used to generate high-quality carrier phase measurements accustomed to each array system. After synchronizing the receiver array output, cycle slips are detected and repaired to further ensure phase data integrity. Only then, a zero-phase detrending technique is applied to the cleaned phase measurements to ensure that no filter delay is introduced by the detrending process.

Next, correlation techniques are applied to the processed carrier phase measurements to obtain time lags of common scintillation features between receiver pairs. The correlation techniques include a time-domain method (TDM) for measurements under ideal signal conditions, as well as a time-frequency-domain method (TFDM) targeting noisier signal environment [*Wang and Morton*, 2015; 2017]. For the latter method, an adaptive periodogram technique (APT) is employed to perform joint time-frequency analysis of the non-stationary signatures of the ionospheric irregularity-induced carrier phase spectrum [*Brenneman et al.*, 2007; *Zhou et al.*, 2008; *Wang et al.*, 2012; *Wang*, 2013].

Measurements from a pair of receivers allows the determination of the one-dimensional (1-D) apparent drift velocity along the receiver pair. To combine these velocity vectors into two-dimensional (2-D), a correlation model is required to account for the shape of the signal diffraction pattern. Three correlation models have been analyzed in detail through their space-time correlation schematics, including the classic isotropy model from Briggs et al. [1950], the front velocity model by *Wang and Morton* [2017] and the anisotropy model following *Rino and Livingston* [1982]. With the understanding of the merits and drawbacks of each method, a hybrid correlation model is developed combining the anisotropy model and the front velocity model [*Wang and Monton*, 2018a]. Finally, with the known receiver and satellite position, the irregularity drift velocity can be estimated. Details of the drift velocity estimation method are described in Chapter 3.

It is worth mentioning that the work presented in *Wang and Morton* [2017], *Wang et al.*, [2018] and this dissertation is in parallel with the work in *Datta-Barua et al.* [2015] and *Su et al.* [2017]. Both studies address the ionospheric drift velocity remote sensing problem using receiver arrays at a similar location.

However, aside from the receiver hardware differences (e.g., *Su et al.* [2017] is GPS only, while this dissertation uses additional signals from GLONASS and Galileo satellites), there are several other distinctions between the two studies. First, the array in *Su et al.* [2017] consists 6 receivers, while *Wang and Morton* [2017] uses a 3-receiver-array with a slightly larger footprint. Next, the two studies use different correlation models to address the shape of the diffraction pattern. *Su et al.* [2017] uses the anisotropy model, while this study uses a hybrid correlation model combining the front velocity model and the anisotropy model. Finally, when analyzing the estimated drift velocities against other measurements, *Su et al.* [2017] focuses on the scintillation events on each individual satellite, while this dissertation focuses on the overall temporal and spatial pattern of the irregularities.

1.2.2. Irregularity Height Estimation

An important parameter in GNSS scintillation studies is the irregularity height. For example, it is one of the key components in scintillation modeling studies [*Secan et al.*, 1995; *Jiao et al.*, 2018]. Also, it impacts the estimation of other irregularity properties in scintillation-based remote sensing studies [*Kil et al.*, 2000; *Wang et al.*, 2018].

In the literature, the irregularity height is often empirically assumed at a fixed value around the shell height following the thin-shell ionospheric model, typically between 350 km and 450 km [*Komjathy and Langley*, 1996; *Ledvinat et al*., 2004]. For one of our receiver array sites, this value can be approximated from the electron density (Ne) profiles measured by the co-located Poker Flat

Incoherent Scatter Radar (PFISR). But for a typical standalone receiver array, such information cannot be taken for granted. Also, during active conditions, it is not uncommon for the shell height to appear outside of the [350 450] km region, especially at high latitudes where scintillation formation can be very complex [*Sojka et al.*, 2009; *Wang and Morton*, 2017]. Besides, whether the shell height is a good approximation to the irregularity height remains a debatable topic.

Focusing on the irregularity height itself, *McClure* [1964] showed an estimation technique based on Low Earth Orbiting (LEO) satellite scintillations, taking advantage of the fact that LEO satellite velocity is much greater than the irregularity drift velocity. But this method is not suitable for scintillations on GNSS signals, whose satellite scan velocity in the ionosphere is comparable to the irregularity drift velocity [*Kintner et al.*, 2004; *Wang et al.*, 2018]. *Carrano et al.* [2017] proposed a method for geolocating ionospheric irregularities along radio occultation (RO) ray-paths between GNSS and LEO satellites. The irregularity height can later be retrieved based on the RO measurements and the positions of the satellites. However, the measurement window of this technique is very limited due to the highly constrained RO geometry [*Kursinski et al.*,1997]. Also, the estimated irregularity height may not be applicable to typical GNSS users, since the RO ray-paths are very different from typical GNSS satellite-receiver ray-paths.

In this dissertation, a more inclusive approach is adopted when calculating the drift velocities by considering a range of irregularity height assumptions approximated from past observations [*Wang et al.*, 2018]. Uncertainties would occur in the drift velocity estimates. But the true drift velocity is also likely to be contained in the corresponding velocity variations. A detailed analysis is provided in Section 6.2.3 using a real-data example.

In addition, another spaced-receiver technique has been developed to estimate the effective irregularity height [*Wang and Morton*, 2018b]. An inversion algorithm is proposed using spaced-

receiver measurements under the framework of the anisotropy model [*Fedor*, 1967]. The gist of the approach is to match the forward propagated anisotropy parameters as in *Rino and Fremouw* [1977] under different height assumptions to the anisotropy parameters estimated from the spaced-receiver measurements as in *Rino and Livingston* [1982]. The effective irregularity height is then determined to be the height assumption at the best match. Although the focus of this study is on high latitude scintillation data, the general approach can be applied to equatorial scintillation studies as well. Note that the effective height here should be separated from the "effective/optimal height" in GNSS total electron content (TEC) studies, whose objectives are usually on the background ionosphere rather than the irregularities [*Birch et al.*, 2002; *Zhao and Zhou*, 2018].

To verify the estimated effective irregularity heights, cross-comparison is conducted against electron density (N_e) profiles measured by the collocated PFISR. In particular, the estimated heights are compared with the depletion and enhancement regions in the Ne profiles, where irregularities are most likely to be present. Case studies in Section 6.8 demonstrate insights into the relationship between the potential irregularity heights observed from the PFISR Ne profiles and the effective heights irregularity estimated from the GNSS receiver array.

1.3. Objectives of Dissertation Research

The main objective of this PhD dissertation research is to develop and validate a spaced-receiver algorithm for estimating the irregularity drift velocity. To achieve this objective, several algorithms and techniques are required to be developed and tested. Also, comparative studies against drift velocity measurements from other instruments are required for algorithm validation. The following is a summary of the objectives in this thesis research:

a) Use scintillation data from spaced-receivers to develop correlation techniques to estimate the time lags across the receiver pairs when observing the same scintillation event;

b) Implement viable correlation models to combine 1-D apparent drift velocity estimations along receiver pairs into a 2-D velocity. Estimate the irregularity drift velocity based on the known satellite-receiver geometry;

c) Verify the self-consistency of the drift velocity estimation algorithm by comparing the estimation results across the available GNSS signals at various frequency bands;

d) Analyze the validity of the drift velocity estimation algorithm by cross-comparing the estimation results against concurrent measurements obtained from other near-by or in-situ instruments such as the Super Dual Auroral Radar Network (SuperDARN), the All-Sky Imager (ASI) and the Incoherent Scatter Radar (ISR);

e) Develop an algorithm to estimate anisotropy parameters as well as the effective irregularity height.

1.4. Dissertation Outline

Chapter 1 gives the background introductions on this PhD dissertation research, including the ionospheric scintillation, the spaced-receiver technique and time-frequency analysis techniques. Chapter 2 introduces both the old and the new receiver array setups used in this study, as well as the pre-processing steps involved in all subsequent spaced-receiver methods. Background information on some co-located ionospheric monitoring instruments is also provided, including the SuperDARN, the ASI and the ISR. Chapter 3 explains the methodology of the scintillation-based spaced-receiver technique for irregularity drift velocity estimation, including the basic theory, satellite scan velocity calculation, time lag estimation, and the drift velocity estimation bounds. For the time lag estimation, two general methods are presented, the TDM and the TFDM. Chapter 4 focuses on the correlation models accounting for different irregularity topology assumptions, including the classic isotropy model, the front velocity model, the

anisotropy model, and a hybrid correlation model combining the latter two models. Chapter 5 demonstrates an inversion technique for estimating the effective irregularity height using the anisotropy model. Chapter 6 presents the main results of this dissertation, including a self-consistency studies and serval cross-comparative studies against measurements from other instruments. Lastly, Chapter 7 summarizes this study.

2. CHAPTER 2 – SYSTEM SETUP, DATA PRE-PROCESSING, AND AN OVERVIEW ON OTHER IONOSPHERE MONITORING INSTRUMENTS

This chapter introduces the hardware setups of the two GNSS arrays used in this dissertation, as well as the data pre-processing steps required for later discussions on spaced-receiver techniques. Background information of some other instruments for ionosphere monitoring is also introduced in this chapter. Sections 2.1 and 2.2 introduce the receiver setups at Gakona, Alaska and the Poker Flat Research Range (PFRR) near Fairbanks, Alaska. Section 2.3 shows the data pre-processing steps involved in this study, including receiver signal processing, receiver array synchronization, carrier cycle slip detection and repairing, and carrier phase detrending. Section 2.4 gives an overview on some other co-located ionosphere monitoring instruments, including the SuperDARN, the ASI, and the PFISR. Section 2.5 elaborates on the common measurement volumes of between these instruments and the GNSS array system, respectively.

2.1. The HAARP (Gakona) Array Setup

In 2009, an event-driven multi-constellation GNSS receiver array has been established at the High Frequency Active Auroral Research Program (HAARP) facility in Gakona, Alaska (62.39°N, 145.15°W) for ionospheric scintillation studies [*Taylor et al.*, 2012]. GNSS receiver measurements were continuously stored, while raw IF samples were recorded by the radio frequency (RF) front ends and tracked by a software-defined receiver (SDR) whenever scintillation events had been detected. These results have been used to characterize high-latitude GNSS scintillations [*Jiao et al.*, 2013]. Figure 2-1 shows a subset of the receiver array and data collection system dedicated in this dissertation. Details of the full system configurations can be found in *Taylor et al.* [2012] and *Taylor et al.* [2013].

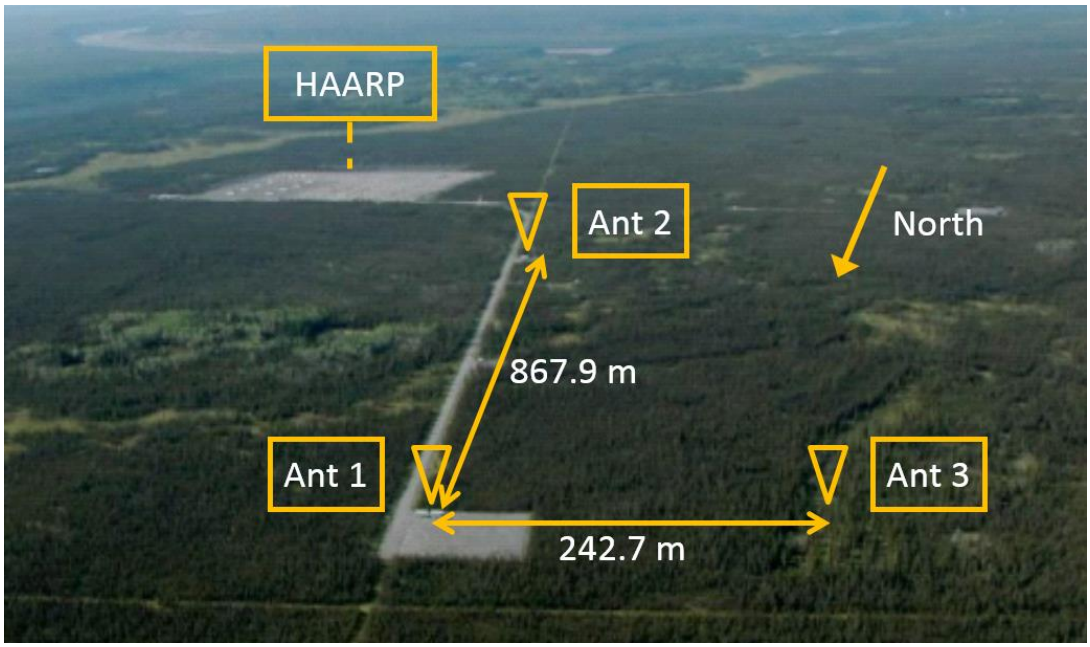

Figure 2-1. HAARP GNSS receiver array setup. The triangles mark the antenna locations, with their spacing being several hundred meters. The HAARP facility is also indicated.

Antenna 1 is connected to a Septentrio PolaRxS ionospheric scintillation monitoring (ISM) receiver, which is driven by a low phase noise, oven-controlled crystal oscillator (OCXO) and generates 100Hz GPS/GLONASS carrier phase measurements [*Taylor et al.*, 2013]. Antennas 2 and 3 are located 867.9 m due south and 242.7 m due west of Antenna 1, respectively. Each antenna is connected to a USRP2 (Universal Software Radio Peripheral, 2nd generation) RF front end stored in a shelter at Antenna 1 location via a cable. These USRP2 front ends are configured to record raw GPS L1/L2C intermediate frequency (IF) samples. Both front ends are externally driven by the OCXO on board the Septentrio ISM receiver to ensure time and frequency coherence of measurements across the array [*Taylor et al.*, 2012]. In addition, Antenna 3 is also connected to a NovAtel GPSation-6 ionospheric scintillation and TEC monitor receiver that outputs 50Hz GPS/GLONASS carrier phase measurements. We shall collectively refer to these commercial receivers as ISMs in the remaining dissertation to distinguish them from the SDR receivers.

The ISM receivers continuously record carrier phase measurements, while the USRP2's only wrote raw IF data to storage when custom designed space weather event trigger software detects a scintillation event. The carrier phase measurements for Antennas 2 and 3 are then obtained via a fine-tuned SDR processing algorithm. Detailed parameters of the SDR receiver algorithm can be found in Section 2.3.1. The performance of USRP2 front ends and software algorithms has been evaluated by [*Peng and Morton*, 2013].

After some pre-processing steps shown in Section 2.3, GPS and GLONASS carrier phase measurements at various data rates are obtained at each antenna. Table 2-1 shows the GNSS bands for the HAARP array, together with their corresponding output data rate at each antenna. Note that the high data rate outputs from the ISM receiver can be resampled to match with the data rate from other devices.

Table 2-1. GNSS bands received at the HAARP array, and output data rate for each antenna.

Device	Antenna	GNSS bands	Data rate (Hz)
Septentrio PolaRxS	A1	GPS L1/L2/L5 GLO L1/L2	100/100/100 100/100
NovAtel GPStation-6	A3	GPS L1/L2/L5 GLO L1/L2	50/50/50 50/50
USRP2	A2, A3	GPS L1/L2C	100/50

A major issue with the HAARP setup is that signal attenuation occurs due to the lengthy cable transmission, causing degradation in the received phase measurements on Antennas 2 and 3. A time-frequency domain correlation scheme is developed to resolve this issue [*Wang and Morton*, 2015]. The gist of the approach is to transform the original time-domain signal into time-frequency domain, so that spectral filtering can be performed while keeping the signal's temporal information. The detailed method is described in Section 3.3.2.

2.2. The Poker Flat Array Setup

In 2014, another event-driven multi-constellation GNSS receiver array was established at the PFRR in Fairbanks, Alaska (65.13 °N, 147.49 °W). Having other co-located ionospheric monitoring instrumentations such as the PFISR and the ASI greatly benefits the GNSS array remote sensing studies. Figure 2-2 illustrates the receiver array arrangement based on a Google Earth image over the PFRR.

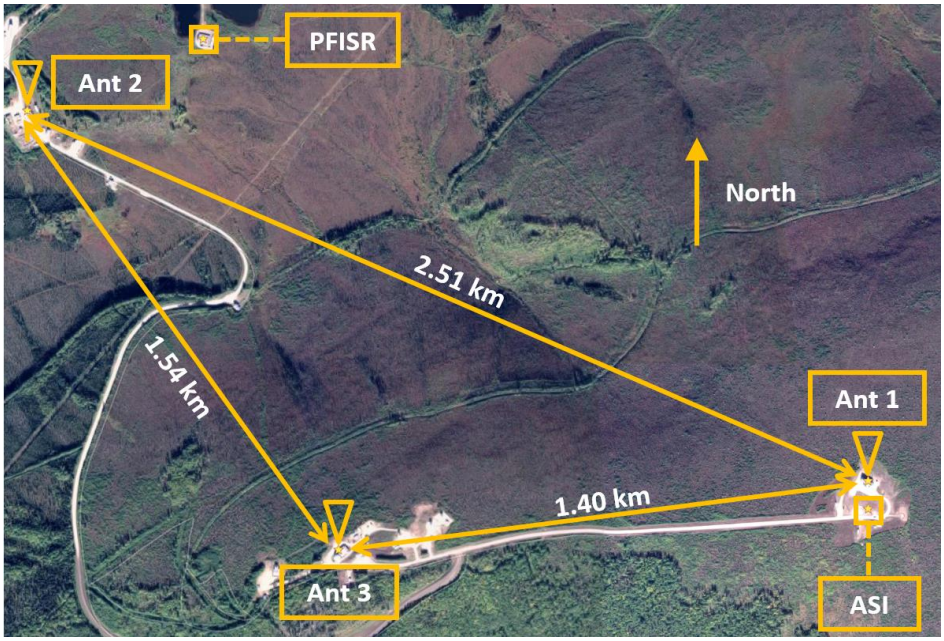

Figure 2-2. Poker Flat GNSS receiver array setup. The triangles mark the antenna locations, with their spacing being several kilometers. The squares mark the PFISR and the ASI locations.

In Figure 2-2, the relative positions of Antennas 1, 2 and 3 are scaled to the real geometry. The relative positions of the PFISR (0.55 km to Antenna 2) and the ASI (near Antenna 1 location) are also shown by the square and the circle, respectively. All three antennas are connected to dedicated Septentrio PolaRxS ISM receivers. In addition to the HAARP receivers' functionalities, these receivers are also capable of producing 100 Hz GALILEO and BEIDOU measurements. Antenna 1 is connected to 7 USRP2 front ends to record GPS, GLONASS, GALILEO and BEIDOU IF samples, driven by the OCXO on board the Antenna 1 ISM receiver. Another

improvement of the Poker Flat setup as opposed to the old HAARP setup is that the data connections from the antennas to the receivers and USRP2's no longer rely on long cables. Each antenna is now directly connected to the receiver located at the nearby PFRR facility. Hence the data attenuation is greatly reduced. All three ISM receivers continuously record GNSS measurements, while the IF data recording on the USRP2's is triggered by the same mechanism as in the HAARP setup.

2.3. Data Pre-processing

2.3.1. Custom Receiver Signal Processing

For the HAARP array, custom software GPS receiver signal processing algorithms were applied to acquire and track both GPS code and carrier signal parameters during phase fluctuation events. The carrier tracking loop is a third-order Costas phase lock loop (PLL) initialized by coarse estimations of carrier Doppler frequency and ranging code phase obtained through a FFT-based acquisition process [*Misra and Enge*, 2006]. The code tracking loop is an early-prompt-late delay lock loop (DLL) with a half chip correlator spacing. For both tracking loops, the coherent integration time is 10 ms. The equivalent noise bandwidths of the loop filters are 15 Hz for PLL and 2 Hz for DLL. The discriminators used for the PLL and DLL are given by:

$$D_{PLL} = \arctan(Q_P / I_P) \quad (2\text{-}1)$$

$$D_{DLL} = \frac{1}{2}\frac{E - L}{E + L} \quad (2\text{-}2)$$

$$\left(E = \sqrt{{I_E}^2 + {Q_E}^2}, L = \sqrt{{I_L}^2 + {Q_L}^2}\right) \quad (2\text{-}3)$$

where I and Q are the I and Q channel correlator outputs, while the subscribes denote Prompt (P), Early (E) and Late (L) correlators, respectively. To ensure that carrier phase disturbances are not filtered out by the PLL, the carrier phase discriminator estimation residual is added back to the

filtered carrier phase measurements [*Van Dierendonck*, 2005]. The output data rate is 100 Hz, which is identical to the ISM receiver data rate. Note that after the navigation data bits are identified, the tracking results can be further improved by replacing the Costas PLL with the coherent PLL discriminator $\left(D_{PLL} = \text{atan2}(Q_P, I_P)\right)$, as it can provide a larger pull-in range to accommodate higher carrier phase dynamics [*Mao and Morton*, 2013].

2.3.2. Synchronization

For any spaced-receiver study, time synchronization across the array of receivers is the crucial first step. For the HAARP array, data recording is performed using the same server and driven by the same timing device for all three receivers, while the SDR front ends are driven by the timing device from the ISM receiver at Antenna 1. For the Poker Flat array, all GNSS channels in each of the three ISMs are internally synchronized to GPS time.

However, hardware delays do exist. To ensure synchronization, the navigation messages of the same satellite at different receivers are decoded and then aligned on a sample-by-sample basis [*Peng et al.*, 2012]. The resulting time resolution is *1/fs* where *fs* is the sampling frequency which is 5 MHz in this project. As a result, the time misalignment does not exceed 200 ns.

2.3.3. Cycle Slip Detection and Repairing

A cycle slip is a discontinuity in a GNSS receiver's carrier phase measurement, often in a form of a sudden jump with an integer (or a half) number of cycles [*Leick*, 1995]. General causes of the discontinuity are either a malfunction in the satellite or the receiver system, or sudden changes in the environment that lead to signal degradations or obstructions [*Seeber*, 2003]. Cycle slips are unpredictable in nature and can easily cause large magnitude of jumps in the phase measurements. Since this entire study is based on GNSS carrier phase measurements, it is crucial to detect and repair the cycle slips before going into subsequent processes.

High rate phase measurement is required for this study. The ISM receivers output high rate (100 Hz) carrier phase measurements in the form of accumulative Doppler range (ADR). The time derivative of ADR is the Doppler frequency, which may vary up to a few kHz in the course of a few hours for a stationary receiver [*Misra and Enge*, 2006]. The nominal Doppler frequency change within the sampling interval (0.01 s) is on the order of 0.001 to 0.01 cycles.

As a result, if a cycle slip of 0.5N cycles ($N \in \mathbb{N}$) occurs in the ADR measurement series, it will be more pronounced in the time differences of that series. Based on this principle, the cycle slip detection and repair are achieved via double difference of the ADR measurements. Assuming a cycle slip of 0.5N occurs at t_i, the detection and repair algorithm can be captured by the following relationship:

$$0.5N \approx (\phi_i + 0.5N - \phi_{i-1}) - (\phi_{i-1} - \phi_{i-2}) \qquad (2\text{-}4)$$

where ϕ denotes the ADR measurement and i denotes the time epoch at 100Hz.

This cycle slip detection and repairing technique is suitable for high rate carrier phase measurement. However, it does come with a few drawbacks. First, the detection and repair rely on nominal ADR measurements prior to the occurrence of the cycle slip. This cannot be always guaranteed, especially at the beginning of the data with lower elevation angles where the signal condition is not optimal. But in post-processing, the starting point of the algorithm can be applied to anywhere in the ADR series and can be used in both forward and backward manners. Second, when no high rate pseudo-range measurements are available, the accuracy in the repaired ADR sample is only within ±0.5 cycles. A compromise is made so that the correlation results associated with the detected cycle slips are discarded in the later processes. Nevertheless, the repairing process is still necessary as it would minimize the impact of cycle slips in the detrended carrier phase data.

Using some phase scintillation data collected by the Poker Flat array, the detected and repaired results for the two days of GPS L1 and L2C data on 2015/12/20 and 2015/12/31 are summarized by Table 2-2. Details on these scintillation events is presented in Section 6.1.2.

Table 2-2. Detected and repaired cycle slips in GPS L1 and L2C signals for Poker Flat array collected data on 2015/12/20 and 2015/12/31.

	GPS bands	A1	A2	A3
Large Slips (≥100 cycles)	L1	10	2	9
	L2C	5	5	30
Small Slips (<100 cycles)	L1	14	11	19
	L2C	3	0	4
Loss of Lock	L1	2	1	2
	L2C	1	2	2

2.3.4. Carrier Phase Detrending

Following the cycle slip detection and repairing process, the raw carrier phase measurements from the tracking loop are detrended using a conventional sixth-order high-pass Butterworth filter with a cutoff frequency of 0.1 Hz. It is designed to remove slowly varying components due to satellite-receiver dynamics, satellite and receiver clock drift, background ionosphere and troposphere gradients, etc. The filter is implemented using both a forward and a backward third-order Butterworth filter, such that the filter has zero-phase (no filter delays) [*Niu et al.*, 2012].

It should be noted that this detrending method may cause "phase without amplitude" scintillation phenomena frequently observed in high latitude regions [*Forte and Radicella*, 2002; *Mushini et al.*, 2012]. *Forte and Radicella* [2002] pointed out that the conventional cutoff frequency of 0.1 Hz may overestimate phase scintillation than amplitude scintillations, causing the correlation between the amplitude and phase scintillation indices to be less than their true values.

Mushini et al. [2012] demonstrated that using a wavelet technique, the correlation between the two indices can be improved.

For the spaced-receiver algorithm, the focus of is not on the phase scintillation at a single receiver, but on the time difference between the phase fluctuations observed at different receivers. For that reason, as long as the fluctuations in the detrended carrier phase are induced by ionospheric irregularities, and all phase data are processed the exact same way, then the detailed implementation of the detrending method is of less concern. In fact, the conventional detrending method works in favor of this study, as the slightly overestimated carrier phase measurements lead to a stronger cross-correlation of the irregularity effects between antennas.

2.4. Other Instruments for Ionosphere Monitoring

2.4.1. All-Sky Imager

An all-sky imager (ASI) is an optical device that provides intensified monochromatic images of auroral and airglow emission for various atmospheric lines of interest associated with distinct heights measured at different wavelengths [*Semeter et al.*, 2001]. Most ASIs can observe the two most intense atmospheric lines: the red atomic oxygen line O(^{1}D) at 630 nm wavelength and the green atomic oxygen line O(^{1}S) at 557.7 nm wavelength. These two lines correspond to altitudes centered at about 200 km and 96 km, respectively [*Culot et al.*, 2004].

The specific ASI used in this dissertation is at PFRR (65.12°N, 147.43°W). It is co-located with the Poker Flat GNSS receiver array as shown in Section 2.2. This imager has a fish-eye lens with a field-of-view of 180° covering the entire sky, and a charge-coupled device camera with a resolution of 512 × 512 pixels. In addition to 630 nm and 557.7 nm images, it is also capable of providing images of blue nitrogen ion line N_2^+ at 427.8 nm and aqua hydrogen atom line H-β at 486.1 nm. Each image shows the integrated camera view over 12.5 seconds to intensify the

observed emissions. Figure 2-3 shows an example of the Poker Flat ASI auroral emission measurements at 427.8 nm, 557.7 nm and 630.0 nm on 2015/12/20.

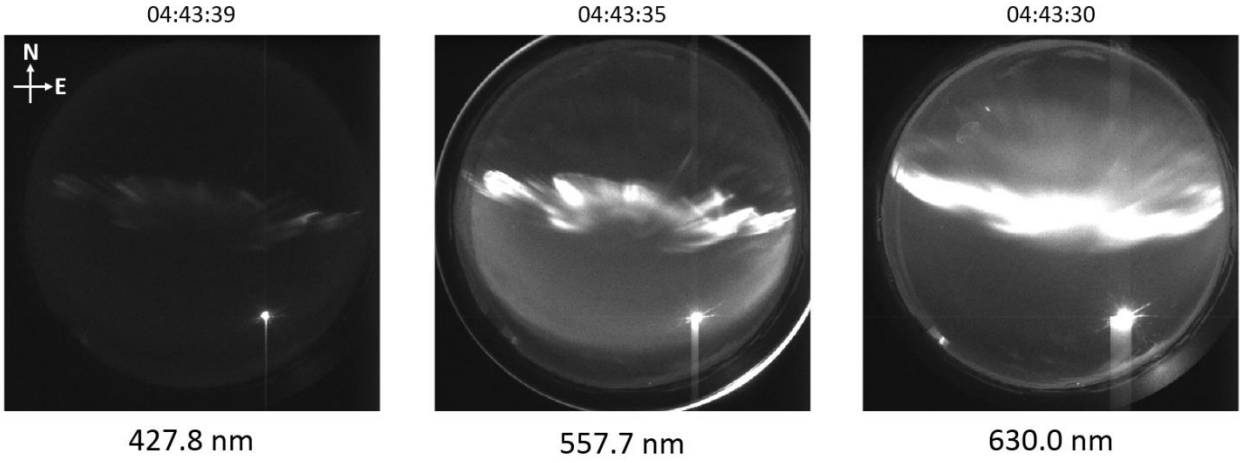

Figure 2-3. Example of consecutive Poker Flat ASI auroral emission images at 427.8 nm, 557.7 nm and 630.0 nm on 2015/12/20 using Universal Time (UT) standard. The geodetic orientation of the images is indicated by the arrows. The bright blob in the lower right of the images is the moon.

In Figure 2-3, each wavelength corresponds to an approximated emission center altitude, 427.8 nm at about 110 km, 557.7 nm at about 96 km, and 630.0 nm at about 200 km. These images are integrated over roughly 12.5 seconds (± 0.07 seconds) of continuous snapshots of the sky for enhanced visualization. In each image, a horizontal belt of auroral emission can be observed near the center. The general shape of the emission is similar between the 427.8 nm and 557.7 nm images. More intense emissions are observed at 557.7 nm and 630.0 nm. But the 630.0 nm image appears blurrier than the crisp images at 427.8 nm and 557.7 nm because red-line emissions can come from a wide range of altitudes. Green and blue lines are much more limited in altitudinal extent and thus better show the inherent horizontal structure of auroral arcs. The crisp and bright 557.7 nm ASI emission data will be used in the comparative studies later against the GNSS results.

The auroral patterns observed by the ASI are amorphous and the scale of these patterns is often much larger than the footprint of the GNSS array. This makes accurate frame-by-frame

estimation of the arc velocity with GNSS derived velocity challenging, but the general direction of the auroral arcs can often be estimated via visual inspection [*Wang et al.*, 2018]. Hence in this dissertation, the ASI measurements are used to identify the auroral emission patterns and to assess the irregularity travel direction estimated by the GNSS receiver array.

2.4.2. Incoherent Scatter Radar

Incoherent Scatter Radars (ISR) are Doppler radars dedicated to ionospheric researches. The term "incoherent scatter" refers to the assumption that all of the Thomson scattering electrons have statistically independent random motions [*Gordon*, 1958; *Evans*, 1969]. Based on the collective backscatter from these electrons, statistics such as the autocorrelation function (ACF) and power spectrum can be established, from which the irregularity drift velocities together with other parameters of the probed plasma irregularities can be inferred [*Kudeki and Milla*, 2012].

The PFISR is also located at the PFRR (65.13°N, 147.47°W) [*Nicolls and Heinselman*, 2007]. It is a 128-panel Advanced Modular Incoherent Scatter Radar (AMISR) system operating at the frequency band of 450 MHz [*Heinselman and Nicolls*, 2008]. Normal user operations have been ongoing since March 2007. The radar is tilted so that its bore sight direction corresponds to elevation and azimuth angles of 74° and 15°, respectively. The PFISR consists of 473 preprogrammed look directions, giving the maximum possible sky coverage under the current radar configuration. A more detailed description of PFISR can be found in *Heinselman and Nicolls* [2008]. The PFISR provides measurements of the drift velocities in the form of vector velocities by combining its line-of-sight (LOS) velocity measurements into a range of geomagnetic latitude bins. Figure 2-4 gives an example of the 2-D horizontal vector velocities on 2012/12/31.

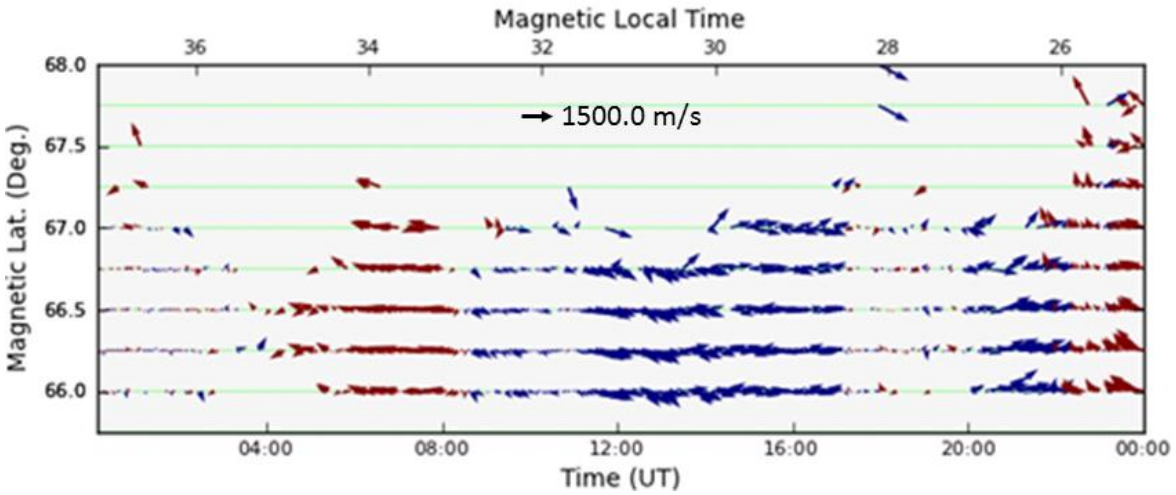

Figure 2-4. Example PFISR horizontal vector velocity measurements from 2015/12/31 00:04:44 to 2016/1/1 00:03:22 UT [Marigal Database, http://isr.sri.com/madrigal/]. These velocities are derived from the horizontal velocity measurements along the perpendicular north and the perpendicular east directions. The velocity magnitudes are indicated by the arrow lengths, with an eastward reference velocity of 1500.0 m/s in the center. The blue arrows are eastward velocities, while the red arrows are westward. The latitudinal resolution is 0.25°.

The spaced-receiver technique presented in this study is only capable of resolving the horizontal velocity components. Hence, the cross-comparison between GNSS and PFISR estimated drift velocities is mainly based on the horizontal vector velocities as in Figure 2-4.

2.4.3. SuperDARN

The Super Dual Auroral Radar Network (SuperDARN) is an international radar network designed primarily for measuring and studying plasma convection. The network is composed of similar pulsed coherent scatter radar arrays in the HF band (8-20MHz), whose combined fields-of-view covers extensive regions of the polar ionospheres in both hemispheres [*Greenwald et al.*, 1995; *Chisham et al.*, 2007].

SuperDARN radars are essentially coherent scatter radars (CSR). These radars are sensitive to coherent scattering (Bragg scattering) from small scale electron density irregularities in the ionosphere, since these irregularities are on the same scale size as the radar half-wavelength. The

geometry of the radar is designed in such a way that the incident radar signal is orthogonal to the geomagnetic field, so that the back scatter from the field-aligned irregularity structures can be maximized [*Greenwald et al.,* 1995].

The HAARP array data was used to conduct a comparison study against SuperDARN measurements. We chose to use the data from the nearest Kodiak SuperDARN (KOD) array at Kodiak, Alaska (57.60°N 152.2°W), since KOD can provide the highest echo power compared to the other SuperDARN arrays in range. Also, the KOD-HAARP geometry is suitable for F region ionosphere studies [*Wang et al*., 2014]. KOD provides a set of echo power and LOS drift velocity measurements for each beam, at every range gate at 1-minute intervals. These measurements are cross-compared with the GNSS array estimated irregularity drift velocities. Figure 2-5 gives an example of the KOD SuperDARN field-of-view plots on 2012/10/13.

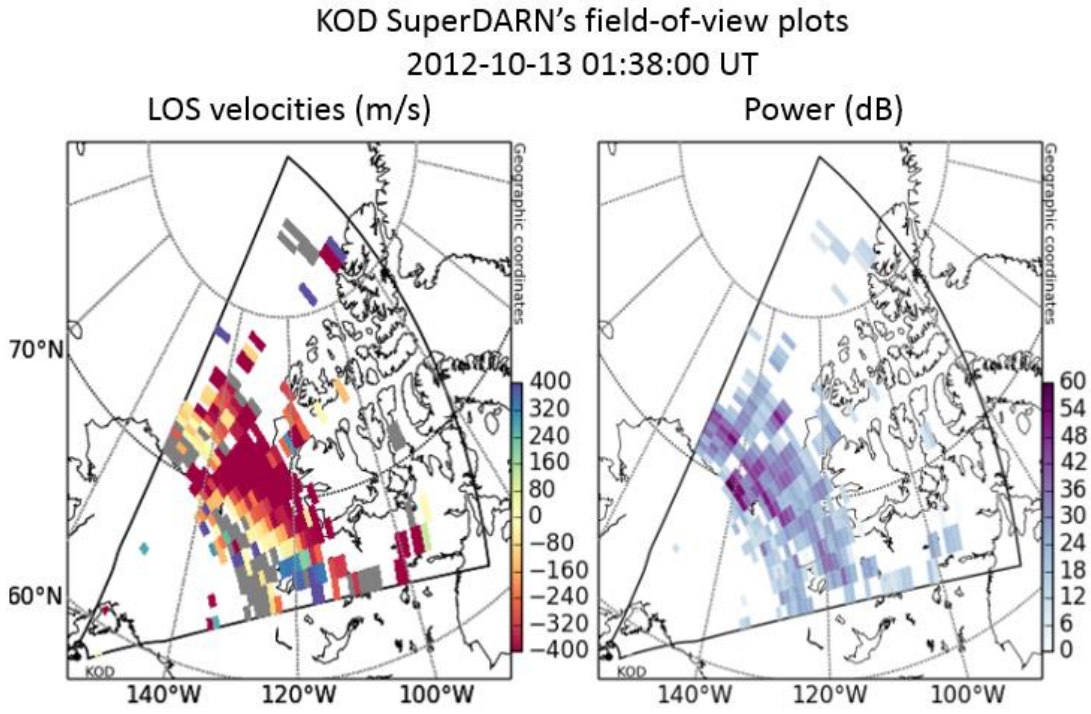

Figure 2-5. Example the KOD SuperDARN's field-of-view plots of LOS velocities (left) and echo power (right) on 2012/10/13.

In Figure 2-5, the left plot is the drift velocity measurement represented by the color code between [-400 400] m/s, while the right plot is the corresponding echo power in the range of [0 60] dB. Note that in the left plot, gray blocks indicate ground scatter and should be discarded during comparison. In addition, echo power can be used to filter the drift velocity measurements to ensure data integrity. In this study, a 3-dB threshold is applied when cross-comparing the GNSS and SuperDARN drift velocity measurements.

2.5. Overview of System Coverages and Cross-Comparison Schemes

In order to conduct a meaningful evaluation of the drift velocity estimation method, the receiver array results are compared with measurements from the instruments mentioned above. A valid comparison must account for differences in spatial coverage between the GNSS receiver array and the other systems. In this section, we characterize the spatial coverage of each system in terms of their observation volume. Cross-comparison schemes between the GNSS results against the PFISR, the SuperDARN and the ASI measurements are also proposed.

2.5.1. GNSS Array Coverage

The spatial coverage of measurements from a GNSS receiver is governed by the satellite-receiver LOS paths and can be determined from the broadcast positions of the visible satellites and the known receiver position. For an array of receivers, the system covers a measurement volume determined by the geometry of the satellites and the receiver array. Figure 2-6 illustrates the overall Poker Flat GNSS array coverage over a full-day in the form of a skyplot on 2017/5/16.

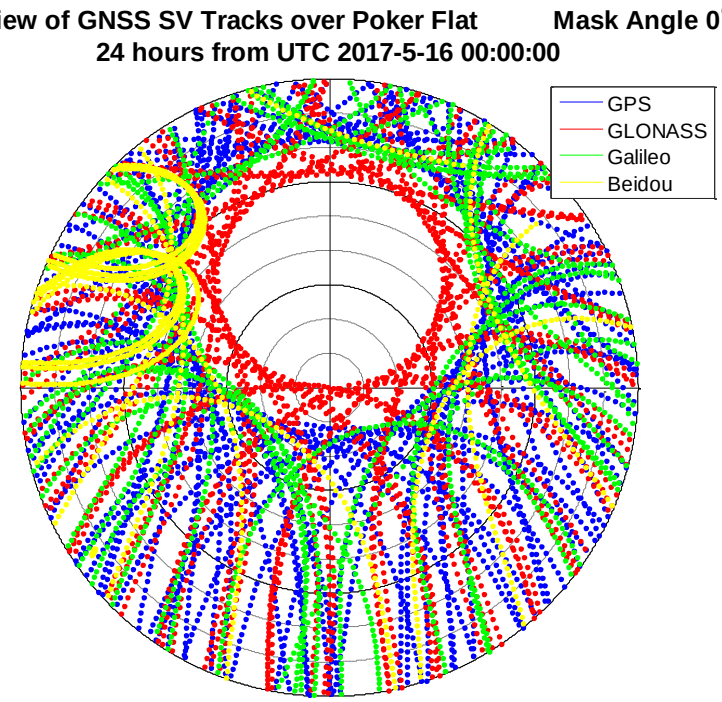

Figure 2-6. Example of Poker Flat GNSS receiver array sky coverage on 2017/5/16 with a 0° mask angle. This skyplot gives the satellites' position via their elevation and azimuth angles at a 5-minute resolution (GPS, blue; GLONASS, red; Galileo, green and Beidou, yellow).

Although Beidou carrier phase measurements are also available at the Poker Flat array, they are not used in this study. This is because at the time of observation, Beidou satellites only had regional coverage towards the northwest part of the sky, while their elevation angles were relatively low (almost always under 40°) at the GNSS array location. They simply failed to provide much admissible drift velocity estimates towards the total results during the scintillation events examined in this study.

2.5.2. ASI Coverage

The ASI coverage is determined by the characteristics of its lenses. In the case of the Poker Flat ASI, the elevation coverage is from 0° to 90°. Note that the ASI is only in operation during local nighttime, limiting its temporal coverage. Figure 2-7 gives an example of the ASI coverage overlaid with the GNSS array coverage at 08:26:40 UT on 2015/12/20.

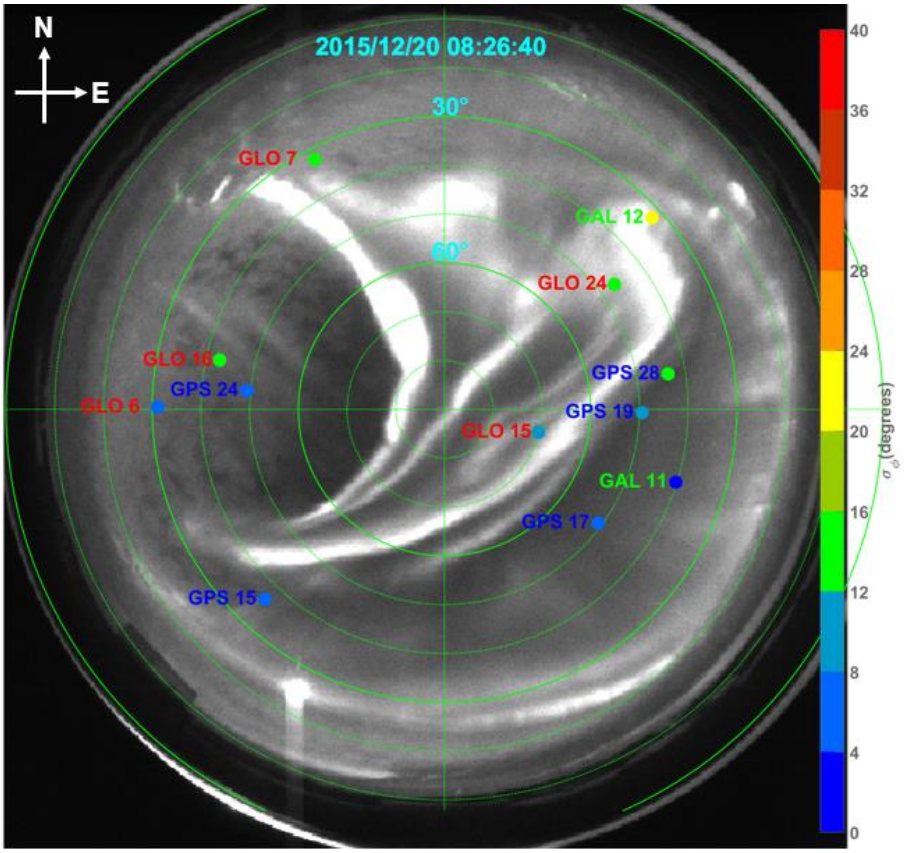

Figure 2-7. Example of Poker Flat ASI sky coverage from a 557.7nm image at 8:26:40 UT on 2015/12/20, overlaid with the GNSS array coverage. The emission intensity is proportional to the ASI image brightness. The numbered dots mark the GNSS satellites' position in the sky (GPS, yellow; GLONASS, red and Galileo, green). The colors of the dots are associated with the phase scintillation strength experienced by each satellite-receiver LOS path, expressed by the color bar based on σ_ϕ values. The geodetic orientation of the image is indicated by the arrows.

2.5.3. PFISR Coverage and Cross-Comparison Scheme

For the PFISR, its coverage is illustrated by all the possible look directions (Figure 1 in *Heinselman and Nicolls* [2008]). Figure 2-8 shows the skyplot of PFISR's coverage, overlaid with the GNSS coverage produced from a full-day example on 2015/3/28 (Figure 2 in [*Wang and Morton*, 2017]).

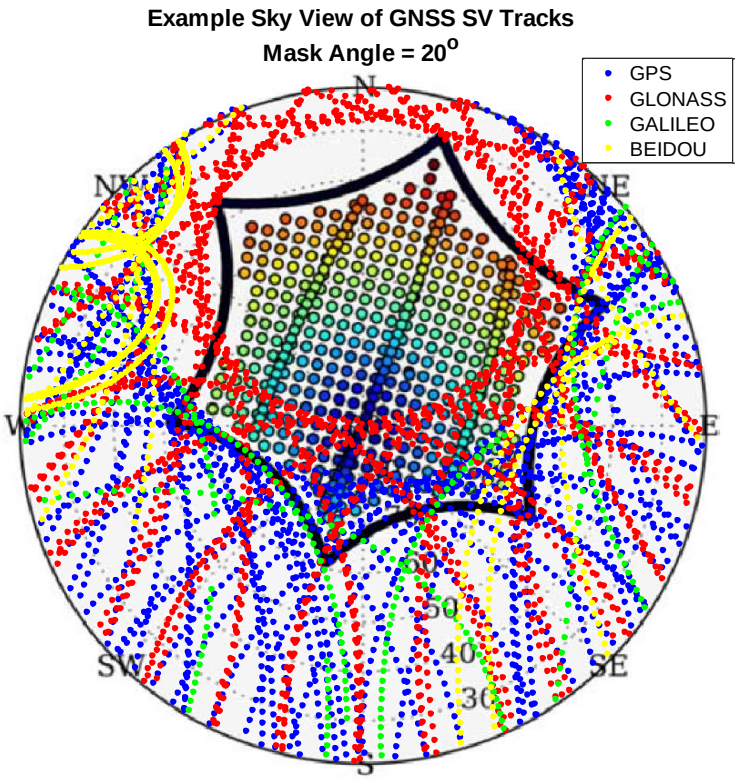

Figure 2-8. Sky coverage of the PFISR expressed in a sky plot covering elevation angles from 20° to 90°, overlaid with the GNSS array coverage on 2015/3/28. The GNSS array's coverage follows the same rubrics as in Figure 2-6. The PFISR's coverage is illustrated by the star-shaped pattern in black, containing all the possible look directions shown by the colored circles (higher elevations, blue; lower elevations, red).

Figure 2-8 shows most of the limited overlapping coverage between the two systems is contributed by the GLONASS satellites. This hinders direct point-to-point comparisons between the two systems. Nevertheless, a cross-comparison scheme is proposed below.

The PFISR provides measurements of the drift velocities in the form of vector velocities binned into geomagnetic latitudes. Therefore, the comparative study of the two systems can be carried out by calculating the geomagnetic latitudes of the GNSS irregularity penetration points (IRPP), and cross-comparing the corresponding velocity values against the PFISR vector velocities. Also, the mean velocities at each epoch across all geomagnetic latitudes within the coverage area are compared between GNSS and PFISR results.

Before going into the details, it is crucial to understand that not only do the two systems observe distinct parts of the sky, but they also have independent schemes for calculating the drift velocities from their measurements. Figure 2-9 illustrates some major differences, while showing the probable geometry of the two systems.

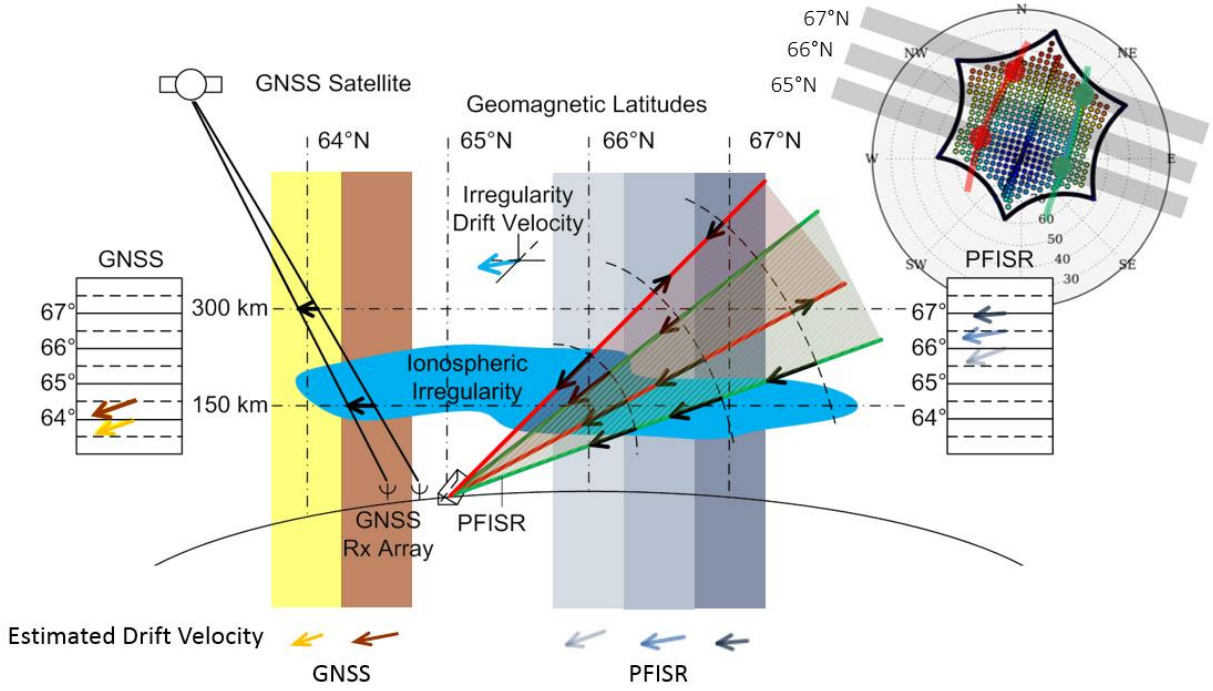

Figure 2-9. Illustration of drift velocity calculation techniques of the GNSS receiver array and the PFISR, as well as the comparison scheme. The pattern in blue outlines an arbitrary scintillation patch, with its true drift velocity given by the blue arrow. For the GNSS array, the black lines represent the satellite-receiver LOS signal paths. The yellow and brown arrows demonstrate different velocity estimations under different IRPP assumptions that are binned into corresponding geomagnetic latitude grids. For the PFISR, 4 beams (2 in green and 2 in red) are selected for velocity calculation, each producing LOS velocity measurements at various range gates specified by the black velocity vectors. These vectors are then binned into different geomagnetic latitude grids (3 blue arrows at different transparency levels). The skyplot in the upper right corner gives the geometry of the beam arrangement.

Focusing on the PFISR's scheme, the LOS velocities from each beam at various ranges are combined into a single velocity at a particular geomagnetic latitude based on a Bayesian approach [*Heinselman and Nicolls*, 2008]. The vector velocities are usually solved over geomagnetic latitudes and represented in three directions with respect to the PFISR look direction: perpendicular

east, perpendicular north, and anti-parallel in the geomagnetic coordinate system. Each selected beam measures up to 1000 km and has a range resolution determined by its programmable coding scheme and pulse arrangement, typically on the order of tens of kilometers. Although the combining algorithm can handle any arbitrary beam arrangement, a favorable scheme would be to choose beams in different meridional planes with large spatial separations (i.e., the red and green planes in Figure 2-9). To summarize, the PFISR's spatial resolution is determined by the beam arrangement, which is typically around several tens of kilometers on the near-end (usually lower latitudes), and around 100 km on the far-end (usually higher latitudes). The radar performance becomes inferior when there's high turbulence or insufficient back scatter, degrading the accuracy in LOS velocity measurements. This is also captured by Figure 2-9.

As for the GNSS array's scheme, the gist of the approach has already been discussed in Section 1.2, while the details of the method can be found in Chapter 3. The main takeaway in this illustration is that different IRPP altitude assumptions not only can lead to numerical differences in the estimated velocities, but also different geomagnetic coordinate projections of these velocities (i.e., the yellow and brown arrows on the left side of Figure 2-9). Another observation of this projection scheme is that during the conversion from the local East-North-Up coordinates into their geomagnetic counterparts, the north component is prone to error caused by the lack of vertical velocity measurement from the spaced-receiver method (refer to equation (4) in *Heinselman and Nicolls*, [2008])

Another difference between the two systems is the temporal resolution. For the PFISR, this is again determined by its pulse arrangement. For the GNSS array, its temporal resolution equals its integration time of the cross-correlations process. In this study, the resolutions turned out to be 5 minutes for the PFISR and 25 seconds for the GNSS array. When cross-comparing the individual

velocity at specific geomagnetic latitude, this difference has no significant impact on the result. However, when cross-comparing the mean velocities, the GNSS results are also averaged over 5 minutes to match the PFISR's resolution.

2.5.4. KOD SuperDARN Coverage and Cross-Comparison Scheme

The KOD SuperDARN consists of 16 radar antennas (beams). These radar beams have a combined azimuthal coverage of 52˚, from approximately 4˚ to 56˚ relative to due north, with individual coverage of 3.24˚. For each beam, the received measurements are divided into 75 range gates with a resolution of 45km. In each full scan, KOD covers 52˚ in azimuth and over 3500 km in range, an area of over 4×106 km² [*Bristow*, 2007]. Based on the KOD SuperDARN topology and the GNSS array location, Figure 2-10 illustrates the sky coverages of (a) an individual beam and (b) the combined array.

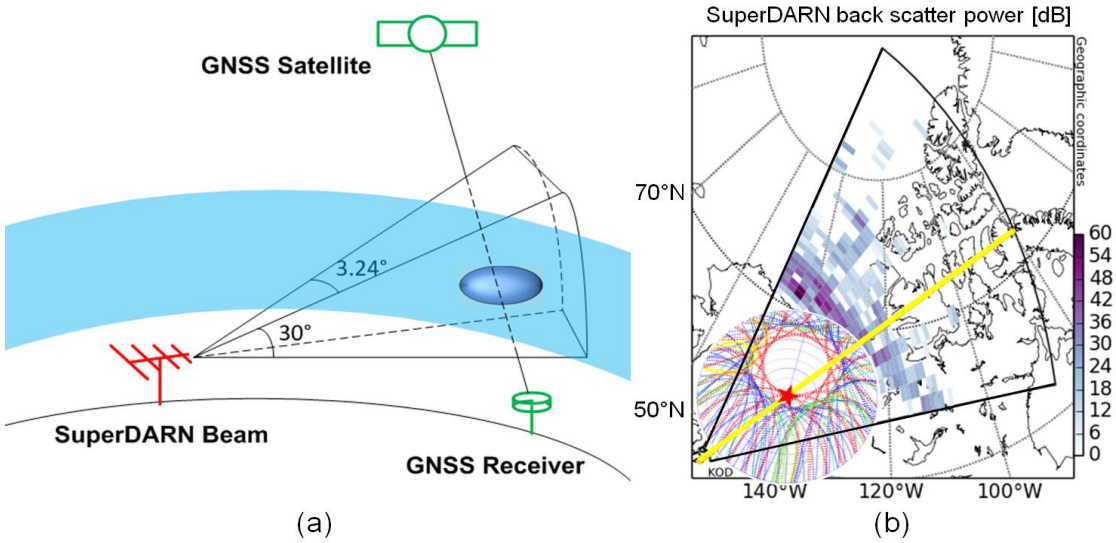

Figure 2-10. Sky coverage of the KOD SuperDARN illustrated in (a) individual beam coverage schematic and (b) the combined array coverage as a field-of-view plot, both accompanied with the GNSS array satellite-receiver LOS topology, respectively. In subplot (a), the satellite-receiver LOS coincides with the SuperDARN-irregularity LOS in the ionosphere (blue belt), showing the common measurement volume. Subplot (b) shows the SuperDARN field-of-view (fan shape) based on the back scatter power measurements (blue rectangles). The GNSS array location is marked by the red star with a yellow beam through the SuperDARN's and GNSS array's locations. A sky plot of satellite tracks is plotted over the GNSS array location, demonstrating the common measurement volume between the two systems.

The general procedure of the cross-comparison scheme between the GNSS array velocity estimates and the SuperDARN measurements can be broken down into the following steps: 1) identify the scintillation GNSS signal IRPP coordinates; 2) calculate the distance and bearing angle from the IRPP location to the SuperDARN location; 3) project the IRPP onto the SuperDARN's field-of-view; 4) identify the corresponding SuperDARN data grid and perform the comparison. Core formulas and detailed procedures can be found in *Wang and Morton* [2015] and *Wang et al.* [2016]. A detailed example is given in Section 6.4.

With the receiver array setup introduced, Chapter 3 demonstrates the detailed methodology of the spaced-receiver techniques for irregularity drift velocity estimation.

3. CHAPTER 3 – SPACED-RECEIVER METHODOLOGY

An overview of the phase scintillation based spaced-receiver method used in this dissertation is given by Figure 3-1 as a block diagram.

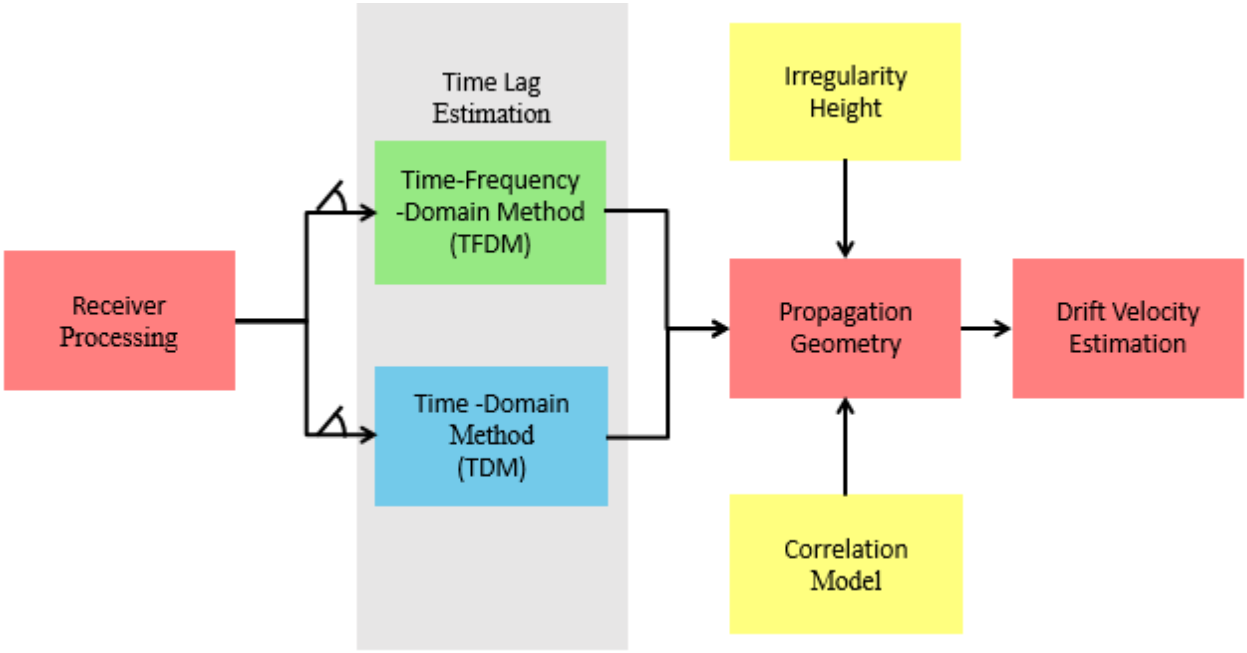

Figure 3-1. Block diagram showing the spaced-receiver methodology. Two correlation methods for 1-D apparent drift velocity estimation are shown in blue (time-domain method, TDM) and green (time-frequency-domain Method, TFDM), respectively. Mutual processing steps are given as the red blocks. The correlation model used to combine the 1-D velocities into 2-D, as well as the irregularity height assumption are shown in yellow blocks.

In this chapter, the basic theory of the scintillation-based spaced-receiver method for estimating the irregularity drift velocity is introduced in Section 3.1. The general method for estimating the satellite scan velocity and the sub-ionospheric distance is shown in Section 3.2. Under the framework of high-latitude phase scintillation, a time-domain method (TDM) and a time-frequency-domain method (TFDM) are presented in Section 3.3 for time lag estimation. In Section 3.4, the estimation bounds for the 1-D apparent irregularity drift velocities along receiver pairs are provided.

3.1. Basic Theory

A receiver array is considered closely-spaced when their distance is on the order of the first Fresnel zone radius at the irregularity structure altitude. The general equation for calculating the n^{th} Fresnel zone radius FR_n at any point along the transmitter-receiver line-of-sight (LOS) is as follows

$$FR_n = \sqrt{\frac{n\lambda d_1 d_2}{d_1 + d_2}} \qquad (3\text{-}1)$$

where n denotes the order of the Fresnel zone, λ is the wavelength of the transmitted signal, and d_1 and d_2 represent the distances from the irregularity to the satellite and receiver, respectively. For the GPS L1 signal ($\lambda \approx 0.19$ m), if the irregularity structure altitude is assumed to be 350 km ($d_2 = 350$ km), then for a satellite at zenith ($d_1 \approx 20192$ km), the first Fresnel zone radius is approximately 256 m.

For a closely-spaced receiver array, assuming that the irregularity structure is "frozen-in" while drifting across the LOS between the receivers and a satellite, the same irregularity structure will cause similar phase fluctuations on all receivers' outputs. Cross-correlation between measurements obtained from any two antennas should contain information on the time differences of the received fluctuations at the two antennas.

Together with the known geometry of the antenna array configuration, the apparent irregularity pattern drift velocity, $\boldsymbol{v}'$, can be estimated along any pair of antennas:

$$\boldsymbol{v}' = \frac{\Delta d}{\Delta t} \qquad (3\text{-}2)$$

where Δt denotes the time lag between the antenna pair observing the same irregularity structure, and Δd denotes the sub-ionospheric distance between their corresponding IRPPs. The difference between Δd and the receiver baseline distance Δd_{RX} is rather small for satellites at high

elevations (>40º), but will notably increase towards low elevations [*Kil et al.*, 2000; *Kil et al.*, 2002], as illustrated in Figure 3-2.

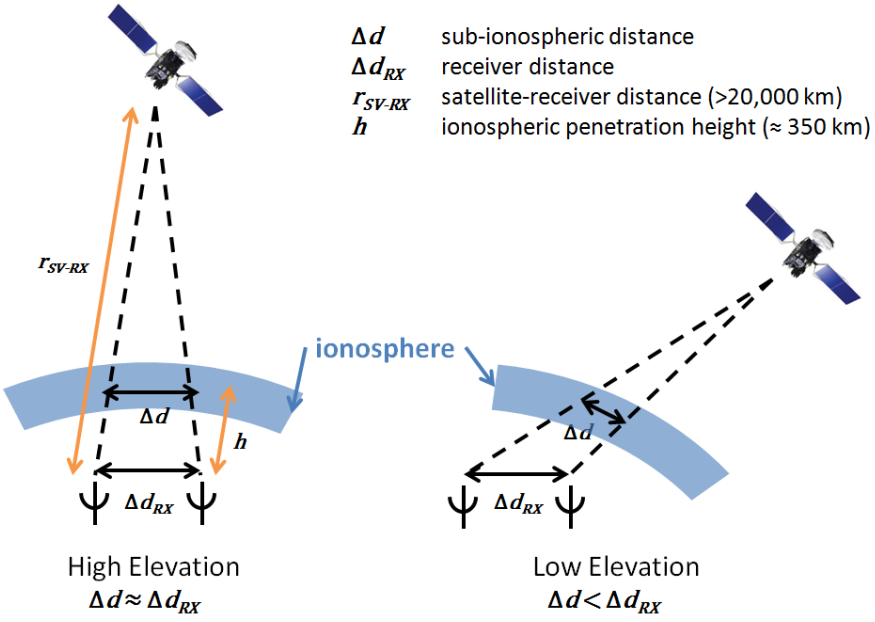

Figure 3-2. Illustration of sub-ionospheric distance Δd vs. receiver distance Δd_{RX}. A high elevation scenario is given on the left while a low elevation scenario is no the right. In the left sublot, the satellite-receiver distance and the IRPP height are marked by the longer and shorter orange lines, respectively.

An approximation of the sub-ionospheric distance Δd calculation will be presented in Section 3.2. The estimated Δd values are then adopted in all subsequent calculations. In this study, only observations made at high elevations are considered, so that the signal fluctuations caused by effects other than ionosphere irregularities, such as multipath and ground-based interference, can be greatly reduced. For the HAARP array, the satellite elevation mask is set to be 40°. For the Poker Flat array, the elevation mask is lowered to 35°, due to improved signal quality.

In order to combine the 1-D apparent drift velocities along the receiver pairs into a 2-D apparent velocity in the horizontal plane, several velocity modeling methods are studied/developed, including the classic isotropy model, a front velocity model and the anisotropy model. These models are described in detail in Chapter 4.

It must be noted that the apparent drift velocity is not the same as the ionospheric irregularity drift velocity. The former is the combined effects observed at the receiver array of irregularity drift velocity and signal scanning velocity at the IRPP. In the case of geostationary (GEO) satellites, the apparent drift velocity and the irregularity drift velocity are essentially equivalent. For non-geostationary GNSS satellites, the satellite motion gives the same effect as the irregularity layers moving in the opposite direction to the satellite [*Kil et al.*, 2000]. The actual ionospheric irregularity drift velocity, $\boldsymbol{v_{ion}}$, can be estimated by the relation

$$\boldsymbol{v_{ion}} = \boldsymbol{v'} + \boldsymbol{v_s}' \qquad (3\text{-}3)$$

where $\boldsymbol{v_s}'$ represents the satellite scan velocity at the irregularity altitude and $\boldsymbol{v'}$ is the apparent irregularity pattern drift velocity. Figure 3-3 illustrates this property in a 1-D scenario, although the general idea holds along any vector component in the zonal-meridional plane.

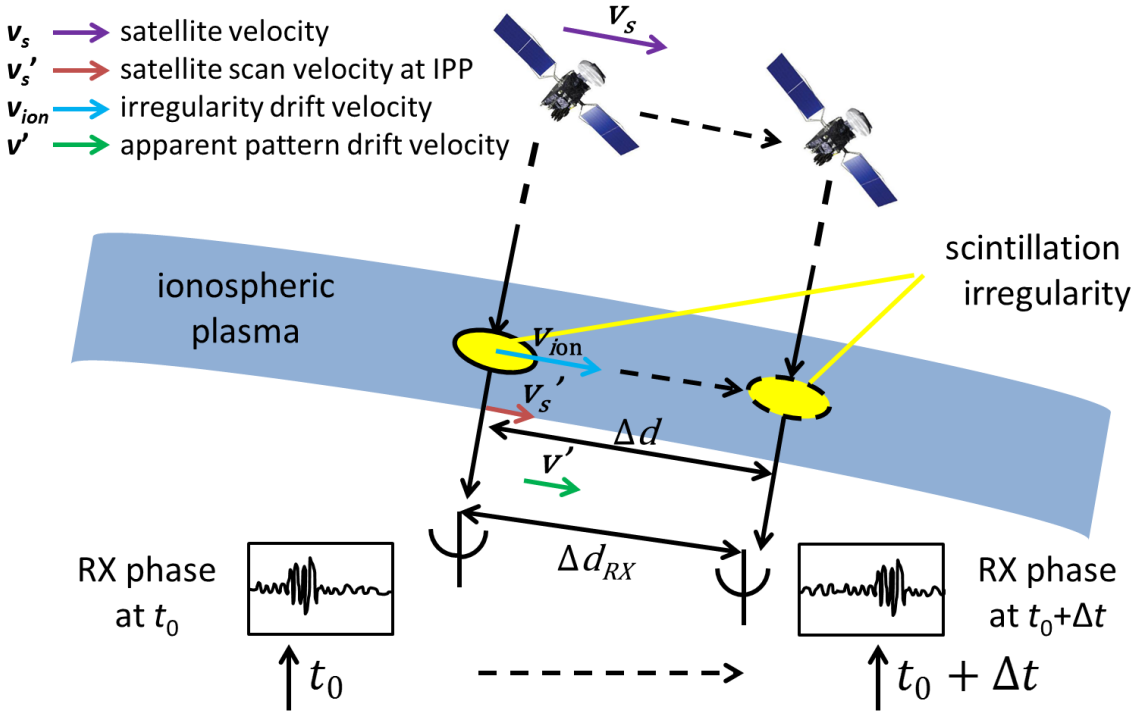

Figure 3-3. Illustration of drift velocity estimation method. A scintillation irregularity is drift from the yellow bubble on the left to the dashed yellow bubble on the right at $\boldsymbol{v_{ion}}$. The receiver on the left detects the scintillation pattern at t_0, while the receiver on the right saw it Δt seconds

later. The focus of this problem is to solve for $\boldsymbol{v_{ion}}$ from the satellite scan velocity $\boldsymbol{v_s'}$ at IRPP height, and the apparent irregularity pattern drift $\boldsymbol{v'}$.

The main purpose of this chapter is to estimate the irregularity drift velocity, which is often assumed to be same as the background plasma drift velocity. The validity of this assumption has been supported by co-located ISR measurements in a number of studies [*Ledvina et al.*, 2004; *Basu et al.*, 1991a; *Kil et al.*, 2002]. On occasion, however, discrepancies between ISR measured plasma drift and spaced-receiver derived irregularity drift have also been found [*Kil et al.*, 2000; *Basu et al.*, 1991b]. *Basu et al.* [1991b] demonstrated that only one out of four data sets for spaced-receiver irregularity drift velocity estimations at high latitudes showed fair agreement with the Sondrestrom ISR measured plasma drift velocities. *Kil et al.* [2000] found the irregularity drift estimations to be on average 10 – 30 m/s larger than radar measured plasma drift at the same latitude. Thus far, existing literature does not reveal a consistent relationship between the irregularity drift and the plasma drift. As will be shown in Chapter 6, the techniques presented in this dissertation can be used in conjunction with ISR to simultaneously measure irregularity and background plasma drift velocities.

Based on Equation 3-3, $\boldsymbol{v_{ion}}$ can be obtained by accurately estimating $\boldsymbol{v'}$ and $\boldsymbol{v_s'}$. Estimation of the satellite scan velocity $\boldsymbol{v_s'}$ at the IRPP is presented in the following section. Estimation of the apparent irregularity pattern drift velocity $\boldsymbol{v'}$ is more challenging and is really the cornerstone of this project. Section 3.3 focuses on the time lag estimation, which is a key component for estimating the 1-D apparent irregularity pattern drift along receiver pairs. To expand the solution into 2-D, a correlation model is required to account for the topology of the irregularity pattern. This is discussed in Chapter 4.

3.2. Satellite Scan Velocity

The instantaneous satellite scan velocity at the IRPP can be estimated by the average scan velocity over a short amount of time. The estimation process is demonstrated by the following steps:

1) Let the time epoch of calculation be t_1, determine the elevation and azimuth angles of the satellite signals exhibiting sufficient phase fluctuation at t_1. This is achieved by estimating the satellite orbit using ephemeris decoded from the receiver output at Antenna 1. Use the same approach to determine another set of elevation and azimuth angles shortly after t_1, say at t_2, with $t_2 - t_1 = \Delta t$. In this dissertation, Δt is taken as 1 second.

2) Compute the IRPP latitudes φ and longitudes λ corresponding to these two sets of elevation and azimuth angles [*Klobuchar*, 1987]:

$$\angle A_i = 90° - \angle ele_i - \arcsin\left(\frac{r_e}{r+h}\cos\angle ele_i\right) \quad (3\text{-}4)$$

$$\varphi_i = \arcsin(\sin\varphi_0 \cos\angle A_i + \cos\varphi_0 \sin\angle A_i \cos\angle azi_i) \quad (3\text{-}5)$$

$$\lambda_i = \lambda_0 + \arcsin\left(\frac{\sin\angle A_i \sin\angle azi_i}{\cos\varphi_i}\right), \quad i = 1,2 \quad (3\text{-}6)$$

where r is the Earth radius, h is the IRPP altitude, φ_0 and λ_0 are the receiver's latitude and longitude, $\angle azi$ and $\angle ele$ are the satellite's elevation and azimuth angles determined from step 1, $\angle A$ is commonly referred as the "Earth angle", and i denotes the time index. Figure 3-4 illustrates the geometry and relationships among these parameters and parameters used in the following steps.

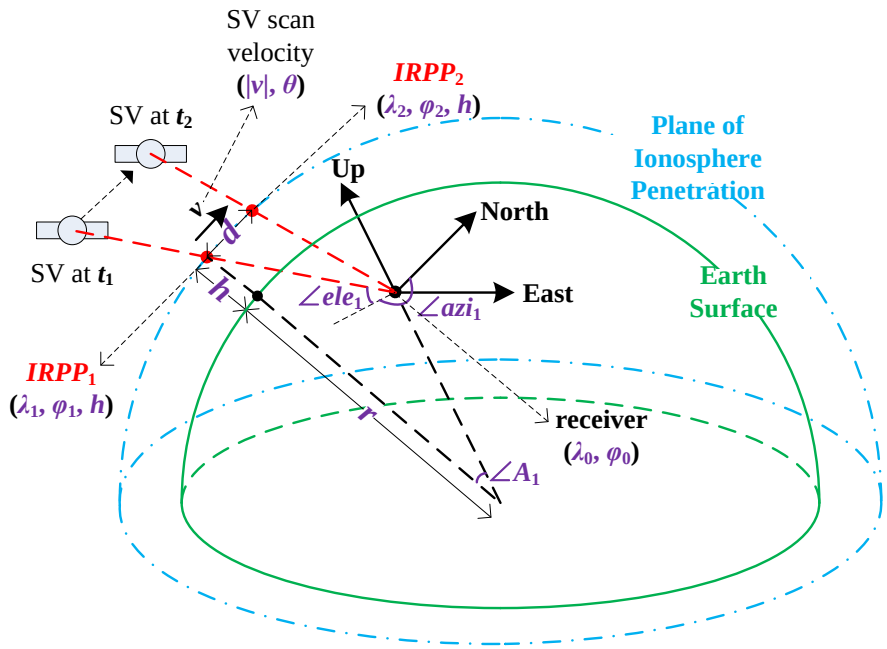

Figure 3-4. Schematic of parameters used in satellite scan velocity estimation. $IRPP_1$ and $IRPP_2$ are determined based on the fixed receiver position and the satellite positions at t_1 and t_2. The satellite scan velocity at IRPP altitude is calculated as the ratio between the displacement d, and the time difference $\Delta t = t_2 - t_1$.

3) Use the 'haversine' formula to calculate the great-circle distance between the two IRPP's, i.e., the shortest distance over the surface at the IRPP altitude [*Robusto*, 1957]:

$$a = \sin^2\left(\frac{\varphi_2 - \varphi_1}{2}\right) + \cos\varphi_1 \cos\varphi_2 \sin^2\left(\frac{\lambda_2 - \lambda_1}{2}\right) \quad (3\text{-}7)$$

$$c = 2 \cdot \arctan\left(\frac{\sqrt{a}}{\sqrt{1-a}}\right) \quad (3\text{-}8)$$

$$d = (r + h) \cdot c \quad (3\text{-}9)$$

where φ and λ are obtained from step 2, and d is the great-circle distance. Unlike the classic 'haversine' formula that assumes the reference frame to be on the surface of the Earth, a modification is made here in the last equation so that the reference frame is now the surface at the IRPP height.

4) Calculate the bearing angle θ between the two IRPP's:

$$y = \sin(\lambda_2 - \lambda_1)\cos\varphi_2 \quad (3\text{-}10)$$

$$x = \cos\varphi_1 \sin\varphi_2 - \sin\varphi_1 \cos\varphi_2 \cos(\lambda_2 - \lambda_1) \quad (3\text{-}11)$$

$$\theta = \arctan\left(\frac{y}{x}\right) \quad (3\text{-}12)$$

5) Now that both d and θ have been found, together with the already known Δt, the average satellite scan velocity between the two IRPP's can be calculated by:

$$|\boldsymbol{v}| = \frac{d}{\Delta t} \quad (3\text{-}13)$$

with the direction of θ, pointing from the IRPP at t_1 to the IRPP at t_2. If Δt is small enough, this average velocity can be approximated to the instantaneous scan velocity $\boldsymbol{v_s}'$.

3.2.1. Sub-Ionospheric Distance

The sub-ionospheric distance is the distance between the IRPPs along the LOS of two receivers observing the same satellite, as illustrated in Figure 3-2. An approximation of the sub-ionospheric distance can be computed using a similar technique demonstrated above. For a particular satellite, the elevation and azimuth angles at each receiver can be estimated using the decoded ephemeris. The corresponding IRPP coordinates can be calculated as in Equations 3-4 through 3-6. Finally, the sub-ionospheric distance between the two IRPPs is found using Equations 3-7 through 3-9.

3.3. Time Lag Estimation

3.3.1. Time-Domain Method

The TDM used in this study follows the conventional time-domain cross-correlation technique [*Kil et al*., 2000]. But as stated in Section 1.2.1, the signal intensity measurements used in the conventional method is not suitable for high-latitude scintillation-based spaced-receiver

technique. Hence, a major modification in the proposed TDM is to apply the time-domain cross-correlation algorithm on GNSS carrier phase measurements instead.

During the process of acquiring the time shifts at correlation peaks (or time lags), the correlation coefficients are generated as by-products. Intuitively, correlation values associated with higher coefficients are desired, as they represent higher confidence levels. Therefore, a correlation coefficient filter can be implemented to ensure the integrity of the calculated time lags. Figure 3-5 is a block diagram demonstrating the TDM.

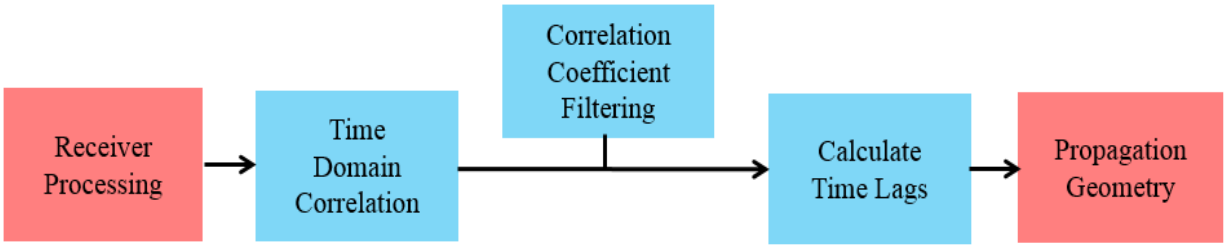

Figure 3-5. Block diagram showing the TDM.

On the other hand, excessively high correlation coefficient thresholds lead to very few admissible time lag estimations, degrading the statistical performance of the algorithm. By matching the GPS L1 estimated drift velocities with the GPS L2C estimations, *Wang and Morton* [2017] proposed a balanced correlation coefficient threshold at 70%, which is adopted in this dissertation as well.

According to the spaced-receiver technique, the drift velocity of an irregularity patch is captured when disturbances occur in the input signals, which are GNSS carrier phase signals in this case. The correlation coefficient filter can guarantee a high confidence level in the estimated time lags, but it cannot separate disturbed signals from quiet conditions. In other words, with the correlation coefficient filter alone, the algorithm may still provide drift velocity estimations even when the receiver array is not observing any significant irregularities.

To further ensure the validity of the algorithm, irregularity strength is estimated, and the calculated time lags are further filtered based on the irregularity strength. The σ_ϕ value is the most commonly adopted metric for GNSS phase irregularities [*Yeh and Liu*, 1982]. In our previous study, a σ_ϕ threshold at 12° is found to be capable of separating irregularities from noise via similar dual frequency self-consistency study, as seen in the above section [*Wang and Morton*, 2016]. This threshold value is adopted for GPS and Galileo satellites in this study. Note that this scintillation strength filtering technique can be applied to the TFDM as well.

Also, the TDM is less applicable under noisy signal conditions, such as the signal attenuation issue at the HAARP array. In this dissertation, the TDM is only applied on data collected from the Poker Flat array.

3.3.2. Time-Frequency-Domain Method

Unlike signal intensity measurements for amplitude scintillations, carrier phase measurements can be plagued with errors from a number of sources. Among them, receiver oscillator-induced phase jitter and multipath are difficult to distinguish from ionospheric irregularity-induced fluctuations. Carrier phase measurements are also susceptible to cycle slips, especially during scintillation events when signals experience fading and/or higher carrier dynamics. Carrier phase detrending processes aimed to remove low frequency components, such as receiver-satellite dynamics, satellite orbit errors, receiver and satellite clock bias, background ionosphere and troposphere induced carrier phase trend, etc., may over- or under-filter fluctuations due to ionospheric irregularities [*Beach*, 2006; *Mushini et al.*, 2012; *Niu et al.*, 2012]. The combined effects of these factors are likely to yield unreliable or inconsistent correlation results when directly applying the TDM. In the case of the HAARP array, the signal condition is inferior due to the notable signal attenuation occurred when long cables were used to connect the antennas

to the receivers and frontends. Figure 3-6 gives an example of detrended GPSL1 carrier phase measurements at the HAARP array.

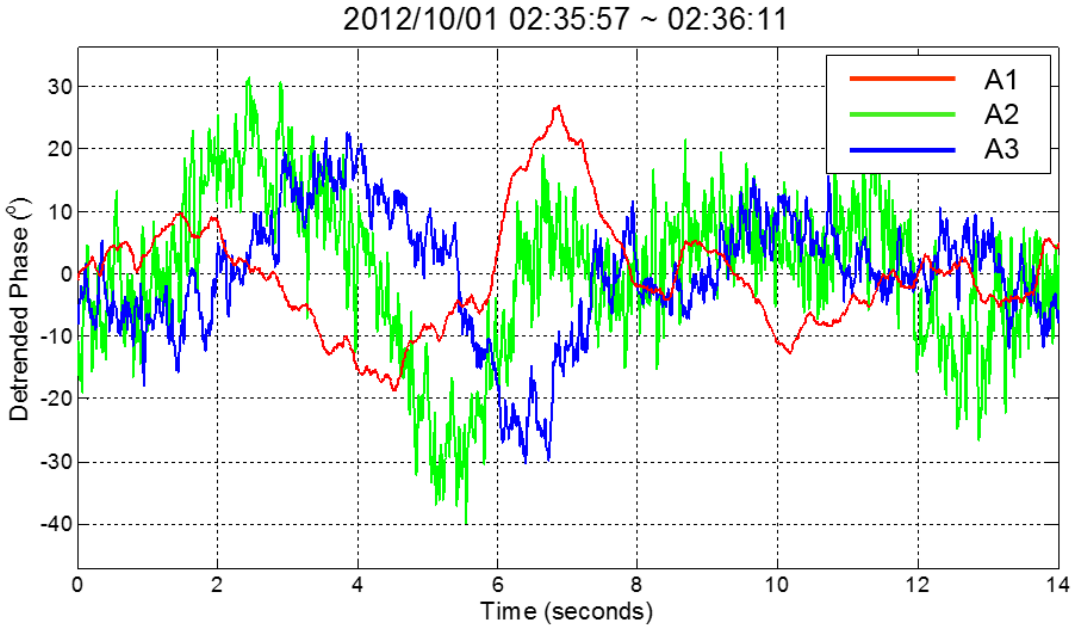

Figure 3-6. Example of detrended carrier phase measurements on GPSL1 at the HAARP array from 02:35:57 to 02:36:11 UT on 2012/10/1. The phase signals are shown in red, green, and blue for Antennas 1, 2 and 3, respectively. The signals received at Antenna 2 and 3 are noisier than the on Antenna 1 because they are connected to the receivers via longer cables

As can be seen in Figure 3-6, there is substantial noise on Antennas 2 and 3, as opposed to the clean signal on Antenna 1. The cable length from Antenna 2 to the equipment shelter is the longest, causing the largest noise corruption on the measurements.

To address these issues, we resorted to time-frequency analysis (TFA). The gist of the approach is to transform the original time-domain phase measurements into time-frequency-domain, so that spectral filtering can be applied without losing the temporal information which is crucial for the correlation process.

TFA techniques are widely used in fields associated with instrumentation and measurement, such as power quality analysis [*Gu and Bollen*, 2000; *Radil et al.*, 2008], fault

detection [*Pineda-Sanchez et al.*, 2010], and biomedical and biometric applications [*Zhou et al.*, 2008; *Chatterjee et al.*, 2010], etc. Most of the techniques stem from spectral estimation methods that fall into two categories: nonparametric and parametric. In nonparametric methods, the signal is assumed to be only composed of sinusoidal components with no dependency on any statistical model. Conversely, in parametric methods, the signal is assumed to follow certain probability distribution models. *Sejdić et al.* [2009] provides a recent review on both categories. In ionospheric scintillation studies, the Nakagami-m and Gaussian distributions are often used to describe amplitude and phase scintillations, respectively [*Pullen et al.*, 1998; *Hegarty et al.*, 2001; *Humphreys et al.*, 2009]. However, these model distributions appear to break down for strong scintillations [*Rino*, 2011]. For this reason, only nonparametric methods are considered in this study. Our previous studies investigated several nonparametric methods. Among them, an adaptive periodogram (APT) method shows superior performance in both time and frequency domains [*Wang et al.*, 2012; *Wang*, 2013]. It can adaptively detect the optimal window length of any frequency component to produce high resolution time-frequency spectrum [*Wang and Morton*, 2015].

Based on the APT method, the TFDM has been developed [*Wang et al*., 2014; *Wang and Morton*, 2015]. After the transforming the time-domain signals into time-frequency domain, additional spectral filtering routines are applied to increase the signal-to-noise ratio of scintillation signatures. As a result, this method is suitable for weak signal conditions. Figure 3-7 is a block diagram demonstrating the TFDM.

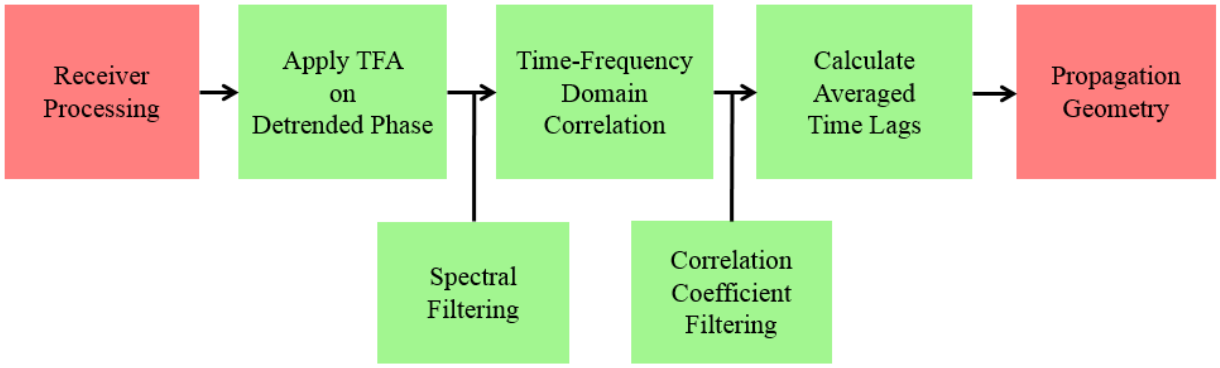

Figure 3-7. Block diagram showing the TFDM.

In the following sections, the APT is explained in Section 3.3.2.1, while the TFDM implementation is demonstrated by an example in Section 3.3.2.2, following the architecture in the above block diagram.

3.3.2.1. Adaptive Periodogram Technique

APT is a joint time-frequency analysis (TFA) method developed to capture the time-varying spectral features of phase fluctuation. Detailed descriptions of the APT algorithm and comparisons of its performance against other joint time-frequency analysis methods can be found in [*Wang et al.*, 2012; *Wang et al.*, 2013; *Wang and Morton*, 2015]. The basis of the APT spectral estimation method is Lomb's periodogram, which is modified from the classic Shuster's periodogram using a least-squares (LS) approach [*Schuster*, 1897; *Lomb*, 1976]. It estimates the spectrum values by LS-fitting sine waves to the signal [*Lomb*, 1976; *Scargle*, 1982]. The method is based on a linear model fitting, which sets up a convenient framework for further analyses [*Zhang et al.*, 2012]. Lomb's periodogram of an input signal x with N points is defined as:

$$P_x(\omega) = \frac{\left(\sum_{i=1}^{N} x(t_i)\cos(\omega t_i)\right)^2}{\sum_{i=1}^{N}\cos^2(\omega t_i)} + \frac{\left(\sum_{i=1}^{N} x(t_i)\sin(\omega t_i)\right)^2}{\sum_{i=1}^{N}\sin^2(\omega t_i)} \qquad (3\text{-}14)$$

Lomb's periodogram only outputs one periodogram value for all N points of the input. Consequently, all time information is discarded. In order to retrieve the time information, Equation 3-14 is modified into:

$$P_x(\omega, n) = \frac{\left(\sum_{i=1}^{n} x(t_i)\cos(\omega t_i)\right)^2}{\sum_{i=1}^{n}\cos^2(\omega t_i)} + \frac{\left(\sum_{i=1}^{n} x(t_i)\sin(\omega t_i)\right)^2}{\sum_{i=1}^{n}\sin^2(\omega t_i)} \qquad (3\text{-}15)$$

The major advantage of Lomb's periodogram as a spectral estimation method is its ability to adaptively detect the window length of any frequency component. The following example illustrates such a property. Let the input signal x be a time series containing a single continuous wave (CW) signal interval. Figure 3-8 demonstrates that the periodogram can accurately detect the endpoints of this CW interval simply by searching for the peak index.

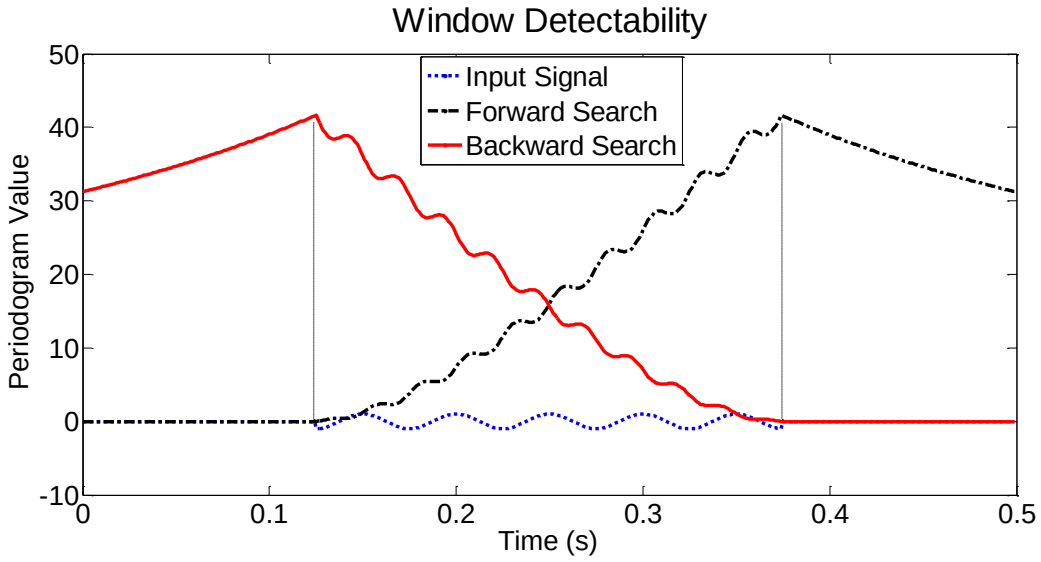

Figure 3-8. Illustration of window detectability of Lomb's periodogram. The black dash-dot and red solid lines demonstrate the forward and backward search, respectively. The search peaks indicate the successful detection of the ending and starting points of the signal window as the blue dashed line.

In Figure 3-8, 500 data points are sampled above the Nyquist rate at 1000 Hz. The input signal (blue dashed line) contains a CW cosine wave between the 126th and 375th data point

simulated at 20 Hz in a noise-free environment. A forward search at 20 Hz (black dash-dot) identifies the CW signal's ending point, while a backward search (red solid) finds the starting point. The peak indices of the two-way search correctly identify the CW signal window.

A trade-off for this window detection ability is that window biases could exist in certain regions of the two-way search depending on the signal frequency and the sampling frequency. Nevertheless, such biases will diminish over time due to the LS-fitting feature [*Wang*, 2013].

This window detection ability of Lomb's periodogram ensures that APT produces a good time resolution. In order for the algorithm to have a good frequency resolution, intuitively, when the periodogram is evaluated at frequencies other than the signal frequency, the periodogram value should remain insignificant. Figure 3-8 illustrates this property.

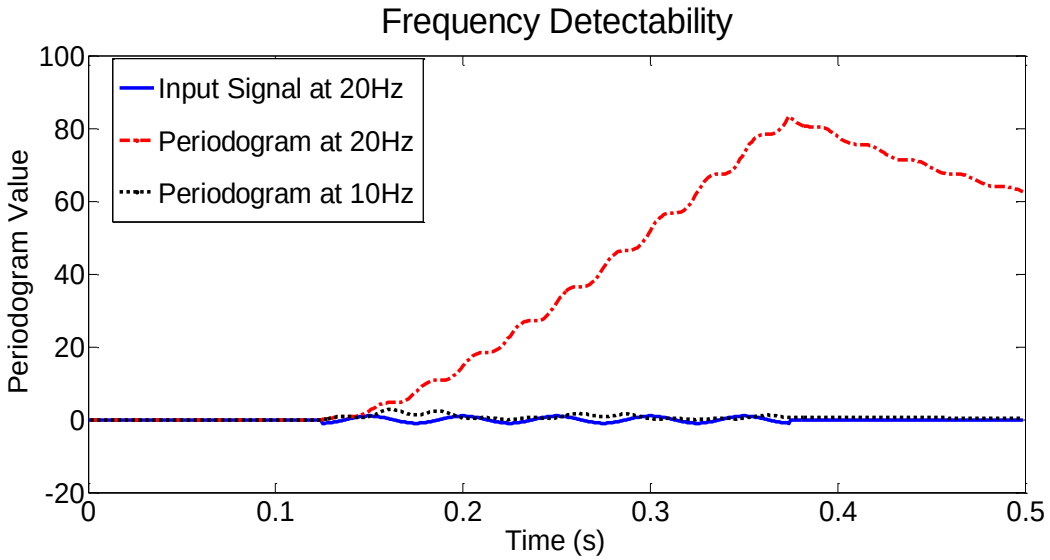

Figure 3-9. Frequency detectability of Lomb's periodogram. The red dash-dot line demonstrates forward search at 20 Hz, the same frequency of the input signal as the blue solid line. The search peak is significantly higher than that of the forward search as the black dashed line at a different frequency of 10 Hz.

In Figure 3-9, the blue solid line represents the CW signal at 20 Hz; the red dash-dot line is the periodogram forward search at the same frequency, while the black dashed line is the

periodogram value at 10 Hz. Evidently, a search for a non-present frequency will yield small values and should not be able to identify the signal. This property can be proved by using the orthonormality relation of the Fourier kernels [*Wang*, 2013]. On the other hand, governed by the Uncertainty Principle, the periodogram value at a frequency very close to the signal's frequency would be much more noticeable [*Cohen*, 1995]. However, it should not exceed the periodogram value at the true frequency.

Based on Lomb's periodogram, the APT power spectrum can be calculated by applying two-way searches scanning across the desired frequencies [*Wang*, 2015]. A byproduct of the algorithm is the APT optimized window lengths. The product of these two gives the APT energy spectrum.

One of the most important properties of any joint time-frequency analysis method is their performance in the presence of noise. *Lomb* [1976] showed that the periodogram at any frequency has a chi-squared distribution with two degrees of freedom. Under such a framework, *Brenneman et al*. [2007] designed a hypothesis test to demonstrate the frequency detection performance of APT under noise. The test reveals the relationship among the desired false alarm rate (α), the missed detection rate $(1-\beta)$, the minimum signal-to-noise-ratio (SNRmin) of the signal, and the required minimum number of data points (η) for the APT algorithm.

In the actual implementation, the optimal window lengths and the separation between peak indices can both be bounded by their corresponding pre-specified ranges. If certain characteristics of the signal structure are known, as is the case for scintillation indicators, these strategies can drastically benefit the computational performance. To improve the visual representation of the resulting spectra, raw APT spectra are converted into decibel (dB) values with respect to their mean spectrum values using base-10 logarithm. Figure 3-10 shows an example of the GPS PRN 8

APT energy spectrum in dB generated from data taken by the ISM receiver from 12:06:17 to 12:11:17 UTC, on 2012/10/13.

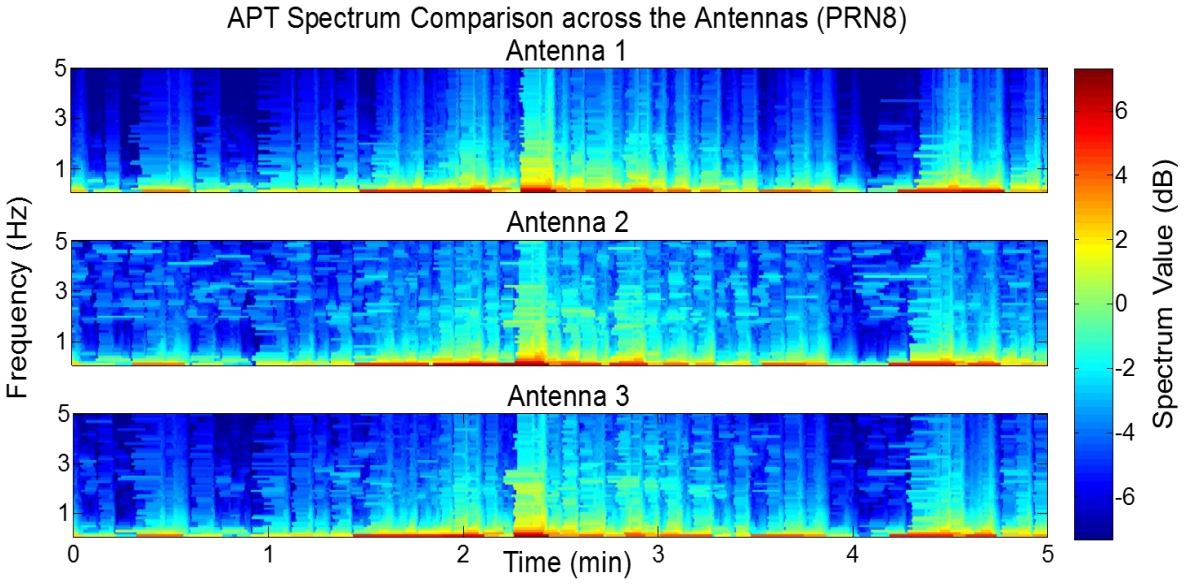

Figure 3-10. Five minutes example of normalized APT energy spectrum comparison across all antennas from 12:06:17 on PRN8. The color bar on the right is in dB with respect to the mean value of the APT spectrum.

The window length bound is set to [50, 6000] (samples), while the peak separation bound is set to [300, 6000] (samples). These APT parameters are adopted throughout this dissertation, based on the study of spectrum analysis presented in [*Wang*, 2013]. The target frequency range in this example is empirically set from 0.05 Hz to 5 Hz with a step size of 0.05 Hz.

3.3.2.2. TFDM Implementation

After applying the APT algorithm, the APT spectra are filtered in order to remove low power level components, which are most likely due to contributions from noise. The cross-correlation function between two APT filtered spectrum outputs, $P_{1,f}$ and $P_{2,f}$, at frequency f, is given by:

$$C_f(\tau) = \frac{\sum_k P_{1,f}(t_k) P_{2,f}(\tau - t_k)}{\sqrt{\sum_k {P_{1,f}}^2(t_k) \sum_k {P_{2,f}}^2(t_k)}} \quad (3\text{-}16)$$

The cross-correlation is carried out during intervals within which the ionospheric irregularity is assumed to be "frozen-in". During each correlation interval, the correlation coefficients and the time lags are both recorded for all frequencies across the APT spectra. Therefore, there are multiple time lags for each time window. Only time lags corresponding to numerically high correlation coefficients (>0.9, for example) are considered to further minimize contributions from irregularities that may have some degree of varying patterns observed by the two antennas. Averaging of these time lags within each window is performed to obtain the time difference of the event's arrival between the antennas. With the calculated sub-ionospheric distances between antennas and averaged time lags, the apparent scintillation pattern drift velocity can be estimated.

We use phase fluctuation events observed on 2012/10/13 by the receiver array at Gakona, Alaska to illustrate the TFDM processing. One-hour data starting from 11:54:17 UTC were recorded on both USRP frond ends and the ISM receiver. Four GPS satellites (PRN 5, 7, 8 and 26) exhibited large phase fluctuations. PRN 7 and PRN 8 stayed at high elevations (>40º) throughout this period, while PRN 5 and PRN 26 were visible at high elevations during most of this period.

Using this phase fluctuation event, 10 minutes of detrended carrier phase measurements of PRN 8 are extracted from both antennas starting from 12:04:17 UTC. As defined in Equation 1-2, the commonly used phase scintillation index, σ_ϕ, is calculated to show the strength of this event. σ_ϕ at 10 s resolution and the detrended carrier phase at 0.01 s resolution are plotted in Figure 3-11 for both antennas.

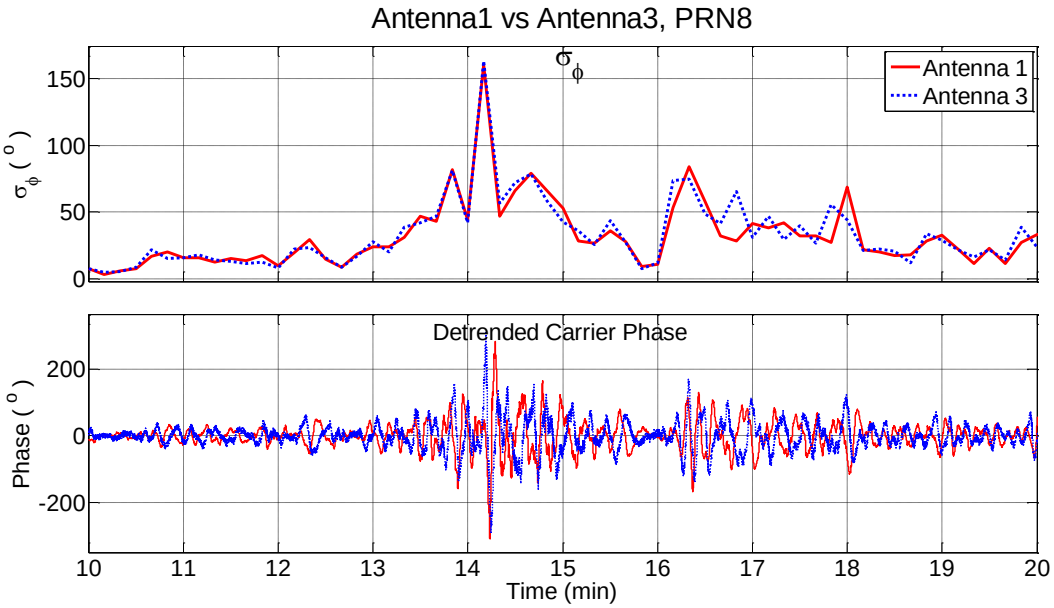

Figure 3-11. Ten minutes of GPS PRN 8 detrended carrier phase standard deviation (top) and carrier phase data (bottom) starting at 12:04:17 UT on 2012/10/13 from Antennas 1 and 3. After zooming into the signals, a slight advance of about 1 second in Antenna 3's σ_ϕ measurement can be observed from the top figure.

In Figure 3-11, large phase fluctuations can be observed for both antennas. From the detrended carrier phase plot (bottom), a small time lag can be observed between the two antennas. After zooming into the signals, a time lag about 1 second can be determined via inspection. However, this feature is less obvious in the σ_ϕ plot (top), due to the averaging process when calculating the σ_ϕ value (see Equation 1-2).

Log-scale APT energy spectra are generated from the detrended carrier phase measurements. An example showing a 5-minute comparison across all three antennas on PRN 8 was given in Figure 3-10 in the previous section. From Figure 3-10, a slight advance on Antenna 3 relative to Antenna 1 can be observed, which is in accord with the previous observation from the σ_ϕ plot in Figure 3-11. Note that the APT spectra of Antennas 2 and 3 are notably noisier than that of Antenna 1 towards higher frequencies, especially in the case of Antenna 2. This is mostly likely

because of the signal attenuation through transmission via long cables. After spectral filtering, the APT spectra on PRN 8 across all three antennas using the same set of data are demonstrated in Figure 3-12.

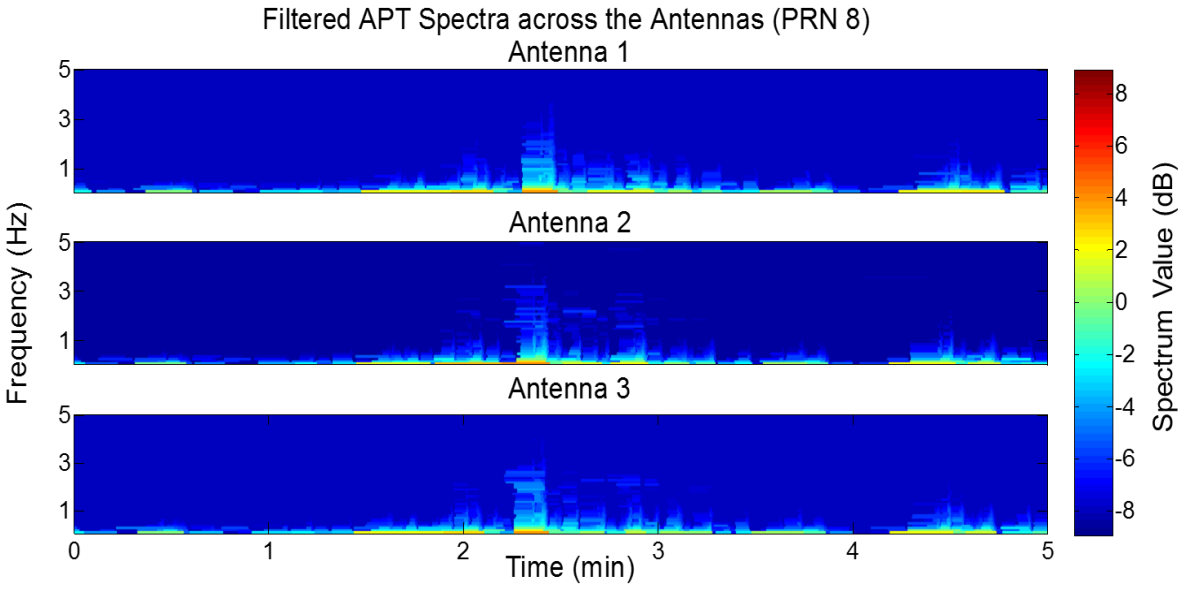

Figure 3-12. Five minutes example of filtered APT spectra across all antennas from 12:06:17 on PRN8.

Comparing Figure 3-10 and Figure 3-12, clearly, the phase noise effects towards higher frequencies have been greatly improved.

The full hour-length raw correlation and filtered results for PRN 8 across the antennas are shown in Figure 3-13 and Figure 3-14, respectively.

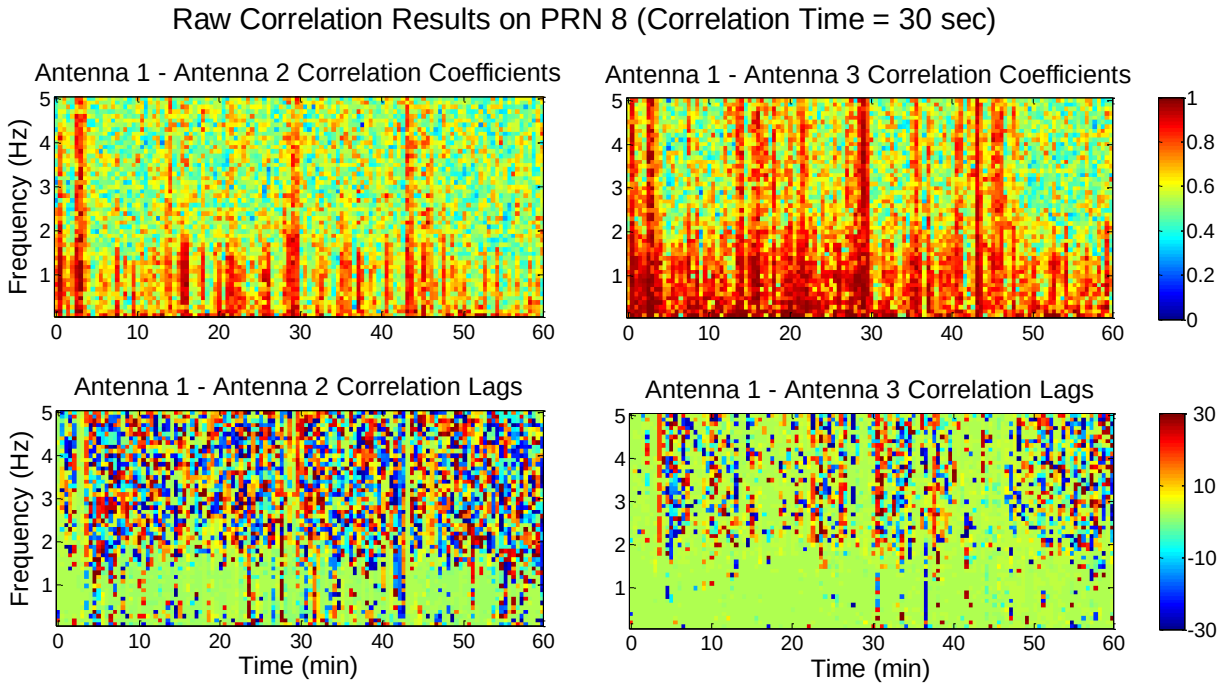

Figure 3-13. Example of full-hour raw correlation results from 11:54:17 UT on 2012/10/13 on PRN8. The top row figures are correlation coefficients, with intensity indicated by the top colorbar. The bottom row figures reflect the correlation lag estimation, with values indicated by the bottom colorbar from -30 to 30 seconds. The left column figures are the correlation results between Antennas 1 and 2, while the right column figures are for Antennas 1 and 3.

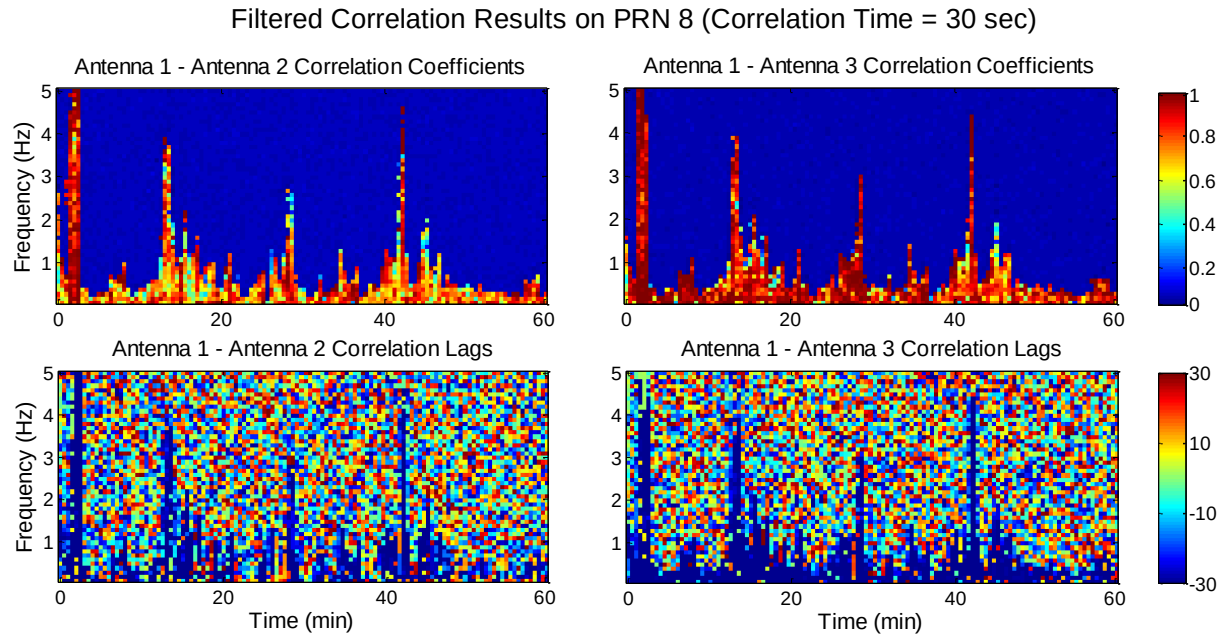

Figure 3-14. Example of full-hour correlation results after spectral filtering following the plotting rubrics in Figure 3-13.

By comparing the top panel coefficient plots in both figures, it can be seen that the high coefficient values in the background towards higher frequencies have been further reduced in Figure 3-14 than in Figure 3-13, leaving more reliable estimations concentrated towards the bottom of the spectra.

Based on procedures described at the beginning of this section, averaged time lags of the irregularity events between antennas are computed. Processed time lags across the antennas on PRN 8 are given by Figure 3-15.

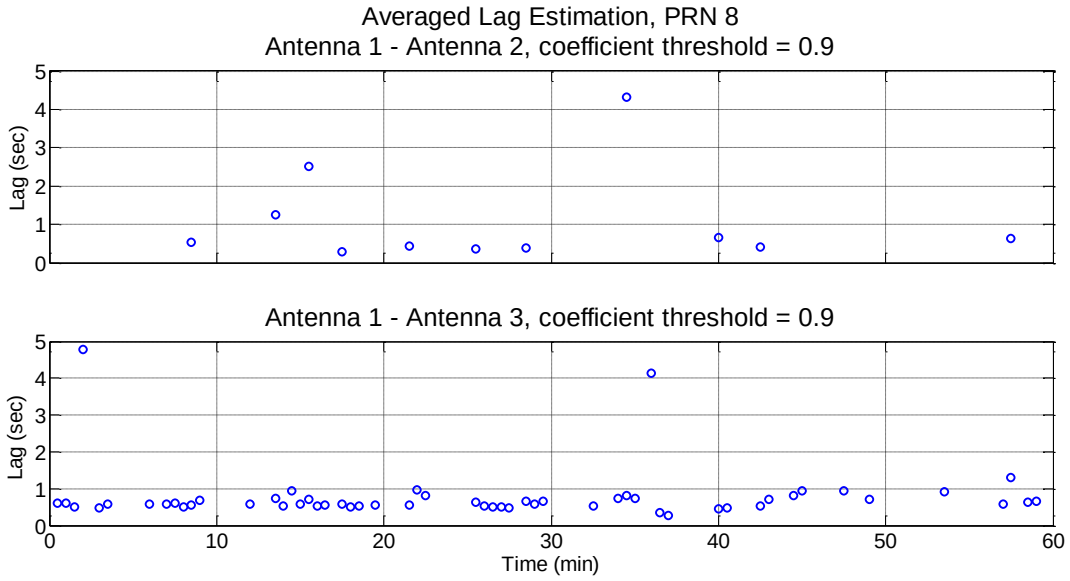

Figure 3-15. Full-hour averaged lag estimation across Antennas 1 & 2 (top), and Antennas 1 & 3 (bottom) from 11:54:17 UT on PRN 8. The estimated values from Antennas 1 & 3 match with the previous inspected values from Figure 3-7 (about 1 second).

In Figure 3-14, the correlation coefficient thresholds are set to 0.9 for both Antenna 1 – Antenna 2 (top plot) and Antenna 1 – Antenna 3 (bottom plot). Note that between 10 min and 20 min, the lags are mostly around 0.5 s, which is again in good agreement with our previous inspected value from Figure 3-11.

On top of the transmission loss issue, it must be noted that the distance between Antennas 1 and 2 is almost 4 times the distance between Antennas 1 and 3. The "frozen-in" assumption faces a stronger challenge over longer distances. The collective result is that the correlation coefficients for Antenna 1 – Antenna 2 tend to be lower than that for Antenna 1 – Antenna 3. Even after spectral filtering, the 0.9 threshold would reject most of the lag results, leaving numerous blanks in the lag estimation (indicated by the zero-lags in the plots). However, further decreasing this threshold would render the results to be more susceptible to noise interference in the estimation and may introduce correlations between different irregularity patterns. In this study, the coefficient threshold is maintained at the high value of 0.9 for the TFDM. In the trade-off between measurement availability and reliability, this choice is in favor of the latter.

3.4. Drift Velocity Estimation Bounds

Now that both the time lag information and the sub-ionospheric distance are obtained, the 1-D apparent irregularity pattern drift velocity, $\boldsymbol{v'_{1-D}}$, can be determined. The upper and lower bounds of $\boldsymbol{v'_{1-D}}$ can be established using system parameters. *Ledvina et al.* [2004] derived simple bounds for the measurable 1-D apparent irregularity pattern drift velocity as:

$$\frac{\Delta d_{RX}}{0.5 t_{corr}} \leq |\boldsymbol{v'_{1-D}}| \leq \frac{\Delta d_{RX}}{\Delta t_{samp}} \qquad (3\text{-}17)$$

where t_{corr} is the correlation time interval, Δd_{RX} is the distance between antennas, and Δt_{samp} is the sampling interval of the data. Note that the baseline distance between antennas is used in place of the sub-ionospheric distance for simplicity. The upper bound is determined by the system setup. It is typically not a limiting factor, especially in this study where $\Delta t_{samp} = 0.01$ s is small enough to provide a sufficiently large upper bound. The lower bound is mainly dependent on correlation time. While a larger t_{corr} will result in a smaller lower bound, it may violate the "frozen in" assumption.

In this study, $t_{corr} = 30$ seconds is used for the HAARP array data, while $t_{corr} = 25$ seconds is used when processing the Poker Flat array data. It should be noted that when t_{corr} is fixed, decreasing the baseline distance between the antennas would further lower the measurable bounds. However, by doing this, the tolerance on the time lag estimation error will also be increasingly stringent. On the other hand, increasing the baseline by too much would eventually violate the closely-spaced assumption, as it far exceeds the first Fresnel zone radius at IRPP altitude.

Thus far, the methodology of phase-scintillation-based spaced-receiver technique has been introduced. Derivation for the satellite scan velocity is presented. The general processes for obtaining the time lag information have been demonstrated through both the TDM and the TFDM. The 1-D apparent irregularity pattern drift velocities along receiver pairs can be determined from the time lag information and the sub-ionospheric distances of the receiver array. The next step is to determine the 2-D apparent pattern drift from these 1-D estimates. This is achieved in Chapter 4 through modeling the received correlation pattern.

4. CHAPTER 4 – CORRELATION MODELS

Knowing the 1-D apparent irregularity drift velocities along the receiver pairs, an intuitive approach for calculating the 2-D drift is through vector addition. For a receiver array (i, j, k) with arbitrary geometry configuration, this process can be generalized into:

$$\boldsymbol{v}' = \frac{\Delta d_{i,j}}{\Delta t_{i,j}} \cdot \boldsymbol{a_{i,j}} + \frac{\Delta d_{i,k}}{\Delta t_{i,k}} \cdot \boldsymbol{a_{i,k}} \qquad (4\text{-}1)$$

where $\boldsymbol{a_{i,j}}$ and $\boldsymbol{a_{i,k}}$ denote the unit vectors along antenna (i, j) and (i, k) pairs, respectively.

However, as pointed out by *Briggs et al.* [1950], this model is rather naïve and is not suitable in the context of spaced-receiver correlation analysis. Because the 2-D apparent drift is caused by the irregularity structure rather than a point object. To correctly reconstruct the 2-D drift, a correlation model is required to account for the irregularity topology.

In this chapter, three correlation models are presented, including the classic isotropy model in Section 4.1, the front velocity model in Section 4.2, and the anisotropy model in Section 4.3. To compare and analyze these correlation models, the space-time correlation schematic of each method is constructed. With the understanding of the merits and drawbacks of each method, a hybrid correlation model is proposed in Section 4.4 based on the front velocity model and the anisotropy model.

Although different correlation models make different assumptions on irregularity pattern topology, all correlation models discussed in this study do share some common assumptions. First, the "frozen-in" assumption assumes minimal evolution in irregularity structure and drift direction within the correlation interval [*Mitra*, 1949]. As a result, similar space-time correlation patterns can be observed at each receiver, while an averaged correlation pattern can be obtained. Second, the correlation functions are assumed to be strictly decreasing functions on both sides of the

correlation peaks [*Armstrong and Coles*, 1972]. Following this assumption, it is feasible to fully characterize the space-time correlation of each correlation model. And lastly, a geometrical optics relationship is assumed to relate election density perturbation in the irregularity structure to the carrier phase fluctuation in the received measurement [*Rino and Fremouw* 1977; *Rino and Livingston*, 1982]. This assumption establishes the relationship between the irregularity in space and the observed correlation pattern on the ground.

At this stage, the irregularity height is still treated as unknown, causing uncertainty in the sub-ionospheric distance calculation. In this chapter, when formulating the drift velocity estimates, the known receiver baseline distances are used in place of the sub-ionospheric distances. By doing so, approximated deterministic drift velocity solutions can be achieved. This alteration effectively puts the focus on the 2-D receiver plane on the ground, rather than the 2-D plane defined by the IRPP's in the ionosphere. Therefore, instead of the term "irregularity pattern drift" used in the previous chapters, we now use the term "diffraction pattern drift" from the literature to describe the 2-D apparent drift [*Livingston et al.,* 1982; *Costa et al.*, 1988]. We also use the upper-case "$\boldsymbol{V}$" to distinguish the diffraction pattern drift from the irregularity pattern drift in lower-case "$\boldsymbol{v}$". Note that the drift velocity estimates can be corrected later once the irregularity height is fixed.

4.1. Classic Isotropy Model

The classic correlation model aiming to resolve the diffraction pattern drift is proposed by *Mitra* [1949] and developed by *Briggs et al.* [1950] and *Briggs* [1968]. This model makes the implicit assumption that the diffraction pattern is statistically isotropic. In this study, this model is referred to as the classic isotropy model. Combining with the common assumptions described above, it follows that the instantaneous spatial correlation pattern observed at the receiver array would take the form of concentric circles with increasing intensity towards the pattern center.

A key issue this model addresses is how to estimate the 1-D drift velocity components along a pair of receivers whose alignment is at an angle to the diffraction pattern drift direction. This is illustrated by the following example: Let RX_1 and RX_2 represent the receiver pair location along the *OX* direction, where RX_1 is at the origin *O*. An isotropic diffraction pattern is drifting at velocity $\boldsymbol{V^D}$ at an angle θ to the *OX*-axis. Let the corresponding time lag at the receiver pair cross-correlation peak be τ_0. Then, the apparent drift velocity between this pair of receivers along the *OX* direction is $\boldsymbol{V_x^A} = \xi_0/\tau_0$, where $\xi_0 = |RX_1 - RX_2|$. Figure 4-1 illustrates this example.

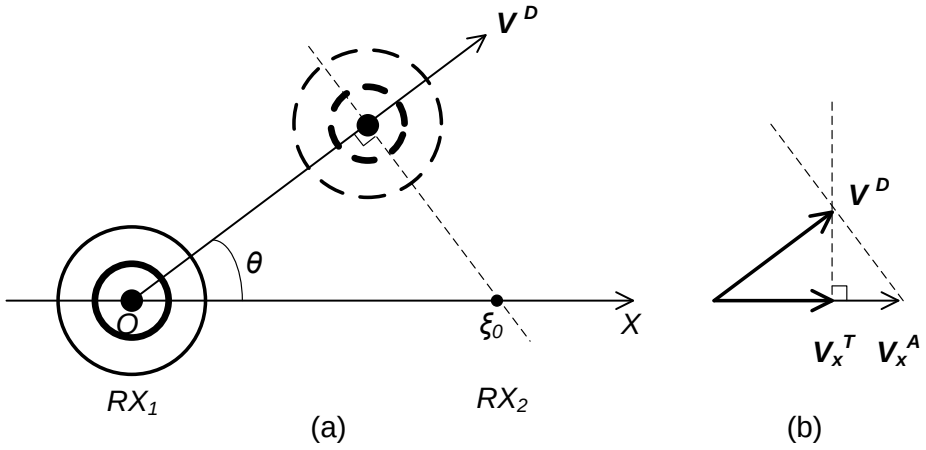

Figure 4-1. Illustration of the classic isotropy model. In subplot (a), the diffraction pattern is drifting at velocity $\boldsymbol{V^D}$ at an angle θ to the *OX*-axis. The solid and dashed concentric circles indicate the observed correlation pattern caused by diffraction, where maximum correlations are observed τ_0 seconds apart at RX_1 and RX_2, respectively. Subplot (b) shows the velocities derived from this configuration.

Note that the concentric circles in subplot (a) are shown with different line widths, reflecting the monotonic decreasing property of the correlation functions. Subplot (b) shows the velocities derived from this configuration, where $\boldsymbol{V^D}$ represents the 2-D diffraction pattern drift and $\boldsymbol{V_x^A}$ is the 1-D apparent drift along the *OX*-axis. As for $\boldsymbol{V_x^T}$, *Briggs et al.* [1950] defines it as the true drift velocity along the receiver pair direction "with which an observer would have to move along *OX* in order to reduce the speed of fading as observed by him to a minimum". Indeed,

an observer moving along the *OX*-axis at $\boldsymbol{V_x^T}$ would find the diffraction pattern fading most slowly in time, as the observer is always at the closest point on *OX* with respect to the diffraction pattern.

This is an intuitive definition under the isotropic assumption, as $\boldsymbol{V_x^T}$ would coincide with the velocity component of $\boldsymbol{V^D}$ along *OX*. Consequently, the 2-D diffraction pattern drift can be reconstructed from these 1-D true drift velocities along receiver pairs via vector addition. The following relationships can be obtained:

$$\boldsymbol{V_x^A} = \boldsymbol{V^D}/\cos\theta\,, \qquad \boldsymbol{V_x^T} = \boldsymbol{V^D}\cos\theta \tag{4-2}$$

However, in reality, the diffraction pattern is expected to be anisotropic due to the high parallel conductivities of the ionosphere [*Mendillo and Baumgardner*, 1982]. In this case, equation set (4-2) may not hold, since both the elongation and orientation of the anisotropic diffraction pattern would impact the projections of $\boldsymbol{V^D}$ onto the *OX*-axis**.**

To account for the above ambiguity, it is more adequate to establish the generalized relationship between these velocities and the correlation functions of receiver array measurements. *Briggs et al.* [1950] proposed a space-time correlation schematic following the monotonic decreasing assumption on the correlation functions.

4.1.1. Space-Time Correlation

The space-time correlation schematic can be a useful tool when analyzing the correlation model. In the literature, it is often only expressed in 2-D along a single spatial dimension (with the second dimension being time) [*Briggs et al.*, 1950; *Kintner et al.*, 2004]. However, it can be very challenging to differentiate between two correlation models based on their correlation surfaces along a single dimension. To better understand and compare different models, it is necessary to construct their full space-time correlation schematics by assembling correlation surfaces in all spatial dimensions.

In this study, using the classic isotropy model as an example, the space-time correlation schematic is constructed as the following. First, space-time correlation surfaces are obtained along selected spatial dimensions for different θ values. This is performed for three diffraction pattern propagation scenarios: a) parallel to the receiver pair orientation ($\theta = 0°$); b) perpendicular to the receiver pair orientation ($\theta = 90°$); c) somewhere between a) and b) ($0° < \theta < 90°$). The corresponding spatial dimensions are denoted as: a) $\zeta_{\parallel}$, b) $\zeta_{\perp}$, and c) ζ_{θ}. Then, with the first two extreme cases and the last general case, the full space-time correlation can be derived. The resulting individual correlation surfaces and the full space-time correlation schematic are shown in Figure 4-2.

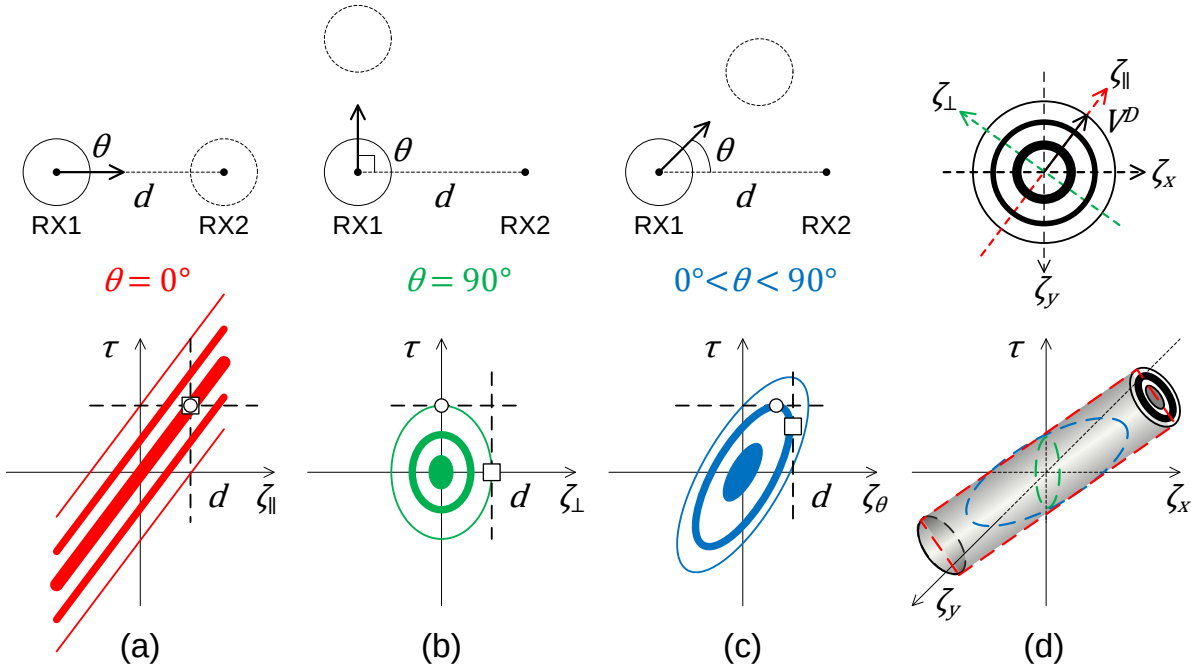

Figure 4-2. Individual space-time correlations along different spatial dimensions for (a) $\theta = 0°$ in red, (b) $\theta = 90°$ in green, and (c) $0° < \theta < 90°$ in blue, as well as the full space-time correlation schematic (d) for the classic isotropy model. For subplots (a), (b) and (c), an illustration is given on top of the correlation pattern for each θ value, while $\zeta_{\parallel}$, $\zeta_{\perp}$, and ζ_{θ} are the corresponding spatial dimensions. *d* marks the distance between receivers RX_1 and RX_2, the square marks the apparent drift velocity, and the circle marks the true drift velocity. For subplot (d), the top row gives the horizontal cut through the ζ_x-ζ_y plane, showing the correlation pattern from diffraction as concentric circles. In the space-time schematic at the bottom, the dashed shapes mark the vertical cuts along each spatial dimension as in subplots (a), (b), and (c).

In Figure 4-2, subplots (a), (b) and (c) illustrate the correlation surfaces in red, green and blue, under the three scenarios. Similar to Figure 4-1, the widths of the lines correspond to different correlation strengths. Along the $\zeta_{\parallel}$, $\zeta_{\perp}$ and ζ_{θ} axes, the estimated true velocities are marked by the circles, while the apparent velocities are marked by the squares. In subplot (d), ζ_x-ζ_y represents the horizontal receiver plane defined by the user. For example, ζ_x can represent the geomagnetic east direction while ζ_y can be the geomagnetic south. In the bottom figure, the grey cylinder represents the full space-time correlation for the classic isotropy model in the space-time domain defined by the ζ_x-ζ_y plane and the τ-axis. The cross-section at the top of the cylinder shows the correlation strengths through the concentric ellipses. The dashed shapes outline the intersections from the vertical cuts along each individual dimension for the three scenarios in red, green and blue, respectively. The cylinder goes through the ζ_x-ζ_y plane at an inclination, which gives the magnitude of $\boldsymbol{V^D}$. A horizontal cut through the cylinder at $\tau = 0$ gives the spatial correlation pattern caused by diffraction. In the case of the classic isotropy model, the resulting cross-section takes the shape of concentric circles. This is characterized by the top figure of subplot (d), while the black arrow along $\zeta_{\parallel}$ shows the direction of $\boldsymbol{V^D}$.

Along each spatial dimension in subplots (a), (b) and (c), the apparent drift velocity (square) is obtained at the cross-correlation peak along the vertical cut of the correlation surface at the receiver distance. Then, tracing the correlation values same as the peak value, a horizontal cut determines the true drift (circle) following the definition by *Briggs et al.* [1950]. In this example, the strict "frozen-in" assumption is applied, that the correlation strength does not decrease over time within the correlation interval. Therefore, the true drift and the apparent drift are the same in subplot (a) when the diffraction pattern happens to be traveling along the receiver pair alignment. This agrees with the aforementioned observation from the literature. As θ

increases, the true drift decreases in magnitude while the apparent drift increases (see subplot (c)). Eventually, when θ approaches 90°, the true drift becomes zero as the apparent drift approaches infinity (see subplot (b)).

4.1.2. Drift Velocity Estimation

To estimate the true drift velocity along any spatial dimension, an analysis is conducted based on the space-time correlation of a general scenario ($0° < \theta < 90°$). Elaborated upon Figure 4-2(c), Figure 4-3 illustrates the schematic of the space-time correlation surface along the spatial dimension along the ζ_θ-axes.

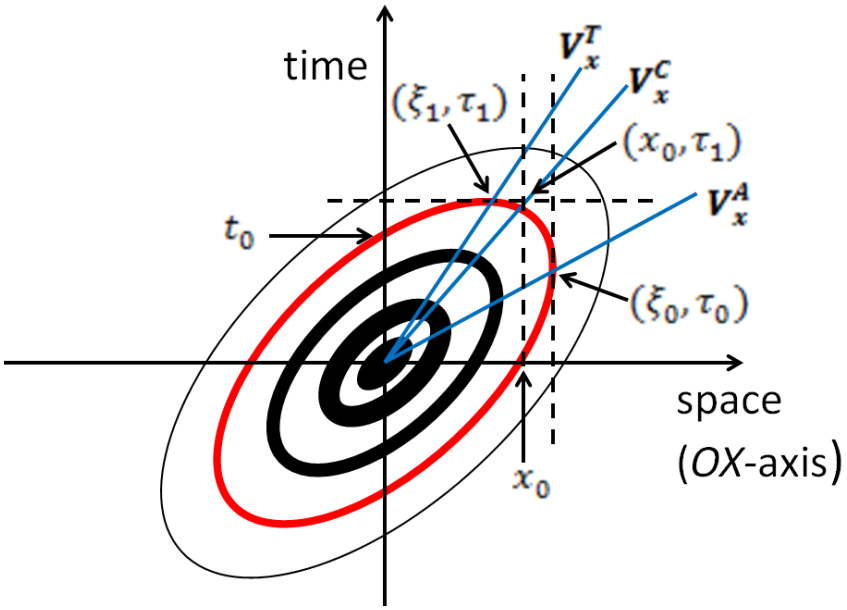

Figure 4-3. Schematic of a correlation surface in the space-time domain. It corresponds to the correlation surface defined in Figure 4-1. The concentric ellipses depict the correlation surface with monotonic decreasing values from the origin. The ellipse in red corresponds to correlation values equal to the cross-correlation peak of carrier phase measurements from the two receivers. It crosses the time-axis at t_0, and the space-axis at x_0. The blue lines give the drift velocity components, with $\boldsymbol{V_x^T}$ associated with displacement ξ_0 at time τ_0, $\boldsymbol{V_x^C}$ associated with x_0 at τ_1, and $\boldsymbol{V_x^A}$ associated with ξ_1 at τ_1.

In this space-time domain, velocities are given by the straight lines through the origin defined as displacement over time (ξ/τ). Hence, their magnitudes are associated with their

inclination angles, i.e., lower inclination angles correspond to larger velocities. In Figure 4-3, the vertical cut tangent to the red ellipse gives the cross-correlation function, with its peak giving the apparent drift velocity $\boldsymbol{V_x^A}(=\xi_0/\tau_0)$. Also, the horizontal cut finds the true drift velocity $\boldsymbol{V_x^T}(=\xi_1/\tau_1)$ at the slowest diffraction pattern fading in time, reflected by the slowest changing in the correlation function. The relationship between these two velocities is given by the following equation [*Kintner et al.*, 2004]:

$$\boldsymbol{V_x^T} = \frac{1}{1+(t_0/\tau_0)^2}\boldsymbol{V_x^A} \qquad (4\text{-}3)$$

where t_0 can also be understood as the time at which the auto-correlation function takes on the peak value of the cross-correlation function. While τ_0 is largely dependent on the inclination of the ellipses related to the drift velocity magnitude, t_0 is closely associated with the elongation of the ellipses. The ratio t_0/τ_0 determines the extent to which the apparent and true velocities are equivalent. *Briggs et al.* [1950] also defined the characteristic velocity $\boldsymbol{V_x^C}$ as a measure of the fading rate of the diffraction pattern:

$$\boldsymbol{V_x^C} = \frac{x_0}{\tau_1} = \frac{t_0/\tau_0}{1+(t_0/\tau_0)^2}\boldsymbol{V_x^A} \qquad (4\text{-}4)$$

For some fixed τ_1 value, as x_0 decreases, the concentric ellipses become increasingly elongated. This leads to faster changing rate in the correlation function, which implies larger diffraction pattern fading rate. From equations (4-3) and (4-4), when the ellipses are highly elongated ($t_0 \to 0$), then there is $t_0/\tau_0 \to 0$, causing $\boldsymbol{V_x^T} \to \boldsymbol{V_x^A}$ and $\boldsymbol{V_x^C} \to 0$.

All velocity components in this spatial dimension share the same subscripts $\boldsymbol{x}$, as they are defined with respect to the *OX*-axis under the configuration of the above example. These subscripts can be altered under different spatial dimensions, or even omitted when the spatial dimension is unspecified.

Previous studies indicated that when receivers are placed along the same geomagnetic latitude in equatorial regions, $\boldsymbol{V^C}$ becomes significant only during periods of irregularity growth and is rather small during other times [*Vacchione et al.*, 1987; *Spatz et al.*, 1988]. On this account, *Kil et al.* [2000] suggested that $\boldsymbol{V^T}$ may be approximated to $\boldsymbol{V^A}$ with errors of less than 10 m/s. *Kintner et al.* [2004] also showed supports for this claim and demonstrated that the direction of equatorial drift is zonal in most cases. To summarize, when the receiver array placement and drift velocity are both zonal, i.e., $\theta \approx 0°$, it follows that $\boldsymbol{V^T} \approx \boldsymbol{V^A}$ and $\boldsymbol{V^C} \approx \boldsymbol{0}$.where $\boldsymbol{V_C}$ is a measure of the diffraction fade pattern change rate. As ${t_0}^2/{\tau_0}^2$ decreases, ${\tau_0}^2/{t_0}^2$ increases, and $\boldsymbol{V_C}$ decreases accordingly.

A major drawback of the classic isotropy model is that the isotropic assumption is not particularly realistic. In fact, ionospheric irregularity structures are expected to be anisotropic and highly elongated along magnetic field lines. This leads to rod-like diffraction patterns instead of circular ones. Another issue is that the definition of the true velocity can sometimes be ambiguous, as it may not equal to the projected velocity component of the 2-D diffraction pattern drift. Consequently, the reconstruction process would be erroneous via vector addition, over-estimating $\boldsymbol{V^D}$. This will be explained in the following sections

4.2. Front Velocity Model

4.2.1. Space-Time Correlation

To better address the anisotropic nature of the ionospheric irregularities, *Wang and Morton* [2017] proposed a front velocity model designed for rod-like irregularities having larger footprints than the receiver array. The method also assumes that the direction of the drift velocity is perpendicular to the velocity front (orientation of the diffraction pattern). This is a valid assumption under nominal conditions as the irregularity is aligned with the B-field and E×B drift is expected.

Under these assumptions, the space-time correlation schematic is constructed for the front velocity model. The results are presented in Figure 4-4 following the rubrics of Figure 4-2.

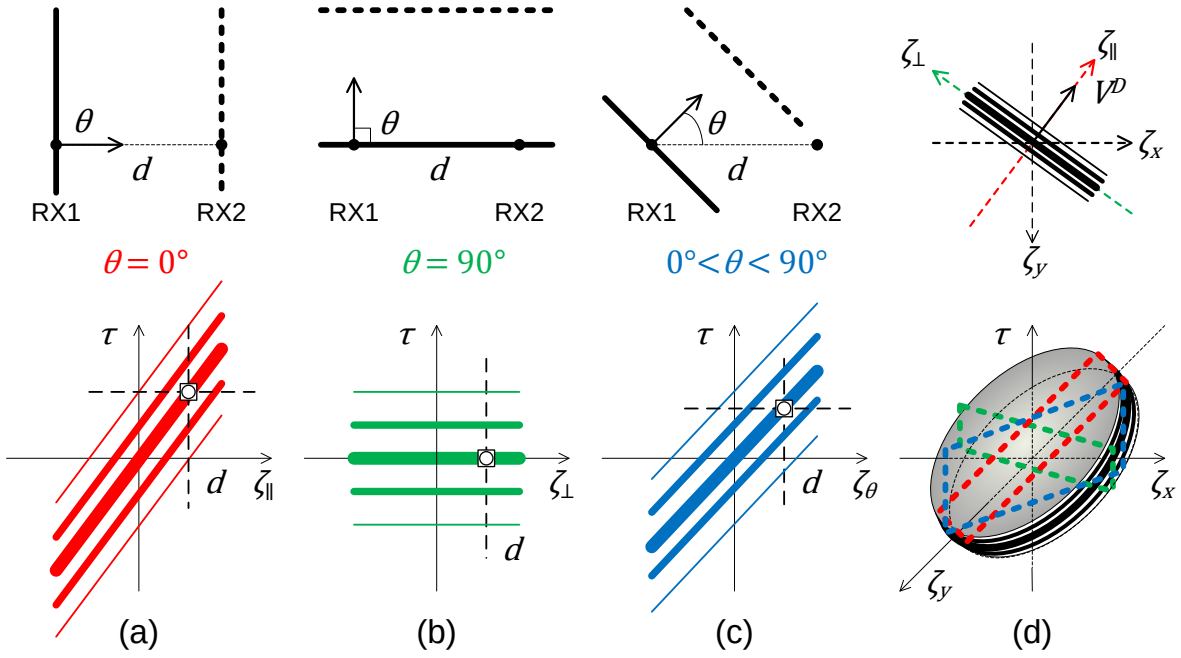

Figure 4-4. Individual space-time correlations along different spatial dimensions (a), (b) and (c), as well as the overall space-time correlation schematic (d) for the front velocity model.

In Figure 4-4, subplots (a), (b) and (c) again give the correlation surfaces along the $\zeta_{\parallel}$, $\zeta_{\perp}$ and ζ_{θ} dimensions. Subplot (d) gives the space-time correlation as a disk, while the correlation strength is represented by the line width. Compared to Figure 4-2, major differences can be found in subplots (b) and (c). They can be understood as the extreme cases of Figures 4-2(b) and 4-2(c) as the diffraction pattern becomes increasingly anisotropic. Like the previous example, the strict "frozen-in" assumption is applied. As a result, subplot (a) is very similar to Figure 4-2(a). Again, a horizontal cut through the disk along the ζ_x-ζ_y plane gives the shape of the diffraction pattern, which is a rod-like pattern as in the top figure of subplot (d). Note that when finite rod length is assumed, disk-like space-time correlation pattern can be observed as in the bottom figure of subplot (d), whereas sheet-like correlation pattern can be observed for infinite rod length. Both

scenarios would lead to the same diffraction pattern drift as long as the rod-like diffraction pattern has a larger footprint than the receiver array baseline.

Unlike the classic isotropy model, the estimated apparent velocities and true velocities coincide in all spatial dimensions for the front velocity model. Therefore, the true velocity as defined in the classic isotropy model does not reflect the velocity component of the 2-D diffraction pattern drift along ζ_x or ζ_y.

4.2.2. Drift Velocity Estimation

To resolve this issue, the front velocity model (and later the anisotropy model) directly calculates the true 2-D diffraction pattern drift velocity, instead of attempting to resolve each individual velocity component of the drift [*Wang and Morton*, 2017]. The gist of the approach is to exploit the assumption that the drift velocity is perpendicular to the velocity front. This leads to potential solutions that lie on circles corresponding to the receiver pairs. For example, consider an arbitrary receiver pair defined by their antenna locations RX_1 and RX_2 The circle for potential solutions is shown in Figure 4-5.

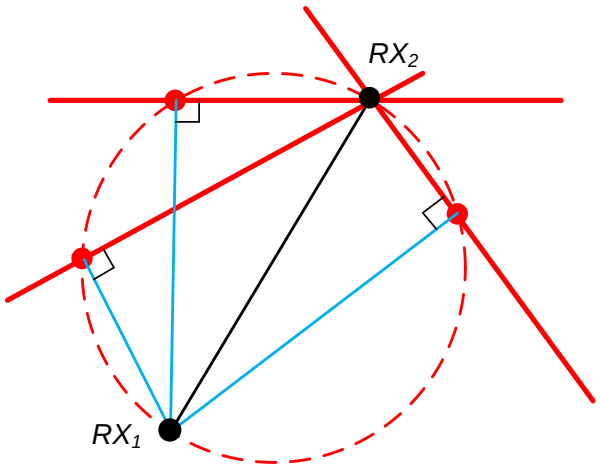

Figure 4-5. Illustration of an arbitrary arrangement of RX_1 and RX_2, with potential positions of the rod-like diffraction pattern. Each red dot gives a potential solution for the irregularity displacement from RX_1. Under the perpendicular assumption between the velocity front and drift direction, all potential solutions would lie on a circle (red dashed line) with the $RX_1 - RX_2$ baseline distance being the diameter.

In Figure 4-5, the receiver arrangement is indicated by the black dots. Assume RX_1 first observed the scintillation pattern, and RX_2 saw the same pattern τ_{12} seconds later. Then, several potential positions of the rod-like irregularity pattern are marked by the red bars. The distances from each potential pattern position to RX_1 are indicated by the blue lines, respectively. Each intersection of the blue and red lines, marked by the red dots, gives a potential solution for the irregularity displacement from RX_1. Note that each red dot together with the two black dots form a right triangle with the hypotenuse being the baseline distance between RX_1 and RX_2. Based on this property, it can be shown that the all potential solutions lie on a circle (red dashed line) with the $RX_1 - RX_2$ baseline distance being the diameter. Again, any point on this circle gives a potential location for the intersection points, which determines the displacement and orientation of the rod-like irregularity from RX_1, associating with a time offset of τ_{12} seconds. With the measurements from an additional antenna RX_3, another circle of potential solutions can be generated, hence more information about the irregularity front can be obtained. Figure 4-6 illustrates the geometry of this antenna array after introducing another arbitrary antenna RX_3.

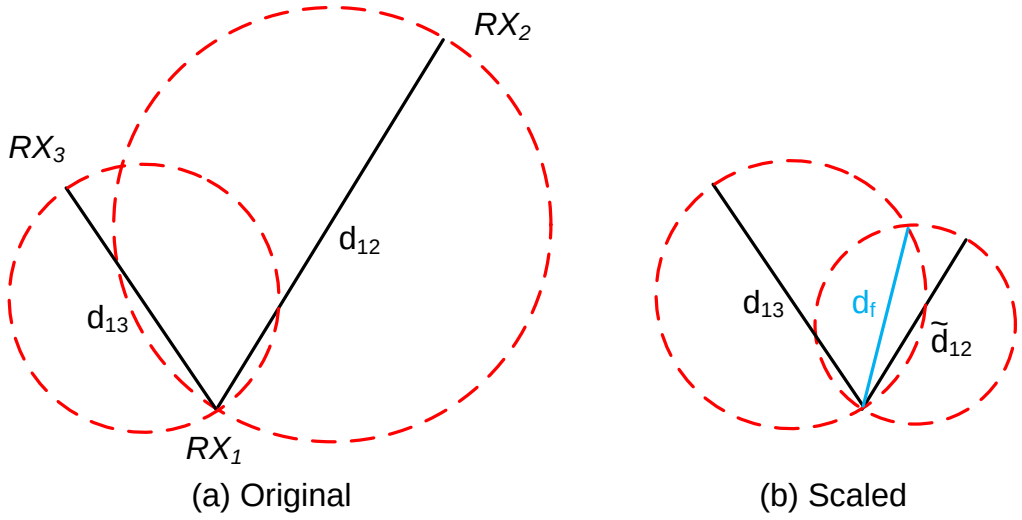

Figure 4-6. Illustration of the geometry of an arbitrary receiver array (RX_1, RX_2, RX_3) following Figure 4-5, together with corresponding circles of potential solutions. With two or more circles of potential solutions, the drift velocity can be resolved.

In Figure 4-6, subplot (a) shows the original geometry of the receiver array. RX_1, RX_2 and RX_3 denote the receiver locations, while d_{12} and d_{13} mark the distances between receiver pairs. The potential solutions are on the red dashed circles. The two circles correspond to apparent time offsets of τ_{12} between RX_1 and RX_2, and τ_{13} between RX_1 and RX_3, respectively. In the original geometry, the intersection of the two circles typically does not have any physical meaning, as they are entirely determined by the fixed antenna arrangement, regardless of the received measurements. However, when $\tau_{12} = \tau_{13}$, this intersection gives the solution to the displacement and orientation of the irregularity front. Based on this observation, we can manipulate one set of distance and time offset such that the apparent velocity gets preserved while having $\tau_{12} = \tau_{13}$. Equation 4-5 demonstrates this technique:

$$\boldsymbol{V}_{\mathbf{12}}^{\boldsymbol{A}} = \frac{d_{12}}{\tau_{12}} = \frac{k d_{12}}{k\tau_{12}} = \frac{\tilde{d}_{12}}{\tau_{13}} \qquad (4\text{-}5)$$

Once d_{12} is scaled to $\tilde{d}_{12}$, a new circle of potential solutions can be produced, as shown by subplot (b) in Figure 4-6. Its intersection with the solution circle from d_{13} directly gives the irregularity front displacement d_f.

The above technique suggests that going from spatial domain into velocity domain can ease the process to obtain meaningful intersections of the potential solution circles. By dividing the known antenna distances by the corresponding time offsets, the magnitudes of the apparent front velocities can be obtained, while the directions of these velocities are aligned with their antenna geometry, respectively. Conveniently, the circular form of the solution surface is preserved in the velocity domain. Figure 4-7 demonstrates the transformed problem in the velocity domain.

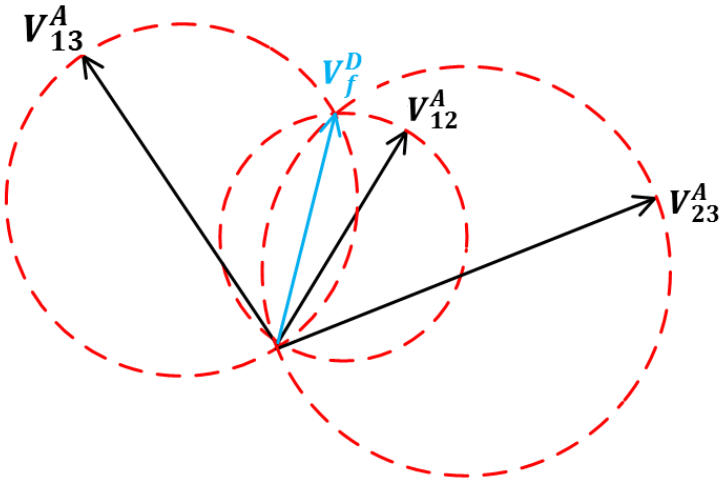

Figure 4-7. Illustration of the transformed problem in the velocity domain. The black arrows correspond to the 1-D apparent drift along each receiver pair. The blue arrow marks the true 2-D diffraction pattern drift found at the intersection of three circles of velocity solution.

In Figure 4-7, the black arrows mark the velocity vectors for the receiver pairs. In addition to RX_1 - RX_2 and $RX_1 - RX_3$, the velocity component from $RX_2 - RX_3$ is included as well. The red dashed circles represent the potential solution circles for the apparent front velocity. Ideally, the three circles will intersect at the same point, which gives the solution to $\boldsymbol{V_f^D}$ marked by the blue arrow. However, the third receiver makes this an over-determined problem, which does not always have a unique solution due to errors in measurements and non-ideal scenarios in the irregularities.

For a spaced-receiver array with an arbitrary number of receivers, a simple approach to solve this system is to find the minimum mean square error (MMSE) estimator, which minimizes the mean square error from $\boldsymbol{V_f^D}$ to all solution circles. The idea is to start with a rough estimate of $\boldsymbol{V_f^D}$, and then refine it iteratively so that the mean square error is minimized. The detailed procedure, generally referred to as Newton-Raphson method, is described in Appendix A.

A practical problem of this approach is that the origin $(0,0)$ is always the global optimal solution, as all potential solution circles intersect at the origin. To avoid this trivial solution, one

can pick an initial guess to be the intersection from two of the receiver pairs. Alternatively, a deterministic solution can be found between any two pairs of receivers. The following example illustrates the implementation. Figure 4-8 shows the solution circles defined by two apparent velocities $\boldsymbol{V_{12}^A}$ and $\boldsymbol{V_{13}^A}$ that correspond to two arbitrary pairs of receivers.

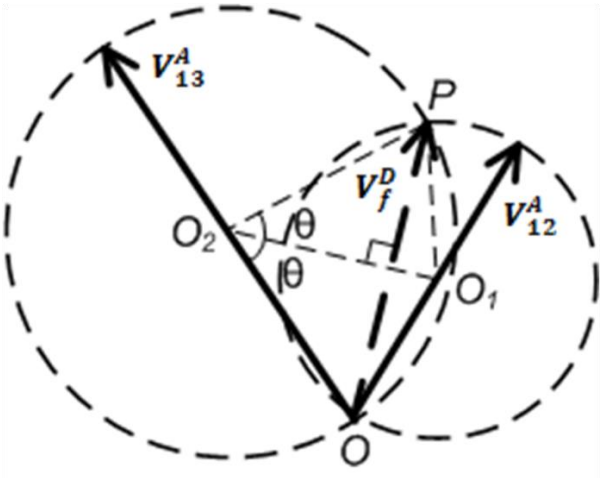

Figure 4-8. Transformed problem in the velocity domain with defined geometry. $\boldsymbol{V_{12}^A}$ and $\boldsymbol{V_{13}^A}$ (solid arrows) are the apparent drifts along the receiver pairs, defining the dashed solution circles. The two circles intersect at point *P*, giving the solution to the diffraction pattern drift velocity $\boldsymbol{V_f^D}$ (dashed arrow). Points O_1 and O_2 are the center of the solution circles in the Cartesian coordinate system with *O* being the origin.

Based on Figure 4-7, Figure 4-8 further defines the geometry of the transformed problem in the velocity domain. In this Cartesian plane, note that the origin is at $O(0,0)$ with the circles' centers at $O_1(x_1, y_1)$ and $O_2(x_2, y_2)$. These coordinates can be directly obtained from the known receiver array geometry.

To solve for $\boldsymbol{V_f^D} = P(x, y)$, note that 1) ΔPO_2O_1 and ΔOO_2O_1 are congruent triangles ($\Delta PO_2O_1 \cong \Delta OO_2O_1$), hence $\angle PO_2O_1 = \angle OO_2O_1 = \theta$; 2) $PO \perp O_2O_1$. By applying dot-product and trigonometry properties to these observations, the following equations can be established:

$$2\cos^2\theta - 1 = \cos 2\theta = \frac{O_2P \cdot O_2O}{|O_2P||O_2O|} = \frac{(x-x_2, y-y_2) \cdot (-x_2, -y_2)}{{r_2}^2} \qquad (4\text{-}6)$$

$$PO \cdot O_2O_1 = (x, y) \cdot (x_1 - x_2, y_1 - y_2) = 0 \quad (4\text{-}7)$$

where r_2 is the radius of the circle defined by RX_1 and RX_3 with $r_2 = \frac{1}{2}\left|\boldsymbol{V}_{\mathbf{12}}^{\boldsymbol{A}}\right|$, and $\cos\theta$ obtained by:

$$\cos\theta = \frac{O_2O_1 \cdot O_2O}{|O_2O_1||O_2O|} = \frac{(x_1 - x_2, y_1 - y_2) \cdot (-x_2, -y_2)}{r_2|(x_1 - x_2, y_1 - y_2)|} \quad (4\text{-}8)$$

Combining the above equations, a unique solution for $P(x, y)$ can be obtained:

$$x = 2r_2^2 \sin^2\theta \frac{y_1 - y_2}{x_2y_1 - x_1y_2} \quad (4\text{-}9)$$

$$y = 2r_2^2 \sin^2\theta \frac{x_2 - x_1}{x_2y_1 - x_1y_2} \quad (4\text{-}10)$$

The above method gives a unique solution for V_f from the 1-D apparent velocity pairs $(\mathbf{v'_{12}}, \mathbf{v'_{13}})$. For a receiver array system with $N \geq 3$ receivers, the system is over-determined. There are $\binom{N}{2}$ such solutions, which can be used to create more robust drift velocity estimates.

It should be noted that due to the inverse relationship between time lag and velocity, any error in time lag measurements can lead to large velocity errors when the time lag value is small. To address this, the algorithm can adaptively reject receiver pair cross-correlation peaks that are associated with the smaller time lag values. This effectively produces more reliable drift velocity magnitude estimates.

The drawback of the front velocity model is inherited from the perpendicular assumption between the velocity front and drift direction. This assumption is suitable for equatorial regions [*Ji et al.*, 2011]. However, it becomes less viable under active geomagnetic conditions, especially at high latitudes, where interplanetary magnetic field and auroral electrojet also play important roles in the direction and magnitude of the drift velocity.

4.3. Anisotropy Model

The anisotropy model is developed to address the more realistic anisotropic nature of the diffraction pattern induced by ionospheric scintillation [*Fedor*, 1967]. The model consists of two parts, the forward propagation model and the correlation model.

The forward propagation model describes the projection from the ionospheric irregularities in space to the diffraction pattern on the receiver plane [*Singleton*, 1970]. The correlation model estimates the anisotropy parameters and diffraction pattern drift velocity from receiver array measurements [*Armstrong and Coles*, 1972]. It assumes that the space-time correlation caused by the diffraction pattern takes the form of concentric ellipsoids [*Rino and Livingston.*, 1982]. The focus of this section is on the correlation model, while the forward propagation model is described in Chapter 5.

4.3.1. Space-Time Correlation

Unlike the cases for the classic isotropy model and the front velocity model, a less-strict "frozen-in" assumption is applied for the anisotropy model by allowing small decrease in the correlation strength within the correlation interval. This adaptation is necessary for the space-time correlation to remain consistent with the "concentric ellipsoids" assumption made by the anisotropy model. The resulting space-time correlation schematic of the anisotropy model is shown in Figure 4-9.

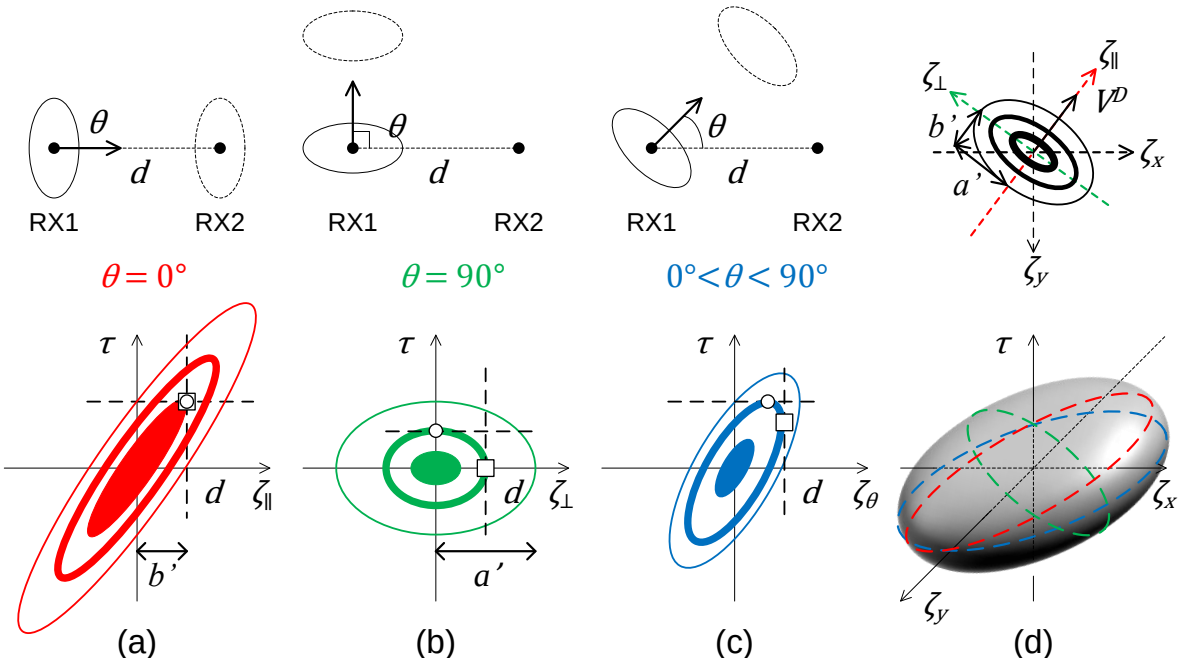

Figure 4-9. Individual space-time correlations along different spatial dimensions (a), (b) and (c), as well as the overall space-time correlation schematic (d) for the anisotropy model. *a'* and *b'* are scaled semi-major and semi-minor axes of the diffraction pattern.

In Figure 4-9, subplots (a), (b) and (c) again give the correlation surface along each spatial dimension, while subplot (d) gives the outline of the overall space-time correlation as an ellipsoid. In addition, *b'* and *a'* mark the intersections between the individual spatial axes with a common correlation ellipsoid in subplots (a) and (b), giving the axial ratio (a': b') of the diffraction pattern. Note that subplot (a) is different from those of Figures 4-2(a) and 4-4(a), instead of straight lines of correlation values, highly-elongated concentric ellipses are obtained. This is a direct corollary of the "concentric ellipsoids" assumption. Although subplots (b) and (c) are very similar to the Figures 4-2(b) and 4-2(c) in the classic isotropy model, the overall space-time correlation in subplot (d) is closer to Figure 4-4(d) in the front velocity model. This is an expected outcome when the axial ratio of the diffraction pattern is large ($a' \gg b'$). In equatorial studies, large axial ratio values are regularly observed [*Kintner et al.*, 2004]. Axial ratio assumptions of a': $b' \geq 50$ are often used in scintillation modeling [*Secan et al.*, 1995; *Carrano et al.*, 2016].

4.3.2. Drift Velocity Estimation

Compared to the isotropic and front models, the anisotropy model is more complex and requires information from the auto-correlation function in addition to cross-correlation functions to solve for the anisotropy. In essence, a space-time correlation ellipsoid of constant correlation can be modeled by the anisotropy parameters $(a', b', \psi, |v|, \theta)$, where $a':b'$ gives the axial ratio of the diffraction pattern, ψ depicts the orientation of the diffraction pattern, $|v|$ is the magnitude of the correlation and θ gives the drift direction.

There are two general methods for solving these anisotropy parameters. The first method, developed based on *Fedor* [1967], focuses on points in auto-correlation and cross-correlation functions with the same correlation value. These points can be associated with a common space-time correlation ellipsoid Therefore, the anisotropy parameter set $(a', b', \psi, |v|, \theta)$ can be solved simultaneously in one step. A recent refinement of this approach is described in *Su et al.* [2017]. The second method, developed based on *Armstrong and Coles* [1972], focuses on intersections between correlation functions. These intersections have the same τ values and can be associated with the same horizontal cut of the space-time correlation ellipsoid. Effectively, this method takes a two-step approach. It first solves for the diffraction pattern parameters (a', b', ψ) based the correlation intersections with additional information at the cross-correlation peaks. It then uses the solution to find the drift velocity parameters $(|v|, \theta)$. Figure 4-10 gives an example showing the different data points used in the one-step approach against the two-step approach.

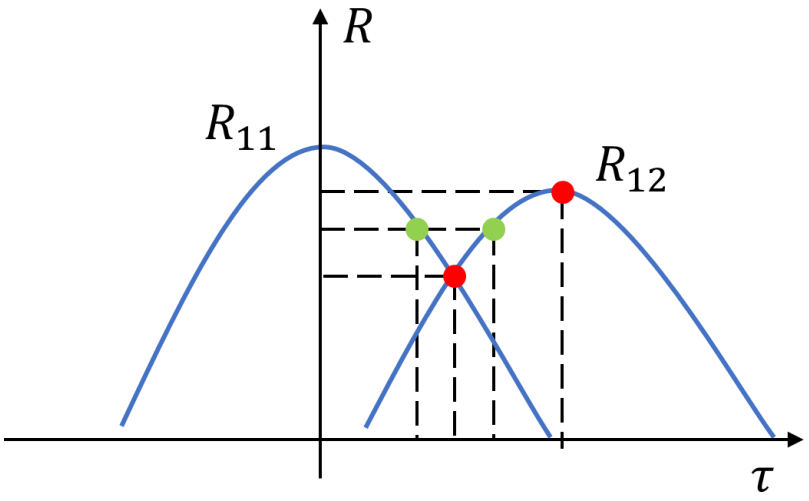

Figure 4-10. Illustration of data points used in the one-step approach (green) and the two-step approach (red) for solving the anisotropy. R_{11} and R_{12} represent the auto-correlation and cross-correlation functions obtained from the receiver pair (RX_1 and RX_2) measurements.

In Figure 4-10, the two green dots represent points on R_{11} and R_{12} at the same correlation value used in the one-step approach. The two red dots represent the intersection between R_{11} and R_{12} and the cross-correlation peak used in the two-step approach. Comparable performances have been observed between these two methods [*Costa et al*., 1988; *Zhudukon et al*. 1994]. This study follows the two-step approach, refined based on the work of *Rino and Livingston* [1982].

For a receiver array of n receivers, *Rino and Livingston* [1982] gave an upper bound for the number of the intersections involved in the calculation:

$$(n^2)^2 - n^2 - 2n(n-1) = n^4 - 3n^2 + 2n \qquad (4\text{-}10)$$

where the subtracted terms account for the intersections of n^2 correlation functions with themselves and the $2n(n-1)$ intersections between the correlation functions and their mirror images. *Zhudukon et al.* [1994] gave the exact number of intersections as

$$n\left[\frac{n(n-1)}{2}\right] + \frac{\frac{n(n-1)}{2}\left[\frac{n(n-1)}{2} - 1\right]}{2} = \frac{n(n-1)(n^2+3n-2)}{8} \qquad (4\text{-}11)$$

where the first term accounts for intersections between R_{ii} and R_{ij}, and the second term accounts for intersections between R_{ij} and R_{ik}. However, when searching for the latter type of intersections, both the $R_{ij} - R_{ik}$ pair and the $R_{ij} - R_{ki}$ pair need to be considered. Hence the number of admissible intersections is

$$n\left[\frac{n(n-1)}{2}\right] + \frac{n(n-1)}{2}\left[\frac{n(n-1)}{2} - 1\right] = \frac{n^4 + 3n^2 - 2n}{4} \qquad (4\text{-}12)$$

To calculate the axial ratio and drift velocity of the diffraction pattern from this system, a two-step MMSE estimator is employed. Details of the method are documented in Appendix B.

As the estimated axial ratio approaches unity $(a' : b' \approx 1)$, the diffraction pattern becomes nearly isotropic rather than anisotropic. This means the diffraction patterns would be very similar when observed from different angles, making it very challenging to determine the orientation of the anisotropy. As a result, small axial ratios carry small confidence levels into the estimated anisotropy parameters. In the implementation, results associated with small axial ratios $(a' : b' < 2)$ are excluded.

Another practical issue of the anisotropy model is that it tends to overestimate the magnitude of the 2-D drift. An example is given in Section 6.6 demonstrating this problem using real data. Unlike the front velocity model, the anisotropy model cannot simply reject receiver estimates that are associated with small time lag values, since dropping correlation functions would quickly lead to an underdetermined system.

4.4. Hybrid Correlation Model

Based on the merits and drawbacks of each correlation method from the analysis above, a hybrid correlation method is proposed. First, the drift velocity direction and the diffraction pattern orientation are obtained using the anisotropy model. Then, taking these parameters as a priori, an adjusted front velocity model is created. It calculates the projection of the apparent velocity onto

the drift direction along the diffraction pattern orientation as the velocity front. Following the adaptive filtering scheme of the front velocity model, the measurement associated with the smallest time lag value is rejected. The remaining measurements are averaged to produce the final estimate of the 2-D diffraction pattern drift.

For example, in the Cartesian plane representing the velocity values, let the apparent 1-D diffraction pattern drift be $\boldsymbol{V_{1-D}^{A}} = (x_{1-D}, y_{1-D})$ along some arbitrary receiver pair. Say the anisotropy model finds the diffraction pattern drift velocity to be $\boldsymbol{V_{a}^{D}} = (x_a, y_a)$, and the velocity front orientation to be $F = (x_f, y_f)$. Then, the hybrid diffraction pattern drift velocity $\boldsymbol{V_{h}^{D}} = (x_h, y_h)$ can be determined as the projection of $\boldsymbol{V_{1-D}^{A}}$ onto $\boldsymbol{V_{a}^{D}}$ based on the orientation described by F. Figure 4-11 illustrates the projection geometry.

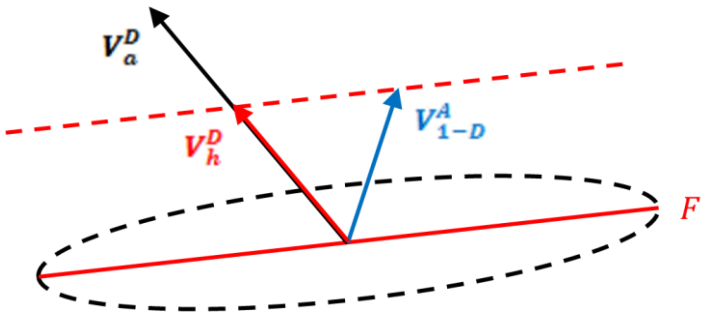

Figure 4-11. Illustration of the projection geometry for hybrid velocity estimation. $\boldsymbol{V_{h}^{D}}$ is the hybrid diffraction pattern drift projected from the 1-D apparent drift $\boldsymbol{V_{1-D}^{A}}$ onto the direction of the anisotropy drift $\boldsymbol{V_{a}^{D}}$ guided by the velocity front *F*. The dashed black ellipse is the solved anisotropy, while the red lines represent the velocity front orientation *F*.

Based on Figure 4-11, the hybrid velocity can be determined as:

$$x = \frac{y_{1-D} - \mathrm{k_f} x_{1-D}}{\mathrm{k_a} - \mathrm{k_f}}, y = \mathrm{k_a} x \qquad (4\text{-}13)$$

where $\mathrm{k_a} = y_a / x_a$, and $\mathrm{k_f} = y_f / x_f$ represent the gradients of the anisotropy drift and the velocity front, respectively. In the case where anisotropy parameters are not measurable, the final 2-D drift estimate takes the front velocity model solution if available.

With the hybrid correlation model, the apparent diffraction pattern drift velocity can be estimated. Given the irregularity height value, corrections can be applied to obtain the apparent irregularity pattern drift. Together with the satellite scan velocity, the irregularity drift velocity can be found.

This chapter concludes the spaced-GNSS receiver techniques for estimating the ionospheric irregularity drift velocity. In Chapter 5, an inversion technique is proposed for estimating the effective height of the irregularity based on the anisotropy model.

5. CHAPTER 5 – EFFECTIVE IRREGULARITY HEIGHT ESTIMATION

Section 4.3 has demonstrated how to estimate the diffraction pattern parameters using the anisotropy correlation model via spaced-receiver analysis. This chapter introduces the spaced-receiver technique for effective irregularity height estimation also based on the anisotropy model. Section 5.1 introduces the forward propagation model depicting how the anisotropic irregularity structure is propagated to form the ground diffraction pattern. The methodology of the effective height estimation technique is given in Section 5.2. The gist of the approach is to formulate an inversion problem trying to match the propagated diffraction pattern to the received diffraction pattern derived from receiver measurements. In Section 5.3, a data-driven technique for estimating the geomagnetic field parameters is demonstrated. This is an important component of the effective height estimation technique, as the inversion process requires high precision geomagnetic field parameters to model the propagated diffraction pattern.

5.1. Forward Propagation Model

5.1.1. Propagation Geometry

The ionosphere is a dispersive medium, causing refraction to radio wave signals, such as the GNSS signals. During ionospheric scintillation, diffraction/interference patterns due to plasma structures can also occur to GNSS signals [*Aarons*, 1982]. The principal propagation direction of the GNSS signal is often oblique to the irregularity layer, in which case signal refraction can be expected. Without the complete knowledge of the atmospheric parameters along the satellite-receiver path, using a fixed coordinate system to capture the entire signal propagation would be impractical [*Rino*, 2011]. To resolve this problem, a continuously displaced coordinate system (CDCS) is introduced [*Budden*, 1965]. This system has a continuously displaced measurement

plane that remains centered along the principal propagation direction. By integrating the signal over the CDCS system, the total diffraction caused by scintillation can be modeled. Figure 5-1 demonstrates the CDCS geometry:

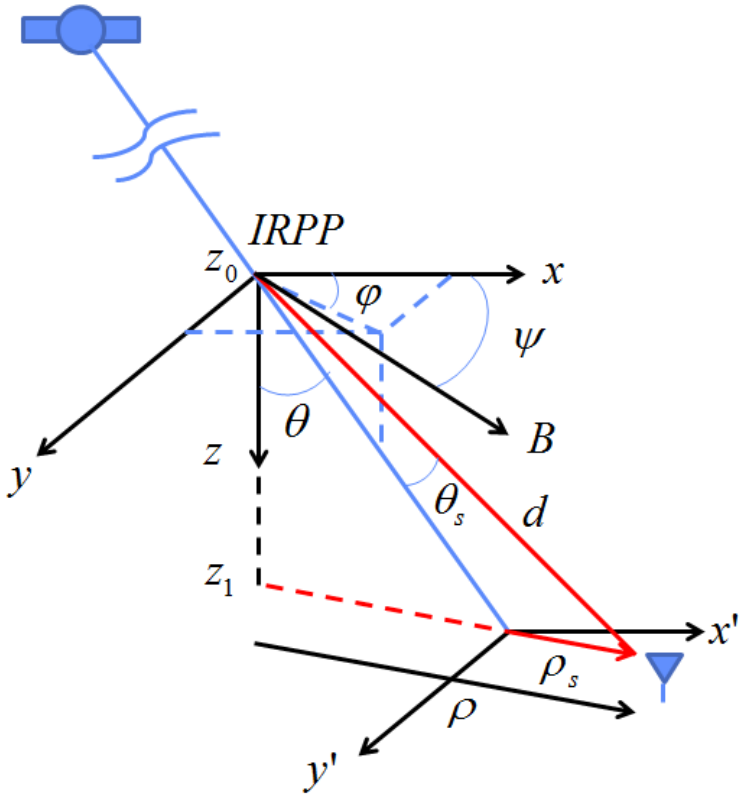

Figure 5-1. Illustration of the Continuously Displaced Coordinate System (CDCS). $x-y$ is the incident plane and $x'-y$' is the displaced plane, both having vertical components z and z' pointing towards Earth's center. θ defines the principal propagation direction. θ_s and $\boldsymbol{\rho}_s$ defines the scattering angle and displacement due to irregularities. The overall displacement $\boldsymbol{d}$ from IRPP is defined by the $(\boldsymbol{\rho}, z)$ system. By defining the $x-z$ plane to be co-planer with the local geomagnetic field direction $\boldsymbol{B}$, the relationship between the CDCS system and the local geomagnetic field system can be established through φ and ψ.

In Figure 5-1, the x-y plane at $z = z_0$ represents the incidence plane at the irregularity layer, while the x'-y' plane at $z = z_1$ represents the receiver plane, or the displaced plane. The principal propagation direction is indicated by the blue line. As the signal hits the irregularity layer, it is scattered by an angle of θ_s. The scattered ray path is indicated by the red line, whose length

equals $\boldsymbol{d}$. The resulting displacement in the x'-y' plane is given by the red vector $\boldsymbol{\rho}_s$, while the displacement in the x-y plane is given by the black vector $\boldsymbol{\rho}$. Here, $\boldsymbol{d}$, $\boldsymbol{\rho}_s$ and $\boldsymbol{\rho}$ are in bold print since they all contain multiple components. The angle θ represents the incidence angle of the principal propagation direction from the z-axis. To fix both x and y axes from free rotation in the horizontal plane, we set the local geomagnetic field vector $\boldsymbol{B}$ to be inclined at an angle ψ in the x-z plane. Then the angle φ is simply the azimuth angle of the principal propagation direction measured from geomagnetic meridian plane. We can now define the principal propagation vector $\mathbf{k}$ as

$$\mathbf{k} = \frac{2\pi}{\lambda}(\sin\theta\cos\varphi\,, \sin\theta\sin\varphi\,, \cos\theta) \qquad (5\text{-}1)$$

where λ is the wavelength of the signal. We also define the transverse component of $\mathbf{k}$ as

$$\mathbf{k}_T = \frac{2\pi}{\lambda}\sin\theta\,(\cos\varphi\,, \sin\varphi) \qquad (5\text{-}2)$$

According to the CDCS definition, the displaced measurement plane remains centered on the principal propagation direction. Therefore, we have:

$$\boldsymbol{d} = \boldsymbol{\rho} + \hat{a}_z z \qquad (5\text{-}3)$$

Consider the transverse coordinates of the scattered ray path in the displaced measurement plane, there is:

$$\boldsymbol{\rho}_s = \boldsymbol{\rho} - \tan\theta\,\hat{a}_{\mathbf{k}_T}(z_1 - z_0) \qquad (5\text{-}4)$$

The above equation applies for the illustrated propagation geometry shown in Figure 5-1. It can be further generalized to the following:

$$\Delta\boldsymbol{\rho}_s = \Delta\boldsymbol{\rho} - \tan\theta\,\hat{a}_{\mathbf{k}_T}\Delta z \qquad (5\text{-}5)$$

where $\Delta\boldsymbol{\rho}_s$, $\Delta\boldsymbol{\rho}$, and Δz represent the displacements in the displaced plane, the incidence plane and the z direction, respectively. From a measurement perspective, $\Delta\boldsymbol{\rho}_s$ captures the known

baseline distances between the receiver pairs. Similarly, the velocity of the anisotropy in the displaced plane can be defined as:

$$\mathbf{v}_s = \mathbf{v}' - \tan\theta\, \hat{a}_{\mathbf{k}_T} \boldsymbol{v}_z \qquad (5\text{-}6)$$

where $\mathbf{v}'$ is the apparent drift velocity defined in Chapter 3.1, and $\boldsymbol{v}_z$ is the velocity component along the z-axis.

5.1.2. Forward Propagation

Following *Briggs and Parkin* [1963] and *Singleton* [1970], we assume that the irregularity structure is anisotropic and has the 3-D shape of an ellipsoid. This ellipsoid is defined with respect to the B-field. Its semi-major axis assumed to be along the B- field direction due to the high parallel conductivities of the ionosphere [*Mendillo and Baumgardner*, 1982]. Following *Rino and Fremouw* [1977], we define a coordinate system (r, s, t), where s is along the B-field vector, t is perpendicular to s and aligned with the Earth's magnetic L-shell (B-field surface of equal magnetic flux), and r is normal to the s-t plane. *Singleton* [1970] showed that the correlation function $R_{\Delta N_e}$ of electron density perturbation ΔN_e is a function of:

$$\left[\left(\frac{\Delta r}{1}\right)^2 + \left(\frac{\Delta s}{a}\right)^2 + \left(\frac{\Delta t}{b}\right)^2\right]^{1/2} \qquad (5\text{-}7)$$

where 1, a and b are scaling factors of the anisotropy ellipsoid along the *r*-axis, *s*-axis and *t*-axis, respectively. The value $a{:}\,b$ gives the axial ratio of the anisotropy. *Livingston et al.* [1982] described several common types of anisotropic irregularity structures. They are called rod-like if $a \gg b \approx 1$, or sheet-like if $a \approx b > 1$, or wing-like if $a > b > 1$. Figure 5-2 illustrates these three types of irregularity structures.

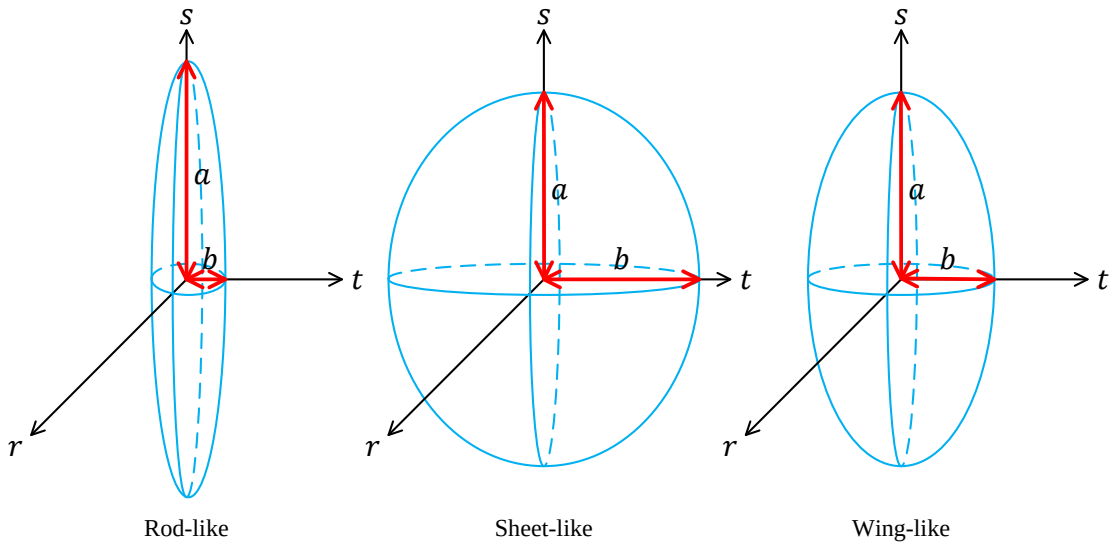

Figure 5-2. Illustration of three types of irregularity structures: rod-like $(a \gg b \approx 1)$; sheet-like $(a \approx b > 1)$ and wing-like $(a > b > 1)$.

To address $R_{\Delta N_e}$ in the $(\boldsymbol{\rho}, z)$ CDCS system, the (r, s, t) Cartesian system needs to be transformed into the $(\boldsymbol{\rho}, z)$ coordinate system. As shown in Figure 5-1, the B-field vector $\boldsymbol{B}$ is at an angle ψ to the x-axis in the x-z plane, while s is along the B-field. Then, the relationship between the two systems can be established as in Figure 5-3.

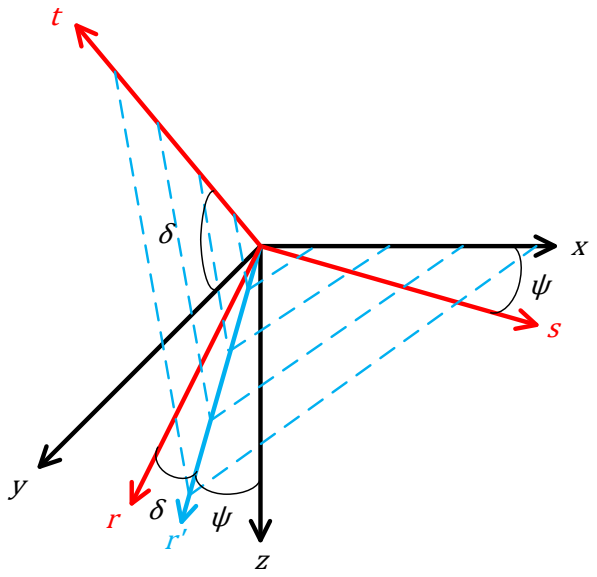

Figure 5-3. Combined geometry of both $(\boldsymbol{\rho}, z)$ and (r, s, t) coordinate systems for the general anisotropic irregularity model.

In Figure 5-3, the black vectors represent the $(\boldsymbol{\rho}, z)$ coordinate system, while the red vectors represent the (r, s, t) coordinate system. The angle between the x-axis and the s-axis is given by ψ, while the blue arrow r' represents the projection of the r-axis onto the x-z plane. Hence the inclination angle from the x-z plane to the r-s plane is captured by δ, the angular difference between r and r'. All 7 vectors in Figure 5-3 live in two planes that are normal to each other. One of them contains (x, s, z, r'), while the other contains (r', r, y, t). This co-planer property is captured by the blue dashed lines. Based on this property, one can derive that the angular difference between y and t axes also equals δ. In practice, δ needs to be fixed so that r-axis and t-axis are not free of rotation. Here, we further assume that δ is 0. This effectively assumes that the *s*-*t* plane of the anisotropy is aligned with the Earth's magnetic L-shell, which corresponds to the magnetic field surface of equal magnetic flux.

Using the above relationships, the appropriate coordinate transformation from the (r, s, t) system into the $(\boldsymbol{\rho}, z)$ system can be derived as:

$$s = x\cos\psi + z\sin\psi \quad (5\text{-}8)$$

$$t = x\sin\psi\sin\delta + y\cos\delta - z\cos\psi\sin\delta \quad (5\text{-}9)$$

$$r = -x\sin\psi\cos\delta + y\sin\delta + z\cos\psi\cos\delta \quad (5\text{-}10)$$

By evaluating $\Delta r^2 + \left(\frac{\Delta s}{a}\right)^2 + \left(\frac{\Delta t}{b}\right)^2$ using the above transformation, a general quadratic form of $R_{\Delta N_e}$ is obtained in terms of Δx, Δy, and Δz. Following *Rino and Fremouw* [1977], $R_{\Delta N_e}$ can be assumed to have the general form:

$$R_{\Delta N_e}(\Delta\boldsymbol{\rho}, \Delta z) = \langle \Delta {N_e}^2 \rangle R\{[(\Delta\boldsymbol{\rho}, \Delta z)^T \mathbf{C} (\Delta\boldsymbol{\rho}, \Delta z)]^2\} \quad (5\text{-}11)$$

where $R(\cdot)$ is the functional form of any valid auto-correlation function, which should always be normalized so that $R(0) = 1$. And the form of the argument is:

$$(\Delta\boldsymbol{\rho}, \Delta z)^T \mathbf{C} (\Delta\boldsymbol{\rho}, \Delta z) = C_{11}{\Delta\rho_x}^2 + C_{22}{\Delta\rho_y}^2 + C_{33}\Delta z^2 + 2C_{12}\Delta\rho_x\Delta\rho_y + 2C_{13}\Delta\rho_x\Delta z + 2C_{23}\Delta\rho_y\Delta z \quad (5\text{-}12)$$

where the elements of the $\mathbf{C}$ matrix are given as:

$$C_{11} = \frac{1}{a}\cos^2\psi + \sin^2\psi\left(\frac{1}{b^2}\sin^2\delta + \cos^2\delta\right) \quad (5\text{-}13)$$

$$C_{22} = \frac{1}{b^2}\cos^2\delta + \sin^2\delta \quad (5\text{-}14)$$

$$C_{33} = \frac{1}{a}\sin^2\psi + \cos^2\psi\left(\frac{1}{b^2}\sin^2\delta + \cos^2\delta\right) \quad (5\text{-}15)$$

$$C_{12} = C_{21} = \left(\frac{1}{b^2} - 1\right)\sin\psi\sin\delta\cos\delta \quad (5\text{-}16)$$

$$C_{13} = C_{31} = \left(\frac{1}{a^2} - \frac{1}{b^2}\sin^2\delta - \cos^2\delta\right)\sin\psi\cos\psi \quad (5\text{-}17)$$

$$C_{23} = C_{32} = -\left(\frac{1}{b^2} - 1\right)\cos\psi\sin\delta\cos\delta \quad (5\text{-}18)$$

Note that when $b = 1$, the horizontal cut of the irregularity in the r-t plane becomes a circle. Hence the dependence on the parameter δ disappears and $C_{12} = C_{21} = C_{23} = C_{32} = 0$.

To propagate the anisotropy forward to the diffracted wave field at the receiver plane, a relationship between the fluctuations in the trans-ionospheric carrier phase signal and the perturbation in the electron density needs to be established. Following *Rino and Fremouw* [1977] and *Rino and Livingston* [1982], geometrical optics relationship between the perturbation $\delta N_e(\Delta\rho, \Delta z; \Delta t)$ and the phase fluctuation $\delta\phi(\Delta\rho, \Delta z; \Delta t)$ is employed, given by:

$$\delta\phi(\Delta\rho, \Delta z; \Delta t) = -r_e\lambda_0 \int \delta N_e(\Delta\rho, \Delta z; \Delta t)\, dl \quad (5\text{-}19)$$

where $r_e (= 2.817 \times 10^{-15}\ \text{m})$ is the classical electron radius and λ_0 is the carrier wavelength of the GNSS signal. Based on this linear ray optics approximation, the spatial auto-correlation function of phase $R_{\delta\phi}(\Delta\rho, \Delta z; \Delta t)$ has the form:

$$R_{\delta\phi}(\Delta\rho, \Delta z; \Delta t) = \langle \delta\phi^2 \rangle R[f(\Delta\rho_s - \mathbf{v_s}\Delta t)] \quad (5\text{-}20)$$

where $\langle \delta\phi^2 \rangle$ is the phase variance. The diffraction pattern caused by the propagated anisotropic irregularity structure is then characterized by the quadratic function:

$$f^2(\Delta\boldsymbol{\rho}_s) = \frac{C\Delta\rho_{s_x}^2 - B\Delta\rho_{s_x}\Delta\rho_{s_y} + A\Delta\rho_{s_x}^2}{AC - B^2/4} \quad (5\text{-}21)$$

where the anisotropy parameters A, B and C are given by:

$$A = \hat{C}_{11} + \hat{C}_{33}\tan^2\theta\cos^2\varphi - 2\hat{C}_{13}\tan\theta\cos\varphi \quad (5\text{-}22)$$

$$B = 2\left[\hat{C}_{12} + \hat{C}_{33}\tan^2\theta\sin\varphi\cos\varphi - \tan\theta\left(\hat{C}_{13}\sin\varphi + \hat{C}_{23}\cos\varphi\right)\right] \quad (5\text{-}23)$$

$$C = \hat{C}_{22} + \hat{C}_{33}\tan^2\theta\sin^2\varphi - 2\hat{C}_{23}\tan\theta\sin\varphi \quad (5\text{-}24)$$

where $\hat{C}_{11}$, $\hat{C}_{22}, \hat{C}_{33}$, $\hat{C}_{12}, \hat{C}_{13}$ and $\hat{C}_{23}$ are the elements of the $\hat{\mathbf{C}}$ matrix, which are obtained from the corresponding elements of the $\mathbf{C}$ matrix by replacing a^2 by $1/a^2$ and b^2 by $1/b^2$ in Equation 5-13 to 5-18, respectively.

At the receiver plane, the shape of the diffraction pattern is characterized by the scaling factors a' and b', along its semi-major and semi-minor axes, giving the axial ratio:

$$a' : b' = \left(\frac{A + C + D}{A + C - D}\right)^{1/2} \quad (5\text{-}25)$$

where

$$D = [(A - C)^2 + B^2]^{1/2} \quad (5\text{-}26)$$

while the orientation angle of the diffraction pattern is the angle from its principal irregularity axis relative to the y-axis:

$$\phi_R = \frac{1}{2}\tan^{-1}\left(\frac{B}{C - A}\right) \quad (5\text{-}27)$$

For more elaborated descriptions and calculations of the forward propagation process, refer to *Rino and Fremouw* [1977] and Appendix A.3 in *Rino* [2011]. In this study, we assert that the

parameters A, B and C together with Equations 5-21 fully characterize the received diffraction pattern anisotropy.

5.2. Effective Irregularity Height Estimation

With the propagated diffraction pattern in Section 5.1 through modeling, and the estimated diffraction pattern in Section 4.3 from measurements, an inversion problem can be established to solve for the effective irregularity height based on the anisotropy model.

5.2.1. Methodology

In Section 5.1.2, the forward propagation process shows how to directly compute the anisotropy parameters (A, B, C) from the satellite-receiver geometry, B-field parameters and the axial ratio $(a:b)$ of the ionospheric irregularity. While the satellite-receiver geometry parameters can be determined from the known receiver position and satellite orbit information, the field parameters and the irregularity axial ratio are essentially unknown. In Section 4.3.2, the spaced-receiver analysis shows how to estimate a scaled version of the anisotropy parameters $(\hat{A}, \hat{B}, \hat{C})$ from receiver array correlation functions. Later in Section 5.2.2, an approximation method is demonstrated, showing how to estimate $(a:b)$ from the axial ratio $(a':b')$ of the observed diffraction pattern. The method also relies on the relationship between the satellite-receiver geometry and the geomagnetic field parameters. Thus far, the only remaining unknown parameters are the geomagnetic field parameters, which are all related to the irregularity height. Section 5.3 shows how the field parameters can be approximated using measurements from a network of magnetometers for a given irregularity height.

Now that both the height-associated modeled anisotropies (A, B, C) and the measured anisotropy $(\hat{A}, \hat{B}, \hat{C})$ can be obtained, the effective irregularity height h^* can be determined when the modeled anisotropy best matches the measured anisotropy. Under the concentric-

ellipsoids assumption of the anisotropy model, the perfect match occurs when a modeled anisotropy is a scaled version of the measured anisotropy, or:

$$(A, B, C) = k\left(\hat{A}, \hat{B}, \hat{C}\right), \qquad k \in \mathbb{R}, k > 0 \tag{5-28}$$

Formally, this matching process can be described by an inversion problem, whose objective is to find the best model parameter h^* such that:

$$k\left(\hat{A}, \hat{B}, \hat{C}\right) = G(h^*) \tag{5-29}$$

where G is the forward operator describing the relationship between and the model parameter h^* and the propagated diffraction pattern parameters (A, B, C) as in Section 2.2. Note that this height h^* is not necessarily the true irregularity height, but rather an effective height constrained by the assumptions involved in the anisotropy model.

In the implementation, the ratios between the anisotropy coefficients, $(A/B, A/C, B/C)$ and $\left(\hat{A}/\hat{B}, \hat{A}/\hat{C}, \hat{B}/\hat{C}\right)$, are first computed. Then the best match can be found when the mean-square difference is minimal:

$$\left\|\left(\frac{A}{B}, \frac{A}{C}, \frac{B}{C}\right) - \left(\frac{\hat{A}}{\hat{B}}, \frac{\hat{A}}{\hat{C}}, \frac{\hat{B}}{\hat{C}}\right)\right\| = \min \left\|\left\{\frac{A}{B}, \frac{A}{C}, \frac{B}{C}\right\} - \left(\frac{\hat{A}}{\hat{B}}, \frac{\hat{A}}{\hat{C}}, \frac{\hat{B}}{\hat{C}}\right)\right\| \tag{5-30}$$

This way, the inversion problem can be solved without calculating the actual value for k. Figure 5-4 illustrates the general methodology for estimating the effective irregularity height.

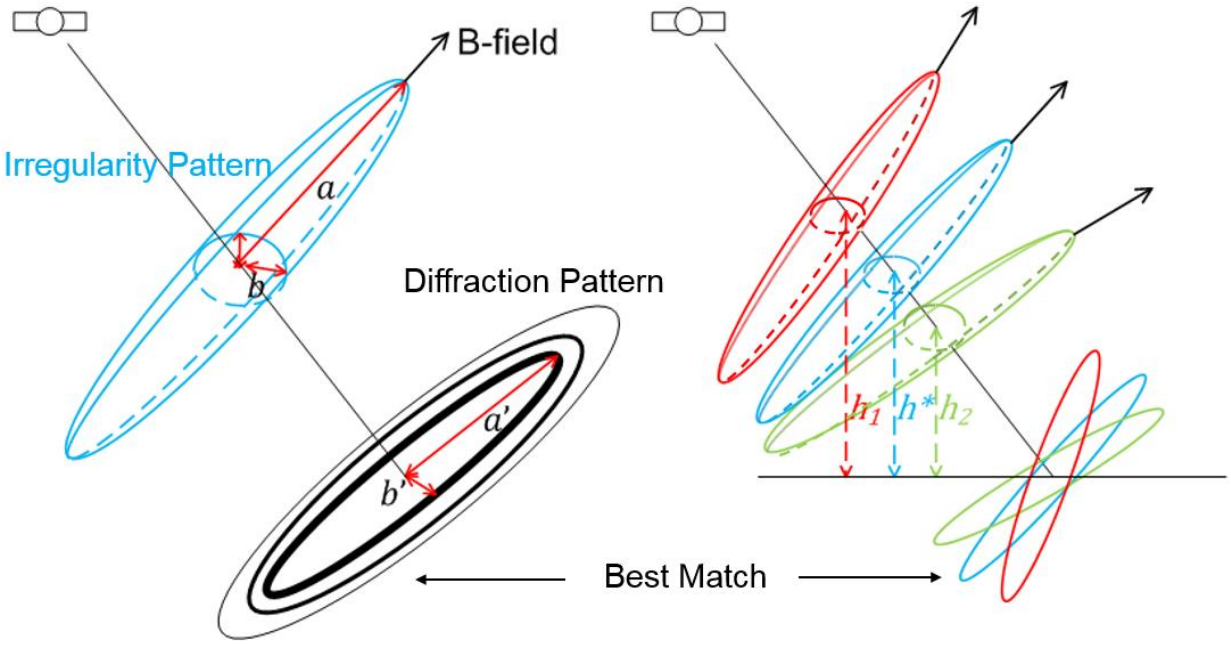

Figure 5-4. Illustration of the effective irregularity height estimation method.

On the left, a diffraction pattern (black ellipses), caused by the irregularity structure (blue ellipsoid) is observed at the receiver array. On the right, three ellipsoids of distinct colors (red, blue and green) mark the potential positions of the ionospheric irregularity under different height assumptions: h_1 (red), h^* (blue) and h_2 (green). These ellipsoids are associated with different B-field parameters, as indicated by their distinct orientations. Three ellipses (red, blue and green), showing the corresponding diffraction patterns, are propagated to the receiver plane. The orientation and shape of the blue ellipse matches best with the observed diffraction pattern on the left. As a result, the irregularity height associated with the blue diffraction pattern, h^*, is determined to be the effective irregularity height. A block diagram is given below in Figure 5-5 to further clarify this procedure.

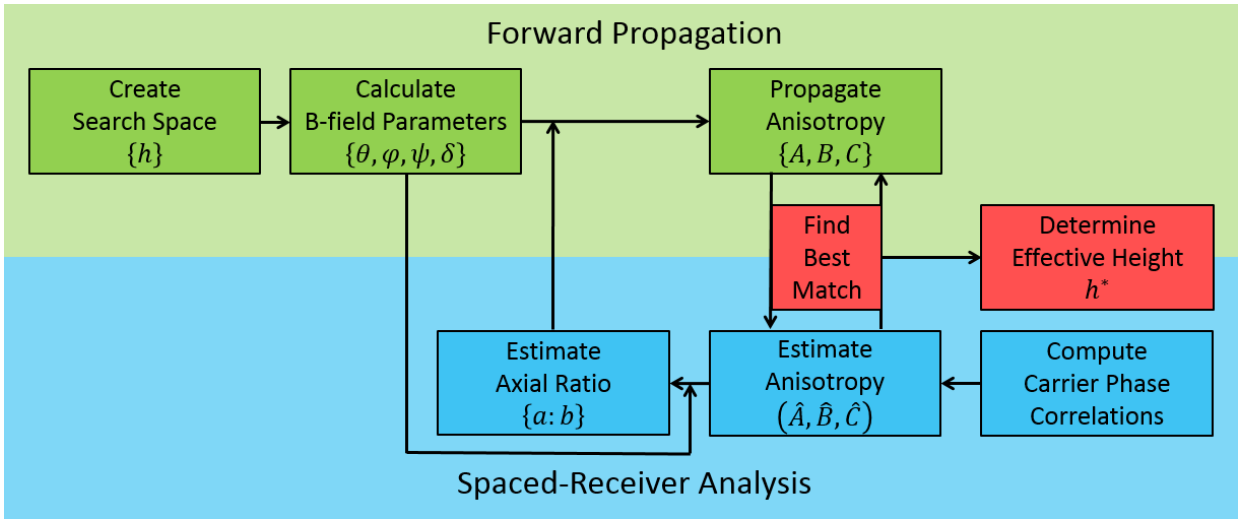

Figure 5-5. Block diagram illustrating the effective irregularity height estimation process. The green blocks represent the forward propagation steps, the blue blocks represent the spaced-receiver analysis steps, and the red blocks shows the matching process. The "{}" represents a set of parameters.

Following Figure 5-5, during the forward propagation process, a set of potential irregularity height values are first selected to form the search space. For example, $\{h\}$ can be a range of height values from 100 km to 400 km. Then the corresponding B-field parameters $\{\theta, \varphi, \psi, \delta\}$ are calculated, where θ can be obtained from the satellite-receiver geometry and the height assumption, φ and ψ can be calculated using real-time geomagnetic field values, and δ is set to be 0. Section 5.3 shows how the B-field values can be approximated from a network of magnetometers. Once the axial ratio of the irregularity pattern is obtained from the bottom track, a set of anisotropy parameters $\{A, B, C\}$ are calculated using the forward propagation model.

On the other hand, the diffraction pattern parameters can be estimated based on the anisotropy correlation model through spaced-receiver analysis. Following Section 4.3.2 and Appendix B, a scaled version of the anisotropy $(\hat{A}, \hat{B}, \hat{C})$ can be estimated. Based on the axial ratio $a': b'$ of the diffraction pattern as well as the B-field parameters from the top track, Section 5.2.2 shows how the axial ratio $\{a: b\}$ of the irregularity pattern can be approximated.

To verify the effectiveness of this inversion algorithm, the estimated effective irregularity heights can be cross-compared with the electron density profile measured by the collocated PFISR. For example, $\{h\}$ can be taken as the height values of the PFISR measurement range gates. Then at the GNSS estimated heights, check for electron density enhancement or depletion in the PFISR Ne profiles, as these phenomena are likely associated with ionospheric irregularities. Case studies are conducted in Section 6.8 based on two intense geomagnetic storm events.

5.2.2. Axial Ratio Approximation

The horizontal slice of the irregularity ellipsoid along the magnetic L-shell is essentially the 2-D irregularity pattern characterized by the semi-major axis $= a$, and the semi-minor axis $= b$. The diffraction pattern is then propagated to the receiver plane with semi-major axis $= a'$, and semi-minor axis $= b'$. If a definitive relationship can be established between these parameters, then the irregularity pattern axial ratio $a:b$ can be derived from the diffraction pattern axial ratio $a':b'$. A simplified geometry of the irregularity and diffraction patterns is shown in Figure 5-6.

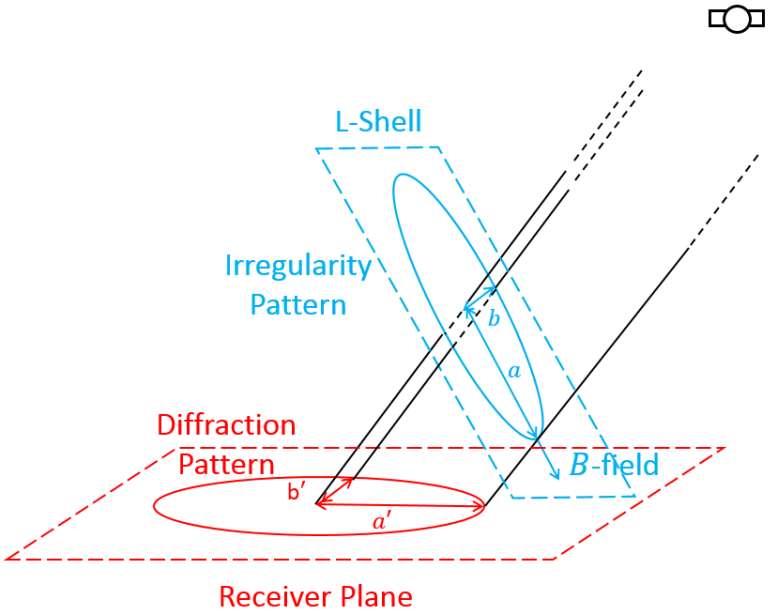

Figure 5-6. Simplified schematics of the propagation geometry. The blue ellipse is the irregularity pattern along the L-shell, while the red ellipse is the propagated diffraction pattern in the receiver plane.

In Figure 5-6, since b is aligned with the L-shell and is perpendicular to the B-field orientation, it is parallel to b' in the receiver plane. It follows that $b \approx b'$, especially when the satellite-receiver distance is much larger than the receiver-irregularity distance. The remaining task is to find the relationship between a' and a, which can be characterized through geometric projection. Since the B-field direction is along the semi-major axis, the same projection can be applied to the B-field vector as well. This projection is illustrated by Figure 5-7.

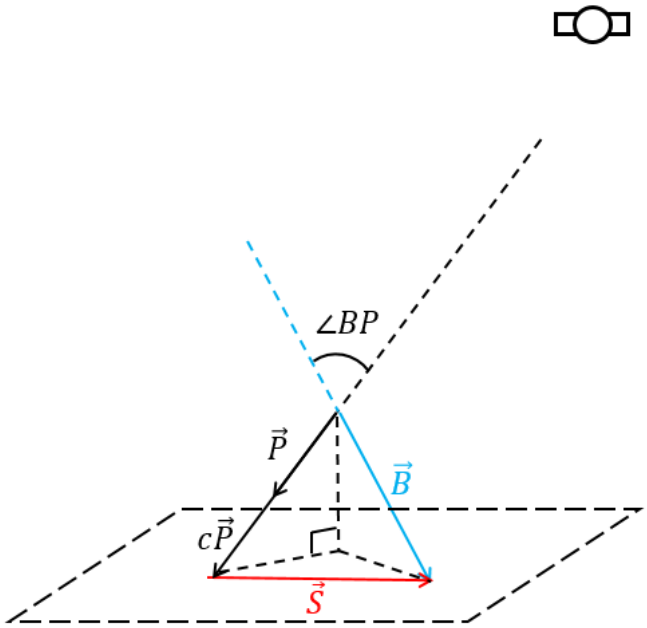

Figure 5-7. Geometric projection from the B-field direction ($\vec{B}$, blue) to the projection vector ($\vec{S}$, red) along the principal propagation direction ($\vec{P}$, black). The Briggs-Parkin angle ($\angle BP$) gives the angle between $\vec{B}$ and $\vec{P}$.

In Figure 5-7, the projection from the B-field vector $\vec{B}$ along the principal propagation vector $\vec{P}$ onto a plane parallel to the receiver plane is the projection vector $\vec{S}$. The Briggs-Parkin angle ($\angle BP$) defines the angle between the B-filed direction and the principal propagation direction [*Briggs and Parkin*, 1963]. It follows that

$$\vec{S} = \vec{B} - c\vec{P} \qquad (5\text{-}31)$$

where c is a scalar. $c\vec{P}$ is a scaled version of $\vec{P}$, such that the vertical component of $c\vec{P}$ is the same as the vertical component of $\vec{B}$. As a result, $\vec{S}$ is in a plane parallel to the receiver plane. Define the scaling parameter between $\|\vec{S}\|$ and $\|\vec{B}\|$ to be S, then there is

$$S = \|\vec{S}\| : \|\vec{B}\| = \|\vec{B} - c\vec{P}\| : \|\vec{B}\| = a' : a \quad (5\text{-}32)$$

Since $b \approx b'$, we finally have

$$S \cdot (a : b) = a' : b' \quad (5\text{-}33)$$

Equation (5-32) provides a coarse estimate of the relationship between $a : b$ and $a' : b'$. In reality, the signal bending through the propagation path and the Earth's curvature would introduce additional effects to S. Therefore, a ±15% uncertainty is allowed when estimating $a : b$ from $a' : b'$.

5.2.3. Anisotropy Errors and Mitigation Techniques

The validity of the effective height estimation technique is largely dependent on the accuracy of the anisotropy parameters. It is important to be able to identify and mitigate potential error sources in these parameters, as they may eventually pollute the effective height estimates.

As mentioned in Section 4.3.2, a practical issue occurs when the estimated diffraction pattern axial ratio approaches unity, i.e., $a' : b' \approx 1$. Combining with the topology of the irregularity structure, this implies one of two possibilities: 1) the irregularity axial ratio is also near unity $(a : b \approx 1)$; or 2) the B-filed direction coincides with the principal propagation direction $(\angle BP \approx 0)$. These two scenarios are illustrated by Figure 5-8.

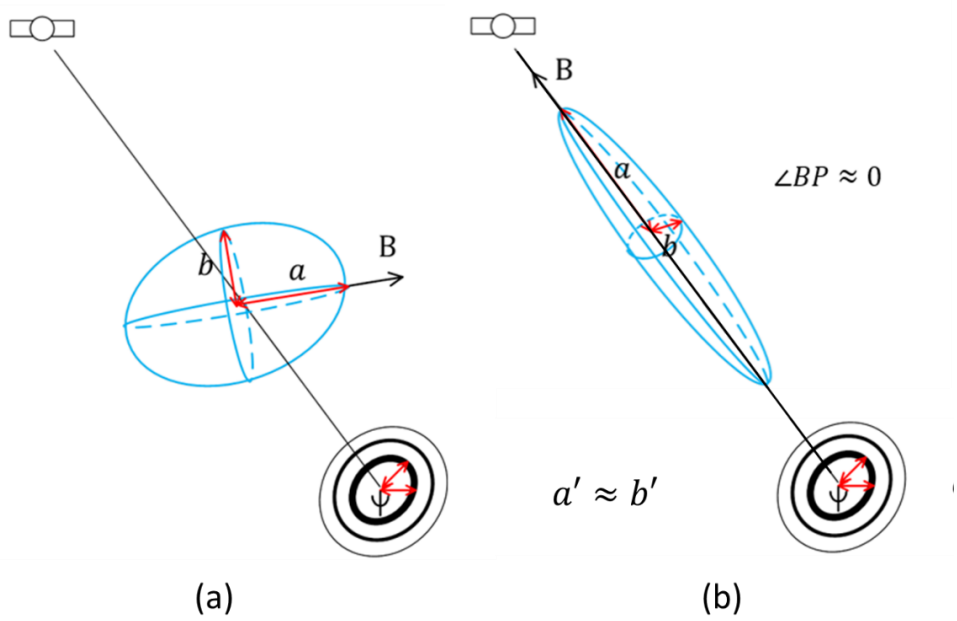

Figure 5-8. Potential scenarios for obtaining unity axial ratio $(a':b' \approx 1)$. Subplot (a) shows the possibility where the irregularity axial ratio is also unity $(a:b \approx 1)$. Subplot (b) shows the possibility where the Briggs-Parkin angle is small $(\angle BP \approx 0)$.

In either case, the diffraction pattern would be practically isotropic, making it very challenging to identify its orientation. As a result, when $a':b' \approx 1$, large errors may persist in the estimated anisotropy parameters. In the implementation, this potential error is mitigated by filtering out the results that are associated with small axial ratios $(a':b' < 2)$. Note that in Figure 5-8(b), even if the axial ratio turns out to be large, the results could still be invalid. Because when $\angle BP \approx 0$, the estimated diffraction pattern would not provide any information on the semi-major axis, which happens to be along the principal propagation direction. In the implementation, this is mitigated by discarding the results associated with small $\angle BP$ values $(\angle BP < 15°)$.

The forward propagation model is established based on the assumption that the ionospheric irregularities are aligned with the B-field. However, during active conditions, this assumption may not hold. In practice, when the orientation of the observed diffraction pattern deviates too much from the B-field direction $(> 30°)$, the corresponding results are rejected.

In addition, only results associated with sufficient phase scintillation ($\sigma_\phi \geq 12°$) are considered, so that the estimated results are indeed reflecting the irregularity heights. Also, an elevation mask for the input phase measurements is set at 35° to mitigate multipath errors.

5.3. Geomagnetic Field Parameter Estimation

Another key component of the height estimation method is the parameter set describing the input B-field. The baseline field parameters can be obtained from heuristic B-field models, such as the International Geomagnetic Reference Field (IGRF) model [*Thébault et al*., 2015]. But during strong geomagnetic activities, strong disturbances exceeding ±1000 nT, can often be observed in addition to the baseline values. Figure 8 demonstrates the magnetometer measurements from the College Station in Fairbanks, Alaska, during a geomagnetic storm event on 2015/12/20. The baseline B-field values are also provided based on the IGRF-12 (the 12th generation) model.

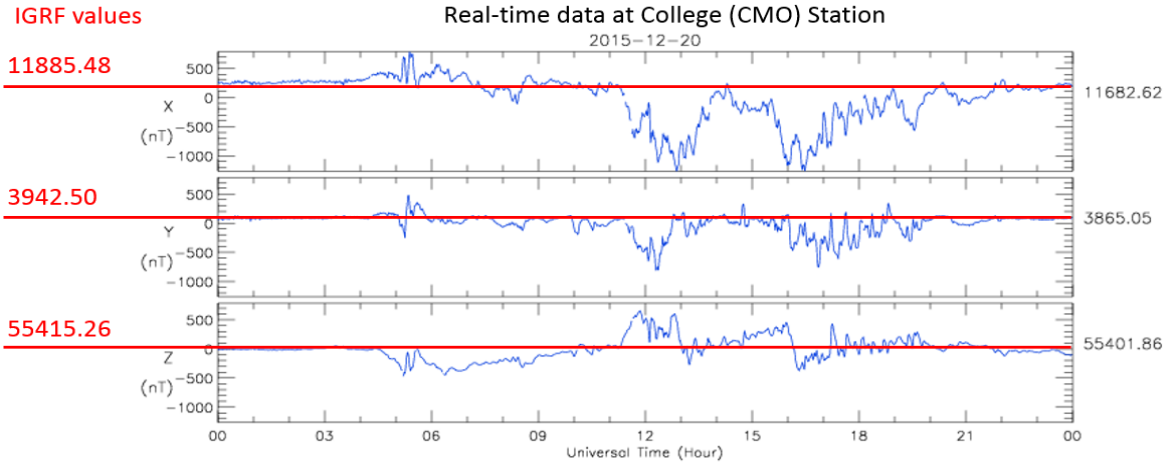

Figure 5-9. Real-time magnetometer measurements at the College Station with IGRF modeled baseline field parameters on 2015/12/20.

In Figure 5-9, the blue lines in the top, middle and bottom rows represent the magnetometer measurements as X (northward), Y (eastward) and Z (downward) components, respectively. The red lines correspond to the IGRF modeled field baseline parameters. The IGRF model appears to

fit very well to the field baseline at the beginning and the end of the day. However, during the active hours from ~0500 to ~2000 UT, the differences between the model and the measurements are substantial (> 1000 nT in the X direction, and >500 nT in the Y and Z directions).

In the inversion algorithm for effective irregularity height estimation, the validity of the results is directly related to the accuracy of the input B-field parameters. The above example suggests that using daily baseline values from the IGRF model could not provide the desired accuracy. An alternative field parameter estimation technique is required. Also, the height estimation method ultimately requires the field parameters over the altitudes of interest in the ionosphere. To achieve these requirements, a two-step approach is proposed: 1) estimate B-field parameters at Earth's surface; and 2) project these parameters onto the altitudes of interest.

In the first step, processed magnetometer data covering the Alaskan region is first obtained from SuperMAG (http://supermag.jhuapl.edu/). Figure 5-10 shows the 8 regional magnetometer stations that were available during the geomagnetic storm events used in this study.

Figure 5-10. Available magnetometer stations from SuperMAG during the observation period, marked by the 7 red pins and the green pin. The green pin near the center also marks the Poker Flat GNSS array location. The white pins mark other magnetometer stations in the region.

The 8 magnetometer stations in Figure 5-10 outline the general Alaskan region, which covers most of the observable region from the Poker Flat GNSS array. The station names, three-letter abbreviations and geodetic coordinates are provided below in Table 5-1 as a reference.

Table 5-1. GNSS bands used in this dissertation, and output data rate at each antenna.

Station Name	Barrow	College	Deadhorse	Shumagin	Sitka	Inuvik	Petersburg	Poker Flat
Station Code	BRW	CMO	DED	SHU	SIT	INK	T22	PKR
Latitude (°N)	71.3	64.9	70.4	55.4	57.1	68.3	56.8	65.1
Longitude (°W)	156.6	147.9	148.8	160.5	135.3	133.3	133.2	147.3

To approximate the geomagnetic parameters within this region, linear interpolation is applied based on the SuperMAG data obtained from these 8 stations. A crucial component of the interpolation process is to create uniformly spaced coordinates covering this region. However, uniform latitude×longitude grid in the geodetic coordinate system does not preserve uniform space. For example, a 1°×1° grid at low latitude would cover a much larger region than a 1°×1° grid near the North Pole. To properly address this issue, the following steps are implemented:

1) Convert the geodetic coordinates of the available magnetometer stations into Earth-Center, Earth-Fixed (ECEF) coordinates. Create a uniform three-dimensional (3-D) mesh bounded by these stations' (x, y, z) coordinates;
2) For each vertex in the 3-D mesh, calculate its geodetic coordinates. For each (x,y) coordinate, find the z coordinate that is associated with the least altitude value. This way, the fitting surface created by points like (x, y, z) can be confined to the Earth's surface;
3) Use the calculated geodetic latitude and longitude coordinates of the fitting surface as the 2-D fitting lattice for linear interpolation.

Using a 50km×50km×10km ECEF grid, the corresponding 2-D fitting lattice is illustrated by Figure 5-11 as an example.

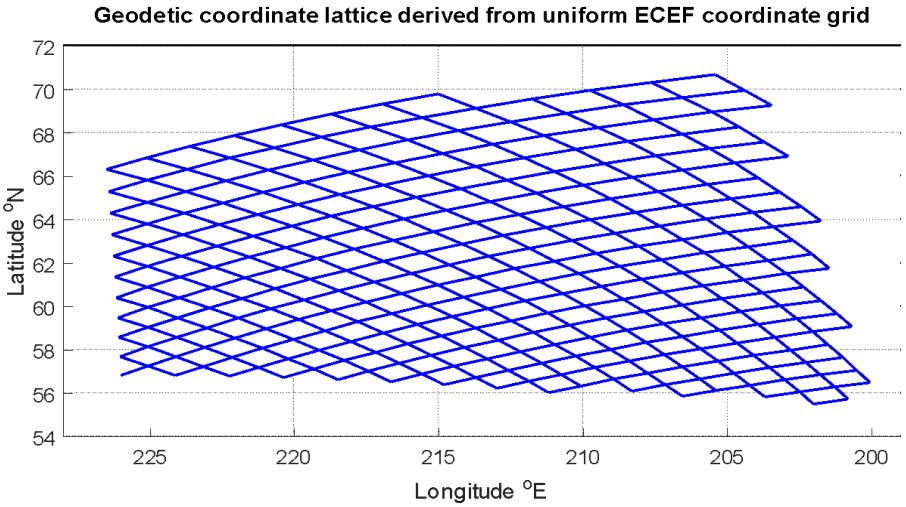

Figure 5-11. Example of the 2-D fitting lattice created from a 50km×50km×10km ECEF grid.

In Figure 5-11, note that the size of an individual lattice at lower latitudes is smaller than that of a lattice at higher latitudes, indicating correct projection. In the actual implementation, a 20km×20km×5km ECEF grid is used for enhanced spatial resolution. Linear interpolation is applied on the 2-D fitting lattice. Figure 5-12 shows an example of fitted results.

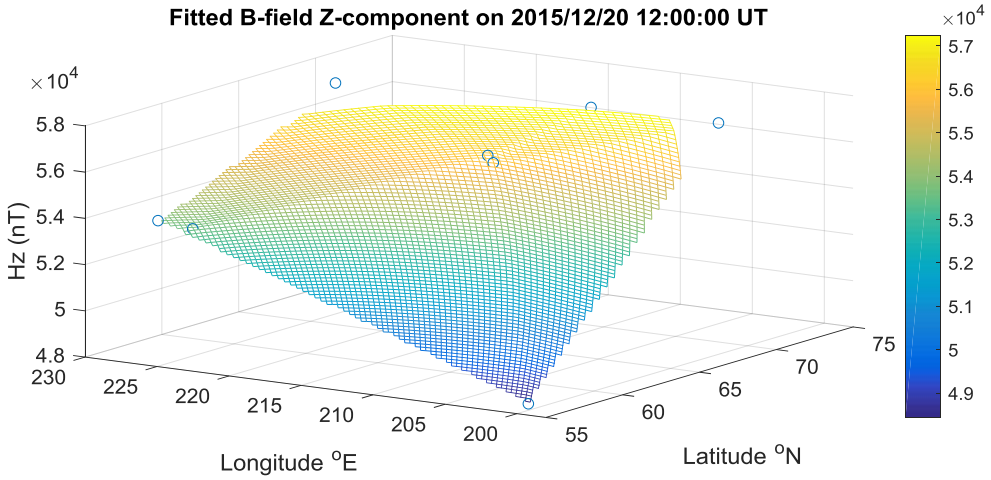

Figure 5-12. Example of interpolated geomagnetic field vertical component H_z (positive downward) at 12:00:00 UT on 2015/12/20. The magnitude of the field values is shown by the color bar in nT. Eastward longitude coordinates are used for fitting purposes.

Note that field strength variation along H_z is nearly 8000 nT in Figure 5-12. This again illustrates the importance of using accurate geomagnetic data to represent the field parameters for the effective irregularity height estimation method.

The above procedure estimates the B-field parameters at Earth's surface. The next step is to project the surface field parameters onto targeted altitudes. One way to accomplish this is through modeling the Earth's magnetic field, which is infeasible when only regional field parameters are considered as in this case. On the other hand, this suggests that established magnetic field models can be employed to carry out the estimation. In this study, we resorted to the IGRF model, which uses the Altitude-Adjusted Corrected Geomagnetic (AACGM) coordinate system to address the altitude variation in the B-field [*Shepherd*, 2014]. The implementation is as the following:

1) Find the IGRF baseline field parameters at the Earth's surface and at the targeted altitude;
2) Calculate the ratio between these two values;
3) Use this ratio as a scaling factor to estimate the field parameter at the targeted altitude based on the interpolated surface field value found in the previous process.

For example, on 2015/12/31, the IGRF daily baseline values for B_z (B-field vertical component) at the PFRR were 55543.8 nT at the Earth's surface, and 50596.2 nT at 200 km altitude. At 1200 UT, the interpolated Bz value at Poker Flat Antenna 1 location was 55818.5 nT. Then the instantaneous Bz value at 200 km above Antenna 1 can be estimated as: $B_{z,200km@A1} = (50596.2\ \text{nT} \div 55543.8\ \text{nT}) \times 55818.5\ \text{nT} = 50846.4\ \text{nT}$.

The IGRF itself is a series of mathematical models of the Earth's main field and its annual rate of change (secular variation). It is updated every five years by the International Association of Geomagnetism and Aeronomy. This dissertation adopts the 12th generation IGRF model released

in December 2014, which is the latest IGRF model as of writing of this dissertation [*Thébault et al*., 2015].

By now, all spaced-GNSS receiver techniques developed in this dissertation have been presented. Ionospheric drift velocities and effective heights can be estimated from GNSS carrier phase measurements during high latitude ionospheric scintillation. To verify the validity of these techniques, self-consistency studies between GNSS frequency bands and cross-comparison studies against measurements from other instruments are conducted. The results of these comparative studies are presented in Chapter 6.

6. CHAPTER 6 – COMPARATIVE CASE STUDIES AND ANALYSIS

Based on the algorithms and procedures described in Chapters 3, 4 and 5, together with the receiver array setup described in Chapter 2, GNSS irregularity drift velocities and effective irregularity heights can be estimated during phase scintillations.

In this chapter, several case studies will be presented to evaluate the accuracy of the methods and compare the results with other co-located instrument observations. Section 6.1 gives the summary of the scintillation events used in this dissertation for both the HAARP array and the Poker Flat array. Error analysis and mitigation techniques are discussed in Section 6.2. In Section 6.3, an inter-frequency self-consistency study has been conducted based on the HAARP array data. Section 6.4 presents a comparative study between the HAARP array drift velocity estimates and the SuperDARN measurements. Section 6.5 focuses on the comparison of the two correlation methods: TDM and TFDM. In Section 6.6, a comparative study between the Poker Flat array drift velocity estimates under different correlation models is conducted. The corresponding background ASI images and PFISR vector velocity measurements are provided as references. In Section 6.7, another comparative study is conducted between velocity estimates from the Poker Flat array and measurements from the PFISR. In Section 6.8, the GNSS array estimated effective irregularity heights are cross-compared with the PFISR electron density profiles.

6.1. Scintillation Events and Example Results

Numerous ionospheric phase scintillation events have been collected by the HAARP array and the Poker Flat array. In this dissertation, the HAARP array data is used for self-consistency study across different GNSS signals, as well as a quantitative cross-comparative study between the GNSS receiver array estimations and the KOD SuperDARN measurements based on a large

amount of scintillation events using the TFDM. The Poker Flat array data is used for a method comparison study between the TDM and the TFDM, as well as a cross-comparative study between the GNSS measurements and the PFISR measurements based on a couple of long-lasting events using the TDM.

6.1.1. HAARP Array Events and Example Results

The HAARP GNSS array system continuously monitored the local ionosphere from 2011/8 to 2013/3. GPS measurements were available throughout this 20-month period, while GLONASS measurements became available for the last 10 months since 2012/6, after a full system update during a 2012 summer campaign [*Taylor et al.*, 2013]. The KOD SuperDARN array also has continuous measurement throughout these 20 months.

To perform the data comparison during ionospheric scintillations, the scintillation events need to be extracted first. From the available data, we examined the phase measurement from each GPS satellite and identified the total scintillation event time to be 224.32 hours [*Wang et al.*, 2016]. Among the 20-month period, 37 days of data are further identified where scintillation events are most concentrated. These selected data have a combined event time of 164.1 hours, covering more than 73% of the total event time. Lastly, the corresponding KOD data are obtained for these 37 days.

Following the procedures described in previous chapters, the apparent irregularity drift velocities are estimated based on the TFDM. In this study, the front velocity model is directly applied to the time lag estimates at the correlation peaks produced by the TFDM. For other correlation models associated with the anisotropy model, additional processing is required to retrieve the full correlation functions. It is not pursued in this study. The drift velocity estimates are obtained using the front velocity model. from Figure 6-1 shows the estimated irregularity drift

velocities for the visible GPS satellites calculated from a scintillation event from 11:51:17 to 12:54:17 UTC on 2012/10/13.

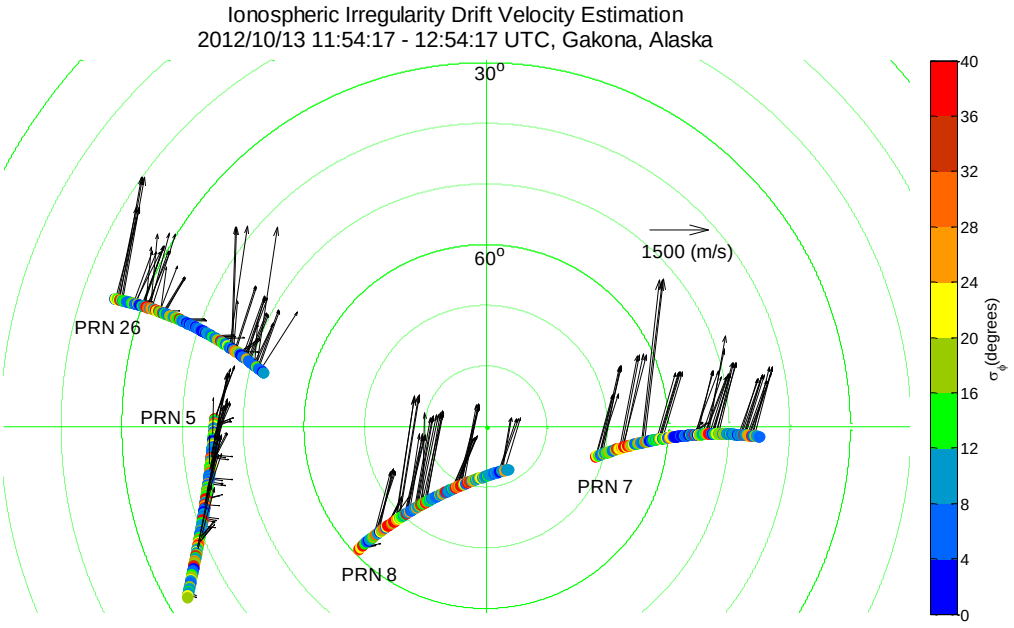

Figure 6-1. Sky vector plot of ionospheric irregularity drift velocity estimation. The color-coded tracks correspond to the $\boldsymbol{\sigma_\phi}$ values of each satellite's detrended phase measurements, with intensity given by the colorbar. The vectors on the satellite tracks illustrate the drift velocity estimation magnitude and direction. A velocity vector of 1500 m/s pointing eastward is given as a reference.

In Figure 6-1, all velocity vectors roughly point to the same north-east direction with magnitudes ranging from 300 to 3000 m/s with most around 1500 m/s. Note that the corresponding σ_φ values of each satellite have also been plotted with color code indicated by the color bar on the right. Intuitively, it is easier for this technique to determine the drift velocity when the phase fluctuation is stronger.

6.1.2. Poker Flat Array Events and Example Results

6.1.2.1. The 2015/12/20 Event

A geomagnetic storm event took place during December 19-21, 2015. The sudden storm commencement (SSC) was documented at 16:16:12 UT on 2015/12/19 at the ground, marking the

initial phase of the storm [Ebre Observatory, http://www.obsebre.es/en/rapid]. Following a 30-hour build-up, the hourly Disturbance Storm Time (Dst) index indicated that the storm reached maximum intensity at -155 nT [World Data Center (WDC) for Geomagnetism, Kyoto, http://wdc.kugi.kyoto-u.ac.jp/wdc/Sec3.html]. Since -200 nT < Dst_{min} < -100 nT, this event can be classified as an intense storm [*Gonzalez et al.*, 1994]. At the meantime, the global geomagnetic Kp index reached 7+. To further describe this event, Figure 6-2 illustrates several selected geomagnetic and interplanetary magnetic field (IMF) parameters from 2015/12/19 to 2015/12/21.

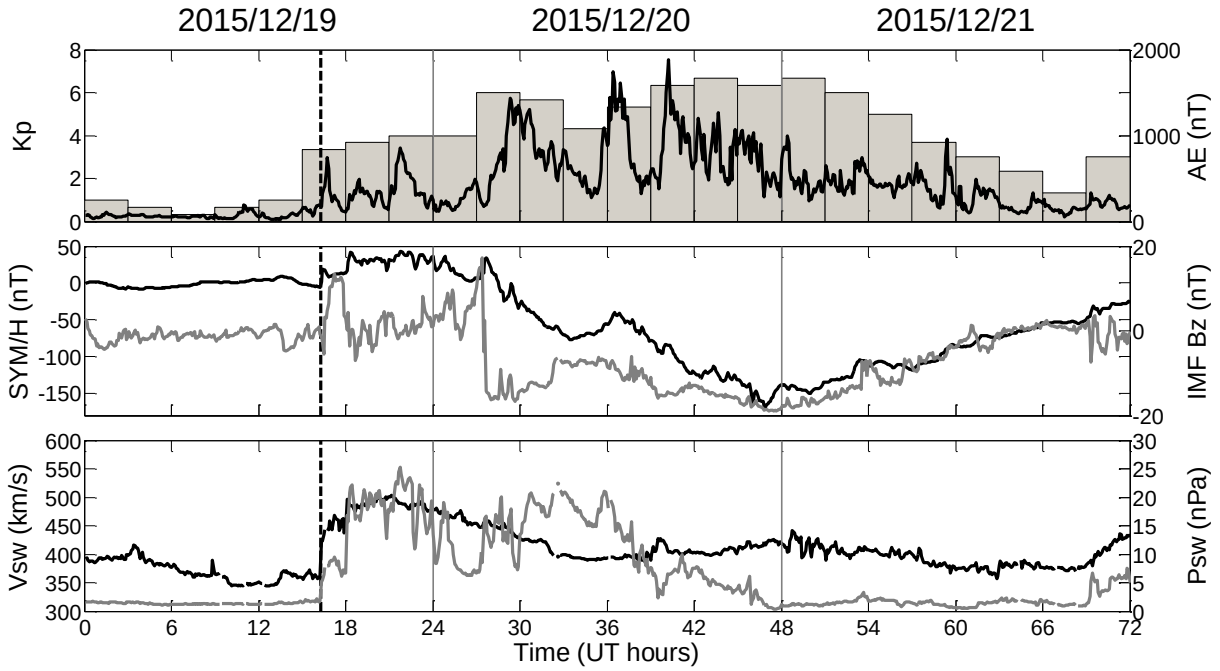

Figure 6-2. Variations of selected geomagnetic and IMF parameters during 2015/12/19-2015/12/21. The vertical dashed line gives the SSC time at 16:16:12 UT on 2015/12/19 [http://www.obsebre.es/en/rapid]. The Kp index is 3-hour averaged. All other parameters are 5-minute averaged. The parameters are further separated into 3 days by the vertical gray lines. In the top subplot, the Kp index is shown by the bar-plot, while the Auroral Electroject (AE) index is shown by the black curve. The middle subplot gives the symmetric (SYM) geomagnetic disturbance index in the horizontal direction (H) in nT (SYM/H, black), as well as the IMF B_Z component in nT (IMF Bz, gray). The bottom subplot gives the Solar wind speed in km/s (Vsw, black), together with the Solar wind pressure in nPa (Psw, gray). The Kp index is obtained from WDC Kyoto Observatory [http://wdc.kugi.kyoto-u.ac.jp/aedir/index.html], while other parameters are acquired through NASA/GSFC's Space Physics Data Facility's OMNIWeb service [http://omniweb.gsfc.nasa.gov/index.html].

In the top subplot of Figure 6-2, the AE index demonstrated small short-term increases following the SSC on 2015/12/19, while much more prominent increases and fluctuations (up to 1883 nT) occurred on 2015/12/20 after ~0300 UT. The Kp index maintained at a high level (between 4 and 7) throughout the main phase of this event. From the middle subplot, the SYM-H index shows a decreasing trend in general until maximum intensity at ~2300 UT on 2015/12/20, with a few upturns indicating substorms [*Lyatskaya et al.*, 2008]. The IMF B_Z component turned northward after the SSC, followed by some fluctuations, until it suddenly turned southward at ~0300 UT on 2015/12/20 and remained southward for more than 30 hours. In the bottom subplot, the solar wind speed shows an abrupt increase at the SSC, along with large fluctuations in the solar wind pressure occurring shortly after and lasting throughout the main phase of the event.

To proceed with the comparative study between GNSS array and PFISR measured drift velocities, the first data period is selected from 00:00:18 to 23:59:53 UT on 2015/12/20. The reasons behind this choice are: (1) both systems have near continuous measurements throughout this period; and (2) strong IMF and geomagnetic activities are captured during this period by Figure 6-2, indicating high potentials for observing ionospheric irregularities on both systems. In fact, according to the International Q-Days (the quietest days) and D-Days (the most disturbed days) service, 2015/12/20 is the most disturbed day in December 2015 in terms of geomagnetic activity [WDC for Geomagnetism, Kyoto, http://wdc.kugi.kyoto-u.ac.jp/qddays/index.html]. As expected, the local magnetometer at Poker Flat observed strong fluctuations during this data period [UAF Alaska Satellite Facility, https://www.asf.alaska.edu/magnetometer]. These measurements are plotted in Figure 6-3, in accordance with the GNSS σ_ϕ measurements.

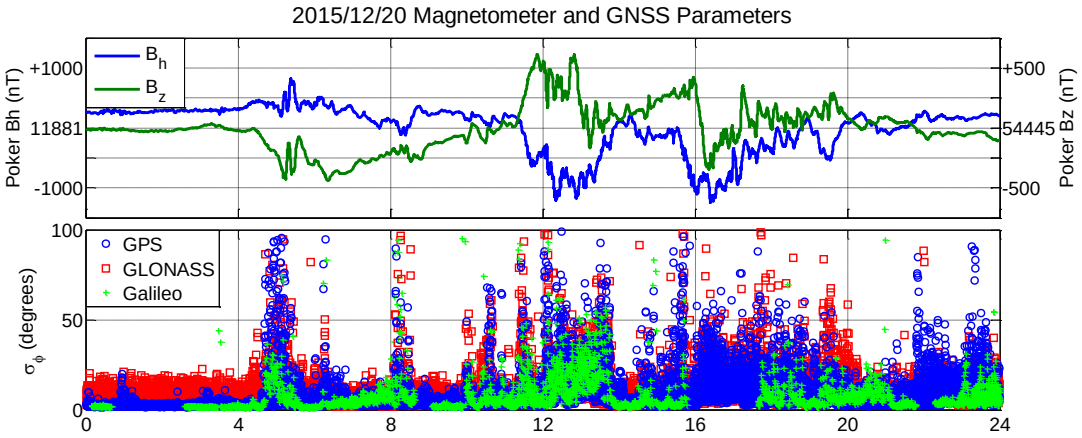

Figure 6-3. Local observations on 2015/12/20 from the Poker Flat Magnetometer and the GNSS array. The top subplot gives the variations of the local B_H component from its mean value in nT (Poker B_h, blue) and the B_Z component (Poker B_z, green). In the bottom subplot, the carrier phase σ_ϕ measurements are plotted for all visible GPS (blue circles), GLONASS (red squares) and Galileo (green plus signs) satellites above 30° elevations. The data resolution is 1 second.

In Figure 6-3, large fluctuations can be observed in both B_H and B_Z components between ~0430 and ~0600 UT, around ~08 UT, and between ~1000 and ~2000 UT. Large disturbances can also be observed in both GPS and Galileo σ_ϕ measurements at these times. The ASI images are also plotted for 2015/12/20 to demonstrate the detected emissions. Figure 6-4 shows the ASI keograms (north-south slices of ASI images at each epoch) for each Poker Flat ASI wavelength.

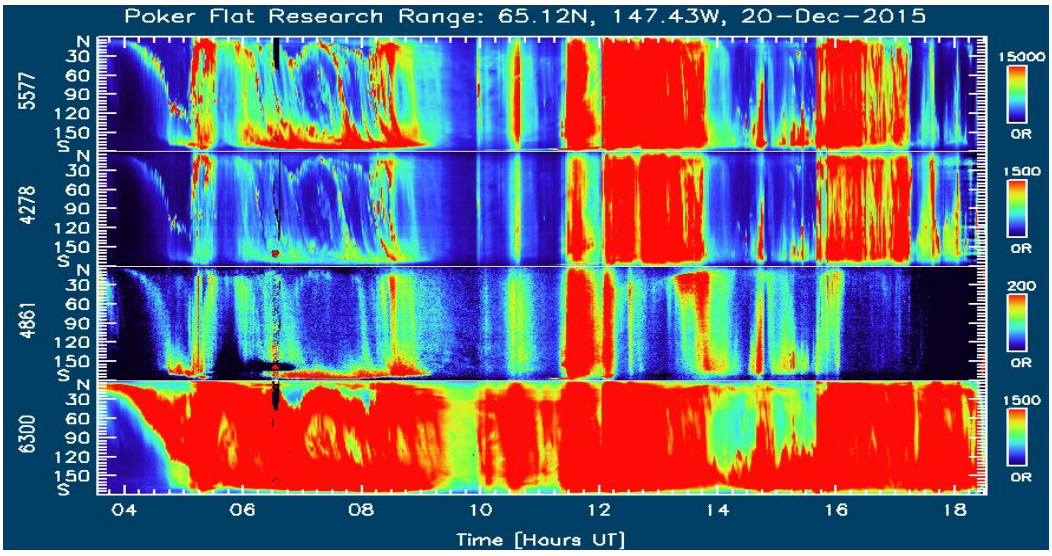

Figure 6-4. ASI keograms of 2015/12/20 at the PFRR from 0330 UT to 1830 UT. The subplots correspond to different measurement wavelength at 557.7 nm, 427.8 nm, 486.1 nm and 630.0 nm, respectively.

In Figure 6-4, consistent results can be observed from all four wavelengths in general, where less particle precipitation is observed at 486.1 nm and the 630.0 nm measurements appear to be under cloudy conditions. Focusing on the 557.7 nm line emission, relatively weak and localized particle precipitation can be observed from ~0500 UT to 0900 UT, while stronger and widely spreading precipitation can be observed between ~1130 UT to 1400 UT, as well as ~1600 UT to ~1730 UT. These results also agree with the event features observed from both the global parameters in Figure 6-2 and the local parameters in Figure 6-4, respectively.

Following the procedures described in the previous sections, the GPS and Galileo carrier phase measurements are used to estimate the irregularity drift velocities. An example of the processed results from 0430 to 0530 UT on 2015/12/20 is plotted in Figure 6-5 as velocity vectors on top of their satellite tracks with σ_ϕ values indicating the phase irregularity strength.

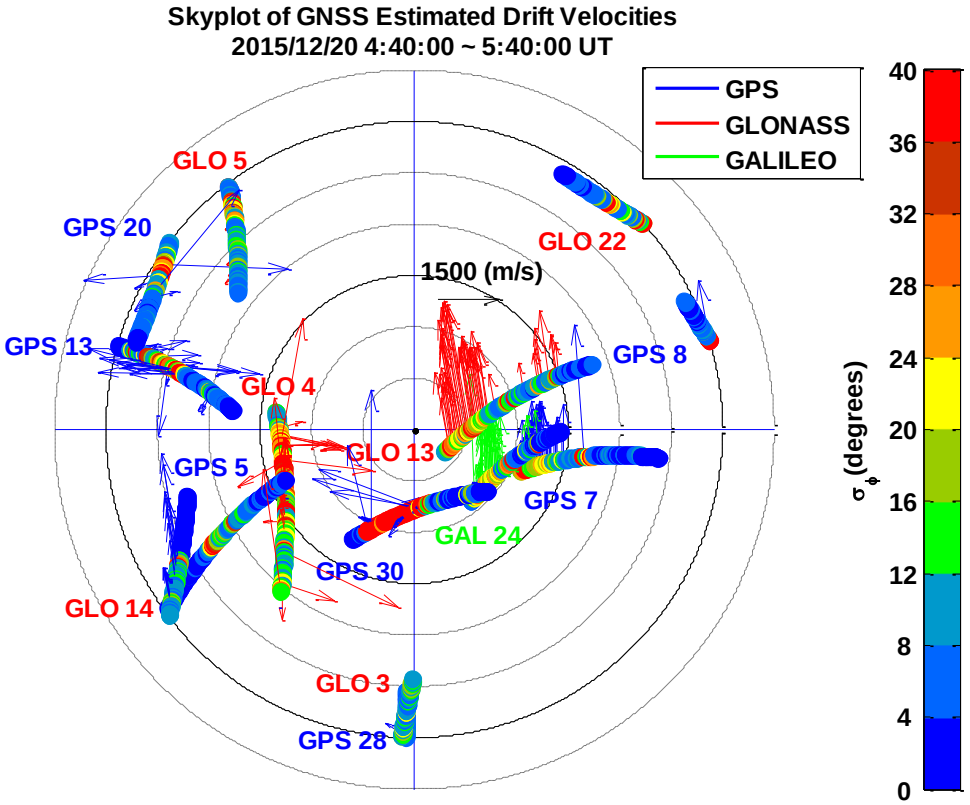

Figure 6-5. Example skyplot of drift velocity estimations from 0440 to 0540 UT on 2015/12/20. The starting location of each satellite is marked by a numbered label (GPS, blue; GLONASS,

red; Galileo, green). The colorbar correspond to the phase scintillation σ_ϕ indices. The estimated drift velocities are illustrated by the quivers, with a reference vector at 1500 m/s pointing eastward.

In this example, 7 GPS satellites (GPS 5, 7, 8, 13, 20, 28 and 30), 6 GLONASS satellites (GLO 3, 4, 5, 13, 14 and 22) and 1 Galileo satellite (GAL 24) were visible above the 30° elevation mask. In the west part of the sky, the irregularity drift pattern appeared to be very turbulent and localized. The irregularity drift velocities were highly variable while GPS 13 and GLO even experienced sudden turns in drift directions. On the other hand, in the east part of the sky, all GNSS satellites experienced northward drift velocities. GPS 7, GAL 24 and GLO 13 all observed dense and consistent drifts in almost the same direction.

6.1.2.2. The 2015/12/31 Event

Another geomagnetic storm event occurred on 2015/12/31-2016/1/1. The SSC was registered at 00:49:36 UT on 2015/12/31 at the ground [Ebre Observatory]. The main phase of this event lasted until ~0130 UT on 2016/01/01, when the Dst index reached as low as -110 nT [WDC for Geomagnetism, Kyoto]. Again, this event can be classified as an intense storm, although slightly less intense than the previously discussed event. The maximum Kp index reached 6. To further describe this event, Figure 6-2 shows the selected geomagnetic and IMF parameters from 2015/12/31 to 2016/1/1. For comparison, 2015/12/30 is included as an example of a quiet-day.

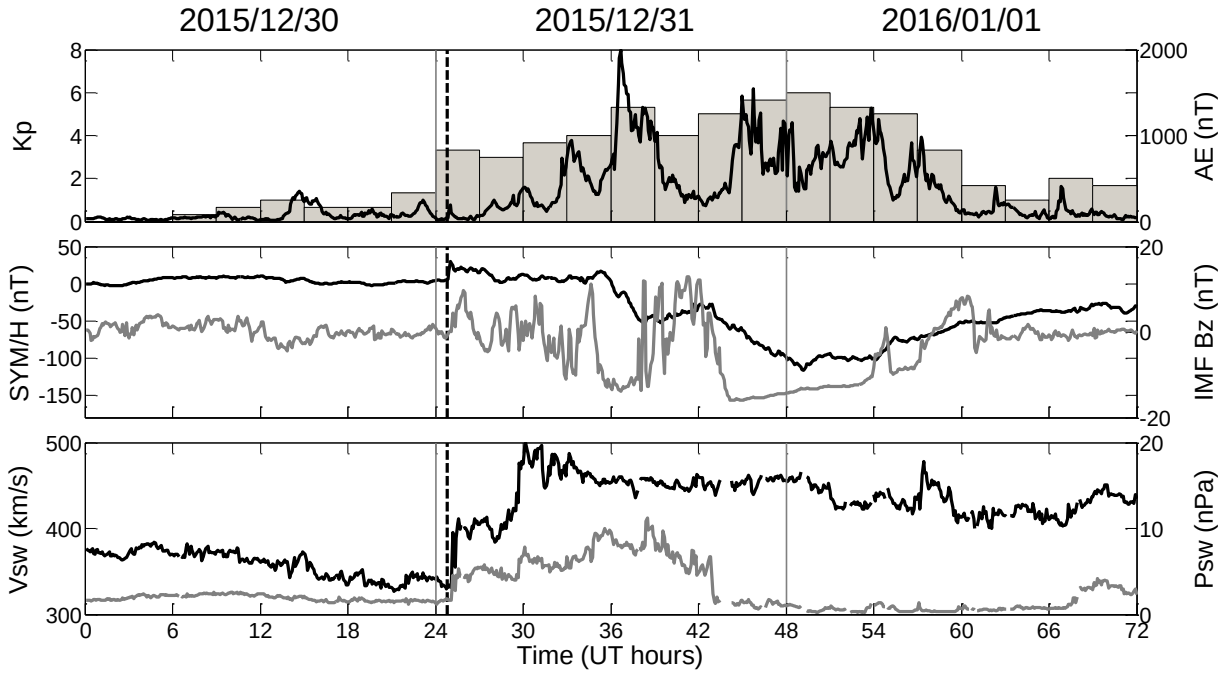

Figure 6-6. Variations of selected IMF and geomagnetic parameters during 2015/12/31-2016/1/1. Refer to Figure 6-2 for the plotting rubrics.

In the top subplot of Figure 6-6, the AE index demonstrated prominent increases and fluctuations (up to 2000 nT) from ~0730 UT on 2015/12/31 to ~1200 UT on 2016/1/1. The Kp index stayed at a high level (between 3 and 6) throughout the main phase of this event. From the middle subplot, the SYM-H index stayed at a high level after the SSC, until ~1130 UT on 2015/12/31, where a general decreasing trend can be observed from then on until reaching maximum intensity at ~0130 UT on 2016/1/1. Large fluctuations in the IMF B_Z component can be observed from the SSC till ~2000 UT on 2015/12/31. In the bottom subplot, two abrupt increases can be observed in the solar wind speed, one at the SSC and the other at ~0600 UT on 2015/12/31. The solar wind pressure also increased at the SSC, and dropped back to nominal values after ~2000 UT on 2015/12/31.

The data period selected for this case study is 00:00:22 to 23:59:57 UT on 2015/12/31. 2015/12/31 is the second most disturbed day in December 2015 in terms of geomagnetic activities

[WDC for Geomagnetism, Kyoto]. The local magnetometer measurements at Poker Flat are plotted in Figure 6-7, in accordance with the GNSS σ_ϕ measurements.

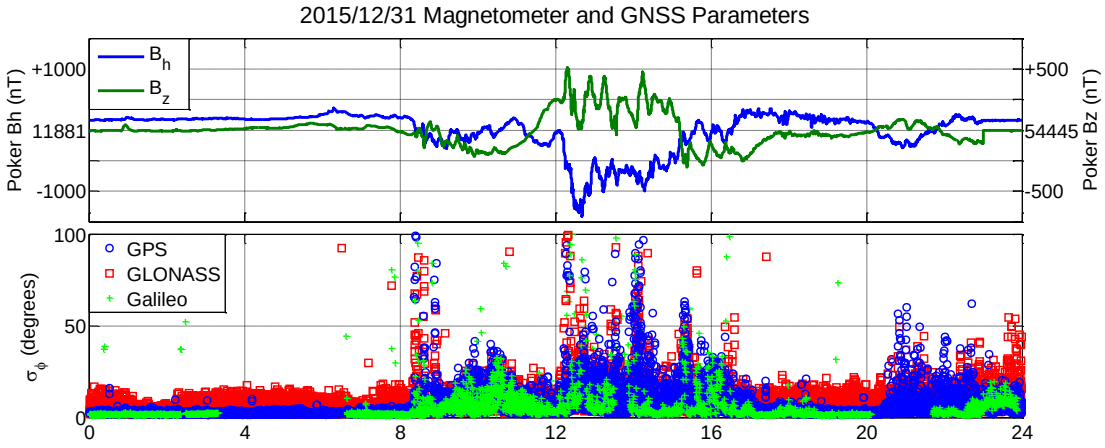

Figure 6-7. Local observations on 2015/12/31 from Poker Flat Magnetometer and the GNSS array. Refer to Figure 6-3 for the plotting rubrics.

In Figure 6-7, large fluctuations can be observed in both B_H and B_Z components between ~0800 and ~1800 UT with smaller fluctuations between ~2000 to 2400 UT. Corresponding disturbances can be observed in both GPS and Galileo σ_ϕ measurements at these times. Similar to Figure 6-4, the ASI keograms are plotted for all Poker Flat ASI wavelengths in Figure 6-8.

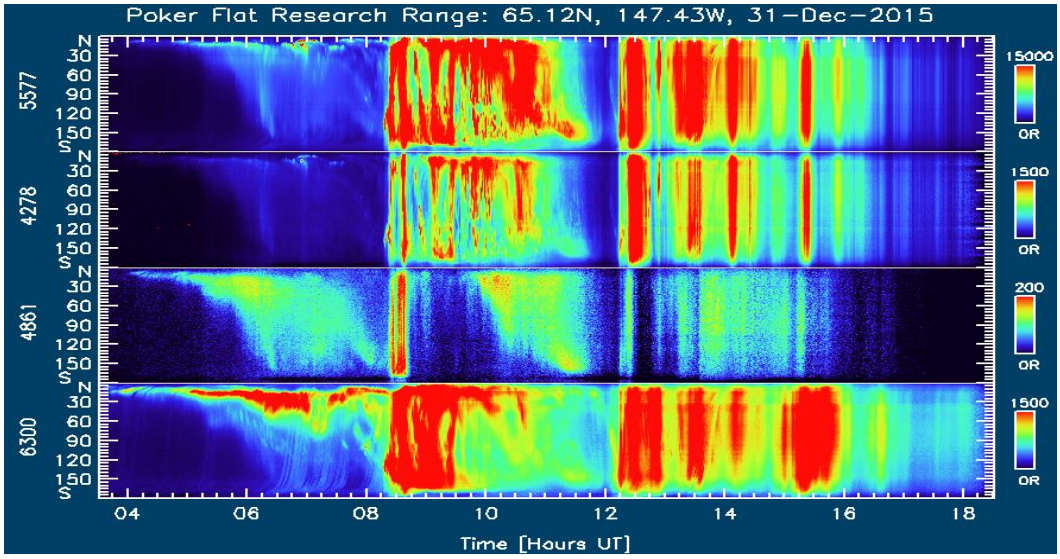

Figure 6-8. ASI keograms of 2015/12/31 at the PFRR from 0330 UT to 1830 UT.

Similar to the 2015/12/20 example, general agreements in the emission features can be observed from all four wavelengths. Focusing on the 557.7 nm, particle precipitation can be observed from ~0830 UT to ~1100 UT and from ~1200 UT to ~1600 UT. Again, these results also agree with the event features observed from both the global parameters in Figure 6-6 and the local parameters in Figure 6-7, respectively

An example of the irregularity drift estimations from 1215 to 1315 UT on 2015/12/31 is plotted in Figure 6-9 as velocity vectors on top of their satellite tracks with σ_ϕ values indicating the phase irregularity strength.

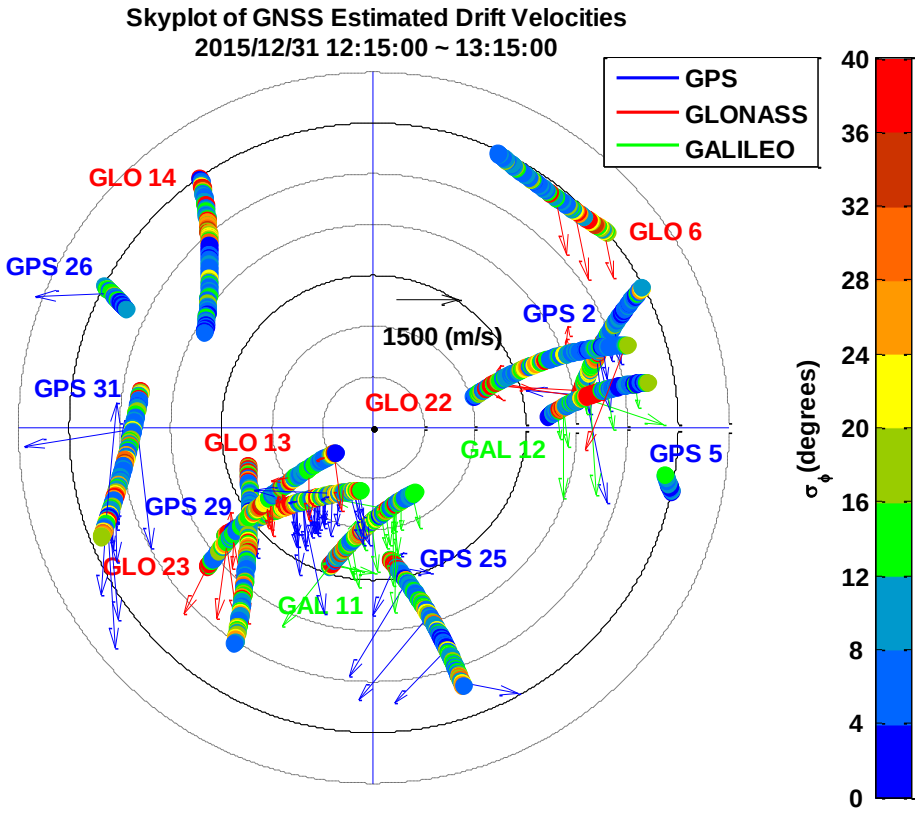

Figure 6-9. Example skyplot of drift velocity estimations from 1215 to 1315 UT on 2015/12/31. Refer to Figure 6-5 for the plotting rubrics.

In this example, 6 GPS satellites (GPS 2, 5, 25, 26, 29 and 31), 5 GLONASS (GLO 6, 13, 14, 22 and 23) satellites and 2 Galileo satellites (GAL 11 and 12) were visible above the 30°

elevation mask. The irregularity drift patterns appeared be converging to the north-to-south direction for both satellite clusters in the south part of the sky and the west-north part of the sky. Again, all GPS, GLONASS and Galileo results show good agreement when the satellite tracks are in the vicinities of each other.

6.2. Error Analysis and Mitigation Techniques

There are several potential error sources in the method described in this study and mitigation methods have been exploited to minimize these errors as part of the integral process during the development of the techniques presented. Below is a summary of these error sources and mitigation techniques.

6.2.1. GNSS Carrier Phase Errors

GNSS carrier phase measurements are estimations generated by receiver PLL. PLL estimated carrier phase errors and carrier phase cycle slips are directly affected by the signal-to-noise ratio (SNR) and can be a major issue for equatorial scintillations when deep signal fading often occur, resulting in 20 dB or more SNR degradation. However, at high latitudes, the observed phase fluctuations are not associated with simultaneous deep fading. Typical observed signal intensity during large phase fluctuations are on the order of a few dB [*Jiao et al.*, 2013], well within the normal performance range of conventional PLL. Because each antenna output is processed by independent PLL tracking channels, the carrier phase noise should be independent from each other and therefore, produce negligible cross-correlations in the technique discussed in this paper.

The receiver oscillator is a major contributor to phase measurement error. For the HAARP array, all three receivers are driven a common high quality, low-phase noise OCXO and the receiver outputs are aligned on a sample-by-sample basis at a 5 MHz sampling rate. Therefore, if there are any prominent phase jitters due to receiver oscillator, they should be synchronized to

within 0.2 μs between antennas. Such a small time lag will be filtered in the phase spectrum correlation product. For the Poker Flat array, all three receivers are driven by the same type of OCXO from the exact same receiver model, Septentrio PolaRxS. Again, these receiver oscillators are of high quality and low-phase noise, and are synchronized to the GPS Time.

Likewise, satellite oscillator plays an as important role as the receiver oscillator. The GNSS constellations used in this dissertation are GPS, GLONASS and Galileo. Among them, GPS and Galileo satellites show comparable phase errors under nominal signal conditions, indicating comparable satellite oscillator performance. But this is not the case for GLONASS satellites, whose phase noise is often much higher. This issue is demonstrated by Figure 6-10.

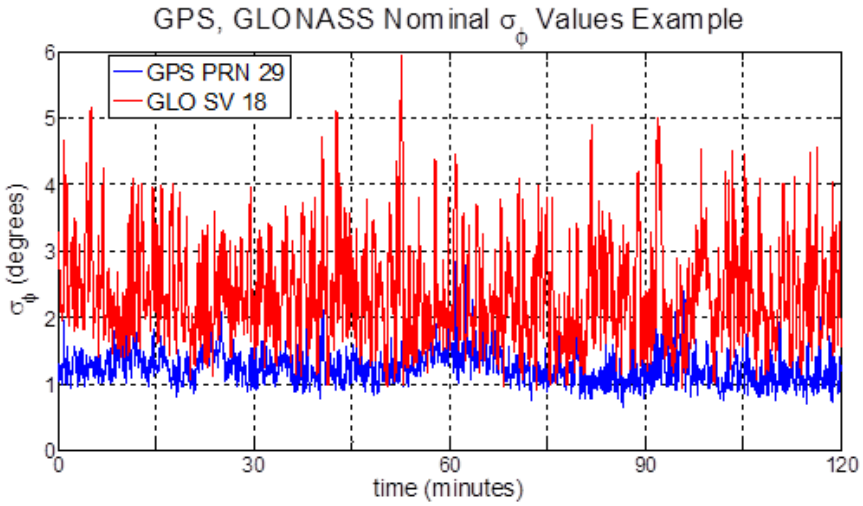

Figure 6-10. Comparison of 2-hour nominal σ_ϕ values on GPS L1 and GLONASS L1 signals from 2012/10/09 19:26:40 UTC at Antenna 1. GPS PRN 29 is shown in red, while GLONASS SV 18 is shown in red. Frequency scaling is applied on GLONASS L1 to match with the GPS L1 measurement.

In Figure 6-10, both data sets are taken during quiet background ionosphere conditions. GPS PRN 29 (blue) traveled from 22º to 76 º elevation angles, while GLONASS SV 18 (red) traveled from 24º to 86º. After carrier phase detrending, the baseline GPS σ_ϕ values slightly fluctuate between 0.7º to 3º, mostly between 1º to 2º, while the baseline GLONASS σ_ϕ values

demonstrate a much larger variation between 1º and 6º, mostly between 1º to 4º. Both the magnitude and variation in the σ_ϕ values of GLONASS satellites are much higher than those of the GPS counterparts. To address this issue, the scintillation strength threshold for GLONASS is set to be 15°, a 3-degree increase from the GPS/Galileo σ_ϕ threshold.

Multipath could be another potential error source. In this study, however, only high elevation satellites which are less susceptible to multipath are used for evaluations. Furthermore, reflective multipath due to objects in the local environment follows a near 24-hour repetitive pattern due to the periodic nature of the GPS satellite orbit. Such repetitive pattern was not found for the phase fluctuation events presented in this study.

Cycle slips may also cause phase errors up to millions of cycles. A cycle slip detection and repairing algorithm suitable for high rate phase measurements has been demonstrated in Section 5.3. The accuracy in the repaired ADR sample is within ±0.5 cycles. To ensure phase measurement integrity, correlation results associated with the detected cycle slips are discarded in the later processes. This would minimize the impact of cycle slips in later detrending process.

As discussed in Section 5.4, the carrier phase detrending process may exaggerate fluctuations caused by ionospheric irregularities. On one hand, this does not have negative impacts on the front velocity model, since the peak correlation indices stay the same, as long as the exact same detrending process is applied to all receivers in the array. On the other hand, the anisotropy model would be affected, since inaccurate detrended phase would lead to distorted correlation surfaces.

6.2.2. Joint Time-Frequency Analysis Error

The APT algorithm has been tested using various simulation data to demonstrate its performance in finding the optimal window length of a coherent spectrum [*Wang*, 2013]. Its

temporal resolution directly determines the time lag precision. It is interesting to note that the "signals" of interests here are the phase fluctuations; therefore, the APT spectral error decreases as the level of ionospheric induced phase fluctuation increases. Noisy APT spectra, such as the ones observed on Antenna 2 in the HAARP setup, result in lower correlation coefficients, leading to difficulties in identifying persistent irregularity patterns across the antenna array, and hence cause errors in time lag estimations. By using higher thresholds, estimates from noisy spectra are filtered, reducing the availability of measurements and hence reducing the temporal resolution. However, the question remains as what is an acceptable correlation threshold? Without the knowledge of the true irregularity drift velocity, it is difficult to have a quantitative answer. Nevertheless, the algorithm seems to produce estimates that are self-consistent, in the sense that the estimates for neighboring satellites are similar to each other. Also, as will be presented in Section 6.3, the algorithm is self-consistent across different GNSS signals towards higher scintillation strength [*Wang et al.,* 2015].

To improve APT spectrum quality, it is necessary to optimize the receiver hardware setup (reduce the cable length to minimize signal loss and use a low phase noise oscillator) and software receiver signal processing algorithms. The cable length issue has been resolved in the Poker Flat array setup.

6.2.3. Irregularity Height Error

For the Poker Flat GNSS array, the peak electron density height, h_mF_2, can be directly obtained from the electron density (Ne) profiles measured by the PFISR. Figure 6-11 shows the Ne profile from the PFISR's zenith beam on 2015/12/20.

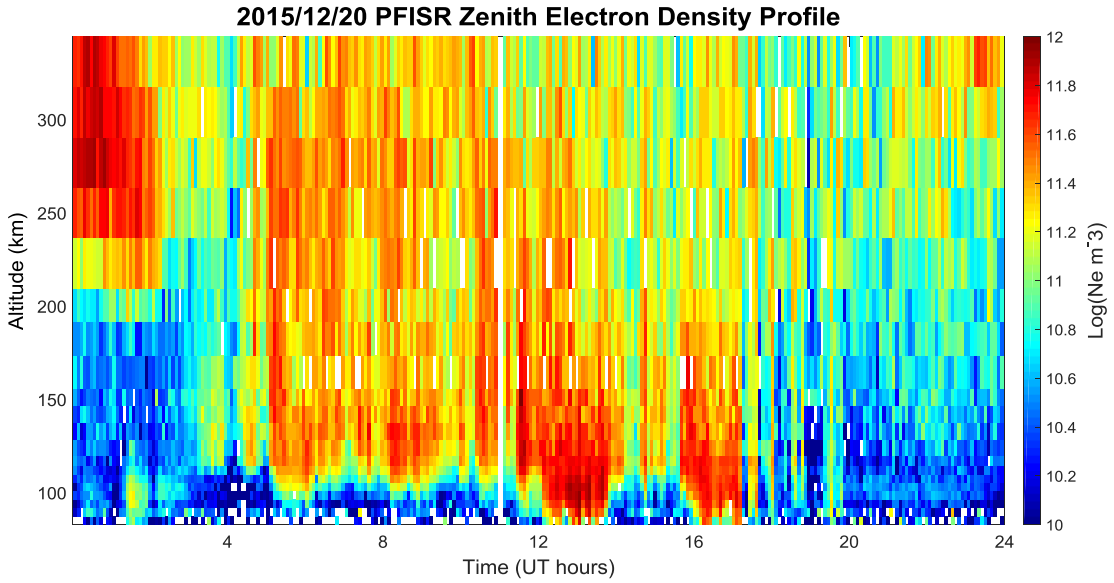

Figure 6-11. PFISR zenith beam Ne profile on 2015/12/20 from 85 km to 344 km using alternating code measurements. The color code corresponds to the log-scaled electron density values. The white strip at ~1100 UT is an intermission between two PFISR experiments.

In Figure 6-11, the ionospheric irregularity altitudes can be identified from enhancement (warmer colors) and depletion (colder colors) regions in the Ne profiles. The irregularities occurred at various heights from ~0400 to ~2000 UT during local night time, mostly concentrated towards lower altitudes around 120 km. During local day time, the irregularities raised to higher altitudes around 300 km. A direct observation from Figure 6-11 is that irregularities can be spread over a wide range of altitude and their heights may not be well-defined.

The above example shows that even when Ne profiles from an incoherent scatter radar is available, it may still be challenging to correctly identified the ionospheric irregularity altitudes from the depletion/enhancement regions. Hence the questions remain: What altitude assumption should be used and how does that effect the irregularity drift velocity estimates? In this study, we take a more inclusive approach by considering a range of irregularity altitudes when calculating drift velocities. We then derive the drift velocity range corresponds to the altitude range.

Sojka et al. [2009] showed that the h_mF_2 values over the PFRR are typically between 175 km and 350 km, concentrated around 250 km. The h_mF_2 increases in local summer and decreases in local winter, associated with the seasonal changes in insolation. But phase scintillations often occur during active conditions, where the local h_mF_2 has been observed to reach 400 km [*Zou et al.,* 2013], while E region irregularity around 100 km is not uncommon [*Sojka et al.*, 2009; *Wang and Morton*, 2017]. Based on these past observations, we set the boundary irregularity altitudes to be [100km, 400 km] for the Poker Flat array. For the HAARP array, this boundary is set to be [150km, 450 km] considering the HAARP site is at a lower latitude.

Data from 2015/12/20 is processed under two irregularity altitude assumptions of 100 km and 400 km. The variations in the estimated drift velocities are analyzed from two aspects: the absolute velocity differences, and the percentage differences relative to results under 100km and 400 km altitude assumption. Meanwhile, elevation masks at 30°, 45° and 60° are employed to demonstrate the impact of satellite elevation angles. The results are shown in table 6-1.

Table 6-1. Percentage fraction of absolute and relative velocity variations under different irregularity altitude assumptions that would fall within certain numerical bounds; for different choices of elevation threshold and size of the bounds

Elev.	Absolute Variations			Percentage Variations (100 km / 400 km)		
	±50 m/s	±100 m/s	±200 m/s	±5%	±10%	±20%
30°	54.1%	72.8%	85.1%	56.5% / 53.6%	71.1% / 74.5%	88.5% / 84.5%
45°	61.5%	80.2%	89.6%	58.3% / 56.3%	77.1% / 82.3%	93.8% / 88.5%
60°	74.2%	93.6%	100%	64.3% / 64.5%	83.9% / 90.3%	100% / 100%

In Table 6-1, take the 100% entry under the Absolute Variations for example, the result shows that the velocity differences between 100 km and 400 km assumptions are all (100%) within ±200 m/s for satellites above 60° elevations. It can be observed that the velocity variations caused

by different irregularity altitude assumptions become smaller towards higher elevation angles. For satellites above 60° elevations, all velocity estimations can be expected to be within ±200 m/s, or ±20% of the truth. For satellite above 45° elevations, nearly 90% of the velocity estimations are within 20% or 200m/s of the true values. The percentage values drop to between 84 and 89 for 30° elevation. Table 6-1 indicates that the irregularity altitude assumption does not play a critical role in the estimated irregularity drift velocity when for satellites at high elevations. Figure 6-12 illustrates this elevation impact on altitude sensitivity of the resulting drift velocity estimations.

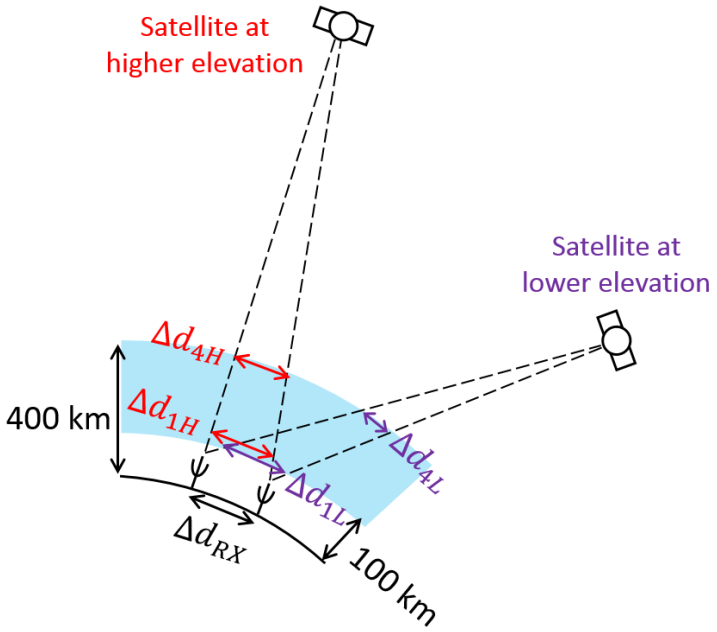

Figure 6-12. Illustration of elevation impact on altitude sensitivity of drift velocity estimation. The blue layer represents the ionosphere with altitude extending from 100 km to 400 km. $\boldsymbol{\Delta d_{RX}}$ marks the receiver distance. The red labels mark the sub-ionospheric distances of the receivers at 100 km ($\boldsymbol{\Delta d_{1H}}$) and 400 km ($\boldsymbol{\Delta d_{4H}}$) for the satellite at higher elevation, while the purple labels mark the lower elevation counter parts ($\boldsymbol{\Delta d_{1L}}$ and $\boldsymbol{\Delta d_{4L}}$).

In Figure 6-12, $\boldsymbol{\Delta d_{1H}}, \boldsymbol{\Delta d_{4H}}, \boldsymbol{\Delta d_{1L}}$ and $\boldsymbol{\Delta d_{4L}}$ represent the sub-ionospheric distances between ionospheric pierce points (IPPs) of the two GNSS receivers under different irregularity altitude assumptions. Under typical GNSS satellite-receiver geometry, orbit altitude $\gg$ IPP altitude. As a result, the relationship $\boldsymbol{\Delta d_{1H} \approx \Delta d_{4H} \approx \Delta d_{1L} > \Delta d_{4L}}$ holds. This supports the

observation from Table 6-1 that altitude of irregularity does not have a significant impact on drift velocity estimations for satellites with relatively high elevation.

6.2.4. Coordinate Transformation Error

When cross-comparing the GNSS estimations against PFISR measurements, the results are eventually transformed into the geomagnetic coordinate system from the local East-North-Up coordinate system. The coordinate transformation algorithm is given as the following [*Heinselman and Nicolls*, 2008]:

$$v_{pe} = v_e \cos\delta + v_n \sin\delta \quad (6\text{-}1)$$

$$v_{pn} = v_z \cos I + \sin I\,(v_n \cos\delta + v_e \sin\delta) \quad (6\text{-}2)$$

$$v_{ap} = v_z \sin I - \cos I\,(v_n \cos\delta + v_e \sin\delta) \quad (6\text{-}3)$$

where v_e, v_n and v_z are the local East, North and Up velocity components, and v_{pe}, v_{pn} and v_{ap} are the geomagnetic Perpendicular North, Perpendicular East and Anti-Parallel velocity components. δ is the geomagnetic declination angle and I is the dip angle (also known as the inclination angle). These angles can be estimated using the IGRF model. For the Poker Flat site, δ is around 22° and I is around 77.5° [*Heinselman and Nicolls*, 2008].

The spaced-receiver technique only estimates the horizontal velocity components. In practice, v_z is often assumed to be zero. As a result, the Perpendicular North component is prone to error due to the uncertainty in the local Up velocity components. To further investigate this transformation error, we resorted to the raw PFISR vector velocity measurements, which provides information on the anti-parallel velocities as well as the error terms associated with them. An example of the PFISR measurements is shown in Figure 6-13.

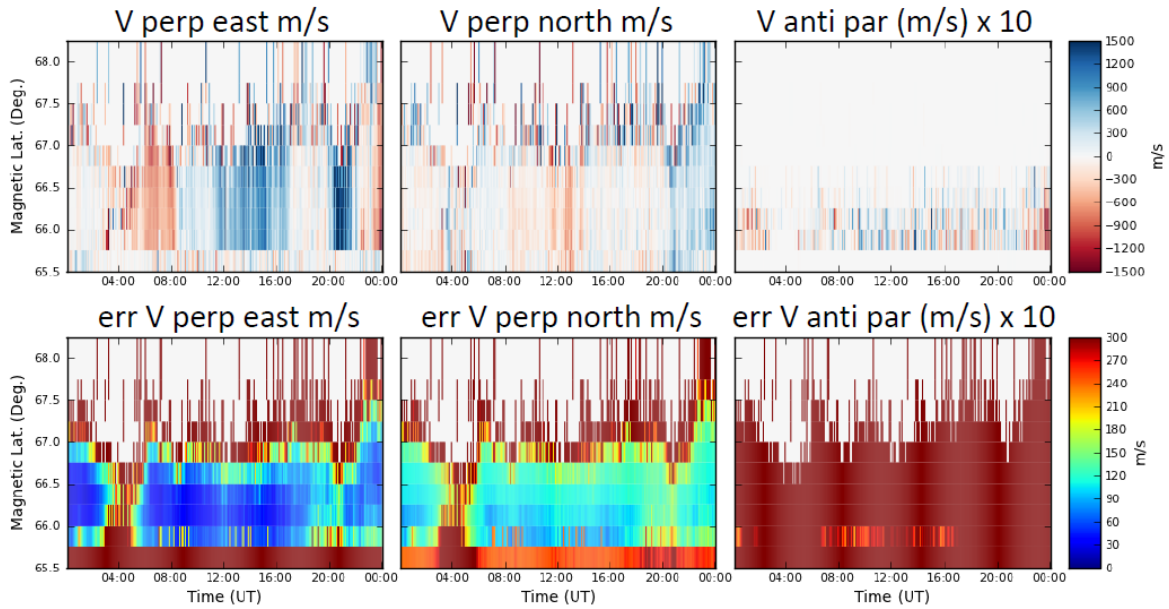

Figure 6-13. Example PFISR vector velocity measurements with associated error terms from 2015/12/31 00:04:44 to 2016/1/1 00:03:22 UT. The two rows from top to bottom show the velocity and velocity error values, while the three columns from left to right show the perpendicular east direction (V perp east), the perpendicular north direction (V perp north), and the anti-parallel direction (V anti par), respectively. The velocity and velocity error values for V anti par are multiplied by 10 for better visual representation. The color bars represent the values for the velocities and velocity errors, respectively. The latitudinal resolution is 0.25° for all subplots.

In Figure 6-13, the velocity values in both v_{pe} (V per east) and v_{pn} (V perp north) directions have large variations, while v_{ap} (V anti par) maintains at small values around zero. v_{pe} and v_{pn} values are higher towards higher latitudes and from 65.5°N to 65.75°N. Note that in the bottom 2-D vector velocity plot, v_{pe} and v_{pn} are filtered too exclude velocities associated with large errors.

Focusing on the anti-parallel direction, both the v_{ap} values and the v_{ap} error terms appears to be relatively large at first glance. However, one must keep in mind that those values have been purposely multiplied by a factor of 10 to enhance visual representation. Through examining the original values from the Madrigal Database, the actual v_{ap} and v_{ap} errors values are found out to be no more than 50 m/s throughout the measurement period. Meanwhile, the

geomagnetic dip angle over the PFISR site is close to 90°, meaning that the impact of the v_z component would be reasonably small on the v_{pn} and v_{ap} components in Equations 6-2 and 6-3. Combining this remark with the small values of v_{ap} and v_{ap} errors observed by the PFISR, a conclusion can be drawn that the potential errors caused by the coordinate transformation should not be significant. A similar conjecture can be deduced from the 2015/12/20 data set. Note, however, even though this conclusion is applicable to these particular events at the Poker Flat site, it's not necessarily the case for the general problem.

6.3. Inter-Frequency Self-Consistency Check

When GNSS signals from different frequency bands traverse from a satellite to the receiver array, the drift velocities estimated from them are expected to be very close. This is because even though the signals correspond to different irregularity scales, they have the same traversing paths through the same background ionosphere. Based on this premise, a self-consistency study is conducted upon the estimated results from various GNSS signals to investigate the validity of this spaced-receiver approach. The similarities/differences in the diffraction patterns caused by irregularities structures at different wavelengths and scales are examined. Data sets from collected by the HAARP array are used for this study. Hence the TFDM is applied.

Referring to Table 2-1, the HAARP data collection system has simultaneous GPS L1 and L2C capability at each antenna, as well as GPS L1/L2/L5 and GLONASS L1/L2 capability between Antenna 1 and Antenna 3. Provided that the signals are of the same format, the spaced-receiver technique can be easily applied to these GNSS signals. The subsections below are dedicated to the estimation results of the irregularity drift velocity between GPS L1 and L2C bands across all antennas, as well as the results between Antennas 1 and 3 on GPS L1/L2/L5 and GLONASS L1/L2.

6.3.1. *GPS L1 vs. GPS L2C*

From the scintillation data set observed at the HAARP array, 4 triggered phase fluctuation events are further selected for the self-consistency study between GPS L1 and L2C signals. These data sets contain strong phase fluctuations on most of the satellites throughout the events. The detailed event date and times, duration, and data availability are specified by Table 6-2.

Table 6-2. Phase fluctuation events with L2C availability.

Date	Starting Time (UT)	Duration (minutes)	GPS L2C (PRN)
2012/11/14	08:51:00	15	5, 7
2013/03/17	09:05:54	14	25, 29, 31
2013/03/17	10:17:10	15	5, 25, 29, 31
2013/03/17	19:08:30	28	1, 17, 31

By applying the spaced-receiver techniques, the GPS L1 and L2C irregularity drift velocities are estimated. An example sky vector plot is produced from the last event on 2013/03/17.

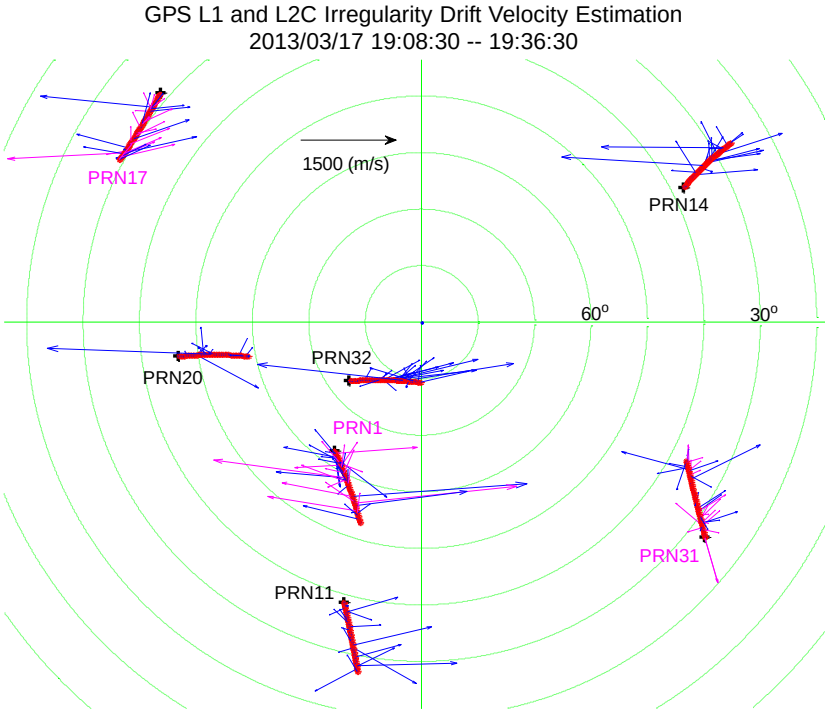

Figure 6-14. Skyplot of irregularity drift velocity estimation based on GPS L1 and L2C measurements from 19:08:30 to 19:36:30 UT on 2013/03/17. Blue arrows represent L1 estimates, while pink arrows represent L2C estimates. The satellites with L2C signals are marked by pink PRN numbers. The satellite paths are shown in red started by the black plus signs.

Figure 6-14 shows the sky vector plot of irregularity drift velocity estimation based on both GPS L1 (blue) and L2C (pink) measurements. Most of the L1 estimated drift velocities agree with the L2C estimations. This is an expected outcome although disagreements between the estimates between L1 and L2C do exist.

There are several possible explanations for these discrepancies. First, due to the dispersive nature of the ionosphere, the two signals may have taken two slightly different paths that have different background drift velocities. In this case, the algorithm still provides the desired outcome, but other instruments with vertical sensing ability need to be employed to further investigate these results. Second, the ionospheric irregularity patches travel and evolve too fast to be measured by the system. In this case, neither the L1 nor the L2 estimation result is reliable. And lastly, the phase fluctuations may not be strong enough to provide high enough SNR for the algorithm to produce compelling results.

A classifying metric is required to differentiate these similarities and differences according to the strengths of the events. The commonly used phase scintillation index, σ_ϕ is employed to categorize these phase fluctuation events on the two GPS bands. Note that a phase fluctuation event of certain σ_ϕ value on GPS L1 band and an event on GPS L2C band of the same σ_ϕ value do not imply the same level of event strength. Instead, for weak scintillation, GNSS phase scintillation index follows the inverse frequency power law, which leads to the following relationship [*Rino*, 1979; *Morrissey et al.*, 2004]:

$$\frac{\sigma_\phi(t)_{RF1}}{\sigma_\phi(t)_{RF2}} = \frac{f_{RF2}}{f_{RF1}} \qquad (6\text{-}4)$$

where $\sigma_\phi(t)$ is the received σ_ϕ measurement at time t, $RF1$ and $RF2$ represent the different GNSS radio frequency signals, and f is the carrier phase frequency.

According to the frequency relationship, an event with 12º σ_ϕ on GPS L1 will have a response of 15.4º σ_ϕ on GPS L2C. Figure 6-15 illustrates such a property using real scintillation measurements.

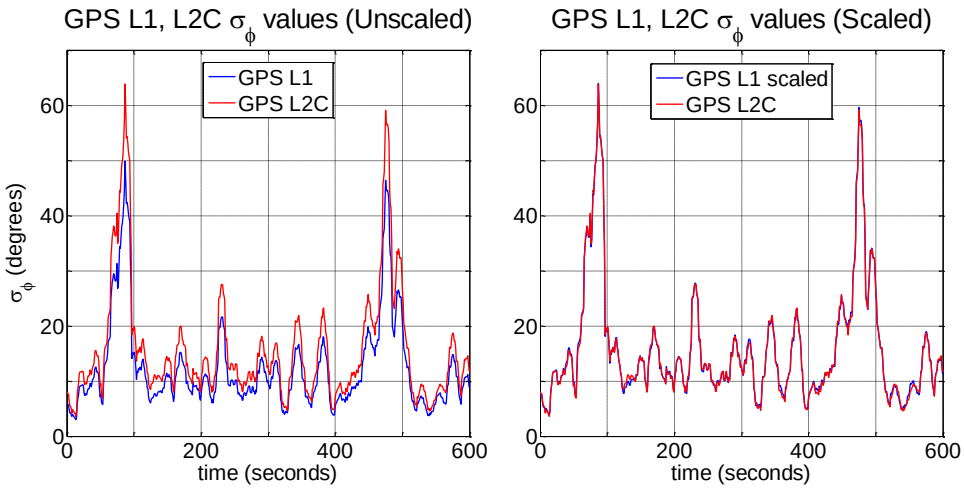

Figure 6-15. Example of σ_ϕ values of GPS L1 and L2C phase measurements from 2013/03/17 19:08:30 on PRN 1. The subplot on the left are the original σ_ϕ values of the two bands. The subplot on the right gives the GPS L1 σ_ϕ values scaled up by 154/120 to match with the GPS L2C band.

In Figure 6-15, the left panel shows direct phase scintillation index σ_ϕ values for GPS L1 (blue) and L2C (red) on March 17, 2013 in Alaska. The right panel shows the same GPS L2C σ_ϕ values and scaled version (by a factor of 154/120) of GPS L1 σ_ϕ values. The scaled GPS L2C and original GPS L1 σ_ϕ values show remarkable agreement. This property of phase measurements is particularly useful when describing and associating the phase fluctuation strengths from different GNSS bands. In order to categorize the levels of the phase fluctuation events for a particular GNSS band, certain σ_ϕ threshold can be employed as the cutoff value. By scaling the phase measurements from all other GNSS bands to this particular frequency band, this σ_ϕ value can also serve as a uniform benchmark in describing the same level of phase fluctuations at all other GNSS bands. In the rest of this paper, all phase calculations are scaled to the equivalent

GPS L2C band. The carrier frequency ratio can be derived from Table 6-3 to be appeared later in this section.

In order to classify the drift velocity estimations, and to establish relationship between the two GPS bands, scatter plots comparing L1 and L2C velocities are generated using all 4 events. The result is illustrated by Figure 6-16.

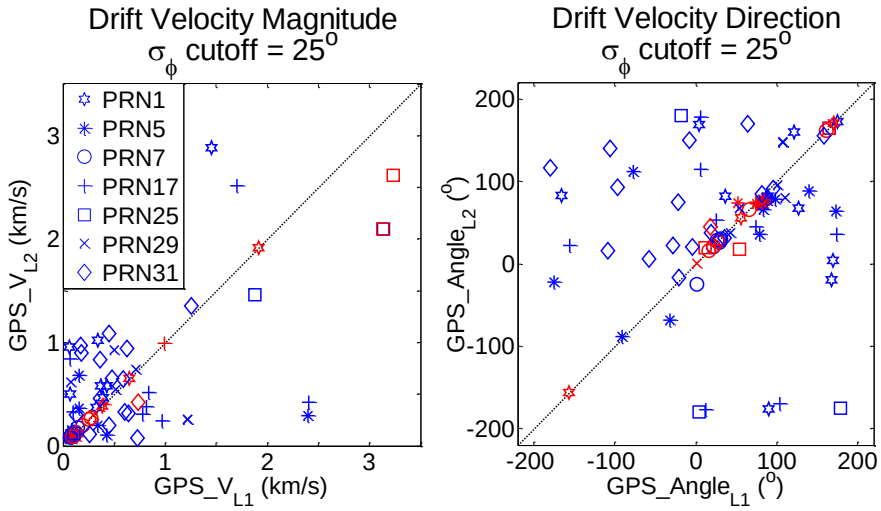

Figure 6-16. Scatter plots of L2C vs. L1 irregularity drift velocity estimations based on data sets in Table 6-2. The subplot on the left shows the velocity magnitude, while the subplot on the right shows the direction of the velocity with respect to due north. An L2C σ_ϕ cutoff is chosen at 25°. Any velocity estimation corresponds to a higher σ_ϕ value is plotted in red. The dashed lines have unity slopes, indicating where L1 and L2C results match with each other.

In Figure 6-16, the GPS L1 estimated irregularity drift velocity magnitude (left) and direction (right) is plotted against their counterparts from GPS L2C estimations. A σ_ϕ cutoff is chosen at 25° to distinguish between the stronger events (red) from the weaker ones (blue). The unity dashed lines in both subplots indicate where L1 and L2C results match. From Figure 6-16, it can be observed that the correlation between L1 and L2C estimation results are weak at lower σ_ϕ values, but fairly strong at higher σ_ϕ values. The 25° cutoff is chosen specifically to support this argument. If the cutoff value is too low, then more scattered points will occur off the unity line. If

it is chosen too high, then the red points will become very sparse. From the left subplot, the magnitudes of most of the drift velocities lie within the [0 1000] m/s range. From the right subplot, two clusters of velocity angles can be observed around 30º and 80º. After carefully examining each piece of data, both clusters can be traced back to the satellites from 2012/11/14. The first cluster (30º east from due north) appears to be mostly contributed by PRN 7, while the second cluster (80º east from due north) appears to be mostly contributed by PRN 5. Both satellites experienced large scale phase fluctuations during that time on 2012/11/14. They both demonstrated good consistency in the velocity directions with relatively low velocity magnitudes (100 to 250 m/s).

Note that Figure 6-16 only applies for the estimations containing simultaneous Antennas 1, 2 and Antennas 1, 3 components, since the 2-D velocity measurements requires simultaneous estimations in both directions. As a result, a lot of useful information from a solitary component might be discarded when there are no concurrent estimations. For this reason, another pair of scatter plots is generated from Antenna 1, 2 and Antenna 1, 3 estimations, respectively. Figure 6-17 illustrates the results, adopting the same L2C σ_ϕ cutoff value at 25º.

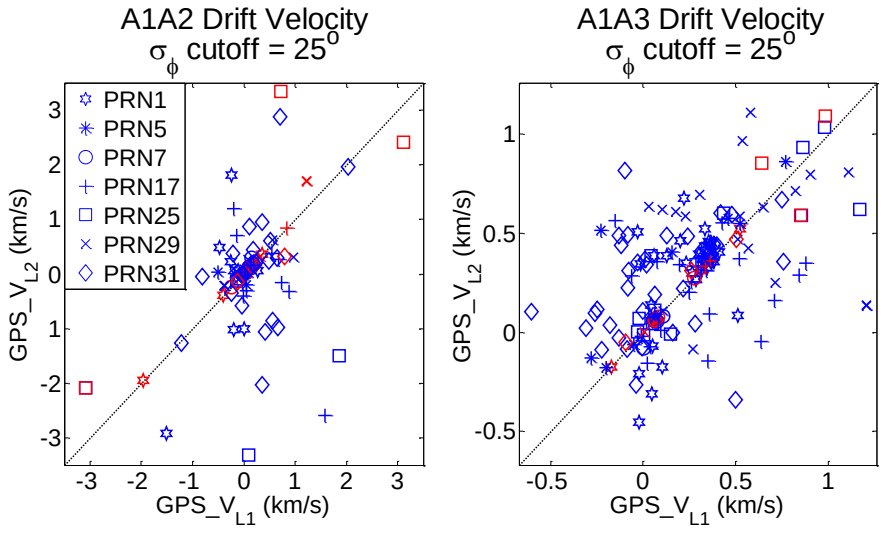

Figure 6-17. Scatter plots of L2C vs. L1 irregularity drift velocity estimations across different two antenna pairs based on data sets in Table 6-2. The subplot on the left shows the Antenna 1, 2 estimation results, while the subplot on the right shows the Antenna 1, 3 results.

In Figure 6-17, the GPS L1 estimated irregularity drift velocity across Antennas 1 & 2 (left) and across Antennas 1 & 3 (right) is plotted against their counterparts from GPS L2C estimations. Similar to previous observations, estimations correspond to higher σ_ϕ demonstrate better consistency between GPS L1 and L2C results in both antenna pairs. From the left subplot, the drift velocities seem to scatter around 0. From the right subplot, most of the results lie in the upper right corner, which corresponds to an eastward drift.

6.3.2. GPS L1 vs. L2C vs. L5 and GLONASS L1 vs. L2

To further study the relationships across different GNSS bands, another triggered phase fluctuation event is selected for irregularity drift velocity estimation across Antennas 1 and 3, 1 hour from 05:00:00 UT on 2012/10/09. This data set contains strong phase fluctuations across most of the GPS and GLONASS satellites throughout the event. Meanwhile, the signal condition across Antennas 1-3 pair is much better than that on Antennas 1-2 pair. Table 6-3 lists the satellites above 30º elevation angles for all available signals at the receivers during this event, as well as the carrier frequencies of the signals. Note that the GLONASS frequencies listed here is the center frequencies of the FDMA signals.

Table 6-3. Visible satellites and signal carrier frequencies for the event from 05:00:00 to 06:00:00 UT on 2012/10/09.

Signal	Carrier Frequency	SV number
GPS L1	1575.42 MHz	1, 11, 14, 20, 32
GPS L2C	1227.60 MHz	1
GPS L5	1176.45 MHz	1
GLONASS L1	1602.0 MHz	5, 6, 7, 15, 21, 22
GLONASS L2	1246.0 MHz	5, 6, 7, 15, 21, 22

Similar to the previous data treatment, all carrier phase measurements are scaled towards the GPS L2C frequency at 1227.60 MHz. For the FDMA signals on GLONASS, each satellite has

varied carrier frequency based on its frequency slot. For GLONASS L1, $f_{L1} = 1602 + n \times 0.5625$ MHz, where $n = -7, -6, \ldots, 0, \ldots, 5, 6$. For GLONASS L2, the frequency step is 0.4375 MHz. Comparing to the magnitude of their center frequencies; the slight variation in each signal frequency is negligible for the purpose of this study. Therefore, the σ_ϕ scaling is only based on the center frequencies on GLONASS signals.

Referring to Table 6-3, the only satellite with all three GPS frequency bands is PRN1. Multi-band irregularity drift velocities across antennas 1 and 3 are estimated for this GPS satellite. Three scatter plots cross-comparing GPS L1, L2C and L5 velocities are generated as in Figure 6-18. The same σ_ϕ cutoff is adopted to be equivalent to 25º on GPS L2C. The other frequencies are scaled to the L2C frequency band accordingly.

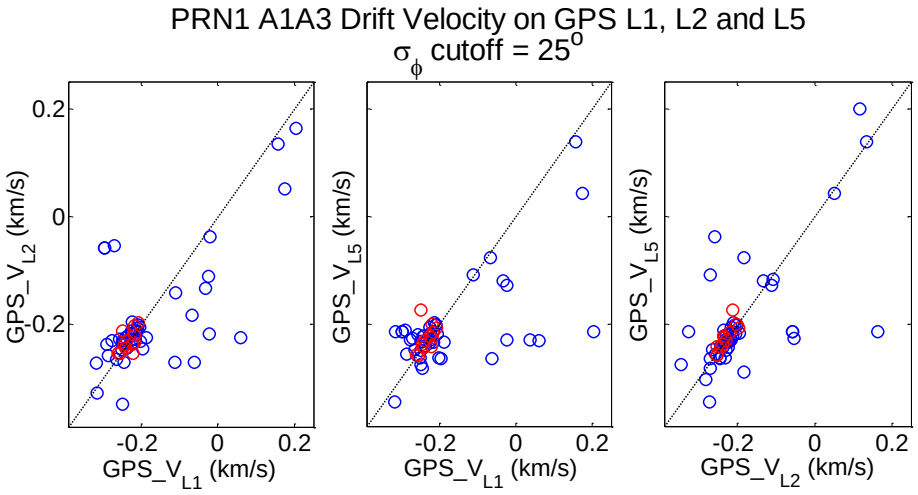

Figure 6-18. Scatter plots of GPS L1 vs. L2C vs. L5 irregularity drift velocity estimations across Antennas 1 & 3 from 05:00:00 UT to 06:00:00 UT on 2012/10/09, GPS PRN1. The left subplot shows the GPS L1 vs. L2C estimation results, the middle subplot shows L1 vs. L5 results, and the right subplot shows L2C vs. L5 results. The σ_ϕ cutoff is at 25° on GPS L2C.

In Figure 6-18, irregularity drift velocity estimations across Antennas 1 & 3 are plotted for GPS L2C vs. L1 (left), L5 vs. L1 (middle) and L5 vs. L2C (right) on PRN 1. The σ_ϕ cutoff is at 25º on GPS L2C. By observing the red circles in all three subplots in Figure 6-18, similar remark

can be drawn as in the previous section, that the correlation between the GPS bands estimation results is fairly strong at higher σ_ϕ values. Moreover, by comparing the right subplot against the other two subplots, it can be seen that the correlation between L2C and L5 velocities is higher than other frequency pairs. This in all likelihood is due to the fact that the carrier frequency between GPS L2C and L5 is closer than L1.

In fact, thanks to the improvement in signal condition, the consistency between the estimated drift velocities of the three GPS bands is preserved when the σ_ϕ cutoff is lowered to 15º. Drift velocity estimations across Antennas 1 & 3 are plotted in Figure 6-19 for GPS L2C vs. L1 (left), L5 vs. L1 (middle) and L5 vs. L2C (right) on PRN 1. The σ_ϕ cutoff is set to be equivalent to 15º on GPS L2C.

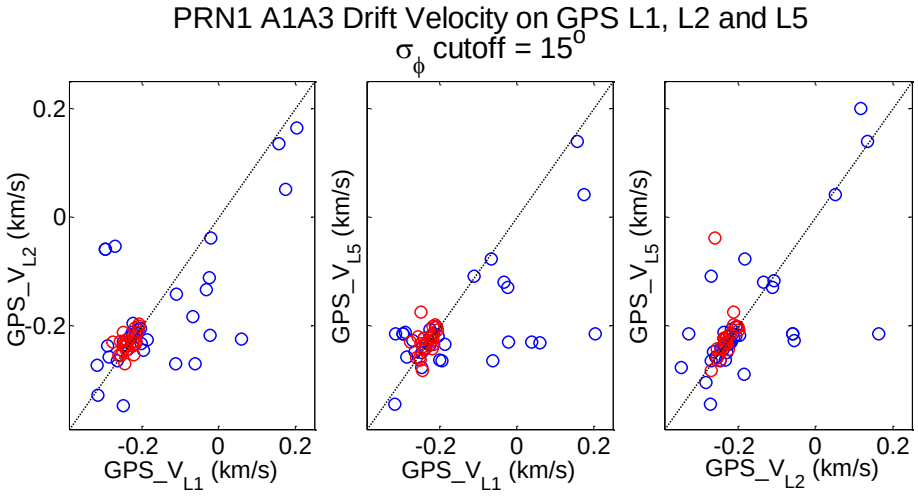

Figure 6-19. Scatter plots of GPS L1 vs. L2C vs. L5 irregularity drift velocity estimations. The σ_ϕ cutoff is at 15° on GPS L2C.

The same process is applied to the GLONASS satellites. Figure 6-20 shows the scattered plot of the derived velocities for GLONASS L1 and L2 bands for all satellites above 30º elevation. The σ_ϕ cutoff is chosen to be equivalent to 25º on GPS L2C.

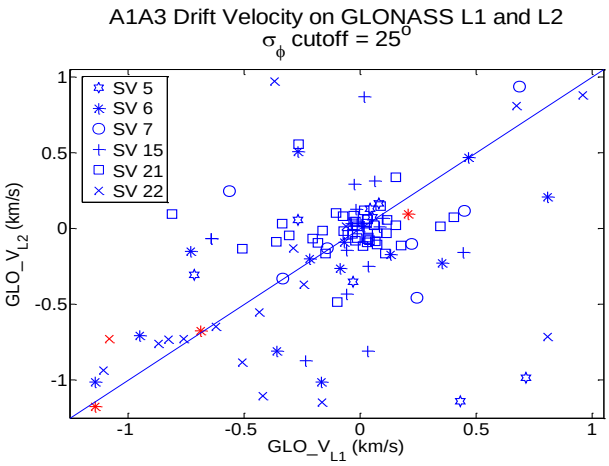

Figure 6-20. Scatter plots of GLONASS L2 vs. L1 irregularity drift velocity estimations across Antennas 1 & 3 from 05:00:00 to 06:00:00 on 2012/10/09. The σ_ϕ cutoff is at 25° on GPS L2C.

Similar observation to that of GPS can be drawn from the red symbols that the consistency between GLONASS L1 and L2 is high towards higher σ_ϕ values. But the number of red points is very limited even though there are 6 GLONASS satellites above 30º elevations. To increase potential matches, the σ_ϕ cutoff is lowered to 15º. Figure 6-21 gives the results.

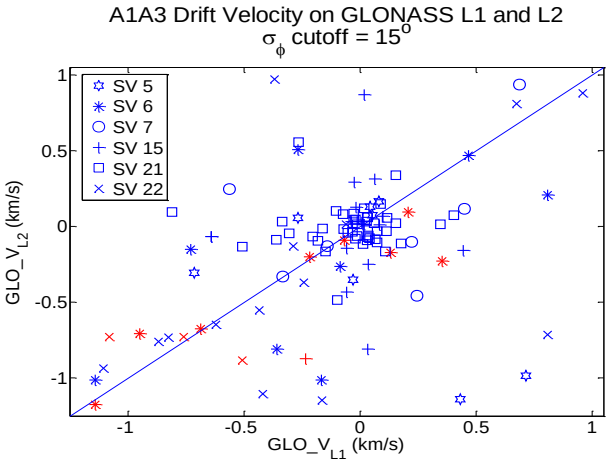

Figure 6-21. Scatter plots of GLONASS L2 vs. L1 irregularity drift velocity estimations. The $\boldsymbol{\sigma_\phi}$ cutoff is at 15º on GPS L2C.

From Figure 6-21, more red symbols can be found than those from Figure 6-20. However, the consistency between the GLONASS bands is notably degraded, unlike the case of GPS signals

shown by Figure 6-19. This is likely because phase noise of GLONASS signal is much higher than that of GPS in general (refer to Figure 6-10).

Up to this point, all data comparison and analysis of the multi-band drift velocity estimations are based on the σ_ϕ value, which measures the strength of the ionospheric irregularities. The results suggest that stronger phase fluctuations yield more consistent estimation results across the available GNSS signals. Therefore, we conclude that σ_ϕ at above appropriate cutoff values is an adequate classifying metric for the self-consistency check of the estimated drift velocities. On the other hand, in Sections 3.3 and 6.2, a scintillation strength filter of $\sigma_\phi = 12°$ (at GPS L1 frequency, or ~15° at L2 frequency) is proposed for separating irregularity patterns from noise. The above self-consistency study supports this choice.

6.4. Cross-Comparison against KOD SuperDARN

In this section, a comparative study between SuperDARN and GNSS array measurements during ionospheric scintillation is carried out. The availability of the matching SuperDARN backscatter data when the GNSS receiver array records ionospheric scintillation events is analyzed in detail. In addition, using the matching data from the two instruments, we cross-compare the SuperDARN's LOS ionospheric irregularity drift velocity measurements against the estimates produced by the TFDM. A more adequate comparison scheme is proposed in contrast to the conventional schemes in the literature, which are described below.

In the literature, most of the comparison studies between the two instruments are not based on direct point-to-point comparison at the IRPP's. Instead, they only utilize the HF backscatter data from a single SuperDARN beam covering the approximated SuperDARN-GNSS receiver LOS direction. An example of such comparison schemes is shown in Figure 6-22, replicated using our GNSS receiver measurements and KOD data.

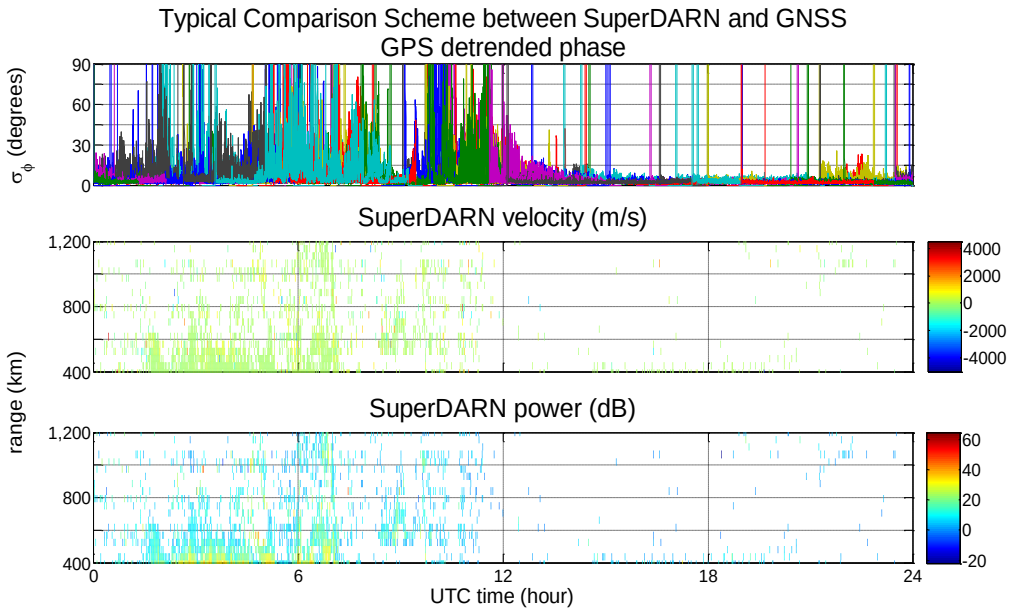

Figure 6-22. Replicated example of previous comparison study between SuperDARN HF backscatter and GNSS receiver measurement. The top plot shows all available GPS satellites' detrended phase measurements. The middle plot shows the SuperDARN measured plasma drift velocity. The bottom plot shows the SuperDARN measured backscatter power.

The example in Figure 6-22 is generated from 2012/10/13 00:00:00 to 2012/10/14 00:00:00 UT. The top plot shows the carrier phase σ_ϕ with an elevation mask of 10º for each visible GPS satellite, indicated by distinct colors. The vertical stripes correspond to phase detrending edge effects from the Butterworth filter. The middle plot and bottom plot are the measurements from the 10th KOD beam for plasma drift velocity and backscatter power, respectively.

Based on the known ground distance between the two facilities (658 km) and an approximated irregularity height (350 km), the distance from the SuperDARN to the overhead irregularity at the GNSS receiver can be estimated (~800 km). By looking at SuperDARN data from regions around the 800-km mark, comparison against the GNSS data is typically made through inspection. In some literature, even this calculation is omitted, while the ground distance is simply used as the center mark.

This one-beam comparison scheme is only capable of observing the general behavior along the LOS beam. It does not account for the ionospheric penetration location of each individual

satellite in the ionosphere, which could potentially be a few hundreds of kilometers away from the LOS beam. As a result, the comparison between the two systems is not accurate and potentially misleading. Moreover, much information from the nearby beams is absent. An improved comparison scheme has been developed to address these issues.

The general procedure of the improved comparison scheme can be broken down into the following steps: 1) identify the scintillation GNSS signal IRPP coordinates; 2) calculate the distance and bearing angle from the IRPP location to the SuperDARN location; 3) project the IRPP onto the SuperDARN's field-of-view; 4) identify the corresponding SuperDARN data grid and perform the comparison [*Wang and Morton*, 2015; *Wang et al.*, 2016]. Core formulas and detailed procedures are given as the followings:

1) Calculate IRPP location based on the elevation and azimuth angles provided by the receivers, as well as the presumed or modeled irregularity heights (refer to Equations 5-5 through 5-7). To mitigate the multipath effects, only satellites at higher elevation angles (≥ 30º) are considered in this study. Note that in order to identify the IRPP, the irregularity height has to be determined first. As stated in Section 6.2.3, the height is assumed to be within the [150 km, 450 km] range for the HAARP site.

2) Obtain the geodetic coordinates of the SuperDARN array, $(\varphi_{SD}, \lambda_{SD}, h_{SD})$, and convert them into the Earth-Center, Earth-Fixed (ECEF) coordinates (x_{SD}, y_{SD}, z_{SD}). Similarly, convert $(\varphi_{IPP}, \lambda_{IPP}, h_{IPP})$ into $(x_{IPP}, y_{IPP}, z_{IPP})$. Use the range equation to identify the distance between these two points.

$$d = \sqrt{(x_{IPP} - x_{SD})^2 + (y_{IPP} - y_{SD})^2 + (z_{IPP} - z_{SD})^2} \quad (6\text{-}5)$$

Then, calculate the bearing angle of IRPP observed from SuperDARN's location based on Section 3.2.

3) Using the calculated parameters θ and d, project the IRPP position onto the SuperDARN's field-of-view.

4) Since the SuperDARN data is sparse in general, the data search is expanded to all available data grids around the projected IRPP, within a certain radius. For this study, 45 km is chosen to be the radius since it is the range gate resolution value of the SuperDARN. Figure 6-23 gives an example of this data finding process.

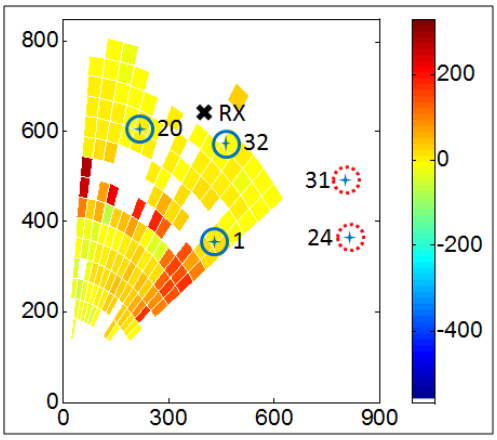

Figure 6-23. Example of data finding. The background plot is a zoomed-in SuperDARN field-of-view. The projected IRPP's are indicated by the blue plus signs, while the GNSS receiver position is given by the black cross. The blue and red circles indicate the matched and mismatched data between SuperDARN and GNSS receiver.

Figure 6-23 is composed of the KOD's field-of-view plot and the skyplot of the projected IRPPs of all visible GPS satellite above an elevation mask of 30º. The field-of-view is zoomed-in to the vicinity of the GNSS receiver, indicated by the black "X". The satellite IRPPs are marked by the blue plus signs, accompanied by the PRN numbers. The circles around the IRPPs illustrate the data search radius (= 45 km). The blue circles illustrate the matched data pairs between SuperDARN and GNSS, while the red circles indicate lack of matches. In this case, the IRPPs of PRN 24 and PRN 31 are outside of KOD's field-of-view, which will not go into the later comparisons. Once the matched data grids have been identified, the corresponding GPS data is extracted, while all available SuperDARN measurements within the search radius are documented.

After the matched data from the two instruments has been identified, statistical comparison is conducted by examining the SuperDARN availability versus ionospheric scintillation strength indicated by GNSS measurements. The estimated plasma drift velocity from the GNSS array is also compared against the measured values from the SuperDARN for some available data.

6.4.1. *Data Availability Based on a Presumed Irregularity Height*

GPS L1 and GLONASS L1 signals are considered for this study. An empirical irregularity height assumption at 350 km is employed to obtain some preliminary comparison results. Using the above matching data finding scheme, data availabilities from the KOD SuperDARN during scintillations for GPS and GLONASS signals are shown in Figure 6-24 based on the data set described in Section 6.1.1.

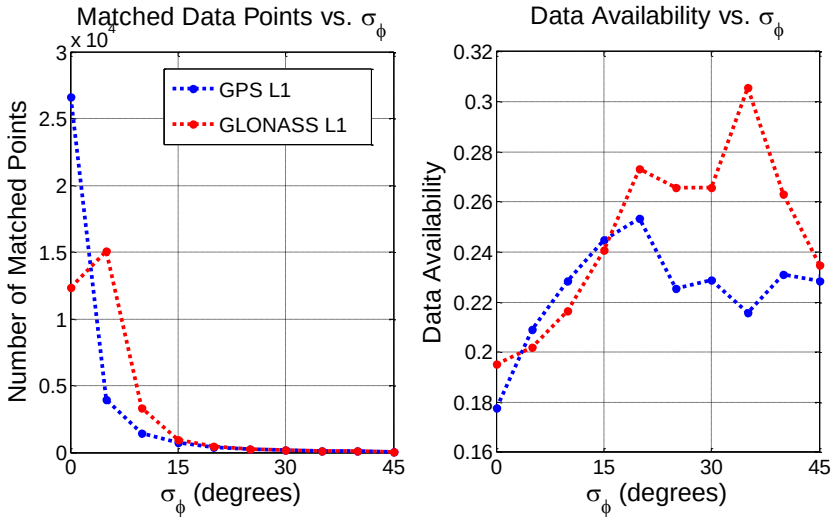

Figure 6-24. Preliminary data availability results based on a presumed irregularity height at 350 km. The left-hand plot shows the total matched data points between the two instruments. The right-hand plot shows the SuperDARN data availability in terms of its probability of detection during scintillation events. The blue points represent GPS data, while red points represent GLONASS data. Both plots are plotted versus σ_ϕ values.

In Figure 6-24, the left-hand plot shows the total matched data points between SuperDARN and GNSS during scintillation events. Both GPS (blue) and GLONASS (red) matched data points decrease significantly towards higher σ_ϕ values. This is an expected result, as stronger

scintillation events are less frequent. Note that the GLONASS result goes up at $\sigma_\phi = 5°$ before it decreases. This is because GLONASS signals have rather noisy baseline values. The right-hand plot captures SuperDARN's ability to detect ionospheric irregularities when GNSS receiver observes scintillation events. It shows the SuperDARN data availability in terms of its probability of detection during scintillation events. Note that even under a reasonably large search radius (45 km) in the data matching scheme, the data matching rates are between 20% to 30% for both GPS and GLONASS measurements.

6.4.2. *Data Availability Based on a Range of Irregularity Heights*

Although 350 km serves as a good approximation for the altitude of ionosphere F-region electron density peak, the true IRPPs are likely to differ and fluctuate over time. In order to obtain an estimate of the IRPPs, a range of irregularity heights from 150 km to 450 km are used in this comparison. Figure 6-25 is generated to justify that this range of irregularity heights is in fact visible from the KOD SuperDARN.

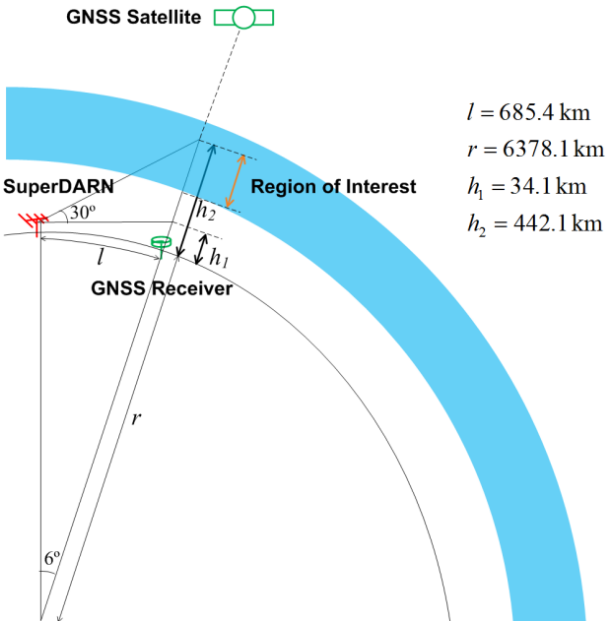

Figure 6-25. SuperDARN coverage at receiver zenith. The SuperDARN and the GNSS receiver positions are indicated by the red antenna and the green receiver, respectively. The visible region of the SuperDARN at the receiver overhead is estimated to be [h1, h2], or [34.1 km, 442.1 km]. The region of interest is marked by yellow from the bottom of the ionosphere (blue) to h2.

In Figure 6-25, l and r represent the known ground distance between the two instruments and the Earth radius, respectively. KOD's elevation coverage is from 0º to 30º from the horizon. Employing the spherical-earth approximation, the lower and upper bounds of KOD's visible region at the receiver overhead are found to be $[h_1, h_2]$ = [34.1 km, 442.1 km], with the beam center at around 200 km altitude. The [150 km, 450 km] assumption is roughly contained in this region. Data availability in Figure 6-24 are reproduced for this range of irregularity height assumptions, with a step size of 25 km. The full-range results are shown in Figure 6-26.

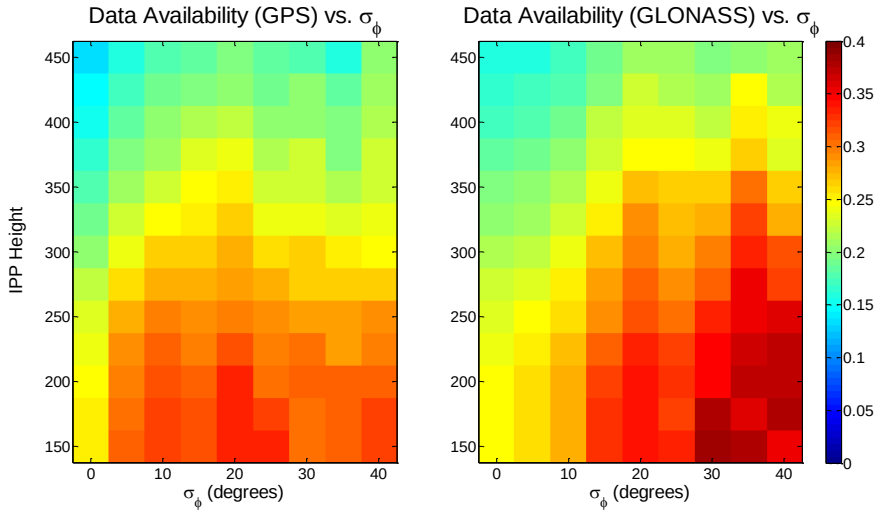

Figure 6-26. Data availability for full range of irregularity heights [150 km, 450 km]. The left-hand plot corresponds to GPS data, while the right-hand plot corresponds to GLONASS data. The color bar indicates the data availability from 0 to 40%.

In Figure 6-26, the left-hand plot shows the SuperDARN data availability for the full-range of irregularity heights, while the right-hand plot shows the comparison results for GLONASS data. An increase can be observed in both plots toward lower irregularity height assumptions around 200 km. This increase in detection can be explained by the SuperDARN-GNSS geometry shown in Figure 6-25, where the center of the SuperDARN beam is at about 200 km. The GLONASS availability results are skewed towards higher σ_ϕ values than the GPS results. This is again due to the higher phase noise on GLONASS signals.

6.4.3. *Drift Velocity Cross-comparison for Available Data*

Thus far, the SuperDARN data availability during GNSS phase scintillations at the HAARP site are found to be at a level between 20% and 35% of the time. Within the matched data, the GNSS estimated irregularity drift velocities are cross-compared with the KOD SuperDARN LOS velocity measurements. Figure 6-26 gives an example of the GPS estimated drift velocities by the HAARP receiver array using the data set from 1:46:00 UT to 2:34:00 UT on 2012/10/01.

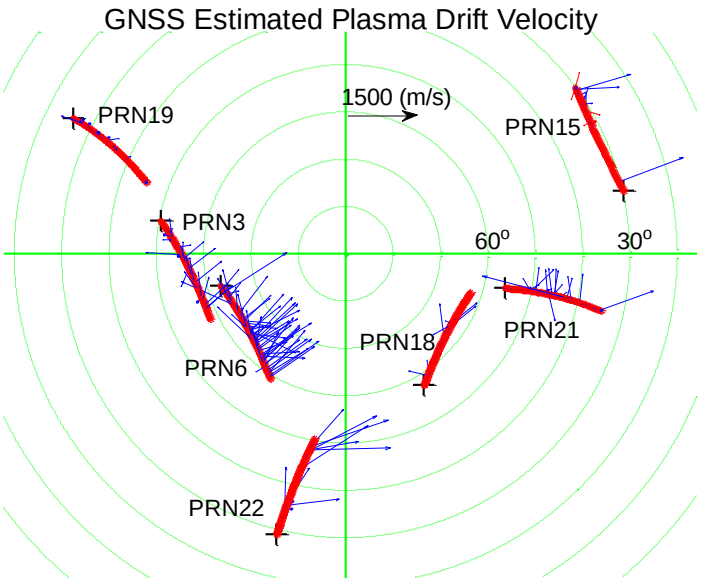

Figure 6-27. Skyplot of HAARP array estimated plasma drift velocity on 2012/10/01.

After projecting the GPS estimated velocities onto SuperDARN's direction, the cross-comparison results against the SuperDARN measured LOS drift velocities are shown in Figure 6-28, with both filtered and un-filtered GPS estimated velocity values.

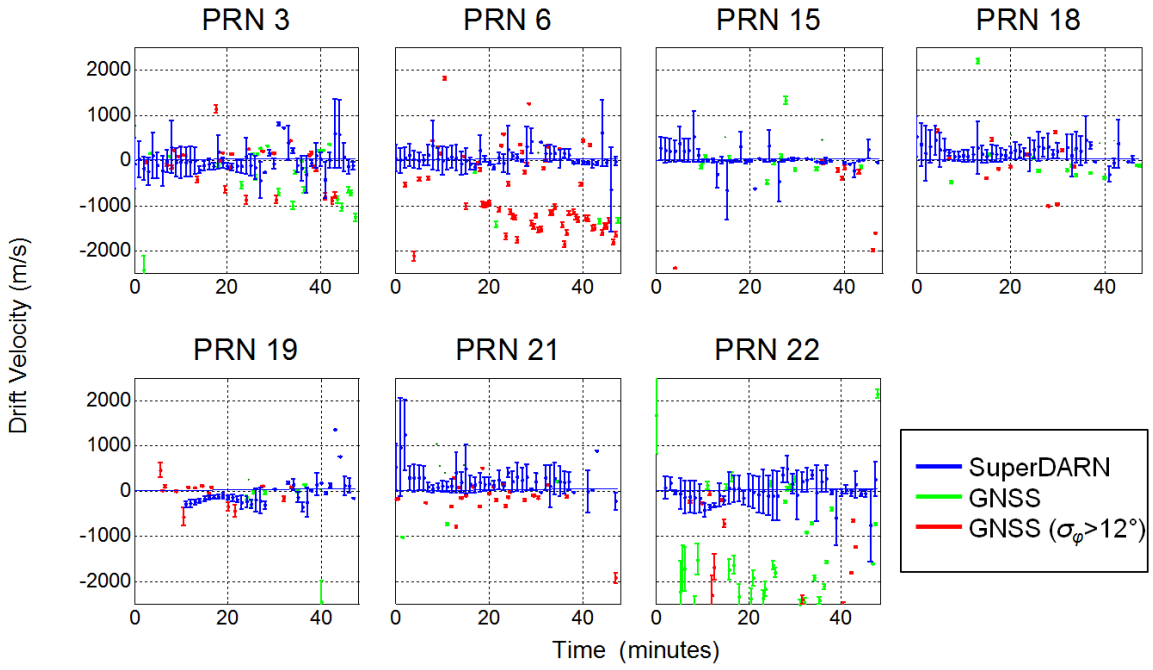

Figure 6-28. Cross-comparison between GPS estimated drift velocities and SuperDARN LOS measurements. The blue bars illustrate the maximum and minimum velocity measurements within the SuperDARN search radius. The green and red bars are the un-filtered and filtered GNSS estimated values based on scintillation strength, respectively.

In Figure 6-28, all results are generated using the same irregularity height range assumption. The blue bars correspond to the maximum and minimum SuperDARN measured velocity within the 45-km search radius at a 1-minute interval. The green and red bars are the un-filtered (regardless of scintillation strength) and filtered (signals with $\sigma_\phi > 12°$) GNSS estimated velocities respectively at a 30-second interval. The uncertainties in the irregularity height assumption are also carried into the estimated velocities. The cross-comparison between the two systems shows poor agreement in general. In particular, on PRN 6, even when the HAARP array produces consistent estimations during strong scintillations, disagreement against SuperDARN measurements can still be observed. SuperDARN measurements demonstrated large variations within the 45-km search radius. This result implies that even when matching SuperDARN data exists; it only represents the averaged behavior of a large volume in the ionosphere. This averaged

behavior may not represent individual GNSS satellite-receiver LOS path, even if that path is within the SuperDARN volume.

6.5. TDM vs. TFDM

For the HAARP array data, only the TFDM is applicable due to its signal conditions. On the other hand, both the TDM and the TFDM are applicable for the data collected by the Poker Flat array. In this section, the two methods are compared in terms of both time lag comparison and drift velocity comparison.

Due to the computational load of the TFDM, only a piece of scintillation data is selected for this comparative study. The data period selected is from 1600UT to 1800UT on 2015/12/20, which was right after the AE index reached maximum value. During this two-hour period, the global geomagnetic Kp index stayed at 7. The following GNSS signals are analyzed: GPS L1, GLONASS L1 and Galileo E1. There are 9 GPS satellites (PRN8, 10, 15, 16, 18, 20, 21, 26 and 27) and 7 GLONASS satellites (GLO 5, 7, 12, 13, 21, 22 and 23) above 30° elevations during this two-hour period. Only 1 Galileo satellite is partially visible in this time interval: GAL 26.

6.5.1. Time Lag Comparison

Time lag estimations are generated for both TDM and TFDM, together with their corresponding correlation coefficients. From 1600 to 1800 UT, 5 out of the 9 GPS satellites (PRN 16, 18, 20, 21 and 27) and 4 out of the 7 GLONASS satellites (GLO 5, 13, 21 and 22) are visible during the majority of the time. An example of the correlation results is given between antenna pairs A2 and A3. Using a correlation coefficient filter at 70%, the GNSS time lag results for the aforementioned GPS and GLONASS satellites are plotted in Figure 6-29, together with the only Galileo example, GAL 26.

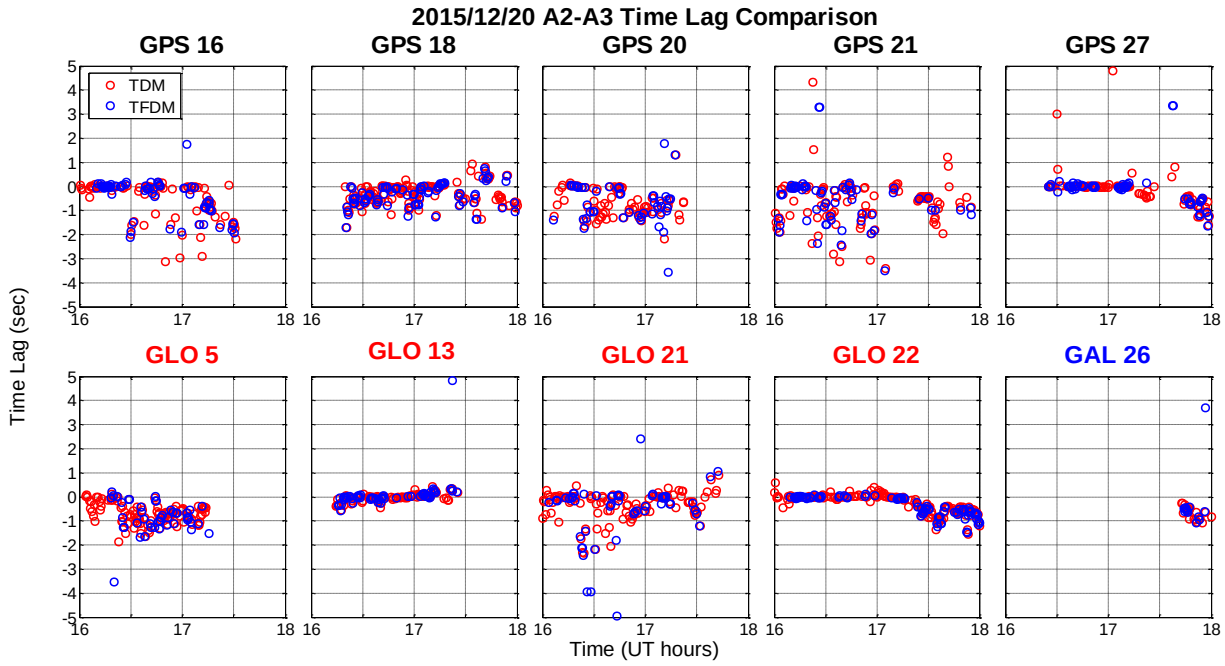

Figure 6-29. Example of time lag comparison between the two methods on A2-A3 antenna pair. Time lag results for GPS (GPS, black) 16, 18, 20, 21 and 27; GLONASS (GLO, red) 5, 13, 21 and 22; Galileo (GAL, blue) 26 are plotted. The red circles represent results for the TDM while the blue circles represent results for the TFDM.

In Figure 6-29, over all, the TDM and TFDM results agree well with each other. Outliers do occur occasionally. Notice that there are more red circles than blue ones on every GNSS satellite, showing the TFDM tends to yield less admissible results than the TDM. This is because TFDM's spectral approach is more rigorous and selective than TDM in terms of finding the time lags. Based on the results for all visible GPS and GLONASS satellites, some statistical parameters of the time lag differences between TDM and TFDM are given in Table 6-4.

Table 6-4. Time lag difference (s) between TDM and TFDM

Antenna pairs	GPS			GLONASS		
	Points	Mean	Std	Points	Mean	Std
A1-A2	166	0.04	1.43	80	-0.22	1.76
A1-A3	289	0.02	0.68	134	0.10	1.74
A2-A3	232	0.10	1.54	196	0.06	0.79

In Table 6-4, the GPS time lag differences have more data points than the GLONASS ones. As a result, the GPS differences are smaller than the GLONASS differences in both mean values and standard deviations. The best matches of the GPS results come from the A1-A3 pair, while the GLONASS results come from the A2-A3 pair. Overall, the time lag discrepancy between TDM and TFDM is small.

6.5.2. Drift Velocity Comparison

Small time lag differences may still lead to large velocity differences. Hence, the drift velocities from both methods are generated for comparison. Figures 6-30 depicts the differences in the velocity estimations between TDM and TFDM for GPS signals.

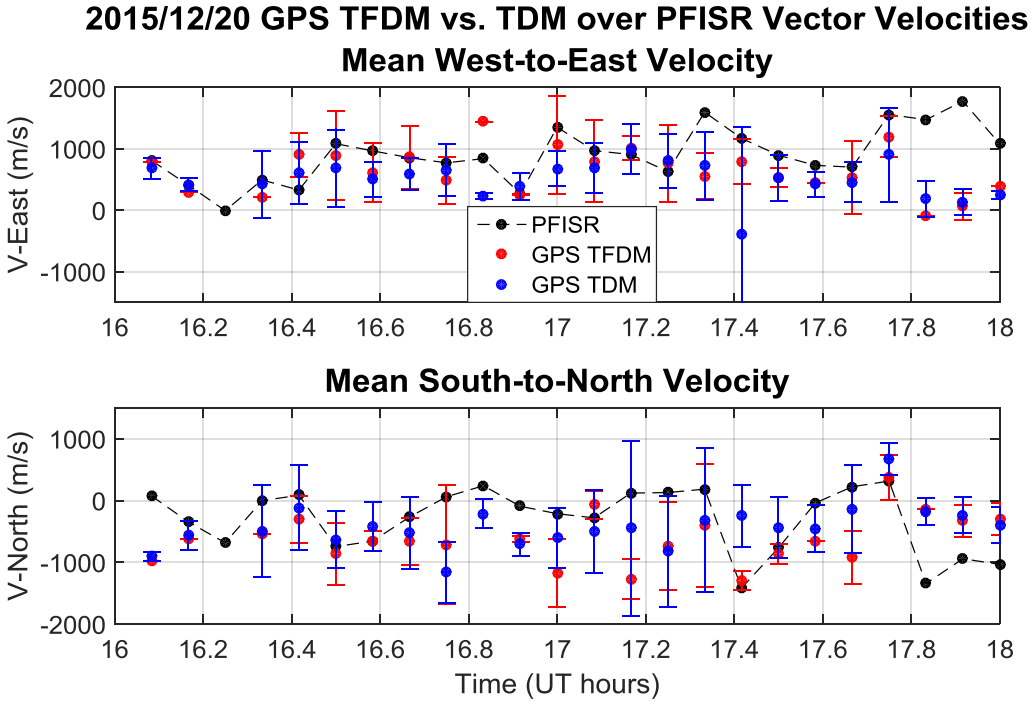

Figure 6-30. TFDM vs. TDM in GPS drift velocity estimations, cross-compared with the PFISR results. The circles represent the mean velocity values: PFISR (black), GPS TFDM (red) and GPS TDM (blue). Error-bars are plotted on top of the GPS mean velocities representing the standard deviations.

In Figure 6-30 the GPS TFDM and TDM results match well against each other, especially in the east-to-west direction. The error-bars of TFDM are shorter than those of the TDM, suggesting better consistency of the time-frequency approach, as expected. The cross-comparison between GPS and PFISR results also show general agreement, except for the last 3 data points.

Figures 6-31 shows the differences in the velocity estimations between TDM and TFDM for GLONASS signals.

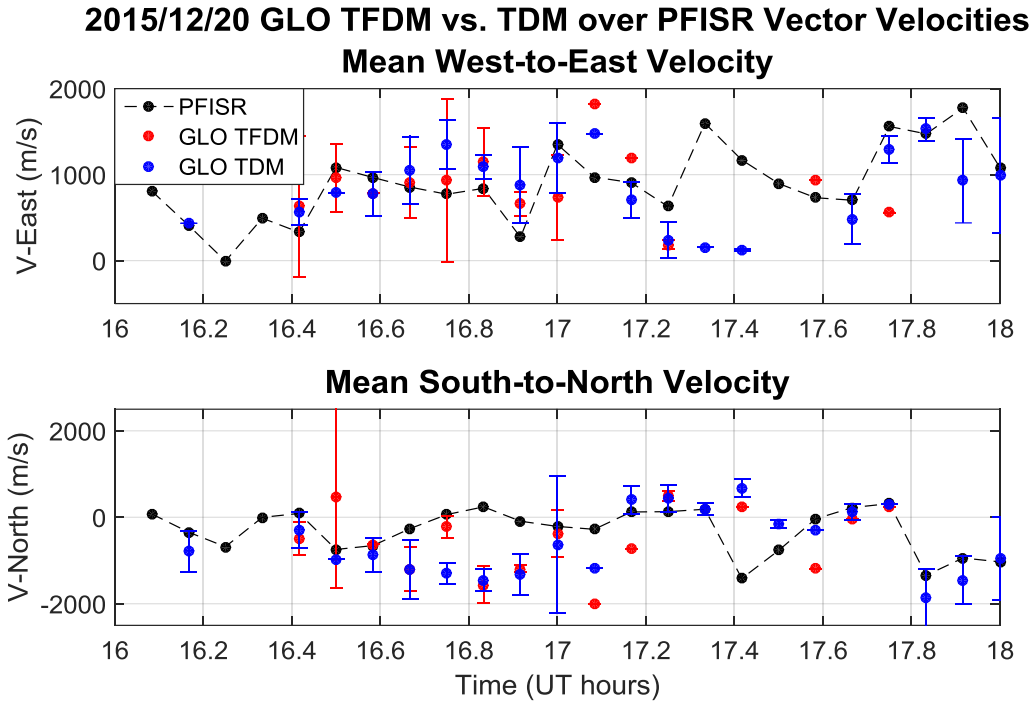

Figure 6-31. TFDM vs. TDM in GLONASS drift velocity estimations, cross-compared with the PFISR results

In Figure 6-31, general agreements can also be observed between TFDM and TDM, and between PFISR and GLONASS. Comparing with the GPS results, the GLONASS error-bars are notably shorter, and sometimes even non-existing. This can be explained by the fewer number of data points on GLONASS than on GPS. Even so, the last few velocity estimations on GLONASS show better agreement with the PFISR measurements. This may due to its better sky coverage.

To summarize, TFDM and TDM produce comparable time lag and drift velocity estimations. TFDM is slightly more consistent than TDM in terms of having smaller variances. Note that when estimating velocities from a large amount of data, TDM is preferred over TFDM, since it costs much less computational resources.

6.6. Comparison between Correlation Models

As noted in Chapter 2, auroral patterns are amorphous. Also, the scale of these patterns is often much larger than the footprint of a GNSS satellite signal's IPP. As a result, accurate frame-by-frame estimation of the arc velocity with GNSS derived velocity can be challenging. On the other hand, the general direction of the auroral arcs can often be estimated via visual inspection. Hence, consecutive ASI images can be used as references to infer the irregularity drift direction.

A case study is conducted based on the intense geomagnetic storm event occurred on 2015/12/20. Ionospheric irregularity drift velocities are estimated based on the hybrid correlation model, together with the satellite scan velocity estimates. Irregularity drift velocities from the front velocity model and the anisotropy model are also calculated for comparison. The irregularity height assumption is taken to be 96 km to match with the emission center of the green atomic oxygen line at 557.7 nm. The corresponding GNSS drift velocity estimates are directly overlaid on top of the ASI 557.7 nm images. The averaged PFISR vector velocity measurements are also provided as references. An elevation angle mask of 35° is applied to minimize the multipath effects. Figure 6-32 shows the comparison results using the geodetic coordinate system for 4 consecutive epochs from 04:39:35 UT with a 25-second interval.

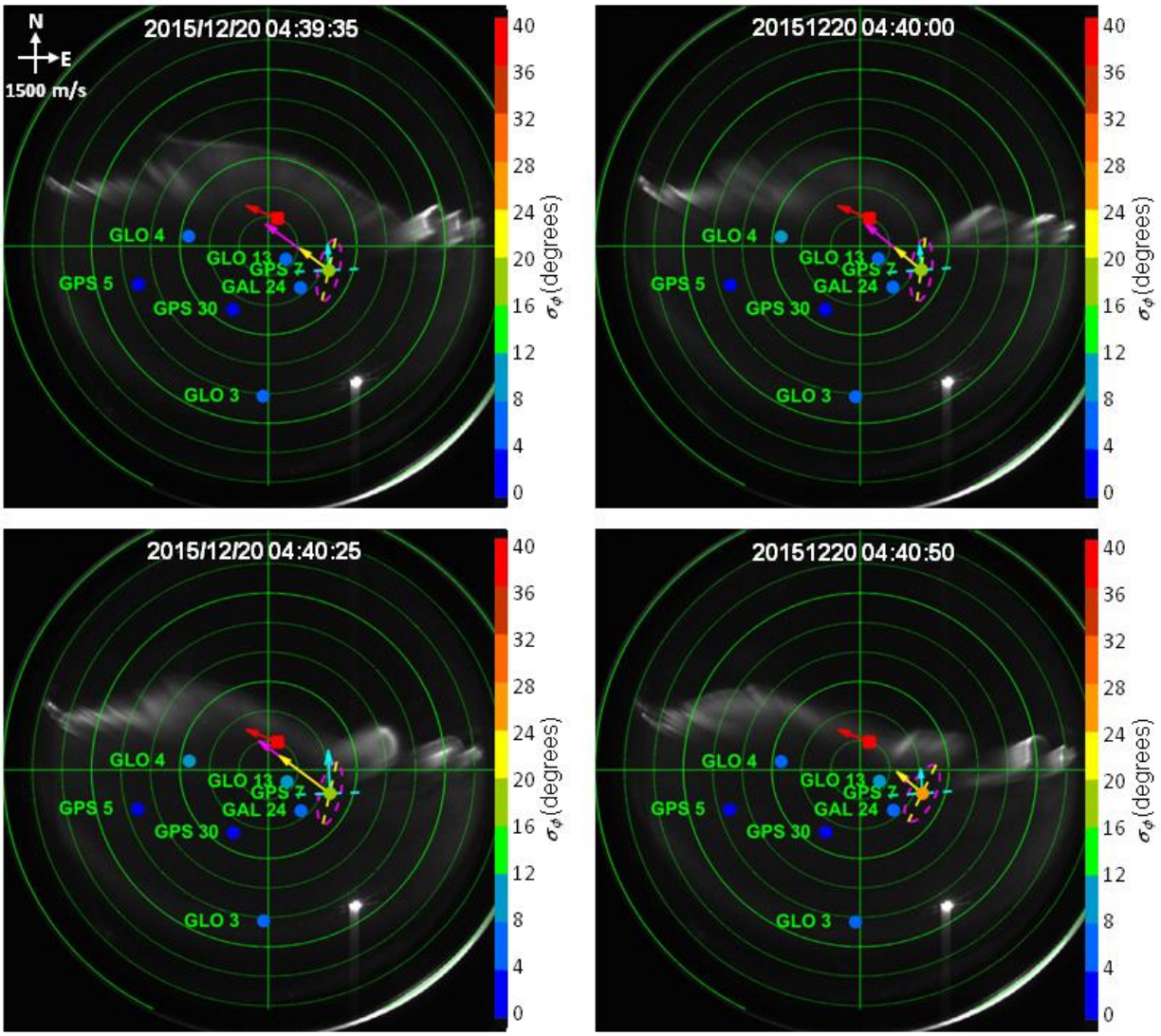

Figure 6-32. Cross-comparison between drift velocity estimates from different correlation methods vs. PFISR vector velocity measurements on top of 557.7 nm ASI images from 04:30:25 to 04:31:40 UT on 2015/12/20. In each subplot, the red square and quiver represent the approximated PFISR beam center and the averaged PFISR vector velocity measurement, respectively. GNSS satellites are plotted as circles with respect their elevation and azimuth angles using three-letter initials for abbreviation (GPS = GPS, GLO = GLONASS, GAL = Galileo). The color of each circle corresponds to the phase scintillation strength observed for each satellite, shown by the color bar. Drift velocity estimates from different correlation methods are given by the colored quivers (pink = anisotropy model, cyan = front velocity model, yellow = hybrid model). The estimated topologies of these models are provided using dashed lines in the same colors. Geodetic reference velocity vectors at 1500 m/s are given in white in the first subplot.

In Figure 6-32, the PFISR beam center is approximated from the four PFISR beams used in this experiment: (14° az, 90° el), (-154.3° az, 77.5° el), (-34.7° az, 66.1° el) and (75° az, 65.6° el) [Marigal Database, http://isr.sri.com/madrigal/]. The PFISR velocity is averaged from measurements within [66°N, 66.75°N] geomagnetic latitudes, where most consistent results are observed. The PFISR velocity stays the same for all four subplots, as this 100-second period is within a 5-minute PFISR data interval. A horizontal arc structure can be observed from the ASI images showing auroral emission. With close examinations, the arc structure is found out to be moving westward during the 100-second observation period. This agrees with PFISR's vector velocity measurements. Meanwhile, good spatial associations can be observed between phase scintillations experienced on GNSS satellites and auroral emissions seen on ASI. Phase scintillation strengths that are above nominal values ($\sigma_\psi > 4°$) are only observed on satellites closest to the irregularity: GPS 7, GLONASS 4 and GLONASS 13. Moderate scintillation is observed on GPS 7, producing measurable space-time correlations for drift velocity estimation.

For the front velocity model, the magnitude of the drift velocity estimates matches well against PFISR's measurement. But the orientation of the velocity front and the direction of the drift don't match with the local B-field topology, whose declination angle was around 18.5°N based the IGRF model [*Thébault et al*., 2015]. For the anisotropy model, as shown by the dashed ellipses, the anisotropy orientation matches with the B-field orientation. Also, the directions of the estimated drift velocities agree with the PFISR results. However, the magnitudes of the velocity estimates are much larger than the PFISR measurements in the first three subplots. Combining the advantages of the front velocity model and the anisotropy model, the hybrid correlation model shows improved performance in both velocity magnitude and drift direction estimation

6.7. Cross-Comparison against the PFISR

6.7.1. Case Study on 2015/12/20

The irregularity drift velocities are calculated using the hybrid correlation model based on the GNSS receiver array measurements. The GNSS estimated velocities originally in the geodetic coordinate system are mapped into the geomagnetic coordinate system. To cross-compare the results against PFISR's measurements, the GNSS estimated velocities are further averaged into geomagnetic latitude bins from 63.5°N to 68°N with a step size of 0.25°. The comparison results are demonstrated by Figure 6-33, while the GNSS results are based on irregularity altitudes observed from PFISR's measurements.

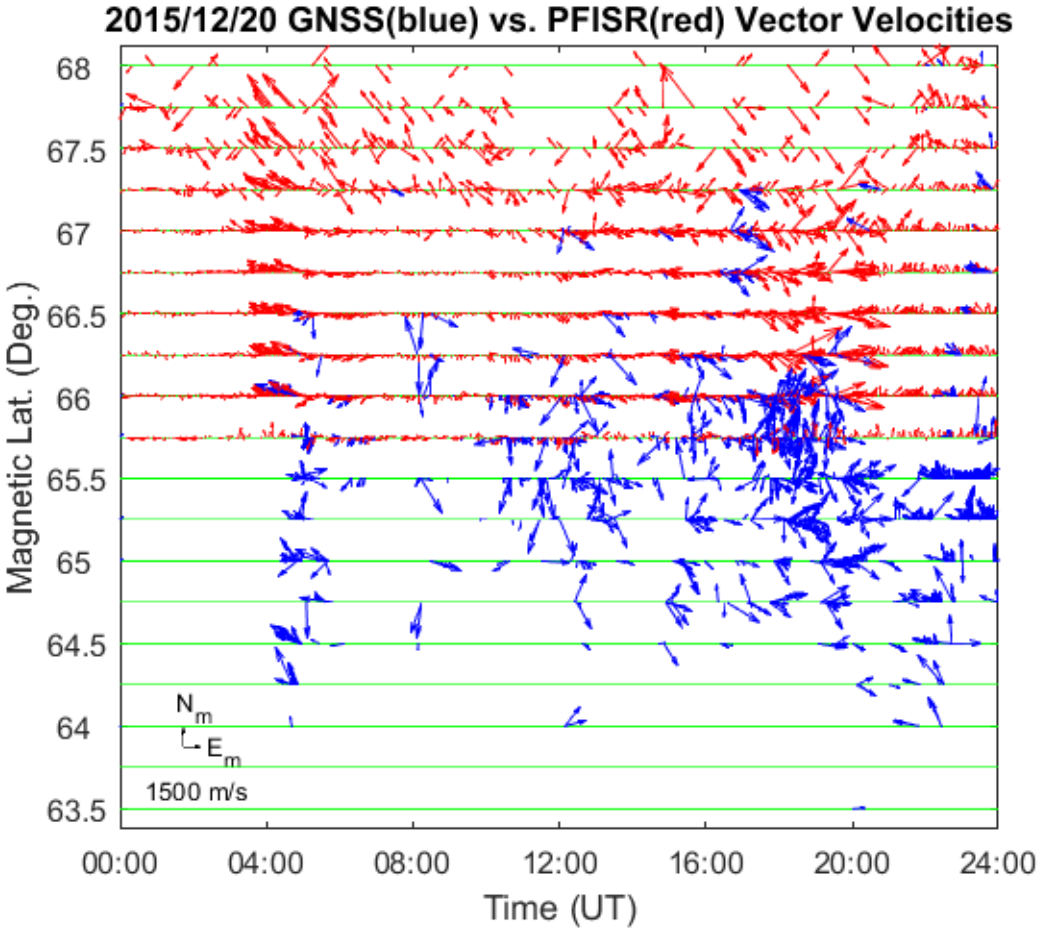

Figure 6-33. Cross-comparison between the GNSS array's estimates (blue) and the PFISR's measurements (red) in geomagnetic latitudes, with reference vectors at 1500 m/s pointing eastward and northward.

In Figure 6-33, the PFISR measurements are most consistent from 66°N to 67°N. Three common features can be identified across these geomagnetic latitudes. First, at around 0400 UT, large north-westward velocity components can be observed, and quickly transitioned into small south-westward components. Second, from ~1500 UT to ~2100 UT, south-eastward drifts persisted with relatively large variations. Finally, from ~2100 UT to 2400 UT, small north-ward components emerged. These features can also be observed on GNSS estimated results. In addition, the GNSS results showed some large fluctuations post 1200 UT towards lower magnetic latitudes. In fact, the timing of these fluctuations corresponds well with a sub-storm occurred during this period (refer to Figures 6-2, 6-3 and 6-4). This sub-storm was likely localized towards the southern half of the sky outside of PFISR's limited observation volume. This observation is supported by Figure 6-35 showing ASI summary images every 10 minutes from 1200 UT to 1350 UT.

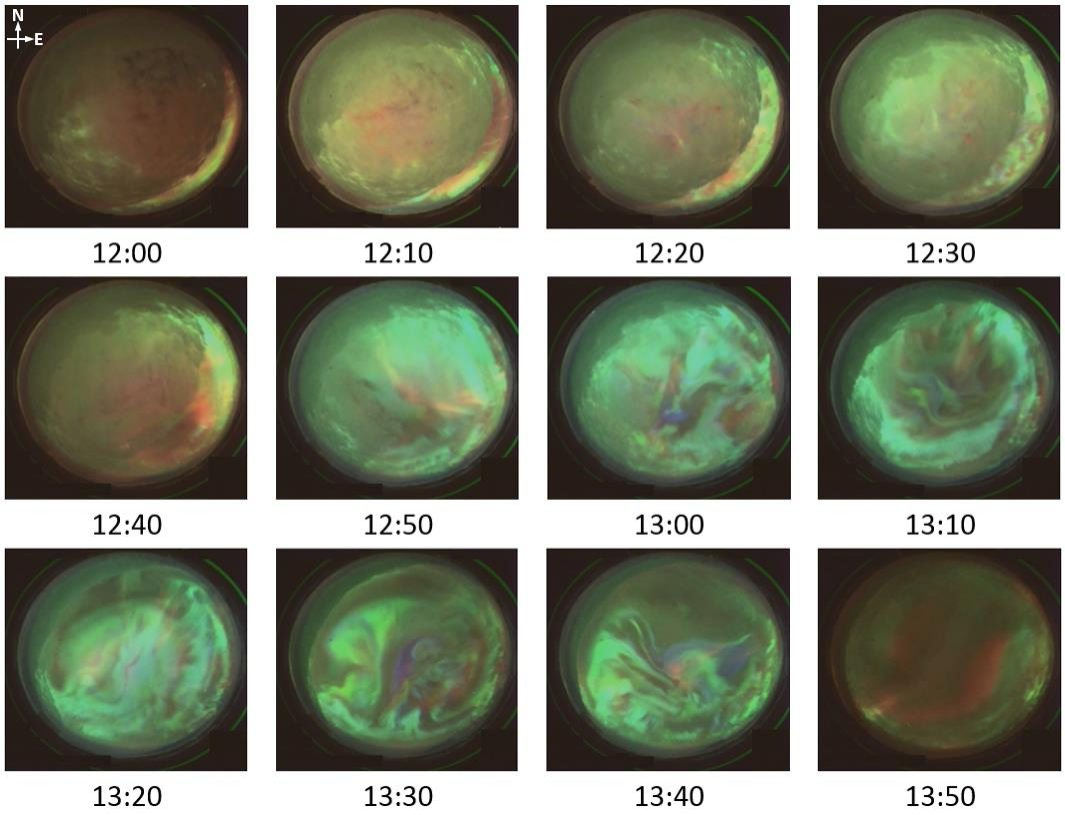

Figure 6-34. ASI summary images every 10 minutes from 1200 UT to 1350 UT on 2015/12/20.

In Figure 6-34, unfortunately, the images in the first 40 minutes and the last image appear to be under cloudy conditions. From 1250 to 1340 UT, the sky is mostly clear. The aurora does appear to be more active and turbulent in the southern half of the sky, especially at 1250, 1310, 1330 and 1340 UT.

A quantitative comparison is carried out by investigating the mean values and standard deviations of PFISR's measurements and the combined velocity estimations from the GNSS receiver array. For the GNSS estimations, the results are binned into 5-minute intervals to match with the PFISR's measurements from the original 25-second resolution. The variations caused by the boundary irregularity altitude assumptions have also been accounted for. The results are shown in Figure 6-35.

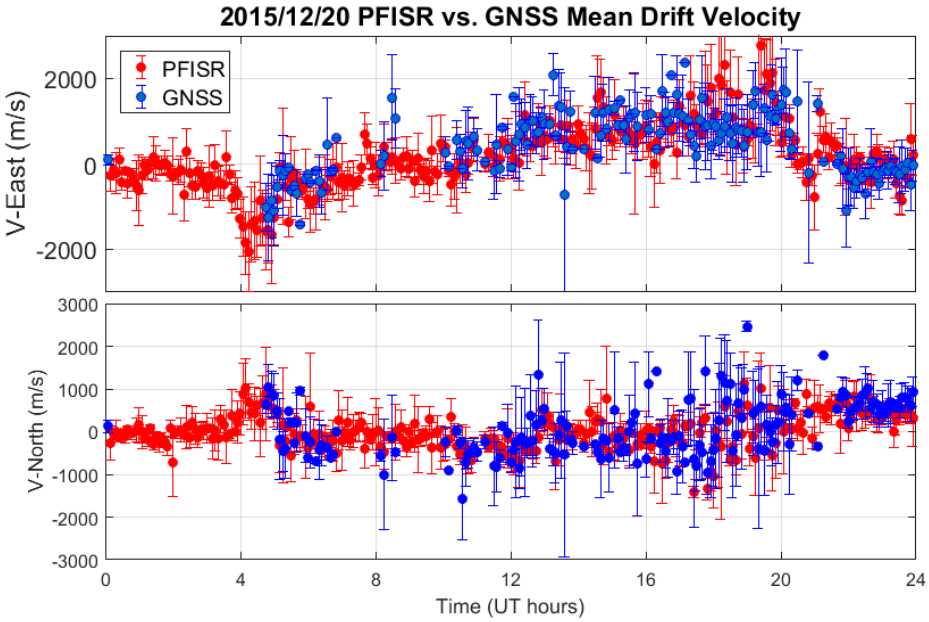

Figure 6-35. Cross-comparison of mean drift velocities between the PFISR (red dots) and the GNSS array (blue dots) on 2015/12/20, together with their standard deviations as error-bars, accounting for irregularity altitude variations.

Figure 6-35 indicates that the cross-comparison results between the GNSS array and the PFISR are again in good agreement. Comparing the mean values, in the east-west direction, the GNSS estimations are reasonably close to the PFISR measurements, and are almost always within

PFIRS's error-bar boundaries. In the north-south direction, the agreement is slightly inferior. This is likely due to the shorter baseline separations in the north-south direction, as well as the possible error occurred during coordinate transformation from geodetic to geomagnetic without knowledge of the vertical velocity component. The error-bars of the GNSS array are also longer in the north-south direction, showing larger velocity variations. As suggested by Table 6-1, the dominate contributor to the GNSS velocity variations would come from the spatial and temporal variations of the irregularity structures. The variations caused by different irregularity altitude assumption only serve a minor role.

The last cross-comparison is on the distribution of the velocity magnitudes. Note that this comparison only focuses on the results from 1000 to 2000 UT, as both the GNSS array and the PFISR have near-continuous data. The variations caused by the boundary irregularity altitude assumptions at [100km, 400km] are also incorporated into the results.

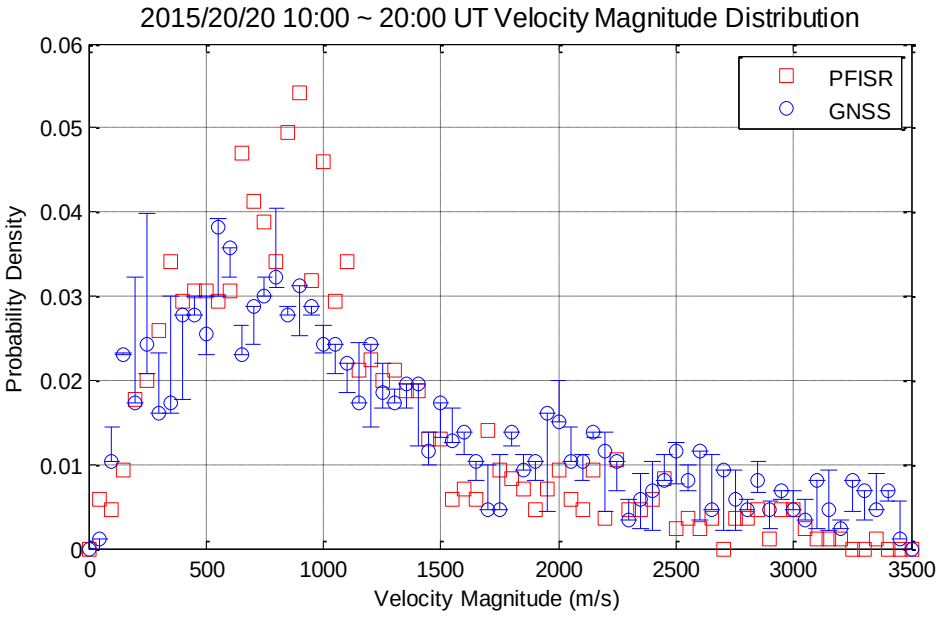

Figure 6-36. Cross-Comparison of the velocity magnitude distributions of the PFISR measurements (red squares) and the GNSS estimates (blue circles with error-bars) between 1000 and 2000 UT on 2015/12/20. The blue circles represent the GNSS distribution under the irregularity altitude assumption based on PFISR's observation, while the error-bars indicate variations associated with the irregularity altitude boundary assumptions.

In Figure 6-36, a general agreement can be seen between the two distributions. The PFISR distribution has a more distinct peak between velocities ranges from 600 m/s to 1100 m/s, while the GNSS distribution shows more proportion towards velocities above 2000 m/s. Overall, the variations caused by different irregularity altitude assumptions are small. However, relatively large variations in the distribution can be observed in velocities under 400 m/s. This is because small velocities are more likely to be influence by different altitude assumptions.

6.7.2. Case Study on 2015/12/31

The GNSS results are again projected onto corresponding geomagnetic latitudes. The results are shown in Figure 6-37, together with the PFISR measurements.

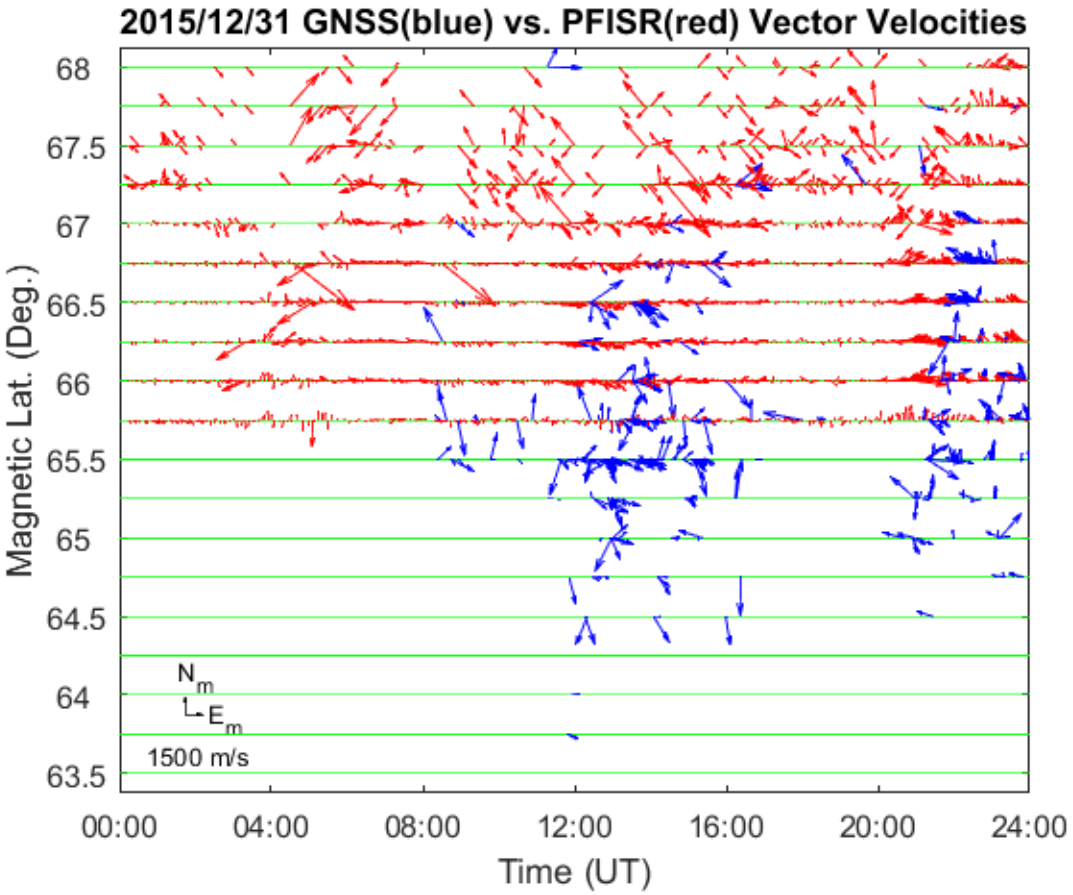

Figure 6-37. Cross-comparison between GPS array estimated and PFISR measured drift velocities for 2015/12/31.

Focusing on results from 65.75°N to 68°N, good agreements can be observed between the GNSS's estimations and the PFISR's results, in the sense that south-eastward arrows can be observed in both figures from 8:00 to 16:00 UT and a change into small northward arrows can be observed after 22:00 UT. For latitudes below 65.75°N, between 8:00 to 16:00 UT, the GNSS results follow the PFISR's pattern, which is dominated by south-eastward velocities, only more turbulent. Towards 24:00 UT from 64.25°N to 65°N, north-westward components can be observed, which agrees well with the trend from the PFISR results.

Similarly, the mean velocities are calculated for both PFISR and GNSS vector velocities along the geomagnetic west-to-east and south-to-north directions. The results are illustrated by Figure 6-38.

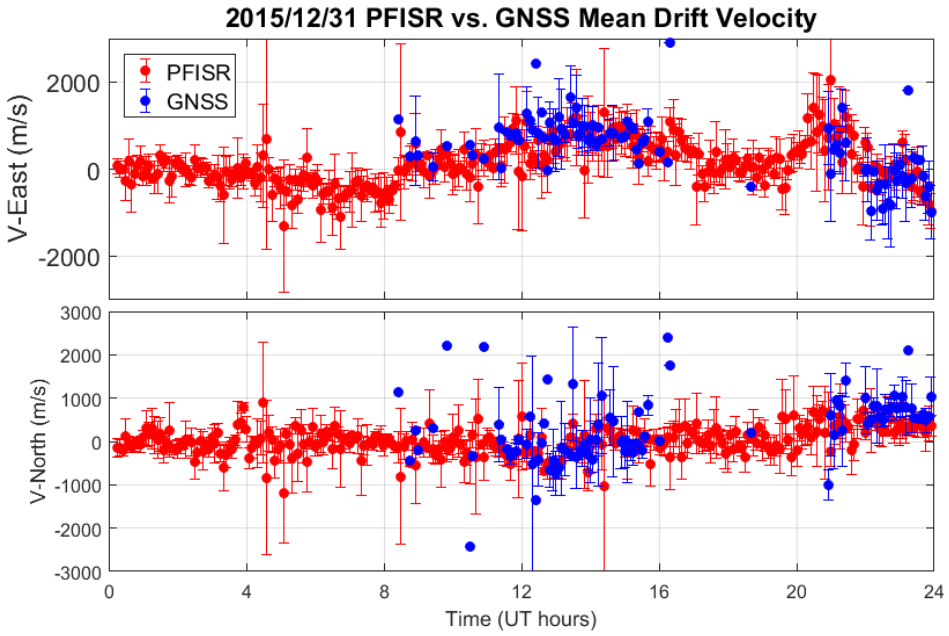

Figure 6-38. Cross-comparison of mean drift velocities between the PFISR and the GNSS array on 2015/12/31.

Again, in both plots of Figure 6-38, both the GNSS mean estimations and their standard deviations in general agree with PFISR's measurements with a few exceptions between 9~11 UT.

In fact, the south-to-north velocities also agree well in general between the two systems, despite the geometry constraint.

For the distribution comparison, measurements from 1130 UT to 1630 UT are considered. In fact, the local geomagnetic disturbances are the greatest during this period (refer to Figure 6-3). The comparison results are plotted in Figure 6-39 below.

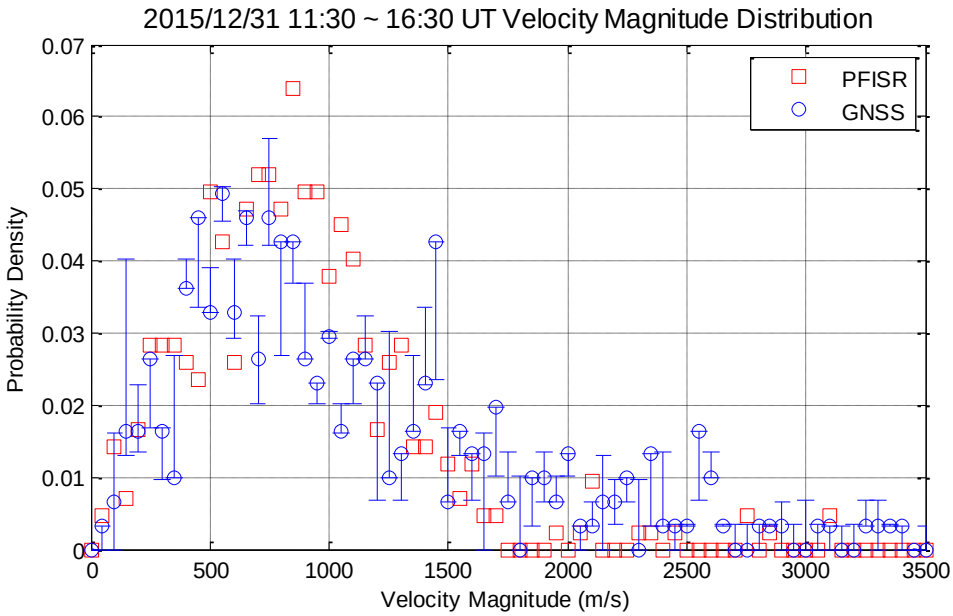

Figure 6-39. Cross-Comparison of the velocity magnitude distributions of the PFISR measurements and the GNSS estimations between 1130 and 1630 UT on 2015/12/31.

In Figure 6-39, a general agreement can again be observed between the two distributions. The GNSS results have slightly more occurrences in the velocities at 1400 m/s and above, while the PFISR results are slightly more concentrated between 500 m/s and 1100 m/s. This distribution comparison is conducted based on 5 hours of near-continuous measurements, which is only half of the time span as in the 2015/12/20 event. As a result, the variations caused by different irregularity altitude assumptions are larger than those from 2015/12/20 (refer to Figure 6-36).

6.8. Effective Irregularity Height Estimation Results

6.8.1. Estimation Results and Cross-comparison against PFISR

Following the technique described in Chapter 5, the effective irregularity heights are estimated for both the 2015/12/20 and the 2015/12/31 events using the Poker Flat array data. To analyze the results, we again resorted to the PFISR. Although PFISR's spatial coverage does not have much overlap with the Poker Flat array, it's electron density profiles often provide useful insights into the ionospheric irregularity heights. Hence a cross-comparison is conducted between the GNSS array estimated results and PFISR's measurements.

6.8.1.1. Results for the 2015/12/20 Event

The GNSS array estimated effective heights are plotted over PFISR's electron density profile from its zenith beam generated by alternating code measurements. Figure 6-41 shows the cross-comparison results. Note that the height estimation method is responsive to both enhancement and depletion of electrons in the irregularity structure. Because diffraction patterns are associated with carrier phase fluctuations, which may occur as the signal passes through either type of structures.

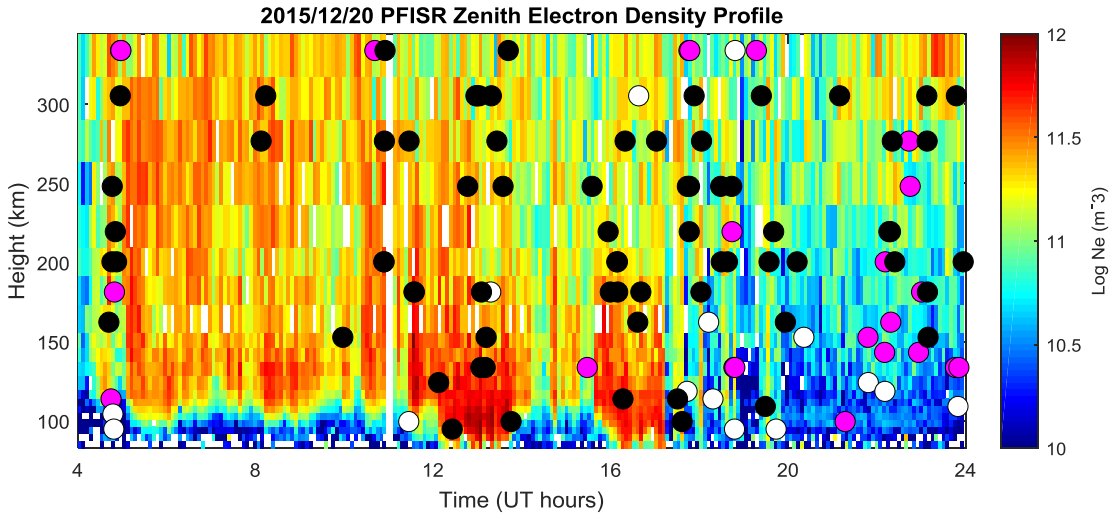

Figure 6-40. Estimated effective irregularity heights over the PFISR electron density profile from 0400 to 2400 UT on 2015/12/20. The estimated heights are represented by the colored dots,

showing whether the height can be associated with a global/local enhancement region (black), or a global/local depletion region (white), or neither (purple).

In Figure 6-40, most of the detected heights can be associated with either enhancement or depletion regions, while more matches can be found at enhancement regions. The GNSS effective heights are estimated every 25 seconds. But the matching process is based on PFISR's data resolution at 5-minute. Therefore, each color dot in Figure 6-40 may represent multiple matching heights between the GNSS and PFISR results. In fact, more than 80% of the time, the GNSS estimated effective heights can be associated with an enhancement/depletion region. This suggests that the effective height estimation method has the potential to provide good approximations to the actual irregularity heights.

To further analyze the cross-comparison result, individual electron density profile at each time epoch is plotted. In addition, the electron density profile from 2015/12/30 (the day with least magnetic activities of the month) at the same time epoch is plotted as a quiet-day reference. This will help us better understand how disturbed the ionosphere was comparing to its normal state. Figure 6-41 shows an example where the effective irregularity height is detected at an enhancement region.

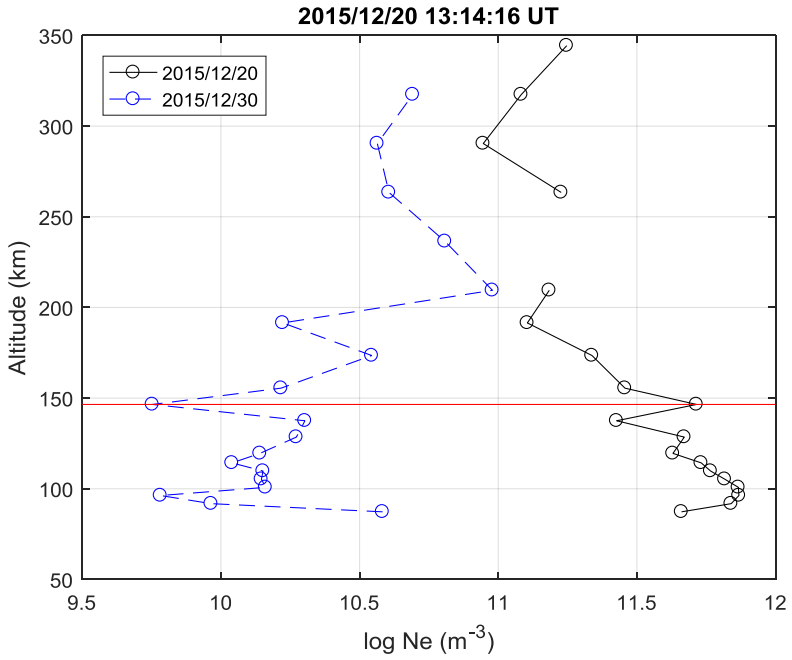

Figure 6-41. Example of estimated effective irregularity heights over individual PFISR electron density profile at 13:14:16 UT on 2015/12/20. The solid black line gives the electron density profile on 2015/12/20, while the dashed blue line gives the reference profile on 2015/12/30. The horizontal red line indicates the GNSS estimated effective irregularity height.

In Figure 6-41, the election density on 2015/12/20 is significantly higher than that on 2015/12/30, especially towards the bottom F-layer, indicating strong activities. The height estimation method identifies the effective irregularity layer at around 145 km. The profile value is registered at more than $10^{11.5}$ electrons per m^3, while the concurrent 2015/12/30 profile value at the same height is less than 10^{10} electrons per m^3. These evidences suggest that the irregularity height has been correctly identified. More examples showing enhancement matches are given in Figure 6-42.

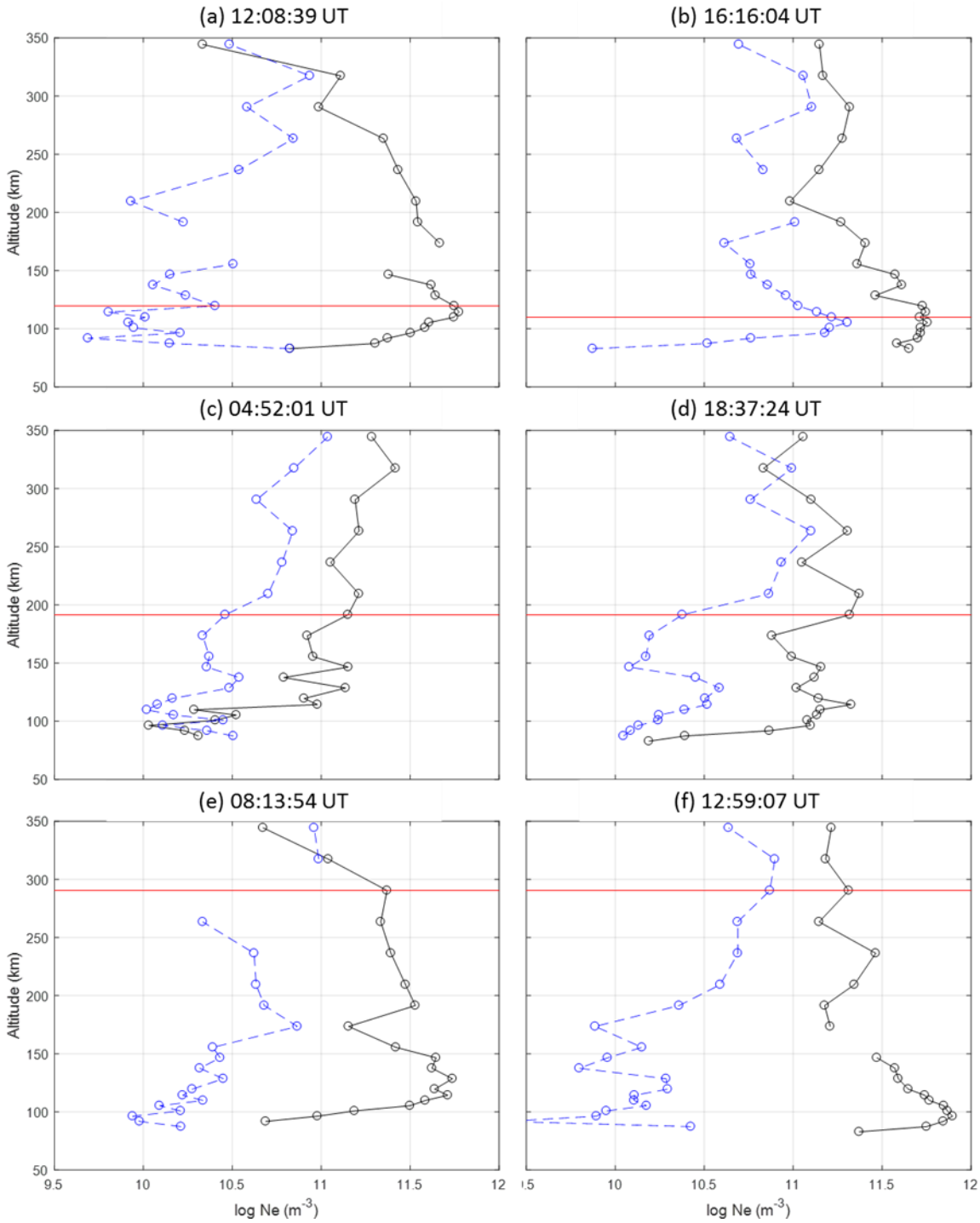

Figure 6-42. Examples of estimated effective irregularity heights matching with PFISR electron enhancement regions on 2015/12/20.

In Figure 6-42, subplots (a) and (b) show matches at/near global density peaks towards lower altitude values. Subplots (c) and (d) show matches at local density peaks near the mean layer

heights around 210 km and 175 km, respectively. Subplots (e) and (f) show matches at/near local density peaks towards higher altitude values. Matches with depletion regions have also been observed. An example is given in Figure 6-46.

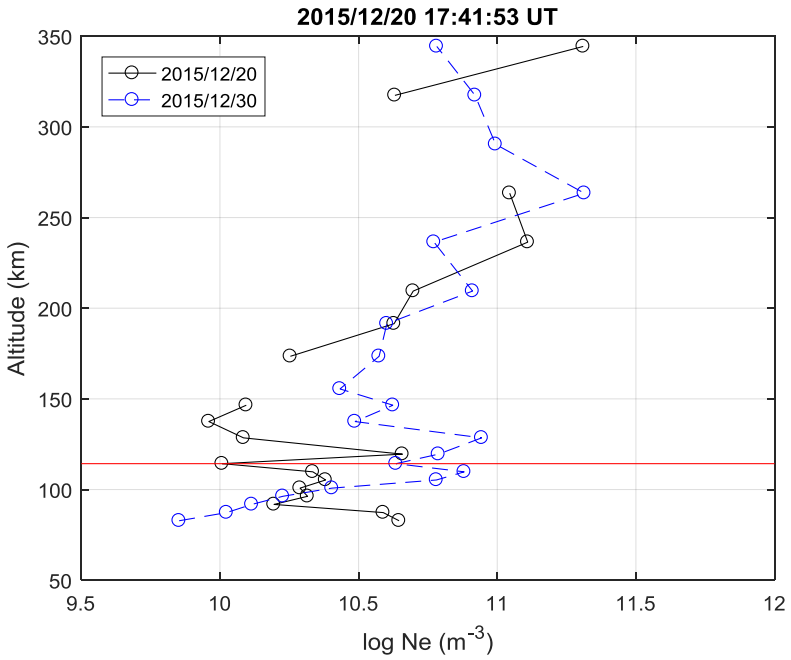

Figure 6-43. Example of estimated effective irregularity heights matching with PFISR electron depletion regions at 17:41:53 UT on 2015/12/20.

In this example, the election density on 2015/12/20 is smaller than that on 2015/12/30. More fluctuations can be observed on the 2015/12/20 profile towards lower altitudes. The estimated effective height appears to be at a local depletion region within the nearby enhancement region. Again, the irregularity height is likely to be correctly identified. More examples showing depletion matches are given in Figure 6-44.

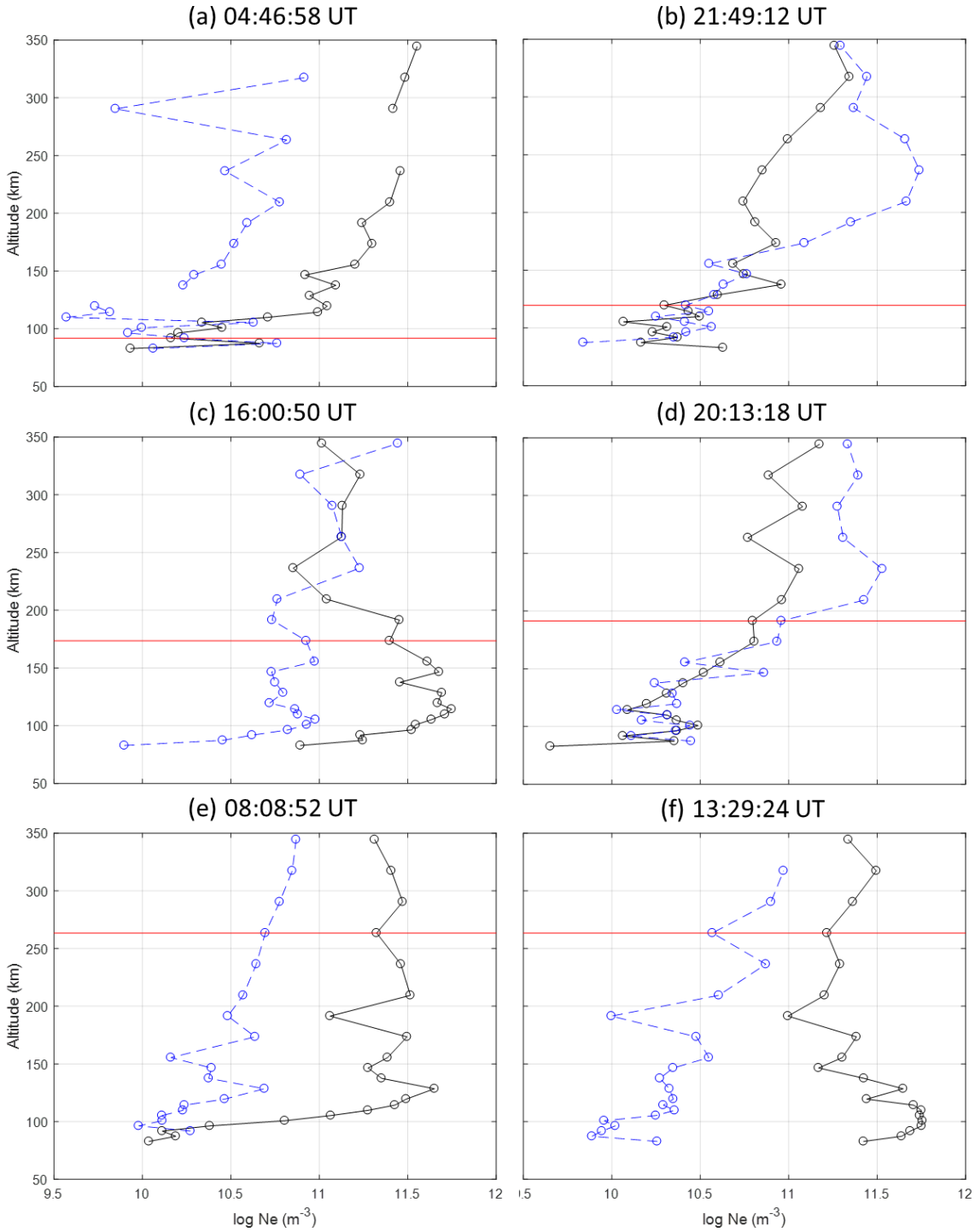

Figure 6-44. Examples of estimated effective irregularity heights matching with PFISR electron depletion regions on 2015/12/20.

In Figure 6-45, subplots (a) and (b) show matches at local depletion within the lowest density layers around 90 km and 120 km, respectively. Subplots (c) and (d) show matches at local

density valley near the mean layer heights around 175 km and 190 km. Subplots (e) and (f) show matches at local density valleys at around 265 km.

There exist cases where multiple satellites detected distinct irregularity heights at the same epoch. Figure 6-48 shows some examples.

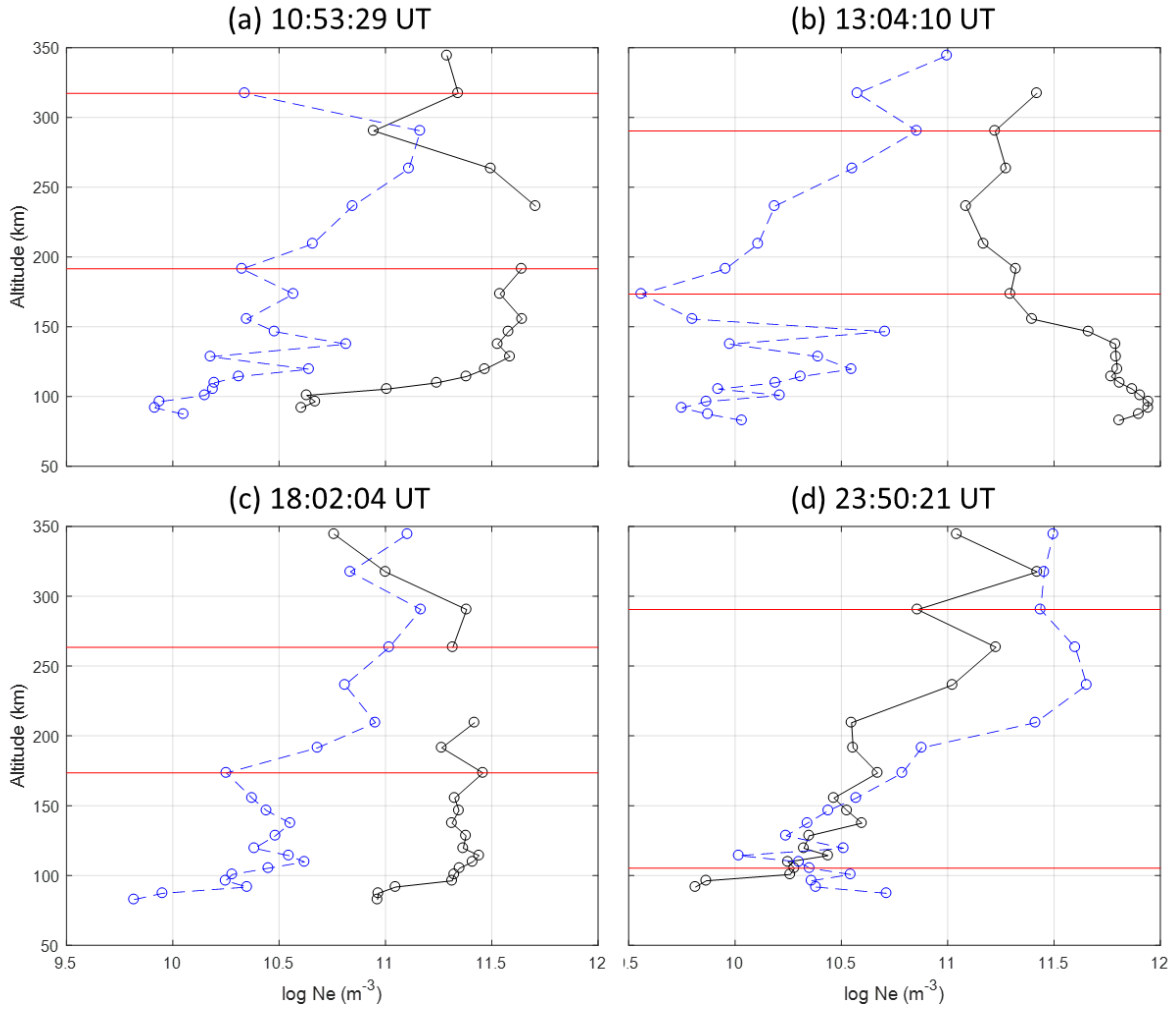

Figure 6-45. Examples of estimated effective irregularity heights matching with multiple PFISR electron enhancement/depletion regions on 2015/12/20

In Figure 6-45, subplot (a) shows two local enhancement matches, one near 190 km, and the other near 320 km. Subplot (b) shows two local depletion matches, both are slightly lower than the detected irregularity heights in subplot (a), respectively. Subplots (c) and (d) each shows an

enhancement match and a depletion match. The estimated irregularity heights in subplot (c) are closer to the 220 km, while the heights in subplot (d) is more spread out toward higher and lower regions in the ionosphere.

There also exist cases where no distinct irregularity structures can be observed near the estimated effective irregularity heights. Figure 6-46 shows an example illustrating this scenario.

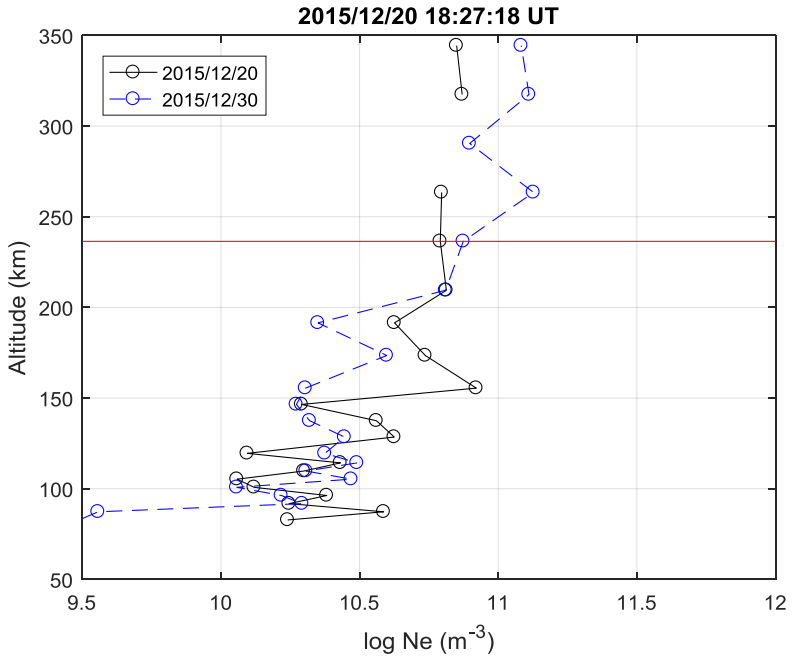

Figure 6-46. Example of estimated effective irregularity heights that does not show good match with electron enhancement/depletion regions from PFISR at 18:27:18 UT on 2015/12/20.

In this example, the overall Ne profile on 2015/12/20 is very similar to that of 2015/12/30, showing no obvious irregularity structures. The GNSS estimated height is likely a false alarm as the height value lands in a region without noticeable depletion or enhancement in the Ne profile.

6.8.1.2. Results for the 2015/12/31 Event

The same estimation and cross-comparison process is applied to the 2012/12/31 event. Similar to Figure 6-40, the overall cross-comparison is illustrated by Figure 6-47.

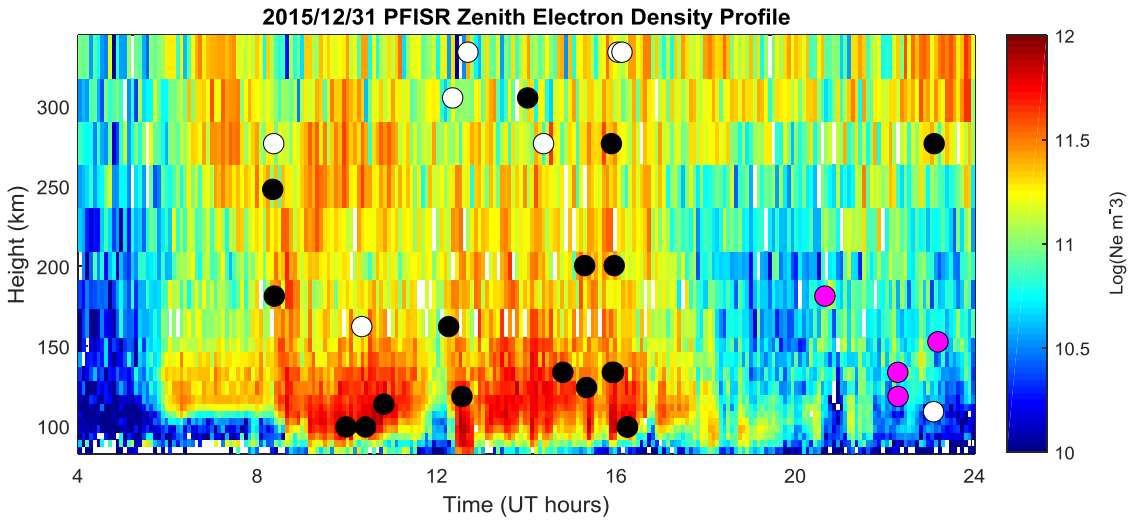

Figure 6-47. Estimated effective irregularity heights over the PFISR electron density profile from 0400 to 2400 UT on 2015/12/31.

Like the 2015/12/20 example, in Figure 6-48, most of the detected heights can be associated with either enhancement or depletion regions. This geomagnetic storm event is not as severe as the case during the 2015/12/20 event. Hence, the total number of detected heights as well as the number of enhancement and depletion matches are less than the previous example. Also, the irregularity structures in the 2015/12/31 event appear to be better defined than those in the 2015/12/20 event. The detected irregularities in Figure 6-47 are not as scattered as in Figure 6-40. Statistics wise, more than 85% of the time, the GNSS estimated effective heights can be associated with an enhancement/depletion region.

Again, the individual cross-comparisons are demonstrated, also using 2015/12/30 as a quiet-day reference. Figure 6-48 shows some examples associated with enhancements in the density.

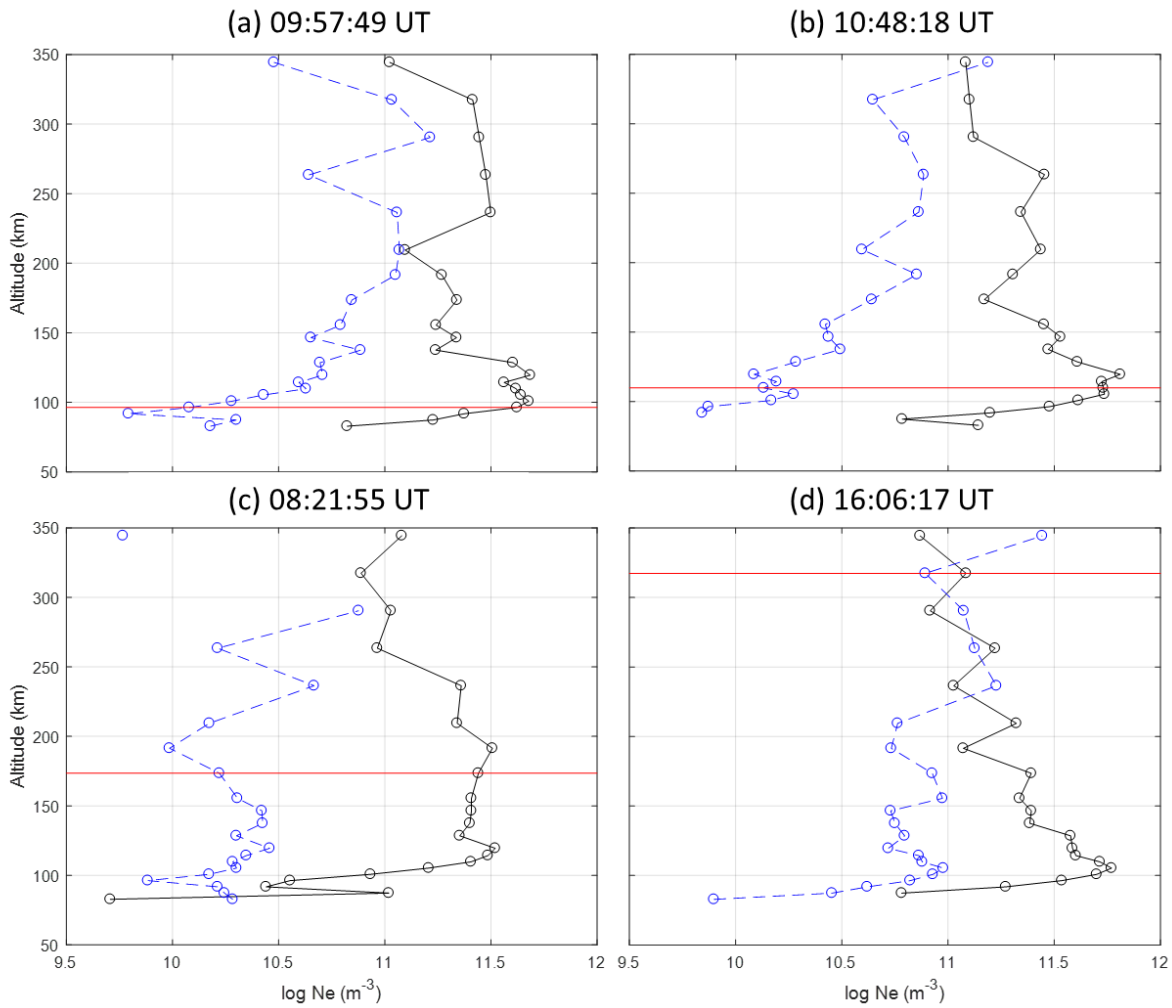

Figure 6-48. Examples of estimated effective irregularity heights matching with PFISR electron enhancement regions on 2015/12/31.

In Figure 6-48, subplots (a) and (b) show matches near the global density peaks around 95 km and 110 km, respectively. As indicated by Figure 6-47, enhancement matches like these are very common for this event. Subplots (c) shows a match at the local density peak near the mean layer heights at 175 km. Subplots (d) shows match at local density peak around 320 km.

Matches with depletion regions have also been observed. Selected examples are given in Figure 6-50.

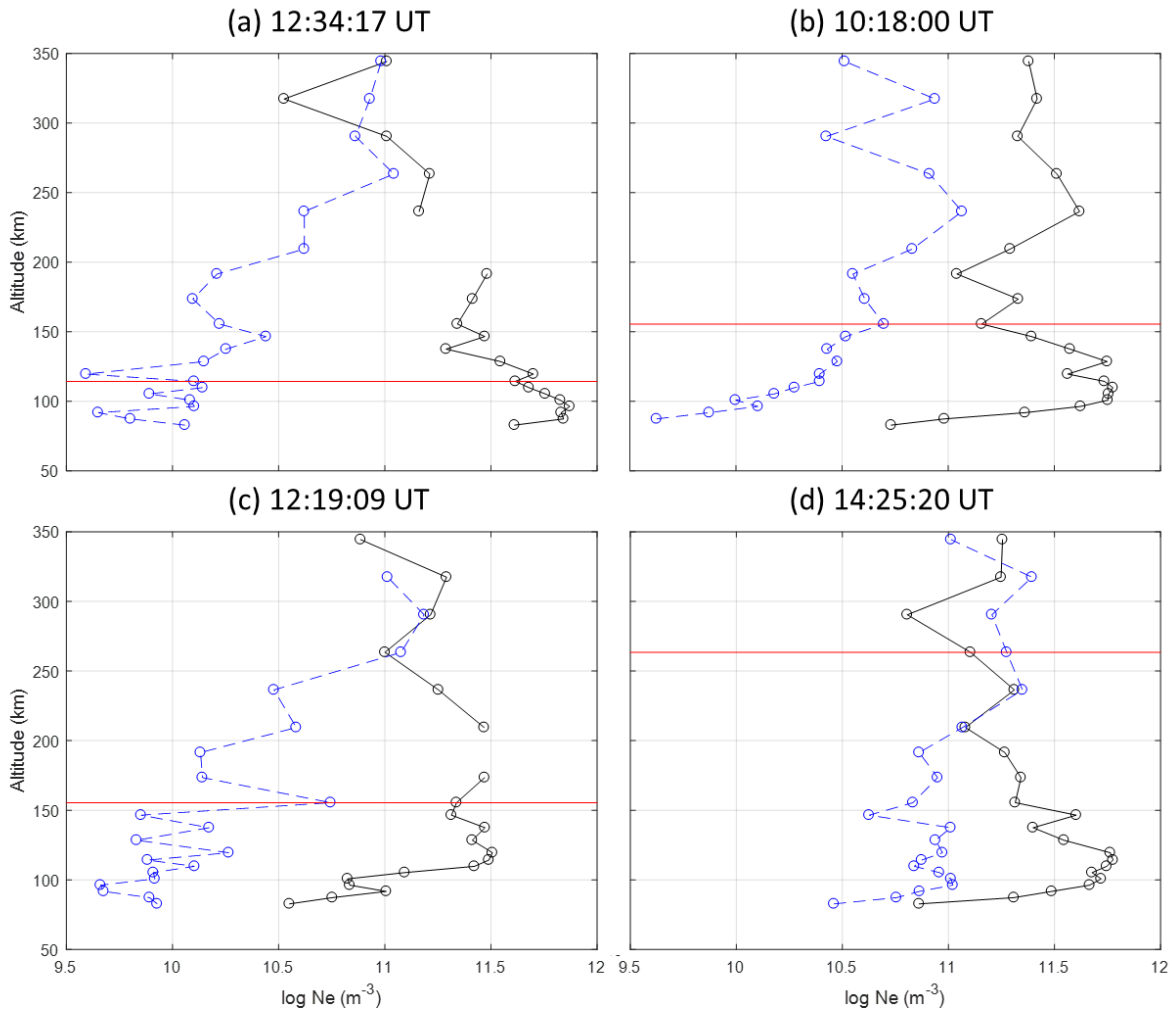

Figure 6-49. Examples of estimated effective irregularity heights matching with PFISR electron depletion regions on 2015/12/31.

In Figure 6-49, subplot (a) shows a match at a local density valley within the peak density layer around 120 km. Subplots (b) and (c) each has a match with the density valley at around 155 km. Subplots (c) and (d) shows a match near the local density valley 200 km. Subplots (d) shows a match near the global density valley around 260 km.

Concurrent detections of effective irregularity heights from multiple satellites have also been observed. Figure 6-50 shows two examples.

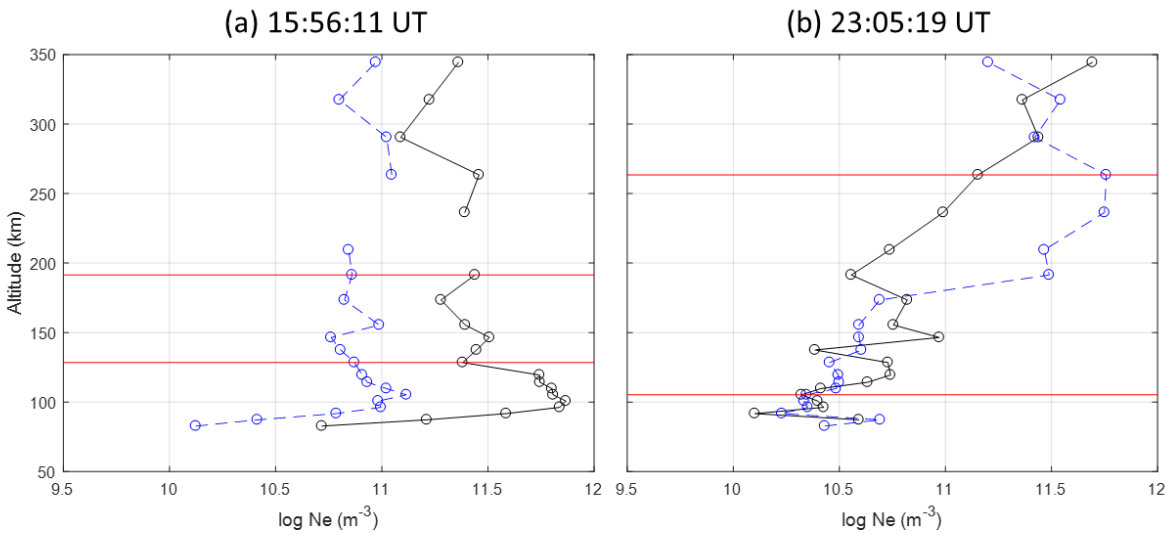

Figure 6-50. Examples of estimated effective irregularity heights matching with multiple PFISR electron enhancement/depletion regions on 2015/12/31.

In Figure 6-50, subplot (a) show one match at a local density valley around 130 km and another match at a local density peak around 190 km. Subplot (b) shows one match at a local density valley around 105 km and another match near a local density peak around 270 km.

7. CHAPTER 7 – SUMMARY

In this dissertation, the ground work for irregularity drift velocity estimation has been established. The main contribution includes the TDM and TFDM for time lag estimation, the hybrid correlation model for apparent irregularity pattern drift estimation, and the inversion technique for effective irregularity height estimation. Using these algorithms, the ionospheric irregularity drift velocity and effective height can be estimated.

A self-consistency study has been conducted utilizing different GNSS signals from the HAARP array data using the TFDM. The results are satisfactory towards stronger scintillation conditions. Another self-consistency study between the TDM and the TFDM has been conducted based on the Poker Flat array data. The two methods demonstrate comparable drift velocity estimations, while the TFDM appears to be producing slightly more consistent results. A comparison study is conducted on the front velocity model, the anisotropy model and the hybrid correlation model. The hybrid model demonstrated superior performance in both velocity orientation and magnitude estimation. This model is employed to calculated drift velocity estimates.

Drift velocity estimation results have been compared against SuperDARN backscatter measurements based on the HAARP array data. Fair correlation between 20% and 30% has been found between GNSS recorded scintillation events and SuperDARN observed backscatters. However, the drift velocity comparison did not yield satisfactory results, which may due to the intrinsic difference between the two systems when measuring the ionosphere irregularities.

Drift velocity estimations have been cross-compared against PFISR vector velocity measurements based on the Poker Flat array data. Two case studies during intense geomagnetic

storm events on 2015/12/20 and 2015/12/31 have been conducted. The cross-comparison results between the GNSS array and the PFISR are favorable in both cases. Similar spatial and temporal features, mean velocity behaviors and velocity magnitude distributions have been observed between the two systems. ASI data and geomagnetic field parameters also supports these results. Based on these results, we conclude that the phase-scintillation-based GNSS spaced-receiver technique for irregularity drift velocity estimation is viable for high latitude studies.

The effective irregularity height estimation method based on the anisotropy model has also been implemented. The technique is applied to both the 2015/12/20 and the 2015/12/31 events using the Poker Flat array data. The estimation results are compared favorably against the electron density profiles from PFISR measurements. More than 80% of the time, the GNSS estimated effective heights can be associated with an enhancement/depletion region in the PFISR Ne profiles.

A key component of this inversion algorithm is to accurately estimate the magnetic field parameters. At high latitudes, in addition to the Earth's magnetic field, the interplanetary magnetic field is also an important governing factor of the scintillation mechanism. Meanwhile, AMPERE (Active Magnetosphere and Planetary Electrodynamics Response Experiment) is able to provide near-realtime global magnetic field measurements using the Iridium satellite constellation at 780 km altitude [*Anderson et al.*, 2008]. This spaceborne system can potentially compliment the B-field estimation method from ground stations described in this study.

Based on these self-consistency tests and cross-comparison studies, the spaced-GNSS receiver techniques developed in this dissertation demonstrated great feasibility and capability in the field of ionosphere remote sensing. The techniques are presented based on GNSS carrier phase measurements obtained from the HAARP array and the Poker Flat array. Nevertheless, the same principle can be applied to any phase-scintillation-based spaced-receiver array system.

In the future, similar spaced-GNSS receiver systems can be deployed to both high-latitude and low-latitude regions to provide continuous ionospheric irregularity drift velocity and effective height estimates during ionospheric scintillations. The AMPERE magnetic field measurements will be investigated to improve the current method. Additionally, more case studies during scintillations will be conducted to further verify this inversion algorithm in both high latitude and equatorial regions.

REFERENCES

Aarons, J. (1982). Global morphology of ionospheric scintillations. *Proceedings of the IEEE*, 70(4), 360-378.

Aarons, J., & Basu, S. (1994). Ionospheric amplitude and phase fluctuations at the GPS frequencies. In *ION GPS-94* (pp. 1569-1578).

Aarons, J., Mendillo, M., Yantosca, R., & Kudeki, E. (1996). GPS phase fluctuations in the equatorial region during the MISETA 1994 campaign. *Journal of Geophysical Research: Space Physics (1978–2012)*, *101*(A12), 26851-26862.

Aarons, J. (1997). Global positioning system phase fluctuations at auroral latitudes. *Journal of Geophysical Research: Space Physics (1978–2012)*, 102(A8), 17219-17231.

Alfonsi, L., Spogli, L., De Franceschi, G., Romano, V., Aquino, M., Dodson, A., & Mitchell, C. N. (2011). Bipolar climatology of GPS ionospheric scintillation at solar minimum. *Radio Science*, *46*(3).

Anderson, D. N., & Mendillo, M. (1983). Ionospheric conditions affecting the evolution of equatorial plasma depletions. *Geophysical research letters*, *10*(7), 541-544.

Anderson, B. J., Korth, H., Waters, C. L., Barnes, R. M., & Weiss, M. B. (2008, December). The Active Magnetosphere and Planetary Electrodynamics Response Experiment (AMPERE): A new facility for real-time magnetosphere-ionosphere monitoring. In *AGU Fall Meeting Abstracts*.

Aquino, M., Moore, T., Dodson, A., Waugh, S., Souter, J., & Rodrigues, F. S. (2005). Implications of ionospheric scintillation for GNSS users in Northern Europe. *Journal of Navigation*, *58*(02), 241-256.

Armstrong, J. W., & Coles, W. A. (1972). Analysis of three-station interplanetary scintillation. *Journal of Geophysical Research*, *77*(25), 4602-4610

Azeem, I., Crowley, G., Reynolds, A., Santana, J., & Hampton, D. (2013). First results of phase scintillation from a longitudinal chain of ASTRA's SM-211 GPS TEC and scintillation receivers in Alaska. *Proc. ION Pacific PNT,* Honolulu, HI.

Basu, S., & Basu, S. (1981). Equatorial scintillations—A review. *Journal of Atmospheric and Terrestrial Physics*, 43(5), 473-489.

Basu, S., & Basu, S. (1985). Equatorial scintillations: Advances since ISEA-6. *Journal of atmospheric and terrestrial physics*, *47*(8), 753-768.

Basu, S., Basu, S., Kuoeki, E., Zengingonul, H. P., Biondi, M. A., & Meriwether, J. W. (1991 a). Zonal irregularity drifts and neutral winds measured near the magnetic equator in Peru. *Journal of Atmospheric and Terrestrial Physics*, *53*(8), 743-755.

Basu, S., Basu, S., Costa, E., Bryant, C., Valladares, C. E., & Livingston, R. C. (1991 b). Interplanetary magnetic field control of drifts and anisotropy of high-latitude irregularities. *Radio science*, 26(4), 1079-1103.

Basu, S., Kudeki, E., Basu, S., Valladares, C. E., Weber, E. J., Zengingonul, H. P. et al. (1996). Scintillations, plasma drifts, and neutral winds in the equatorial ionosphere after sunset. *Journal of Geophysical Research: Space Physics (1978–2012)*, *101*(A12), 26795-26809.

Basu, S., Groves, K. M., Basu, S., & Sultan, P. J. (2002). Specification and forecasting of scintillations in communication/navigation links: Current status and future plans. *Journal of atmospheric and solar-terrestrial physics*, *64*(16), 1745-1754.

Beach, T. L. (2006). Perils of the GPS phase scintillation index (σϕ). *Radio science*, *41*(5).

Béniguel, Y., Romano, V., Alfonsi, L., Aquino, M., Bourdillon, A., & Cannon, et al. (2009). Ionospheric scintillation monitoring and modeling. *Annals of Geophysics*, 52(3-4), 391-496.

Birch, M. J., Hargreaves, J. K., & Bailey, G. J. (2002). On the use of an effective ionospheric height in electron content measurement by GPS reception. *Radio Science*, *37*(1).

Brenneman, M., Morton, Y., Zhou, Q., & Distler, G. (2007). GPS interference sources angle of arrival estimation using an adaptive periodogram technique. *Proc. ION NTM*, San Diego, CA.

Briggs, B. H., Phillips, G. J., & Shinn, D. H. (1950). The analysis of observations on spaced receivers of the fading of radio signals. *Proceedings of the Physical Society. Section B*, *63*(2), 106.

Briggs, B. H., & Parkin, I. A. (1963). On the variation of radio star and satellite scintillations with zenith angle. *Journal of Atmospheric and Terrestrial Physics*, *25*(6), 339-366.

Briggs, B. H. (1968). On the analysis of moving patterns in geophysics—I. Correlation analysis. *Journal of Atmospheric and Terrestrial Physics*, *30*(10), 1777-1788.

Bristow, W. A. (2007). Super Dual Auroral Radar Network – SuperDARN. *CEDAR-DASI Workshop*, Santa Fe, NM.

Bristow, W. A., Sofko, G. J., Stenbaek-Nielsen, H. C., Wei, S., Lummerzheim, D., & Otto, A. (2003). Detailed analysis of substorm observations using SuperDARN, UVI, ground-based magnetometers, and all-sky imagers. *Journal of Geophysical Research: Space Physics*, *108*(A3).

Budden, K. G. (1965). The amplitude fluctuations of the radio wave scattered from a thick ionospheric layer with weak irregularities. *Journal of Atmospheric and Terrestrial Physics*, *27*(2), 155-172.

Carrano, C. S., Groves, K. M., Rino, C. L., & Doherty, P. H. (2016). A technique for inferring zonal irregularity drift from single-station GNSS measurements of intensity (S4) and phase (σφ) scintillations. *Radio Science*, *51*(8), 1263-1277.

Carrano, C. S., Groves, K. M., Rino, C. L., & McNeil, W. J. (2017, January). A propagation model for geolocating ionospheric irregularities along radio occultation ray-paths. In *Radio Science Meeting (USNC-URSI NRSM), 2017 United States National Committee of URSI National* (pp. 1-2). IEEE.

Chatterjee, A., Fournier, R., Naït-Ali, A., & Siarry, P. (2010). A postural information-based biometric authentication system employing S-transform, radial basis function network, and extended Kalman filtering. *Instrumentation and Measurement, IEEE Transactions on*, *59*(12), 3131-3138.

Chisham, G., Lester, M., Milan, S. E., Freeman, M. P., Bristow, W. A., Grocott, A., ... & Greenwald, R. A. (2007). A decade of the Super Dual Auroral Radar Network (SuperDARN): Scientific achievements, new techniques and future directions. *Surveys in Geophysics*, *28*(1), 33-109.

Cohen, L. (1995). Uncertainty principles of the short-time Fourier transform. *SPIE's 1995 International Symposium on Optical Science, Engineering, and Instrumentation*, 80-90.

Costa, E., Fougere, P. F., & Basu, S. (1988). Cross-correlation analysis and interpretation of spaced-receiver measurements. *Radio science, 23(02)*, 141-162.

Crowley, G., Bust, G. S., Reynolds, A., Azeem, I., Wilder, R., O'Hanlon, B. W., ... & Bhatti, J. A. (2011). CASES: A novel low-cost ground-based dual-frequency GPS software receiver and space weather monitor. *Proc. ION GNSS*, 1437-1446, Portland, OR.

Culot, F., Lathuillere, C., Lilensten, J., & Witasse, O. (2004). The OI 630.0 and 557.7 nm dayglow measured by WINDII and modeled by TRANSCAR. In *Annales Geophysicae* (Vol. 22, No. 6, pp. 1947-1960)

Deshpande, K. B., G. S. Bust, C. R. Clauer, C. L. Rino, and C. S. Carrano (2014), Satellite-beacon Ionospheric-scintillation Global Model of the upper Atmosphere (SIGMA) I: High-latitude sensitivity study of the model parameters, *J. Geophys. Res., Space Physics*, *119, 4026–4043, doi:10.1002/2013JA019699*.

Doherty, P. H., Delay, S. H., Valladares, C. E., & Klobuchar, J. A. (2003). Ionospheric scintillation effects on GPS in the equatorial and auroral regions. *Navigation*, *50*(4), 235-245.

Dyrud, L., Bhatia, N., Ganguly, S., & Jovancevic, A. (2005). Performance analysis of software based GPS receiver using a generic ionospheric scintillation model. *Proc. ION GNSS*, 1402-1414, Fort Worth, TX.

Evans, J. V. (1969). Theory and practice of ionosphere study by Thomson scatter radar. *Proceedings of the IEEE*, *57*(4), 496-530.

Fedor, L. S. (1967). A statistical approach to the determination of three-dimensional ionospheric drifts. *Journal of Geophysical Research*, *72*(21), 5401-5415.

Forte, B., & Radicella, S. M. (2002). Problems in data treatment for ionospheric scintillation measurements. *Radio Science*, *37*(6), 8-1.

Fortes, L. P. S., Lin, T., & Lachapelle, G. (2015). Effects of the 2012–2013 solar maximum on GNSS signals in Brazil. *GPS Solutions, 19(2)*, 309-319.

Fremouw, E. J., Livingston, R. C., & Miller, D. A. (1980). On the statistics of scintillating signals. *Journal of Atmospheric and Terrestrial Physics*, *42*(8), 717-731.

Gonzalez, W. D., Joselyn, J. A., Kamide, Y., Kroehl, H. W., Rostoker, G., Tsurutani, B. T., and Vasyliunas, V. M. (1994). What is a geomagnetic storm?. *Journal of Geophysical Research: Space Physics*, *99*(A4), 5771-5792.

Greenwald, R. A., Baker, K. B., Dudeney, J. R., Pinnock, M., Jones, T. B., Thomas, E. C., ... & Hunsucker, R. D. (1995). Darn/Superdarn. *Space Science Reviews*, *71*(1-4), 761-796.

Groves, K. M., Basu, S., Quinn, J.M., Pedersen, T.R., Falinski, K., Brown A., Silva, R., & Ning, P. (2000). A comparison of GPS performance in a scintillating environment at Ascension Island. *Proc. ION GPS*, Salt Lake City, UT.

Gu, Y. H., & Bollen, M. H. (2000). Time-frequency and time-scale domain analysis of voltage disturbances. *Power Delivery, IEEE Transactions on*, *15*(4), 1279-1284.

Hegarty, C., El-Arini, M. B., Kim, T., & Ericson, S. (2001). Scintillation modeling for GPS-Wide Area Augmentation System receivers. *Radio Science*,*36*(5), 1221-1231.

Heinselman, C. J., & Nicolls, M. J. (2008). A Bayesian approach to electric field and E-region neutral wind estimation with the Poker Flat Advanced Modular Incoherent Scatter Radar. *Radio Science*, *43*(5).

Humphreys, T. E., Psiaki, M. L., Hinks, J. C., O'Hanlon, B., & Kintner, P. M. (2009). Simulating ionosphere-induced scintillation for testing GPS receiver phase tracking loops. *Selected Topics in Signal Processing, IEEE Journal of*,*3*(4), 707-715.

Humphreys, T. E., Psiaki, M. L., & Kintner, P. M. (2010). Modeling the effects of ionospheric scintillation on GPS carrier phase tracking. *IEEE Transactions on Aerospace and Electronic Systems*, *46*(4), 1624-1637.

Hysell, D. L., & Kudeki, E. (2004). Collisional shear instability in the equatorial F region ionosphere. *Journal of Geophysical Research: Space Physics*, *109*(A11).

Ji, S., Chen, W., Ding, X., & Zhao, C. (2011). Equatorial ionospheric zonal drift by monitoring local GPS reference networks. *Journal of Geophysical Research: Space Physics (1978–2012)*, *116*(A8).

Jiao, Y., Morton, Y. T., Taylor, S., & Pelgrum, W. (2013a). High latitude ionosphere scintillation characterization. *Proc. ION ITM,* San Diago, CA.

Jiao, Y., Morton, Y., Taylor, S., & Pelgrum, W. (2013b). On the correlation between ionospheric scintillation and geomagnetic field activities, Proc. ION GNSS+, 77-83, Nashville, TN.

Jiao, Y., Morton, Y. T., Taylor, S., & Pelgrum, W. (2013c). Characterization of high-latitude ionospheric scintillation of GPS signals. *Radio Science*, 48(6), 698-708.

Jiao, Y. (2013). High latitude ionospheric scintillation characterization. *Master Thesis*, Miami University, Oxford.

Jiao, Y., Morton, Y., & Taylor, S. (2014a). Comparative studies of high-latitude and equatorial ionospheric scintillation characteristics of GPS signals. In *2014 IEEE/ION Position, Location and Navigation Symposium-PLANS 2014* (pp. 37-42). IEEE.

Jiao, Y., Y. Morton, S. Taylor, and M. Carroll (2014b), Characteristics of low-latitude signal fading across the GPS frequency bands, Proc. ION GNSS+, 1203-1212, Tampa, FL, US.

Jiao, Y., Y. Morton, D. Akos, and T. Walter (2015), A comparative study of triple frequency GPS scintillation signal amplitude fading characteristics at low latitudes, Proc. ION GNSS+, Tampa, FL,.

Jiao, Y., and Y. Morton (2015), Comparison of the effect of high-latitude and equatorial ionospheric scintillation on GPS signals during the maximum of solar cycle 24, *Radio Sci., 50*(9), 886-903, doi: 10.1002/2015RS005719.

Jiao, Y., Xu, D., Rino, C. L., Morton, Y. T., & Carrano, C. S. (2018). Multi-frequency GPS Signal Strong Equatorial Ionospheric Scintillation Simulator: Algorithm, Performance, and Characterization. *IEEE Transactions on Aerospace and Electronic Systems*. doi: 10.1109/TAES.2018.2805232.

Kelley, M. C., Larsen, M. F., LaHoz, C., & McClure, J. P. (1981). Gravity wave initiation of equatorial spread F: A case study. *Journal of Geophysical Research: Space Physics*, *86*(A11), 9087-9100.

Kersley, L., Pryse, S. E., & Wheadon, N. S. (1988). Amplitude and phase scintillation at high latitudes over northern Europe. *Radio Science*, *23*(3), 320-330.

Kersley, L., Russell, C. D., & Rice, D. L. (1995). Phase scintillation and irregularities in the northern polar ionosphere. *Radio science*, *30*(3), 619-629.

Khudukon, B. Z., Tereshchenko, E. D., Galinov, A. V., Popov, A. A., & Nygren, T. (1994). Determination of drift velocity and anisotropy of irregularities in the auroral ionosphere using radio source scintillation. *Journal of atmospheric and terrestrial physics*, *56*(1), 93-102.

Kil, H., Kintner, P. M., Paula, E. R., & Kantor, I. J. (2000). Global Positioning System measurements of the ionospheric zonal apparent velocity at Cachoeira Paulista in Brazil. *Journal of Geophysical Research: Space Physics (1978–2012)*, *105*(A3), 5317-5327.

Kil, H., Kintner, P. M., de Paula, E. R., & Kantor, I. J. (2002). Latitudinal variations of scintillation activity and zonal plasma drifts in South America. *Radio Science*, *37*(1), 6-1.

Kintner, P. M., Ledvina, B. M., De Paula, E. R., & Kantor, I. J. (2004). Size, shape, orientation, speed, and duration of GPS equatorial anomaly scintillations. *Radio Science*, *39*(2).

Kintner, P. M., and Ledvina, B. M. (2005). The Ionosphere, radio navigation, and global navigation satellite systems. *Advances in Space Research, 35, 788-811*.

Kintner, . M., Ledvina, B. M., & De Paula, E. R. (2007). GPS and ionospheric scintillations. *Space weather*, *5*(9).

Klobuchar, J. A. (1987). Ionospheric time-delay algorithm for single-frequency GPS users. *Aerospace and Electronic Systems, IEEE Transactions on*, (3), 325-331.

Komjathy, A., & Langley, R. B. (1996, March). The effect of shell height on high precision ionospheric modelling using GPS. In *Proceedings of the 1996 IGS Workshop International GPS Service for Geodynamics (IGS)* (Vol. 203).

Kursinski, E. R., Hajj, G. A., Schofield, J. T., Linfield, R. P., & Hardy, K. R. (1997). Observing Earth's atmosphere with radio occultation measurements using the Global Positioning System. *Journal of Geophysical Research: Atmospheres*, *102*(D19), 23429-23465.

Leick, A. (1995): GPS Satellite Surveying, 2nd edition, *John Wiley & Sons, Inc.,* New York, 352-357.

Ledvina, B. M., Kintner, P. M., & de Paula, E. R. (2004). Understanding spaced-receiver zonal velocity estimation. *Journal of geophysical research*,*109*(A10), A10306.

Li, G., Ning, B., Ren, Z., & Hu, L. (2010). Statistics of GPS ionospheric scintillation and irregularities over polar regions at solar minimum. *GPS solutions*, *14*(4), 331-341.

Liu, Z. (2011). A new automated cycle slip detection and repair method for a single dual-frequency GPS receiver. *Journal of Geodesy*, 85(3), 171-183.

Livingston, R. C., Rino, C. L., Owen, J., & Tsunoda, R. T. (1982). The anisotropy of high-latitude nighttime F region irregularities. *Journal of Geophysical Research: Space Physics*, *87*(A12), 10519-10526.

Lomb, N. R. (1976). Least-squares frequency analysis of unequally spaced data. *Astrophysics and space science*, *39*(2), 447-462.

Lyatskaya, S., Lyatsky, W., and Khazanov, G. V. (2008). Relationship between substorm activity and magnetic disturbances in two polar caps. *Geophysical Research Letters, 35*(20).

Mao, X., & Morton, Y. (2013). GNSS Receiver Carrier Tracking Loop Impact on Ionosphere Scintillation Signal C/N0 and Carrier Phase Estimation. *Proc. ION GNSS, Nashville, TN.*

Martin, E., & Aarons, J. (1977). F layer scintillations and the aurora. *Journal of Geophysical Research*, *82*(19), 2717-2722.

McClure, J. P. (1964). The height of scintillation-producing ionospheric irregularities in temperate latitudes. *Journal of Geophysical Research*, *69*(13), 2775-2780.

Mendillo, M., & Baumgardner, J. (1982). Airglow characteristics of equatorial plasma depletions. *Journal of Geophysical Research: Space Physics*, *87*(A9), 7641-7652.

Misra, P., & Enge, P. (2006). Global Positioning System: Signals, Measurements and Performance Second Edition. *Massachusetts: Ganga-Jamuna Press*, 449-450.

Mitra, S. N. (1949). A radio method of measuring winds in the ionosphere. *Proceedings of the IEE-Part III: Radio and Communication Engineering*, *96*(43), 441-446.

Morrissey, T. N., Shallberg, K. W., Van Dierendonck, A. J., & Nicholson, M. J. (2004). GPS receiver performance characterization under realistic ionospheric phase scintillation environments. *Radio Science*, *39*(1).

Morton, Y., Bourne, H., Carroll, M., Jiao, Y., Kassabian, N., Taylor, S., ... & Yin, H. (2014). Multi-constellation GNSS observations of equatorial ionospheric scintillation. In *General Assembly and Scientific Symposium (URSI GASS), 2014 XXXIth URSI* (pp. 1-4). IEEE.

Mushini, S. C., Jayachandran, P. T., Langley, R. B., MacDougall, J. W., & Pokhotelov, D. (2012). Improved amplitude-and phase-scintillation indices derived from wavelet detrended high-latitude GPS data. *GPS solutions*, 16(3), 363-373.

Myers, W. J., Gjeldum, R. J., Liu, C. H., & Yeh, K. C. (1979). A study of ionospheric scintillations of phase and quadrature components. *Journal of Geophysical Research: Space Physics (1978–2012)*, *84*(A5), 2039-2048.

Nicolls, M. J., and C. J. Heinselman (2007), Three-dimensional measurements of traveling ionospheric disturbances with the Poker Flat Incoherent Scatter Radar, *Geophys. Res. Lett.*, 34, L21104, doi:10.1029/2007GL031506.

Niu, F., Morton, Y., Wang, J., & Pelgrum, W. (2012). GPS carrier phase detrending methods and performances for ionosphere scintillation studies. *Proc. ION GNSS*, 2000, 1462-1467.

Niu, F. (2012), Performances of GPS signal observables detrending methods for ionosphere scintillation studies, A Master Thesis.

O´Hanlon, B., Psiaki, M., Powell, S., Bhatti, J., Humphreys, T. E., Crowley, G., & Bust, G. (2011). CASES: A smart, compact GPS software receiver for space weather monitoring. *Proc. ION GNSS*, Portland, OR.

Otsuka, Y., K. Shiokawa, and T. Ogawa (2006). Equatorial ionospheric scintillations and zonal irregularity drifts observed with closely-spaced GPS receivers in Indonesia. J. meteorological Society of Japan, 84A, 343-351.

Pelgrum, W., Morton, Y., Van Graas, F., Vikram, P., & Peng, S. (2011). Multi-domain analysis of the impact on natural and man-made ionosphere scintillations on GNSS signal propagation. *Proc. ION GNSS*, 617-625, Portland, OR.

Peng, S., & Morton, Y. (2013). A USRP2-based reconfigurable multi-constellation multi-frequency GNSS software receiver front end. *GPS Solutions*, *17*(1), 89-102.

Pi, X., Mannucci, A. J., Lindqwister, U. J., & Ho, C. M. (1997). Monitoring of global ionospheric irregularities using the worldwide GPS network. *Geophysical Research Letters*, *24*(18), 2283-2286.

Pineda-Sanchez, M., Riera-Guasp, M., Antonino-Daviu, J. A., Roger-Folch, J., Perez-Cruz, J., & Puche-Panadero, R. (2010). Diagnosis of induction motor faults in the fractional Fourier domain. *Instrumentation and Measurement, IEEE Transactions on*, *59*(8), 2065-2075.

Prikryl, P., Jayachandran, P. T., Mushini, S. C., & Chadwick, R. (2011), Climatology of GPS phase scintillation and HF radar backscatter for the high-latitude ionosphere under solar minimum conditions, *Ann. Geophys*., *29*, 377-392.

Pullen, S., G. Opshaug, A. Hansen, T. Walter, P. Enge, B. Parkinson (1998). A preliminary study of the effect of ionospheric scintillation on WAAS user availability in equatorial regions. *Proc. ION GPS, Nashville, TN, 1998.*

Radil, T., Ramos, P. M., Janeiro, F. M., & Serra, A. C. (2008). PQ monitoring system for real-time detection and classification of disturbances in a single-phase power system. *Instrumentation and Measurement, IEEE Transactions on*, *57*(8), 1725-1733.

Rino, C. L., & Fremouw, E. J. (1977). The angle dependence of singly scattered wavefields. *Journal of Atmospheric and Terrestrial Physics*, *39*(8), 859-868.

Rino, C. L. (1979a). A power law phase screen model for ionospheric scintillation: 1. Weak scatter. *Radio Science*, *14*(6), 1135-1145.

Rino, C. L. (1979b). A power law phase screen model for ionospheric scintillation: 2. Strong scatter. *Radio Science*, *14*(6), 1147-1155.

Rino, C. L., & Livingston, R. C. (1982). On the analysis and interpretation of spaced-receiver measurements of transionospheric radio waves. *Radio Science*, *17*(4), 845-854.

Rino, C. L., Livingston, R. C., Tsunoda, R. T., Robinson, R. M., Vickrey, J. F., Senior, C., ... & Klobuchar, J. A. (1983). Recent studies of the structure and morphology of auroral zone F region irregularities. *Radio science*, *18*(6), 1167-1180.

Rino, C. L. (2011). *The theory of scintillation with applications in remote sensing*. John Wiley & Sons. 147-148.

Robusto, C. C. (1957). The cosine-haversine formula. *American Mathematical Monthly*, 38-40.

Seeber, G. (2003). *Satellite geodesy: foundations, methods, and applications*. Walter de Gruytern, Berlin, 277-281.

Semeter, J., Lummerzheim, D., & Haerendel, G. (2001). Simultaneous multispectral imaging of the discrete aurora. *Journal of Atmospheric and Solar-Terrestrial Physics*, *63*(18), 1981-1992.

Shepherd, S. G. (2014), Altitude-adjusted corrected geomagnetic coordinates: Definition and functional approximations, *J. Geophys. Res. Space Physics*, 119, 7501–7521.

Scargle, J. D. (1982). Studies in astronomical time series analysis. II-Statistical aspects of spectral analysis of unevenly spaced data. *The Astrophysical Journal*, *263*, 835-853.

Schuster, A. (1897). On lunar and solar periodicities of earthquakes. *Proceedings of the Royal Society of London*, *61*(369-377), 455-465.

Secan, J. A., Bussey, R. M., Fremouw, E. J., & Basu, S. (1995). An improved model of equatorial scintillation. *Radio Science*, *30*(3), 607-617.

Sejdić, E., Djurović, I., & Jiang, J. (2009). Time–frequency feature representation using energy concentration: An overview of recent advances. *Digital Signal Processing*, *19*(1), 153-183.

Seo, J., Walter, T., Marks, E., Chiou, T. Y., & Enge, P. (2007, June). Ionospheric scintillation effects on GPS receivers during solar minimum and maximum. In *Proceedings of the International Beacon Satellite Symposium* (pp. 11-15).

Shanmugam, S., Jones, J., MacAulay, A., & Van Dierendonck, A. J. (2012). Evolution to modernized GNSS ionospheric scintillation and TEC monitoring. *Proc. IEEE/ION PLANS*, Myrtle Beach, SC.

Singleton, D. G. (1970). Saturation and focusing effects in radio-star and satellite scintillations. *Journal of Atmospheric and Terrestrial Physics*, *32*(2), 187-208.

Singleton, D. G. (1974). Power spectra of ionospheric scintillations. *Journal of Atmospheric and Terrestrial Physics*, *36*(1), 113-133.

Skone, S., Knudsen, K., & De Jong, M. (2001). Limitations in GPS receiver tracking performance under ionospheric scintillation conditions. *Physics and Chemistry of the Earth, Part A: Solid Earth and Geodesy*, *26*(6), 613-621.

Skone, S., Man, F., Ghafoori, F., & Tiwari, R. (2008). Investigation of scintillation characteristics for high latitude phenomena. *Proc. ION GNSS,* Savana, GA.

Smith, A. M., Mitchell, C. N., Watson, R. J., Meggs, R. W., Kintner, P. M., Kauristie, K., & Honary, F. (2008). GPS scintillation in the high arctic associated with an auroral arc. *Space Weather*, *6*(3).

Sojka, J. J., Nicolls, M. J., Heinselman, C. J., & Kelly, J. D. (2009). The PFISR IPY observations of ionospheric climate and weather. *Journal of Atmospheric and Solar-Terrestrial Physics*, *71*(6-7), 771-785.

Spatz, D. E., Franke, S. J., & Yeh, K. C. (1988). Analysis and interpretation of spaced receiver scintillation data recorded at an equatorial station. *Radio Science*, *23*(3), 347-361.

Su, Y., Datta-Barua, S., Bust, G. S., & Deshpande, K. B. (2017). Distributed sensing of ionospheric irregularities with a GNSS receiver array. *Radio Science, 52(8)*, 988-1003.

Suzuki, S., Shiokawa, K., Otsuka, Y., Ogawa, T., & Wilkinson, P. (2004). Statistical characteristics of gravity waves observed by an all-sky imager at Darwin, Australia. *Journal of Geophysical Research: Atmospheres*,*109*(D20).

Taylor, S., Morton, Y., Jiao, Y., Triplett, J., & Pelgrum, W. (2012). An improved ionosphere scintillation event detection and automatic trigger for a GNSS data collection system. *Proc. ION ITM,* Newport Beach, CA.

Taylor, S., Marcus, R.J., Bourne, H., Morton, Y., & Pelgrum, W. (2013). Ionosphere scintillation receiver performances based on high latitude experiments. *Proc. ION Pacific PNT*, Honolulu, HI.

Thébault, E., Finlay, C. C., Beggan, C. D., Alken, P., Aubert, J., Barrois, O., ... & Canet, E. (2015). International geomagnetic reference field: the 12th generation. *Earth, Planets and Space*, *67*(1), 1-19.

Tsunoda, R. T. (1985). Control of the seasonal and longitudinal occurrence of equatorial scintillations by the longitudinal gradient in integrated E region Pedersen conductivity. *Journal of Geophysical Research: Space Physics*,*90*(A1), 447-456.

Tsunoda, R. T. (1988). High-latitude F region irregularities: A review and synthesis. *Reviews of Geophysics, 26*(4), 719-760.

Vacchione, J. D., Franke, S. J., & Yeh, K. C. (1987). A new analysis technique for estimating zonal irregularity drifts and variability in the equatorial F region using spaced receiver scintillation data. *Radio science*, *22*(5), 745-756.

Valladares, C. E., Hagan, M. P., Sheehan, R., & MacKenzie, E. (2002). Studies of ionospheric structures and their effects on systems, Air Force Research Laboratory Report, AFRL-VS-TR-2002-1668.

Van Dierendonck, A. J., Klobuchar, J., & Hua, Q. (1993). Ionospheric scintillation monitoring using commercial single frequency C/A code receivers. *Proc. ION GPS*, 93, 1333-1342.

Van Dierendonck, A. J., Hua, Q., Fenton, P., & Klobuchar, J. (1996). Commercial ionospheric scintillation monitoring receiver development and test results. *Proc. ION GPS,* 573-582, Cambridge, MA.

Van Dierendonck, A. J., & Arbesser-Rastburg, B. (2004). Measuring ionospheric scintillation in the equatorial region over Africa, including measurements from SBAS geostationary satellite signals. *Proc. ION GNSS*, 316, Long Beach, CA.

Van Dierendonck, A. J. (2005). How GPS receivers measure (or should measure) ionospheric scintillation and TEC and how GPS receivers are affected by the ionosphere. *Proc. 11th International Ionospheric Effects Symposium*, Alexandria, VA.

Wang, J., Morton, Y., Zhou, Q., Pelgrum, W., & Van Graas, F. (2012). Time-frequency analysis of ionosphere scintillations observed by a GNSS receiver array. *Proc. IEEE/ION PLANS*, Myrtle Beach, SC.

Wang, J. (2013). Spectral characterization of ionosphere scintillation: algorithms and applications. *Master Thesis*, Miami University, Oxford.

Wang, J., Morton, Y., Spaleta, J. & Bristow W (2014)., Spatial Characterization of High Latitude Ionosphere Scintillation Using an Array of Software Receiver Measurements *Proc. ION GNSS+ 2014*, Tampa, FL.

Wang, J., & Morton, Y. T. (2015). High-Latitude Ionospheric Irregularity Drift Velocity Estimation Using Spaced GPS Receiver Carrier Phase Time–Frequency Analysis. *IEEE Transactions on Geoscience and Remote Sensing*, *53*(11), 6099-6113.

Wang, J., Morton, Y., Spaleta, J. & Bristow W (2016). A Comparative Study of Ionospheric Irregularity Drift Velocity using a GNSS Receiver Array and SuperDARN at High Latitude. *Proc. ION ITM 2016*, Monterey, CA.

Wang, J., & Morton, Y. T. (2017). A Comparative Study of Ionospheric Irregularity Drift Velocity Derived from a GNSS Receiver Array and PFISR Measurements during High Latitude Ionospheric Scintillation. *J. Geophys. Res. Space Physics*, 122, 2017. doi:10.1002/3028JA024015.

Wang, J., Morton, Y. J., & Hampton, D. (2018). New Results on Ionospheric Irregularity Drift Velocity Estimation Using Multi-GNSS Spaced-Receiver Array During High-Latitude Phase Scintillation. *Radio Science*, *53*(2), 228-240.

Wang, J., & Morton, Y. J. (2018a). A Hybrid Correlation Model for the Spaced-Receiver Technique. Submitted to *Radio Science*.

Wang, J., & Morton, Y. J. (2018b). An Inversion Algorithm for Estimating the Effective Irregularity Height under the Anisotropy Model during High Latitude Ionospheric Scintillation. Submitted to *J. Geophys. Res. Space Physics*.

Wernik, A. W., Liu, C. H., & Yeh, K. C. (1983). Modeling of spaced-receiver scintillation measurements. *Radio science*, *18*(5), 743-764.

Xu, D., & Morton, Y. (2015). GPS signal fading and carrier phase variations during strong equatorial ionospheric scintillation, Proc. ION ITM, Dana Point, CA.

Xu, D., & Morton, Y. T. (2017). A Semi-Open Loop GNSS Carrier Tracking Algorithm for Monitoring Strong Equatorial Scintillation. *IEEE Transactions on Aerospace and Electronic Systems*.

Yeh, K. C., & Liu, C. H. (1982). Radio wave scintillations in the ionosphere. *Proceedings of the IEEE*, *70*(4), 324-360.

Zhang, L., & Morton, Y. (2013). GPS Carrier Phase Spectrum Estimation for Ionospheric Scintillation Studies. *Navigation*, *60*(2), 113-122.

Zhang, Z., Chan, S. C., & Wang, C. (2012). A new regularized adaptive windowed Lomb periodogram for time–frequency analysis of nonstationary signals with impulsive components. *Instrumentation and Measurement, IEEE Transactions on*, *61*(8), 2283-2304.

Zhao, J., & Zhou, C. (2018). On the optimal height of ionospheric shell for single-site TEC estimation. *GPS Solutions*, *22*(2), 48.

Zhou, Q., Brenneman, M., & Morton, Y. (2008). Analysis of EEG data using an adaptive periodogram technique. In *BioMedical Engineering and Informatics, 2008. BMEI 2008. International Conference on* (Vol. 2, pp. 353-357). IEEE.

APPENDIX

A. MMSE Solution for the Front Velocity Model

Denote the true MMSE solution $\boldsymbol{V}_f = (x, y)$ in a Cartesian velocity plane. Let the center of each potential solution circle be at $\boldsymbol{c}_{ij} = (x_{ij}, y_{ij})$, and let $i < j$ to remove redundancy. For example, $c_{12} = (x_{12}, y_{12})$ denotes the center of the solution circle obtained from d_{12} and t_{12}. The radius of each circle is given by $r_{ij} = d_{ij}/2\tau_{ij}$. The formula describing each circle with an error term ε_{ij} is given by:

$$r_{ij} = \sqrt{(x_{ij} - x)^2 + (y_{ij} - y)^2} + \varepsilon_{ij} = \left\|\boldsymbol{c}_{ij} - \boldsymbol{V}_f\right\| + \varepsilon_{ij} \quad \text{(A-1)}$$

Let $\boldsymbol{V}_0 = (x_0, y_0)$ be the initial guess of the solution to front velocity. Let $r_{0,ij}$ be the corresponding distances from the initial guess to each center of the circles. Then there is:

$$r_{0,ij} = \left\|\boldsymbol{c}_{ij} - \boldsymbol{V}_0\right\| \quad \text{(A-2)}$$

Let $\delta\boldsymbol{V} = (\delta x, \delta y)$ represent the difference between the true velocity and the guessed velocity. Then there is $\boldsymbol{V}_f = \boldsymbol{V}_0 + \delta\boldsymbol{V}$. We now develop a system of linear equations in which $\delta\boldsymbol{V}$ is the unknown to be determined. The difference between $r_{0,ij}$ and r_{ij} is given by δr_{ij}, where:

$$\delta r_{ij} = r_{ij} - r_{0,ij} \quad \text{(A-3)}$$

$$= \left\|\boldsymbol{c}_{ij} - \boldsymbol{V}_f\right\| + \varepsilon_{ij} - \left\|\boldsymbol{c}_{ij} - \boldsymbol{V}_0\right\| \quad \text{(A-4)}$$

$$\approx \frac{(\boldsymbol{c_{ij}} - \boldsymbol{V}_0)}{\left\|\boldsymbol{c_{ij}} - \boldsymbol{V}_0\right\|} \cdot \delta\boldsymbol{V} + \varepsilon_{ij} \quad \text{(A-5)}$$

$$= -\mathbf{1}_{ij} \cdot \delta\boldsymbol{V} + \varepsilon_{ij} \quad \text{(A-6)}$$

where a Taylor series approximation of a vector norm has been used to linearize the problem in Equation A-5. Here, $\mathbf{1}_{ij}$ is a shorthand notation for the term $(\boldsymbol{c}_{ij} - \boldsymbol{V}_0)/\left\|\boldsymbol{c}_{ij} - \boldsymbol{V}_0\right\|$.

Based on Equation A-6, the set of $\binom{N}{2}$ linearized equations can be written in a matrix form as:

$$\delta \boldsymbol{r} = \begin{bmatrix} \delta r_{12} \\ \delta r_{13} \\ \delta r_{14} \\ \vdots \\ \delta r_{N-1N} \end{bmatrix} = \begin{bmatrix} (-\mathbf{1}_{12})^T \\ (-\mathbf{1}_{13})^T \\ (-\mathbf{1}_{14})^T \\ \vdots \\ (-\mathbf{1}_{N-1N})^T \end{bmatrix} \begin{bmatrix} \delta x \\ \delta y \end{bmatrix} + \begin{bmatrix} \varepsilon_{12} \\ \varepsilon_{13} \\ \varepsilon_{14} \\ \vdots \\ \varepsilon_{N-1N} \end{bmatrix} \tag{A-7}$$

or more compactly as:

$$\delta \boldsymbol{r} = G \delta \boldsymbol{V}^T + \boldsymbol{\varepsilon} \tag{A-8}$$

where

$$G = \begin{matrix} (-\mathbf{1}_{12})^T \\ (-\mathbf{1}_{13})^T \\ (-\mathbf{1}_{14})^T \\ \vdots \\ (-\mathbf{1}_{N-1N})^T \end{matrix}, and\ \boldsymbol{\varepsilon} = \begin{bmatrix} \varepsilon_{12} \\ \varepsilon_{13} \\ \varepsilon_{14} \\ \vdots \\ \varepsilon_{N-1N} \end{bmatrix} \tag{A-9}$$

For an over-determined system, the MMSE solution $\delta \boldsymbol{V}$ is that which minimizes the sum of squared residuals: $\min \|\delta \boldsymbol{r} - G \delta \boldsymbol{V}^T\|^2$. And the solution is given by:

$$\delta \widehat{\boldsymbol{V}}^T = (G^T G)^{-1} G^T \delta \boldsymbol{r} \tag{A-10}$$

The new, improved estimate of the front velocity is now:

$$\widehat{\boldsymbol{V}}_f = \boldsymbol{V}_0 + \delta \widehat{\boldsymbol{V}} \tag{A-11}$$

The observation equations may now be linearized about these new estimates of the front velocity. This process can be iterated many times to get closer to the best MMSE solution, when the change in the estimates is sufficiently small.

B. Anisotropy Parameters Estimation

We formulate the correlation model according to the forward propagated diffraction pattern as in Equation 5-21. It is more convenient to rewrite Equation 5-21 in terms of the matrix form:

$$f^2(\Delta\boldsymbol{\rho}_s) = \Delta\boldsymbol{\rho}_s{}^T \mathcal{E} \Delta\boldsymbol{\rho}_s \qquad \text{(B-1)}$$

where $\mathcal{E}$ is a 2×2 matrix:

$$\mathcal{E} = \frac{1}{AC - B^2/4}\begin{bmatrix} C & -B/2 \\ -B/2 & A \end{bmatrix} \qquad \text{(B-2)}$$

For a system of n spaced receivers, the total number of correlation functions is n^2. Denote each correlation function as $R_{ij}(\Delta t)$, where i and j represent specific receiver pairs with $i, j = 1, 2, \ldots, n$. This includes both auto-correlation functions $(i = j)$ and cross-correlation functions $(i \neq j)$. Based on the model described in the previous section, these correlation functions will take the general form:

$$R_{ij}(\Delta t) = R_{ij}\left[f\left(\Delta\boldsymbol{\rho}_{ij} - \mathbf{v}_s\Delta t\right);\ \Delta t\right] \qquad \text{(B-3)}$$

In the next step, these correlation functions are paired with each other to reveal more information about the anisotropy. For the convenience of problem formulation, the n^2 correlation functions are indexed consecutively from 1 to n^2 based on cardinality. For example, the auto-correlation function R_{11} is now labeled as R^1, and the cross-correlation function R_{13} is now labeled as R^3. Then Equation B-3 can be rewritten as the following form using a single superscript notation:

$$R^i(\Delta t) = R[f\left(\Delta\boldsymbol{\rho}^{(i)} - \mathbf{v}_s\Delta t\right);\ \Delta t] \qquad \text{(B-4)}$$

where i takes the values from 1 to n^2.

Following the method of *Armstrong and Coles* [1972], the intercept time delay τ_{jk} between any pair of correlation functions is identified by:

$$R\left[f\left(\Delta\boldsymbol{\rho}^{(j)} - \mathbf{v}_s\tau_{jk}\right);\ \tau_{jk}\right] = R\left[f\left(\Delta\boldsymbol{\rho}^{(k)} - \mathbf{v}_s\tau_{jk}\right);\ \tau_{jk}\right] \qquad \text{(B-5)}$$

By using the same matrix notation used in the previous section, it follows that Equation B-5 holds only if:

$$\left(\Delta\boldsymbol{\rho}^{(j)} - \mathbf{v}_s\tau_{jk}\right)^T \mathcal{E}\left(\Delta\boldsymbol{\rho}^{(j)} - \mathbf{v}_s\tau_{jk}\right) = \left(\Delta\boldsymbol{\rho}^{(k)} - \mathbf{v}_s\tau_{jk}\right)^T \mathcal{E}\left(\Delta\boldsymbol{\rho}^{(k)} - \mathbf{v}_s\tau_{jk}\right) \qquad \text{(B-6)}$$

or

$$\mathbf{v}_s{}^T \mathcal{E}\left(\Delta\boldsymbol{\rho}^{(j)} - \Delta\boldsymbol{\rho}^{(k)}\right) = \frac{1}{2\tau_{jk}}\left[\Delta\boldsymbol{\rho}^{(j)T}\mathcal{E}\Delta\boldsymbol{\rho}^{(j)} - \Delta\boldsymbol{\rho}^{(k)T}\mathcal{E}\Delta\boldsymbol{\rho}^{(k)}\right] \qquad \text{(B-7)}$$

If $\mathcal{E}$, the anisotropy term is known, then the above equation constitutes an over-determined system while $\mathbf{v}_s$ can be solved using the least squares method [*Armstrong and Coles*, 1972; *Rino and Livingston*, 1982]. In order to determine the anisotropy parameters, another set of equations are introduced by considering the time lag τ_i produced when the correlation between a receiver pair is at maximum, including auto-correlation with the receiver itself, which leads to $\tau_i = 0$. Note that for a cross-correlation, τ_i is exactly the time lag used to determine the apparent velocity in the previous sections. By direct computation under the frozen-in assumption, *Rino and Livingston* [1982] showed that τ_i must satisfy the relation:

$$\mathbf{v}_s{}^T \mathcal{E}\Delta\boldsymbol{\rho}^{(i)} = \tau_i \boldsymbol{v}_{\text{eff}}^2 \qquad \text{(B-8)}$$

where

$$\boldsymbol{v}_{\text{eff}} = f(\mathbf{v}_s) = \left(\frac{C\mathrm{v}_{s_x}^2 - B\mathrm{v}_{s_x}\mathrm{v}_{s_y} + A\mathrm{v}_{s_x}^2}{AC - B^2/4}\right)^{1/2} \qquad \text{(B-9)}$$

By substituting Equation B-8 into Equation B-7, there is:

$$\Delta\boldsymbol{\rho}^{(j)T}[\mathcal{E}/\boldsymbol{v}_{\text{eff}}^2]\Delta\boldsymbol{\rho}^{(j)} - \Delta\boldsymbol{\rho}^{(k)T}[\mathcal{E}/\boldsymbol{v}_{\text{eff}}^2]\Delta\boldsymbol{\rho}^{(k)} = 2\tau_{jk}(\tau_j - \tau_k) \qquad \text{(B-10)}$$

This system of equation is in general over-determined, hence can be used to solve for $[\mathcal{E}/\boldsymbol{v}_{\text{eff}}^2]$ using least squares. Moreover, knowing $[\mathcal{E}/\boldsymbol{v}_{\text{eff}}^2]$ is sufficient to determine $\mathbf{v}_s$ in the

system of equations described by Equation B-8, as we can simply divide both sides by an arbitrary $\boldsymbol{v}_{\text{eff}}^2$ to turn $\mathcal{E}$ into $[\mathcal{E}/\boldsymbol{v}_{\text{eff}}^2]$. To better formulate the system of equations into a least squares problem, Equation B-10 is rewritten in a more compact form by defining the $N_I \times 3$ matrix:

$$\mathcal{D} = \begin{bmatrix} D_{xx}^{(1)} & D_{xy}^{(1)} & D_{yy}^{(1)} \\ \vdots & \vdots & \vdots \\ D_{xx}^{(N_I)} & D_{xy}^{(N_I)} & D_{yy}^{(N_I)} \end{bmatrix} \tag{B-11}$$

with the elements

$$D_{xx}^{(i)} = \Delta\rho_x^{(j)^2} - \Delta\rho_x^{(k)^2} \tag{B-12}$$

$$D_{xy}^{(i)} = \Delta\rho_x^{(k)}\Delta\rho_y^{(j)} - \Delta\rho_x^{(j)}\Delta\rho_y^{(k)} \tag{B-13}$$

$$D_{yy}^{(i)} = \Delta\rho_y^{(j)^2} - \Delta\rho_y^{(k)^2} \tag{B-14}$$

where i takes on all $N_I = (n^4 + 3n^2 - 2n)/4$ admissible pairs of intersection points, while j and k correspond to the indexed receiver pairs. We also define the $N_I \times 1$ vector:

$$\mathbf{T} = \left[2\tau_{jk}^{(1)}\left(\tau_j^{(1)} - \tau_k^{(1)}\right), \ldots, 2\tau_{jk}^{(N_I)}\left(\tau_j^{(N_I)} - \tau_k^{(N_I)}\right)\right]^T \tag{B-15}$$

and the 3×1 vector

$$\mathbf{X} = [C/E, B/E, A/E\,]^T \tag{B-16}$$

where

$$E = \boldsymbol{v}_{\text{eff}}^2(AC - B^2/4) \tag{B-17}$$

Now, the system of equations described by Equation B-10 can be written in matrix form as

$$\mathcal{D}\mathbf{X} = \mathbf{T} \tag{B-18}$$

which has the least squares solution:

$$\hat{X} = [\mathcal{D}^T\mathcal{D}]^{-1}\mathcal{D}^T T \tag{B-19}$$

It should be noted that knowing $\widehat{\mathbf{X}} \approx [C/E, B/E, A/E\,]^T$ is equivalent as knowing $[\mathcal{E}/\boldsymbol{v}_{\text{eff}}^2]$, since

$$\frac{\mathcal{E}}{v_{eff}^2} = \frac{1}{v_{eff}^2(AC - B^2/4)}\begin{bmatrix} C & -B/2 \\ -B/2 & A \end{bmatrix} = \begin{bmatrix} C/E & -B/2E \\ -B/2E & A/E \end{bmatrix} \quad \text{(B-20)}$$

Based on Equation B-8, the following relationship can be established:

$$\mathbf{v}_s{}^T[\mathcal{E}/\boldsymbol{v}_{\text{eff}}^2]\left(\Delta\boldsymbol{\rho}^{(j)} - \Delta\boldsymbol{\rho}^{(k)}\right) = \tau_j - \tau_k \quad \text{(B-21)}$$

As discussed before, we now can solve this system of equations using the solved $[\mathcal{E}/\boldsymbol{v}_{\text{eff}}^2]$. Similarly, we first define the $N_I \times 2$ matrix:

$$\mathcal{J} = \begin{bmatrix} I_x^{(1)} & I_y^{(1)} \\ \vdots & \vdots \\ I_x^{(N_I)} & I_y^{(N_I)} \end{bmatrix} \quad \text{(B-22)}$$

where

$$I_x^{(i)} = \frac{C}{E}\left(\Delta\rho_x^{(j)} - \Delta\rho_x^{(k)}\right) - \frac{B}{2E}\left(\Delta\rho_y^{(j)} - \Delta\rho_y^{(k)}\right) \quad \text{(B-23)}$$

$$I_y^{(i)} = -\frac{B}{2E}\left(\Delta\rho_x^{(j)} - \Delta\rho_x^{(k)}\right) + \frac{A}{E}\left(\Delta\rho_y^{(j)} - \Delta\rho_y^{(k)}\right) \quad \text{(B-24)}$$

and the $N_I \times 1$ vector $\boldsymbol{\chi}$ with elements:

$$\chi^{(i)} = \tau_j^{(i)} - \tau_k^{(i)} \quad \text{(B-25)}$$

together with the 2×1 vector $\mathbf{v}_s = [\mathrm{v}_{s_x}, \mathrm{v}_{s_y}]^T$ to be solved for.

Equation B-21 can now be written in matrix form as:

$$\mathcal{J}v_s = \chi \quad \text{(B-26)}$$

which has the least squares solution:

$$\hat{\mathbf{v}}_s = [\mathcal{J}^T\mathcal{J}]^{-1}\mathcal{J}^T\boldsymbol{\chi} \quad \text{(B-27)}$$

Equations B-19 and B-27 give the scaled anisotropy by $\boldsymbol{v}_{\text{eff}}^2$ and the true pattern velocity derived from a set of receiver temporal correlation functions.

To review this process, we first generate all auto-correlation and cross-correlation functions from the n spaced-receiver measurements. Next, we determine τ_i, the time lag at which each

correlation functions achieves its maximum value. Then, we determine the $N_I = (n^4 + 3n^2 - 2n)/4$ admissible pairs of intersection points between any receiver pair. With all these information, we can finally formulate the least square problem for solving the scaled anisotropy and the true irregularity pattern velocity.

In general, however, not all possible intersections can be computed accurately. *Rino and Livingston* [1982] discussed two situations on this issue. First, if the correlation time is long compared with the data interval, then small errors in the correlation function estimate can lead to large errors in τ_{jk}. To avoid this situation, one can reject intersections that lie outside a preselected subinterval within the correlation time. Second, at the other extreme of short correlation times, τ_{jk} would fall into the noise. To avoid this situation, one can reject τ_{jk} values that occur beyond some preselected decorrelation time, typically the time to 70% decorrelation.